

**STRONG SCATTERING OF
ULTRASONIC WAVES IN
FLUIDIZED SUSPENSIONS:
WAVE PROPAGATION,
SPECTROSCOPY TECHNIQUES
AND PARTICLE DYNAMICS**

By

MICHAEL L. COWAN

**A Thesis
Submitted to the Faculty of Graduate Studies
in Partial Fulfillment of the Requirements
for the Degree of**

DOCTOR OF PHILOSOPHY

**Department of Physics and Astronomy
University of Manitoba
Winnipeg, Manitoba**

© June, 2001



National Library
of Canada

Acquisitions and
Bibliographic Services

395 Wellington Street
Ottawa ON K1A 0N4
Canada

Bibliothèque nationale
du Canada

Acquisitions et
services bibliographiques

395, rue Wellington
Ottawa ON K1A 0N4
Canada

Your file Votre référence

Our file Notre référence

The author has granted a non-exclusive licence allowing the National Library of Canada to reproduce, loan, distribute or sell copies of this thesis in microform, paper or electronic formats.

L'auteur a accordé une licence non exclusive permettant à la Bibliothèque nationale du Canada de reproduire, prêter, distribuer ou vendre des copies de cette thèse sous la forme de microfiche/film, de reproduction sur papier ou sur format électronique.

The author retains ownership of the copyright in this thesis. Neither the thesis nor substantial extracts from it may be printed or otherwise reproduced without the author's permission.

L'auteur conserve la propriété du droit d'auteur qui protège cette thèse. Ni la thèse ni des extraits substantiels de celle-ci ne doivent être imprimés ou autrement reproduits sans son autorisation.

0-612-62630-X

Canada

THE UNIVERSITY OF MANITOBA
FACULTY OF GRADUATE STUDIES

COPYRIGHT PERMISSION PAGE

**Strong Scattering of Ultrasonic Waves in Fluidized Suspensions: Wave Propagation,
Spectroscopy Techniques and Particle Dynamics**

BY

Michael L. Cowan

**A Thesis/Practicum submitted to the Faculty of Graduate Studies of The University
of Manitoba in partial fulfillment of the requirements of the degree
of
Doctor of Philosophy**

Michael L. Cowan@ 2001

**Permission has been granted to the Library of The University of Manitoba to lend or sell
copies of this thesis/practicum, to the National Library of Canada to microfilm this
thesis/practicum and to lend or sell copies of the film, and to Dissertations Abstracts
International to publish an abstract of this thesis/practicum.**

**The author reserves other publication rights, and neither this thesis/practicum nor
extensive extracts from it may be printed or otherwise reproduced without the author's
written permission.**

Abstract

This thesis presents the results of three main experimental projects; a study of ultrasonic wave propagation in strongly scattering materials, the use of the results of this first study to develop new techniques in ultrasonic correlation spectroscopy, and the use of these techniques to measure the dynamics of particles in fluidized beds. The first project involves the investigation of wave propagation in random, inhomogeneous materials that scatter ultrasound strongly (i.e. materials where the scattering mean free path is comparable to the ultrasonic wavelength λ). I have measured the velocities of the weak ballistic pulse that travels through these materials without scattering out of the forward direction. In the intermediate frequency regime, where $\lambda \sim$ the size of the scatterer, these measurements reveal strong dispersion in the ballistic modes, caused by both resonant scattering in the material and tortuosity effects. The dependence of the dispersion on the volume fraction of scatterers is investigated; very good agreement between the ballistic velocities and an effective medium theory, based on a spectral function approach, is found at all volume fractions. The diffusion approximation for the scattered waves is tested by measuring the ensemble-averaged transmitted intensity in pulsed ultrasonic experiments. The volume fraction dependence of the wave diffusion coefficient and the absorption time is investigated experimentally, and parameters that govern diffusive propagation are modeled using an extension of the spectral function approach.

Using the results of this wave propagation study, we have developed two new

ultrasonic spectroscopy techniques. Dynamic Sound Scattering (DSS) uses singly scattered sound to measure the rms velocity of scatterers. Diffusing Acoustic Wave Spectroscopy (DAWS) uses multiply scattered sound, described by the diffusion approximation, to measure the relative motion of scatterers. This thesis explains the underlying principles governing these techniques and the ways that these techniques can be implemented in practice to provide powerful new methods for investigating the dynamics of strongly scattering materials. I also take advantage of the ability of ultrasonic detectors to detect the wave field directly to test the Siegert relation. The Siegert relation is a simple relationship between the field and intensity temporal autocorrelation functions, and is frequently used in the interpretation of analogous light scattering techniques. I have elucidated the conditions under which the Siegert relation is obeyed through a systematic study of this basic wave relation for both single and multiple scattering. We also take advantage of our ability to measure the phase of the scattered waves, and show how the statistics underlying their temporal fluctuations can be used to investigate the scatterer's dynamics.

Using DAWS and DSS, I have investigated the dynamics of particles suspended against sedimentation by a fluid flowing upwards in a fluidized bed. Since ultrasonic wavelengths are on the order of millimeters, the suspensions that can be probed contain particles with diameters on the millimeter scale; this corresponds to a regime that is of interest in industrial applications. Thus DAWS and DSS are well suited to the high Reynolds number, high volume fraction suspensions to which other current techniques are least suited. In our experiments, the velocity fluctuations and velocity correlation lengths

are measured as a function of the volume fraction and sample size for a range of Reynolds numbers. At high volume fractions of particles ($\phi > 0.15$), we find surprisingly large values of the rms velocity fluctuations and instantaneous correlation length, with a different dependence on volume fraction to that seen at low ϕ . The relationship between the velocity and correlation length is explained for all volume fractions by accounting for the fundamental importance of number fluctuations in setting the scale of the dynamics. As the sample size is increased, simple scaling theories predict that the velocity fluctuations will diverge, but some experiments and simulations have suggested that the fluctuations may saturate for large samples. The exact nature of this saturation, and what sets the magnitude of the velocity correlation length that cuts off this divergence, is not well understood; our experiments address this question. At low Reynolds numbers, I find convincing evidence of the importance of cell walls in setting the magnitude of the correlation length, and hence the velocity fluctuations. Furthermore, by measuring all three components of the rms velocity fluctuations, I have discovered simple scaling laws for their dependence on the thinnest dimension of the cell that have not been expected in previous theoretical work. At higher Reynolds numbers, I show that inertial effects modify the dynamics at all length scales, and can be the limiting factor in determining the correlation length. Thus our experiments make a significant contribution in elucidating the mechanisms involved in determining the velocity correlation length, and hence the remarkably large velocity fluctuations, in fluidized suspensions.

Acknowledgements

First I would like to thank my supervisor John H. Page, whose tireless guidance and unselfish support was much appreciated throughout the course of this work.

I would also like to thank Gilles Roy and all of the technical staff, without whose help the experimental work would have been much less enjoyable.

A special thank you to my family, who encouraged me during the many years of my studies.

And finally to my wife; I don't know if I would have made it through this final year without your love and support.

Table of Contents

List of Figures	(x)
List of Tables	(xiv)
1. Introduction	1
1.1 Strong Scattering of Classical Waves	2
1.2 Fluidized and Sedimenting Particles	7
1.3 Structure of the Thesis	9
2. Theory	10
2.1 Ballistic Transport	11
2.1.1 Pulses in Dispersive Media	11
2.1.2 The Wave Equation and Green's Functions	15
2.1.3 The Spectral Function Approach	20
2.2 Diffusive Transport	29
2.2.1 Diffusion Theory	29
2.2.2 Boundary Conditions	32
2.2.3 Calculation of Diffusion Parameters	34
2.3 Temporal Autocorrelations	37
2.3.1 Dynamic Sound Scattering (DSS)	37
2.3.2 Diffusing Acoustic Wave Spectroscopy (DAWS)	41
2.3.3 Continuous Wave DAWS	47
2.3.4 Phase Difference Statistics	48
2.3.5 Siegert Relation	50
2.4 Suspended Particle Motion	55
2.4.1 Sedimentation and Fluidization	55
2.4.2 Velocity Fluctuations and Correlations	58
3. Apparatus	65
3.1 Mechanical Apparatus	66
3.1.1 Water Tanks	66
3.1.2 Temperature Control Systems	68

3.1.3 Pumping System	69
3.2 Sample Preparation	72
3.2.1 Fluidized Bed Construction	72
3.2.2 Glass Beads	76
3.2.3 Fluids	77
3.3 Generation and Detection of Ultrasound	79
3.3.1 Piezo-Electric Effect	79
3.3.2 Plane Wave Immersion Transducers	79
3.3.3 Focusing Immersion Transducers	85
3.3.4 Hydrophones	86
3.4 Generating Electronics	87
3.4.1 Overview	87
3.4.2 Fluke Frequency Synthesizer	88
3.4.3 Stanford Delay Generator	88
3.4.4 Mixers	89
3.4.5 AR Power Amplifier	89
3.4.6 Alan and Telonic Attenuators	90
3.4.7 Power Splitters	90
3.5 Receiving Electronics	91
3.5.1 Overview	91
3.5.2 Matec Receiver Amplifier	92
3.5.3 LC Filters	92
3.5.4 Tektronics Digital Oscilloscope	93
3.5.5 Gage Digital Oscilloscope	93
3.5.6 Boxcar Integrators	94
4. Experiments	95
4.1 Pulsed Transmission Measurements	96
4.1.1 Setup	96
4.1.2 Ballistic Measurements	98
4.1.3 Diffusive Measurements	105
4.2 DAWS Field Measurements	108
4.2.1 Pulsed Measurements	108
4.2.2 Continuous Wave Measurements	118
4.3 DSS Near-Field Measurements	122

4.4 DSS Far-Field Measurements	124
4.5 Phase Measurements	130
4.5.1 Setup	130
4.5.2 Phase and Amplitude Extraction	131
4.6 Simultaneous Intensity and Field Measurements	137
4.7 Non-Linearity Tests	140
5. Results and Discussion	143
5.1 Wave Propagation	144
5.1.1 Ballistic Propagation in Glass Bead Suspensions	144
5.1.2 Scattering in Glass Bead Suspensions	155
5.2 Spectroscopy Techniques	166
5.2.1 Diffusing Acoustic Wave Spectroscopy	166
5.2.1.1 Test of the Approximations	166
5.2.1.2 Comparison of Transmission Techniques	170
5.2.2 Dynamic Sound Scattering	173
5.2.2.1 Test of the Far-Field Technique	173
5.2.2.2 Comparison of DSS Techniques	175
5.2.3 Phase Measurements	177
5.2.3.1 Wrapped Phase Statistics	177
5.2.3.2 Cumulative Phase Statistics	183
5.2.4 Siegert Relation	185
5.2.4.1 Single Scattering Test	185
5.2.4.2 Pulsed DAWS Test	192
5.2.4.3 Continuous Wave Test	198
5.3 Fluidized Bed Dynamics	200
5.3.1 Fluidization Velocities	201
5.3.2 Cell Uniformity	203
5.3.3 RMS Velocities	205
5.3.4 Local Relative Velocity Fluctuations	212
5.3.5 Velocity Correlation Lengths	219
5.3.6 Discussion of the Volume Fraction Dependence	224
5.3.7 Sample Size Dependence	234
5.3.8 Reynolds Number Dependence	249
6. Conclusions	266

6.1 Wave Propagation	266
6.2 Spectroscopy Techniques	268
6.3 Fluidized Bed Dynamics	271
Appendices	276
A. Average Wall Reflection Coefficient	276
B. DAWS Wall Timing Corrections	279
C. Near-Field DSS Calculations	282
D. Ballistic Results used in DAWS and DSS	290
References	295

List of Figures

1.1.1 Speckle pattern	6
2.1.1 Pulse propagation in dispersive media	12
2.1.2 Coated sphere model	24
2.1.3 Spectral function calculations	27
2.2.1 Random walk paths and the diffusion approximation	31
2.3.1 Single scattering paths with moving scatterers	40
2.3.2 Multiple scattering paths with moving scatterers	41
2.4.1 Sample cell geometry	62
3.1.1 Small tank geometry	66
3.1.2 Large tank geometry	67
3.1.3 Small tank pumping system	70
3.1.4 Large tank pumping system	71
3.2.1 Small fluidized bed design	72
3.2.2 Large fluidized bed design	74
3.2.3 Stability of fluidized beds	75
3.3.1 Plane wave transducer design	80
3.3.2 Geometry for a thin disk radiator	81
3.3.3 Thin disk radiator intensity, on the z-axis	83
3.3.4 Plane wave transducer beam pattern	84
3.3.5 Focusing transducer design and beam pattern	85
3.4.1 Generating electronics	87
3.4.2 Pulses with the Stanford	89
3.5.1 Receiving electronics	91
3.5.2 LC filter schematic	92
4.1.1 Setup for pulsed propagation measurements	97
4.1.2 Averaging the transmitted field	98

4.1.3 Determining the scattering mean free path	101
4.1.4 Digital filtering of short ballistic pulses	103
4.1.5 Removing the ballistic component from the transmitted field	106
4.2.1 DAWS field measurements setup	109
4.2.2 Pulsed DAWS sampling times	110
4.2.3 Pulsed DAWS field fluctuations	111
4.2.4 DAWS wall corrections	113
4.2.5 Relative mean square displacements	115
4.2.6 Noise effects	117
4.2.7 CW and pulsed mean square displacements	120
4.3.1 DSS near-field calculation	123
4.4.1 DSS far-field geometry	124
4.4.2 DSS reflection electronics	125
4.4.3 Beam spread for vertical and horizontal geometry	126
4.4.4 Effect of the finite pulse width on the spread of scattering angles	127
4.4.5 Reflection scattering angles	128
4.5.1 Phase measurement electronics	131
4.5.2 Fluctuations in the amplitude	133
4.5.3 Fluctuations in the wrapped phase	134
4.5.4 Fluctuations in the cumulative phase	135
4.6.1 Electronics for amplitude and field measurements	137
4.6.2 Amplitude and field fluctuations	138
4.7.1 Dependence of the phase velocity and transmission on input amplitude	141
4.7.2 Check for frequency doubling	142
5.1.1 Phase velocity data	145
5.1.2 Group velocity data	146
5.1.3 Scattering mean free path data	147
5.1.4 Average energy density calculation	151

5.1.5	Spatial distribution of the sound energy in a coated sphere	154
5.1.6	Calculated ratio of I^* to I_s	156
5.1.7	Calculated ratio of v_E to v_g	157
5.1.8	Ensemble-averaged intensity and fits of diffusion theory for $L_z = 12.8\text{mm}$	159
5.1.9	Ensemble-averaged intensity and fits of diffusion theory for $L_z = 36.5\text{mm}$	160
5.1.10	Diffusion coefficients from the fits	162
5.1.11	Absorption length vs. volume fraction	163
5.1.12	Absorption length vs. frequency	165
5.2.1	Relative mean square displacements at different sampling times	167
5.2.2	Measured relative mean square velocity versus the number of scatterings	169
5.2.3	Comparison of point source and plane wave configurations	171
5.2.4	Far-field single scattering test	173
5.2.5	Far-field reflection geometry test	175
5.2.6	Transmitted phase probability distribution in a multiply scattering sample	177
5.2.7	Phase difference probability distribution at four different τ	179
5.2.8	Phase difference probability distribution at an early time	180
5.2.9	Mean square transmitted phase change vs. mean square phase change of a path	181
5.2.10	Comparison of field and phase methods	182
5.2.11	Cumulative phase difference probability distribution	184
5.2.12	Siegert comparison of the singly scattered field and intensity correlation functions	185
5.2.13	Spatial correlations derived from the failure of the Siegert relation	186
5.2.14	Scattering volume geometry	187
5.2.15	Particle separation calculation	189
5.2.16	Single scattering, particle separation distribution	191
5.2.17	Multiply scattered pulsed Siegert comparison, $\phi = 0.245$	192
5.2.18	Multiply scattered pulsed Siegert comparison, $\phi = 0.30$	193

5.2.19	Multiply scattered pulsed Siegert comparison, $\phi = 0.50$	194
5.2.20	Siegert deviations vs. number of scattering events	195
5.2.21	Multiply scattered continuous wave, Siegert comparison	198
5.3.1	Fluidization velocities and fit	202
5.3.2	Local volume fraction vs. height in the cell	204
5.3.3	Examples of single scattering field autocorrelation functions	206
5.3.4	RMS velocities normalized by V_o	208
5.3.5	Ratio of the rms velocity components	209
5.3.6	RMS velocities normalized by V_f	211
5.3.7	Examples of instantaneous velocity correlations from DAWS and DSS	213
5.3.8	Scaled velocity correlations	215
5.3.9	Transport mean free paths compared to the average particle separation	216
5.3.10	Local relative velocity fluctuations and strain rate	218
5.3.11	Components of the dynamic velocity correlation lengths	220
5.3.12	Instantaneous and dynamic velocity correlation lengths	223
5.3.13	“Blob” model of the volume fraction scaling	228
5.3.14	Local dynamics model of the volume fraction scaling	233
5.3.15	RMS velocity components for all L_z	235
5.3.16	L_z dependence of the RMS velocities	236
5.3.17	Dynamic correlation length components for all L_z	238
5.3.18	Full dynamic correlation length for all L_z	239
5.3.19	Instantaneous correlation length for all L_z	240
5.3.20	Scaling of the correlation lengths with L_z	242
5.3.21	Scaling of the x - z anisotropy with L_z	244
5.3.22	Comparison of our data with other techniques	246
5.3.23	RMS velocity components at different Reynolds numbers	250
5.3.24	Ratios of the velocity components	252
5.3.25	Full rms velocity at different Reynolds numbers	253

5.3.26	Dynamic correlation lengths at different Reynolds numbers	255
5.3.27	The 3d dynamic correlation lengths at different Reynolds numbers	256
5.3.28	Local rms relative velocity at different Reynolds numbers	257
5.3.29	The instantaneous correlation lengths at different Reynolds numbers	259
5.3.30	Scaling of the velocity with L_z and Re	261
5.3.31	Scaling of the correlation lengths with L_z and Re	262
5.3.32	Volume fraction scaling as a function of Re	265
A.1	Wall geometry for reflection coefficients	276
B.1	Wall corrections for DAWS	280
C.1	Near-field DSS timing calculation	282
C.2	Allowed scattering and input angles	284
C.3	Scattering vector geometry	285
C.4	Comparison of shear and longitudinal modes	289

List of Tables

3.1	Fluid properties	78
3.2	Summary of the ultrasonic properties of the sample constituents	78
3.3	Summary of the fluidized suspension dimensions	78
3.4	Plane wave transducer properties	84
5.1	Comparison of the near- and far-field DSS techniques	176
5.2	Comparison of the velocity correlation volumes to the scattering volumes	196
B.1	DAWS timing corrections	281
D.1	Ballistic parameters used in DAWS & DSS	290

1. Introduction

This thesis contains three interrelated and intertwining topics, all involving systems of solid spherical particles fluidized by flowing the surrounding liquid upwards to counteract sedimentation. First, I investigate the propagation of classical waves, in particular ultrasound, through strongly scattering glass bead suspensions. Then the results of the theory and experiments from this first study are used to develop two new experimental techniques in ultrasonic correlation spectroscopy, which use temporal fluctuations of scattered waves to measure the motion of the scatterers in the fluidized suspension. These techniques are then used to investigate the dynamics of particles in liquid-solid fluidized bed systems. Thus, the wave propagation and fluidized bed studies are bridged by the experimental techniques in ultrasonic correlation spectroscopy, which are developed using the wave propagation results.

This chapter introduces these three topics. In the first section, wave propagation and spectroscopy in strongly scattering media are discussed, followed by a section on the physics of sedimentation and fluidization of solid particles in a liquid. The chapter ends with a brief outline of how the thesis is organized.

1.1 Strong Scattering of Classical Waves

The study of random or disordered systems has become an important field of physics, in part because the properties of ordered systems are now generally quite well understood, but also because disorder is found everywhere in nature. Thus, in order to have a deep understanding of nature, the properties of random systems must be understood.

An important and obvious aspect of the study of randomness is the study of wave propagation through random, inhomogeneous media. Waves are the basic mode of energy propagation in nature, be they light (electromagnetic waves) or sound (vibrational waves and thermal phonons) or even gravitational waves. Regardless of the kind of classical wave studied, the basic description using the wave equation remains remarkably general. In recent years, much progress has been made in learning how wave propagation through these materials works, but there still are open questions, especially when the inhomogeneities scatter the waves very strongly. Much of this progress has been achieved using visible or near visible light [e.g. Sheng 1995 and references therein], but the basic results should apply to all kinds of classical waves.

The simplest realization of a random medium consists of scattering inhomogeneities of uniform size (a), embedded in a homogeneous background material at a concentration specified by the scatterer volume fraction ϕ . At high frequency, $\lambda \ll a$ the propagation of the wave is determined by the individual properties of each component of the material, depending on which region the wave is in. At low frequency, when $\lambda \gg a$, wave propagation is determined by an average of the properties of the scatterers

and background. This result is the origin of effective medium theories, and the popular coherent potential approximation (CPA) [Sheng 1995]; because the wavelength is too large for the wave to resolve the scatterers, it sees an effective medium, whose properties are some sort of average of those of the separate materials in the system. These two extreme cases are well understood, but in the intermediate frequency regime ($\lambda \sim a$), the wave is able to resolve the scatterers, and there can be strong scattering resonances. In this regime, there still are unanswered questions, especially when the scattering is very strong.

In the intermediate frequency regime, wave propagation in random media can be split into two components. The ballistic component consists of the unscattered and forward scattered waves, and retains spatial and temporal coherence with the input wave. Here coherence means that there is a definite phase relation between the input and ballistic waves. The scattered or diffusive component is the superposition of all of the many scattered waves. Because of this complex and random interference, the phase and amplitude of the scattered component depend sensitively on both the position of the detector and the exact positions of all of the scatterers, whereas the ballistic wave is independent of the positions of the scatterers, as long as ϕ remains the same.

Even when the scattering is very strong, there still is a small ballistic component. But in the intermediate frequency regime, the CPA approximation breaks down, requiring a new theory to describe the coherent wave propagation. One part of this thesis is a critical test of a new theoretical model, based on a Green's function approach [Jing *et al.* 1992, Sheng 1995, Cowan *et al.* 1998]; this work expands on the tests performed by

Schriemer [1997] in a static close-packed system. We also address questions about the volume fraction dependence of the dispersion, such as whether or not dispersion effects are washed out at large volume fractions [Sheng 1995, Busch *et al.* 1996]. There also have been questions about whether the strong dispersion in these materials invalidates the concept of the group velocity as the velocity of pulse transport [van Albada *et al.* 1991, van Tiggelen *et al.* 1992]. To test these ideas one must be able to extract the coherent ballistic part of the wave from the much larger scattered component. This is extremely difficult to do in a light scattering experiment, as light detectors are sensitive only to the intensity. However, ultrasonic detectors measure the field, and by averaging the field over many different configurations of the scatterers, the incoherent part of the wave will be averaged away, leaving only the ballistic wave.

Much progress in understanding the properties of multiply scattered waves was made once it was realized that their propagation could be modeled using the diffusion approximation [Ishimaru 1967]. The diffusion approximation views wave propagation as a random walk from one scattering event to the next, giving information about the average intensity transport, and neglecting all interference effects. Tests of the diffusion approximation have been performed using both light [Lagendijk & van Tiggelen 1996 and references therein] and sound [Page *et al.* 1995, Weaver & Sachse 1995 and Schriemer *et al.* 1997], showing that it is very effective in describing the average intensity transport through a strongly scattering medium. To go beyond the average intensity and look at the spatial fluctuations in the output intensity, the phase information and interference between all of the different paths through the sample must be included. This leads to a speckle

pattern at the output face of the sample, with the amplitude of the transmitted wave fluctuating over regions larger than the coherence area, which is $\sim \lambda^2$ in the near-field [Fig. 1.1.1].

When the scatterers move, the speckle pattern of Fig. 1.1.1 will change with time, because the phase of each of the scattering paths is changing. The central part of this thesis involves the development of ultrasonic spectroscopy techniques, which use these temporal fluctuations to measure the average motion of the scattering particles. Optical techniques that use singly scattered light to measure the motion of particles are quite well established [Ishimaru 1967, Berne & Pecora 1976]. More recently, Diffusing Wave Spectroscopy (DWS), an optical technique that uses multiply scattered light, has been developed through the use of the diffusion approximation [Maret & Wolf 1987, Pine *et al.* 1988]. This thesis describes analogous ultrasonic techniques, continuing from a preliminary study done by Jones [1996]. Dynamic Sound Scattering (DSS) uses singly scattered ultrasound to measure the root mean square particle velocity and Diffusing Acoustic Wave Spectroscopy (DAWS) uses multiply scattered ultrasound to measure the relative motion of the particles. By combining these two techniques, the spatial velocity correlation function of the particles can also be measured [Cowan *et al.* 2000]. These new measurement techniques are ideally suited to the study of fluidized beds, where the scattering particles are suspended against sedimentation by a fluid flowing upwards. In particular, since ultrasonic wavelengths are on the order of millimeters, the particles of similar size are non-Brownian, and the suspensions can have Reynolds numbers that approach those found in fluidized beds that are used for many applications in industry.

Near-Field Speckle Pattern
 $a = 0.5 \text{ mm}$, $L = 10.1 \text{ mm}$,
 $f = 3.5 \text{ MHz}$, $\lambda = 0.43 \text{ mm}$

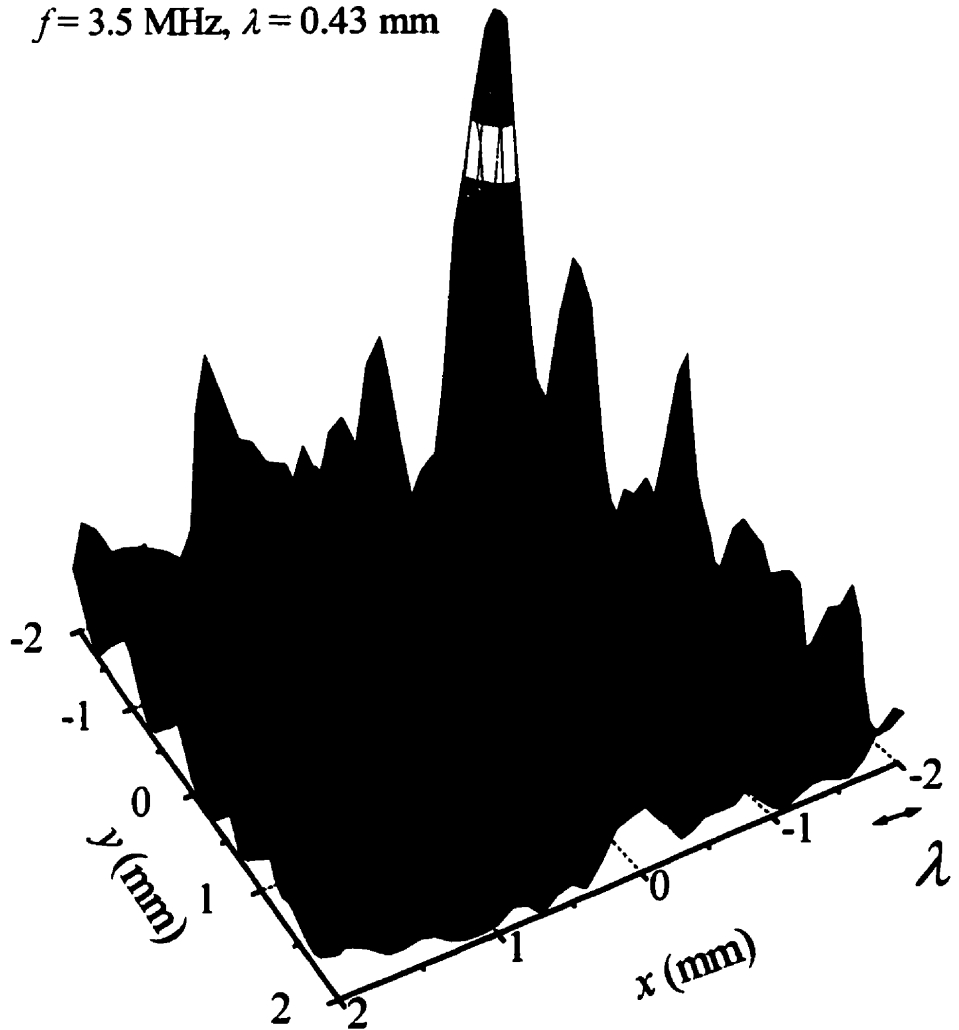


Figure 1.1.1: Transmitted intensity across the output face of a strongly scattering sample [from Schriemer 1997].

1.2 Dynamics of Fluidized and Sedimenting Particles

If one considers a single solid sphere falling in a fluid, its velocity can be found by balancing the gravitational force with the viscous drag force exerted by the fluid. But as more falling spheres are added, the system becomes more complicated, since the spheres begin to interact. When a sphere moves through a viscous fluid it drags along the fluid around it, thereby affecting other spheres. The effective hydrodynamic interaction between particles is long range ($\sim r^{-1}$), and leads to a reduction in the average sedimentation velocity of the particles, when compared to the single particle velocity [Russel *et al.* 1989]. The interaction force also leads to large velocity fluctuations, and its long range nature leads to the theoretical prediction that the fluctuations will diverge with sample size [Caflisch & Luke 1985]. However, most experiments and simulations do not agree with this scaling prediction [Nicolai & Guazzelli 1995, Segrè *et al.* 1997], although some do [Ladd 1996]. Recently models that cut off velocity fluctuations at a length scale ξ have been proposed as a way to remove the divergence and reconcile theory and experiment [Koch & Shaqfeh 1991, Levine *et al.* 1998, Brenner 1999]. Segrè *et al.* [1997] have also experimentally shown the existence of this length scale ξ , identified as the velocity correlation length. However, the exact nature of this cutoff, and its underlying cause remains uncertain.

Our experiments have looked at fluidized suspensions, whose dynamics should be quite similar to those in sedimentation, but transformed into the reference frame of the average sedimentation velocity. This is convenient experimentally, because the average velocity of the particles is zero, and because the particles can be followed indefinitely

without the system completing its sedimentation. However, care must be taken when comparing fluidization to sedimentation, as they may not be completely equivalent. Nonetheless, fluidized systems are interesting in their own right, and have many applications in the chemical industry, where the scaling with system size has direct design relevance. In addition, as mentioned previously, ultrasonic length scales correspond to non-Brownian particles with intermediate to high Reynolds numbers. This regime is of interest both from a fundamental physics point of view, since most experiments and theory in sedimentation have been done with smaller particles at low Reynolds numbers, and from the point of view of industrial applications. Using our new ultrasonic spectroscopy techniques, we have investigated the scaling of the velocity fluctuations and correlation lengths with volume fraction, sample size and Reynolds number.

1.3 Structure of the Thesis

The theory used to interpret the experiments reported in this thesis is presented in Chapter 2. Sections 2.1 and 2.2 present the theoretical basis of ballistic and scattered wave propagation, and give details of the theoretical model used to calculate ballistic velocities. Section 2.3 develops the theory used to relate the temporal fluctuations in scattered ultrasound to the motion of the scatterers. Section 2.4 introduces sedimentation and fluidization, and presents some current theoretical ideas relating to sample size scaling of the velocity fluctuations.

Chapter 3 describes all of the experimental apparatus used. Chapter 4 lays out how the apparatus was set up to perform the experiments, and gives some details of the analysis and interpretation of the data.

The core of the thesis is Chapter 5, where the results of our experiments are presented and discussed. This chapter is split into three sections, corresponding to the three main parts of the thesis. Section 5.1 discusses the results of our basic wave propagation measurements, and compares these results to our theoretical predictions. Section 5.2 gives more detail about the interpretation and use of the new ultrasonic correlation spectroscopy techniques. Section 5.3 presents the results of our investigation of fluidized bed dynamics, and their scaling with volume fraction, system size and Reynolds number. Finally, the conclusions for each of the three main parts are presented in Chapter 6, and some extra details given in the appendices.

2. Theory

In this chapter, the theory describing the propagation of ultrasound in strongly scattering media is developed, and the theoretical underpinnings of the description of particle dynamics in fluidized suspensions are discussed. Several different sections deal with aspects of the propagation of ultrasound in strongly scattering media. The first section describes the propagation of the ballistic portion (consisting of the portion of the wave not scattered out of the forward direction) of the ultrasound through strongly scattering media. In contrast to the scattered waves, the ballistic component is temporally and spatially coherent with the input pulse. Yet, although it is unscattered, it is still strongly affected by the scatterers in the medium. The second section introduces the diffusion model for the multiply scattered sound. The diffusion approximation essentially reduces the propagation of the sound through the medium to a random walk problem. The third section deals with how to describe the changes in the scattered signal when the scatterers are in motion, and presents the theory that allows us to use the observed temporal field autocorrelation functions to measure the motion of these scatterers. In the final section, I discuss some of the motions that particles suspended in fluidized beds can undergo, as well as various theoretical predictions of bed behavior.

2.1 Ballistic Transport

No matter how strong the scattering in a sample, there is a small portion of the transmitted wave which has either not been scattered, or has been scattered in the forward direction, and is therefore still temporally and spatially coherent with the input wave. One would expect this coherent intensity to decay exponentially as it penetrates the sample, with the energy being both scattered out of the beam and absorbed.

Ballistic pulses in strongly scattering materials are generally dispersive, and in the first section, the basic parameters describing the propagation of a pulse in a dispersive material are described [c.f. Saleh *et al.* 1991]. The second section introduces the Green's function for the wave equation, and the final section uses this formalism to develop the model used to calculate ballistic parameters for our strongly scattering samples.

2.1.1 Pulses in Dispersive Media

A dispersion curve describes the relationship between the frequency (f) and wavelength (λ) of propagating excitations in a material. Generally it is represented by writing the angular frequency, $\omega = 2\pi f$, as a function of the wave vector, $k = 2\pi/\lambda$. In a non-dispersive material, the dispersion curve can be written as, $\omega = v_p k$, where v_p is the phase velocity (the velocity of the motion of the surface of constant phase through the material) which is constant. A pulse propagating in a non-dispersive material will retain its shape and move with a velocity equal to the phase velocity. However, in a dispersive material this is no longer the case, because ω can vary non-linearly with k [Fig. 2.1.1].

Pulses propagating through dispersive materials have two characteristic velocities. The most fundamental is the phase velocity, but it now varies with frequency and no

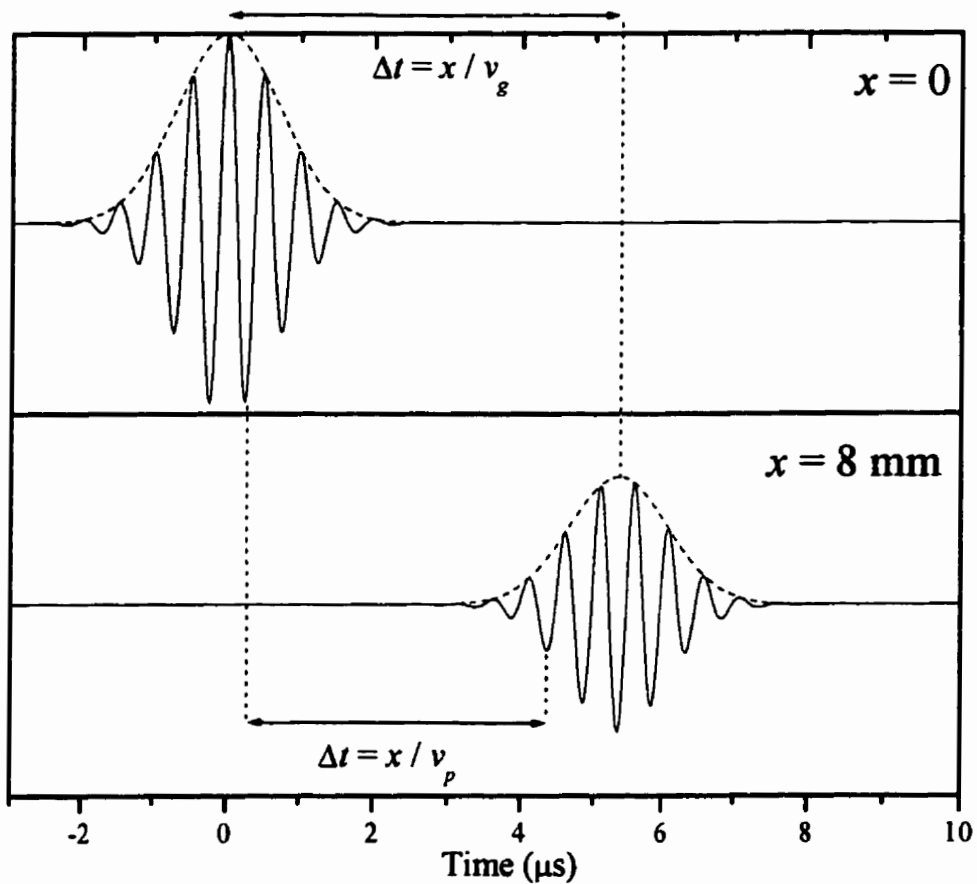


Figure 2.1.1: Pulse propagation in dispersive media.

longer equals the velocity that describes the motion of the envelope of the pulse. A pulse contains a finite range of frequencies, which all move with different phase velocities and interfere to produce a pulse whose envelope travels at a different velocity, the group velocity, as shown in Fig. 2.1.1.

In order to model this situation consider an input pulse at $x = 0$ of the form

$$\psi(x = 0, t) = e(t) \exp[i\omega_0 t] \quad (2.1)$$

where $e(t)$ is the envelope of the pulse, symmetric about $t = 0$, and ω_0 is the central frequency. We can calculate the frequency spectrum of Eq. (2.1) by taking the Fourier Transform

$$\Psi(\omega) = \Im[\psi(t)] = E(\omega - \omega_0), \quad (2.2)$$

where $E(\omega)$ is the Fourier Transform of $e(t)$. After traveling a distance x through the material the resulting wave will be

$$\psi(x, t) = \Im^{-1} \left[\exp \left[-\frac{x}{2l_e} \right] E(\omega - \omega_0) \exp[-ikx] \right], \quad (2.3)$$

where l_e is the extinction length in the material, and k is the wave vector, which is related to the frequency through the dispersion curve. If we expand $k(\omega)$ in a Taylor Series about the carrier frequency ω_0 :

$$k(\omega) = k_o + k'_o \{\omega - \omega_0\} + \frac{1}{2!} k''_o \{\omega - \omega_0\}^2 + \dots, \quad (2.4)$$

where k_o is the wave vector at the carrier frequency ω_0 , k' the first derivative, etc. $\psi(x, t)$ then becomes

$$\begin{aligned} \psi(x, t) &= \exp \left\{ -\frac{x}{2l_e} \right\} \exp \{-ik_o x\} \cdot \\ &\quad \Im^{-1} \left[E(\omega - \omega_0) \exp \left\{ -ik'_o \{\omega - \omega_0\} x \right\} \exp \left\{ -i \frac{1}{2} k''_o \{\omega - \omega_0\}^2 x \right\} \dots \right] \\ &\equiv \exp \left\{ -\frac{x}{2l_e} \right\} \exp \{-ik_o x\} \exp \{i\omega_o t\} \Im^{-1} \left[E(\omega) \exp \left\{ -ik'_o x \omega \right\} \exp \left\{ -i \frac{1}{2} k''_o x \omega^2 \right\} \right] \quad (2.5) \\ &= \exp \left\{ -\frac{x}{2l_e} \right\} \exp \left[i\omega_o \left\{ t - \frac{x}{v_p} \right\} \right] \left\{ \delta \left(t - \frac{x}{v_g} \right) \oplus e(t) \oplus \Im^{-1} \left[\exp \left\{ -i \frac{1}{2} k''_o x \omega^2 \right\} \right] \right\} \end{aligned}$$

where $v_p = \omega_0 / k_0$ is the phase velocity of the carrier frequency, $v_g = \frac{d\omega}{dk} \Big|_{k_0}$ is the group velocity, and \oplus denotes convolution. If the dispersion curve does not deviate too far from a quadratic polynomial over the bandwidth of the pulse, then we can ignore the terms after the quadratic term in the wave vector expansion. The quadratic term in Eq. (2.5) is an even function of ω so its inverse Fourier Transform is even in time. The convolution of the envelope (assumed to be an even function) with an even function will only increase the width of the envelope, not change the time of its center. If we call this modified envelope $e_1(t)$, then at a distance x into the material, the pulse is given by

$$\psi(x, t) = \exp\left\{-\frac{x}{2l_e}\right\} e_1\left(t - \frac{x}{v_g}\right) \exp\left[i\omega_0\left(t - \frac{x}{v_p}\right)\right]. \quad (2.6)$$

Thus, in effect, the phase of the pulse has propagated at the phase velocity of the central frequency, and the envelope of the pulse has propagated at the group velocity of the central frequency as it is defined above. The cubic term in the wave vector expansion will lead to asymmetries in the transmitted pulse envelope if it is non-negligible, calling into question the validity of the group velocity as a description of the pulse velocity. This analysis also assumes that the transmission through the sample is essentially constant over the bandwidth of the pulse. Both of these conditions can generally be arranged by adjusting the width of the pulse to produce a sufficiently narrow frequency bandwidth, ensuring that the group velocity is well defined.

The other parameter describing ballistic propagation is the extinction mean free path, which describes the loss of ballistic intensity due the combined effects of scattering

and absorption. The scattering mean free path, l_s , and the absorption length, l_a , both contribute to the extinction mean free path:

$$\begin{aligned}\frac{I(x)}{I(0)} &= \exp\left\{-\frac{x}{l_s}\right\} \exp\left\{-\frac{x}{l_a}\right\} = \exp\left\{-x\left[\frac{1}{l_s} + \frac{1}{l_a}\right]\right\} \\ &\equiv \exp\left\{-\frac{x}{l_e}\right\}.\end{aligned}\tag{2.7}$$

However, in the samples used in these experiments, scattering dominates losses due to absorption, thus the extinction mean free path is approximately equal to the scattering mean free path:

$$\frac{I(x)}{I(0)} \approx \exp\left\{-\frac{x}{l_s}\right\}.\tag{2.8}$$

The scattering mean free path can be roughly interpreted as the average distance traveled between scattering events.

2.1.2 The Wave Equation and Green's Functions

In general, sound propagates as a full elastic wave in a solid, i.e. with both shear and longitudinal components, but only as a longitudinal wave in a liquid. Our samples consisted of solid spheres suspended in a liquid. Since the particles do not form a connected network through the sample, wave propagation can be viewed as longitudinal waves travelling between the solid scatterers, where it is only the details of the scattering from the particles that is influenced by their elastic nature. Both for this reason, and to simplify the presentation, this section will focus on the scalar wave equation, which describes the propagation of longitudinal waves. The next section will show how the effects of the elastic waves on the scattering properties of the particles were included in

the calculations of the ballistic propagation parameters.

For an angular frequency ω and a position dependent phase velocity c (note that throughout this thesis I will use c for the phase velocities in the homogeneous components of the microstructure, and v_p for the effective average phase velocity in the overall structure), the scalar wave equation can be cast into the form

$$\left[\nabla^2 + \frac{\omega^2}{c^2(\vec{r})} \right] \psi(\vec{r}) = 0. \quad (2.9)$$

In principle, this equation includes all of the effects of scattering and disorder in the system, for one particular realization of the scatterer positions. However, even if one were to solve this equation for a particular realization, it is not clear that this would be of much help in describing the general properties of the disordered system, as there would just be too much detailed information. This is somewhat analogous to trying to describe the thermodynamic properties of a gas by explicitly solving the equations of motion for all of the molecules. The calculation would give a lot of detailed information about what the molecules do given particular starting conditions, but in the end, it would not be as informative as a statistical approach. Therefore, what we are really interested in, both theoretically and experimentally, are the ensemble-averaged transport properties of equivalent realizations of the disordered system. Experimentally this is done by averaging over the different positions of the scatterers as they move in a fluidized bed. If the ergodic hypothesis holds for the fluidized bed, then the experimental time average will be equivalent to the theoretical ensemble average.

The Green's function will turn out to be the building block in developing a

statistical framework to describe wave propagation problems in disordered media. It is essentially a solution of the wave equation (2.9), with a delta function excitation, $\delta(t)$, originating from a point source at \vec{r}' . If one considers its frequency components, it is given by

$$\left[\nabla^2 + \frac{\omega^2}{c^2(\vec{r})} \right] G(\omega, \vec{r}, \vec{r}') = \delta(\vec{r} - \vec{r}'), \quad (2.10)$$

where boundary conditions and causality must also be applied to obtain a unique solution [Sheng 1995]. The Green's function is so useful because it can excite all frequency and spatial modes of the system, and because given the Green's function, it is straightforward to construct a solution for any arbitrary source through the principle of superposition.

Before attempting to apply the Green's function to a disordered system, it will be informative to consider the simple case of a uniform medium. In that case, the velocity in Eq. (2.10) is constant, and the Green's function only depends on the separation between the source and detection points. To solve for the Green's function, it is convenient to transform to k space:

$$G(\omega, \vec{r} - \vec{r}') = \int \frac{d^3 k}{[2\pi]^3} \exp[i\vec{k} \cdot \{\vec{r} - \vec{r}'\}] G(\omega, \vec{k}) \quad (2.11)$$

$$\delta(\vec{r} - \vec{r}') = \int \frac{d^3 k}{[2\pi]^3} \exp[i\vec{k} \cdot \{\vec{r} - \vec{r}'\}].$$

Substituting Eq. (2.11) into (2.10) gives

$$\int \left[-k^2 + \left(\frac{\omega}{c} \right)^2 \right] G(\omega, \vec{k}) \frac{d^3 k}{[2\pi]^3} \exp[i\vec{k} \cdot \{\vec{r} - \vec{r}'\}] = \int \frac{d^3 k}{[2\pi]^3} \exp[i\vec{k} \cdot \{\vec{r} - \vec{r}'\}]. \quad (2.12)$$

Setting the k -components equal to each other results in

$$G(\omega, \vec{k}) = \frac{1}{\frac{\omega^2}{c^2} - k^2} = \frac{1}{k_o^2(\omega) - k^2}. \quad (2.13)$$

This gives the response of the system to a plane wave excitation with frequency ω and wave vector k . The Green's function diverges when excited with a wave vector $k = k_o$, which is expected since this is the natural mode of the medium. To avoid problems with the divergence when transforming back to the spatial domain, the standard procedure is to add a small imaginary part to the denominator of Eq. (2.13), and take the limit as it goes to zero [Sheng 1995]. The result is

$$\begin{aligned} G(\omega, \vec{k}) &= \lim_{\epsilon \rightarrow 0} \frac{1}{k_o^2(\omega) - k^2 + i\epsilon} \\ &= \left\{ P \left[\frac{1}{k_o^2 - k^2} \right] - i\pi\delta(k_o^2 - k^2) \right\}, \end{aligned} \quad (2.14)$$

where P represents the Cauchy principle value [Flanigan 1972]. The transformation to the spatial domain gives a spherical wave

$$G(\omega, \vec{r} - \vec{r}') = -\frac{\exp[ik_o|\vec{r} - \vec{r}'|]}{4\pi|\vec{r} - \vec{r}'|}. \quad (2.15)$$

The main point of interest in Eq. (2.14) is that the imaginary part of the Green's function diverges along the dispersion curve of the system. Because of the way it identifies the modes of the system, it is often referred to as the spectral function

$$S(\omega, \vec{k}) = -\text{Im} G(\omega, \vec{k}). \quad (2.16)$$

For the case of a uniform medium that attenuates exponentially, the wave equation can be written in the same form, but the wave vector k_o will now be complex, with the

imaginary part representing the decay of the wave:

$$\tilde{k} = \frac{\omega}{c} + i \frac{1}{2l_e} = k_o + i \frac{1}{2l_e}. \quad (2.17)$$

Here l_e represents the attenuation length, with the symbol chosen in anticipation of future developments. Substituting the complex wave vector \tilde{k} in place of k_o in Eq. (2.13) for the Green's function gives

$$\begin{aligned} G(\omega, \tilde{k}) &= \frac{1}{k_o^2 - k^2 - \left[\frac{1}{2l_e} \right]^2 + i \frac{k_o}{l_e}} \\ S(\omega, \tilde{k}) &= -\text{Im } G \\ &= l_e^2 \frac{k_o l_e}{\left[\{k_o l_e\}^2 - \{k l_e\}^2 - \frac{1}{4} \right]^2 + \{k_o l_e\}^2}. \end{aligned} \quad (2.18)$$

Thus the spectral function no longer diverges, but it does have peaks when

$$\{k_o l_e\}^2 - \{k_{peak} l_e\}^2 - \frac{1}{4} = 0, \quad (2.19)$$

giving

$$\begin{aligned} k_o &= k_{peak} \sqrt{1 + \left\{ \frac{1}{2k_{peak} l_e} \right\}^2} \\ &\approx k_{peak} \left[1 + \frac{1}{8} \left[k_{peak} l_e \right]^{-2} \right]. \end{aligned} \quad (2.20)$$

Thus the peaks in the spectral function now are an excellent approximation to the modes of the system, with a correction that only becomes significant in the extreme case when the attenuation length is considerably less than the wavelength (corresponding to the localization regime).

The next section will show how this argument can be extended to find the modes of the ballistic wave in a disordered material. In this case, the ballistic wave sees a uniform effective medium, which takes into account all of the scattering in an average sense. The modes of the system are attenuated due to the scattering, so the spectral function no longer diverges but forms peaks. Nonetheless, as discussed above, the dispersion curve can still be determined from the peaks in the spectral function.

2.1.3 Spectral Function Approach

In a disordered medium, the Green's function gives the response of a particular realization of the system to an excitation. To extract information about the general properties of disordered systems, as opposed to the particular properties of individual realizations, the probability distribution over all ensembles, $P(G)$, must be investigated. In this section, we are interested in the coherent or ballistic beam, which is given by the first moment of the probability distribution, $\langle G \rangle$, since only the coherent components of G will survive the averaging process.

The approach used here to calculate $\langle G \rangle$ overcomes the limitations of the traditional CPA approach, thereby allowing ballistic transport properties to be calculated in the frequency regime where the wavelength is comparable to the size of the scatterers. The method uses the spectral function, following the procedure that is outlined by Sheng [1995], Page *et al.* [1996] and Cowan *et al.* [1998], and described in detail by Jing *et al.* [1992]. As shown in the last section, in a uniform medium with no attenuation the spectral function has poles at frequencies corresponding to the modes of the system, and

peaks that accurately identify the modes in an attenuating system, so long as $kl_e > 1$.

Therefore we calculate the spectral function of the ensemble-averaged or ballistic Green's function, and use the peaks to identify the modes of the system. We will also show that these peaks correspond to minima in the scattering from a single scatterer, which gives the physically intuitive picture that the propagating mode is the one that is scattered the least.

Consider the wave equation in the presence of disorder, Eq. (2.9). The equation can be written in a different way by adding and subtracting a constant

$$\left[\nabla^2 + \frac{\omega^2}{v_{\text{eff}}^2} - \left\{ \frac{\omega^2}{v_{\text{eff}}^2} - \frac{\omega^2}{c^2(\vec{r})} \right\} \right] \psi(\omega, \vec{r}) = 0, \quad (2.21)$$

where v_{eff} is a dummy variable representing an effective medium phase velocity. The Green's function of this equation is given by

$$\left[\nabla^2 + \frac{\omega^2}{v_{\text{eff}}^2} - \left\{ \frac{\omega^2}{v_{\text{eff}}^2} - \frac{\omega^2}{c^2(\vec{r})} \right\} \right] G(\omega, \vec{r}, \vec{r}') = \delta(\vec{r} - \vec{r}'). \quad (2.22)$$

Equation (2.22) can be rearranged to read

$$\left[\nabla^2 + \frac{\omega^2}{v_{\text{eff}}^2} \right] G(\omega, \vec{r}, \vec{r}') = \delta(\vec{r} - \vec{r}') + \left\{ \frac{\omega^2}{v_{\text{eff}}^2} - \frac{\omega^2}{c^2(\vec{r})} \right\} G(\omega, \vec{r}, \vec{r}'). \quad (2.23)$$

To solve this equation, consider an inhomogeneous equation of the form

$$\left[\nabla^2 + \frac{\omega^2}{v_{\text{eff}}^2} \right] \varphi(\omega, \vec{r}) = f(\vec{r}). \quad (2.24)$$

Using the principle of superposition, $\varphi(\omega, r)$ can be written in terms of a Green's function,

$$\varphi(\omega, \vec{r}) = \varphi_o(\omega, \vec{r}) + \int G_o(\omega, \vec{r} - \vec{r}') f(r') dr', \quad (2.25)$$

where φ_o is the homogeneous solution and G_o is the Green's function of the uniform medium:

$$\left[\nabla^2 + \frac{\omega^2}{v_{\text{eff}}^2} \right] G_o(\omega, \vec{r} - \vec{r}') = \delta(\vec{r} - \vec{r}'). \quad (2.26)$$

Combining Eqs. (2.23) to (2.26) and using the boundary condition that $G \rightarrow 0$ as $|\vec{r} - \vec{r}'| \rightarrow \infty$ to eliminate the homogeneous term, we have

$$\begin{aligned} G(\omega, \vec{r}, \vec{r}') &= \int G_o(\omega, \vec{r} - \vec{r}'') \left\{ \delta(\vec{r}'' - \vec{r}') + \left[\frac{\omega^2}{v_{\text{eff}}^2} - \frac{\omega^2}{c^2(\vec{r}'')} \right] G(\omega, \vec{r}'', \vec{r}') \right\} d\vec{r}'' \\ &= G_o(\omega, \vec{r} - \vec{r}') + \int G_o(\omega, \vec{r} - \vec{r}'') V(\vec{r}'') G(\omega, \vec{r}'', \vec{r}') d\vec{r}''. \end{aligned} \quad (2.27)$$

Here $V(\vec{r}'') = \left[\frac{\omega^2}{v_{\text{eff}}^2} - \frac{\omega^2}{c^2(\vec{r}'')} \right]$ is the impurity operator, defined with respect to the effective medium. In operator notation $G(\omega, r, r')$ can be written in the form

$$\mathbf{G} = \mathbf{G}_o + \mathbf{G}_o \mathbf{V}_{\text{eff}} \mathbf{G}. \quad (2.28)$$

This equation can be iterated on \mathbf{G} to give

$$\begin{aligned} \mathbf{G} &= \mathbf{G}_o + \mathbf{G}_o \mathbf{V} [\mathbf{G}_o + \mathbf{G}_o \mathbf{V} \{ \mathbf{G}_o + \mathbf{G}_o \mathbf{V} \dots \}] \\ &= \mathbf{G}_o + \mathbf{G}_o \mathbf{V} \mathbf{G}_o + \mathbf{G}_o \mathbf{V} \mathbf{G}_o \mathbf{V} \mathbf{G}_o + \dots \end{aligned} \quad (2.29)$$

or

$$\mathbf{G} = \mathbf{G}_o + \mathbf{G}_o \mathbf{T} \mathbf{G}_o, \quad (2.30)$$

with the scattering operator

$$\begin{aligned} \mathbf{T} &= \mathbf{V} + \mathbf{VG}_o\mathbf{V} + \mathbf{VG}_o\mathbf{VG}_o\mathbf{V} + \dots \\ &= \mathbf{V}[\mathbf{I} - \mathbf{G}_o\mathbf{V}]^{-1}. \end{aligned} \quad (2.31)$$

Taking an ensemble average of Eq. (2.30) gives

$$\langle \mathbf{G} \rangle = \mathbf{G}_o + \mathbf{G}_o \langle \mathbf{T}_{\text{eff}} \rangle \mathbf{G}_o. \quad (2.32)$$

Here, all of the effects of the scattering on the ballistic wave are contained in the ensemble-averaged scattering operator. Also, $\langle \mathbf{G} \rangle$ only depends on the separation, $\vec{r} - \vec{r}'$, since the medium is on average uniform. This means that both $\langle \mathbf{G} \rangle$ and $\langle \mathbf{T}_{\text{eff}} \rangle$ depend only on one k in the wave vector representation. The CPA condition is that $\langle \mathbf{T}_{\text{eff}} \rangle = n \mathbf{T}_{\text{eff}}^{(s)} = 0$, where $\mathbf{T}_{\text{eff}}^{(s)}$ is the matrix for a single scatterer and n is the number density of the scatterers. This means that $\langle \mathbf{G} \rangle = \mathbf{G}_o$, which gives a propagating mode with phase velocity v_{eff} . However, in the intermediate frequency range, where the wavelength is of the same order as the size of the scatterer, the CPA condition cannot be satisfied, and the method breaks down. Therefore we use the spectral function approach here.

To further simplify Eq. (2.32), one can define a self-energy operator as

$$\langle \mathbf{G} \rangle^{-1} = \mathbf{G}_o^{-1} - \Sigma_{\text{eff}} \quad (2.33)$$

or, using Eq. (2.32),

$$\Sigma_{\text{eff}} = \langle \mathbf{T}_{\text{eff}} \rangle [\mathbf{I} + \langle \mathbf{T}_{\text{eff}} \rangle \mathbf{G}_o]^{-1}. \quad (2.34)$$

Since \mathbf{G}_o is a uniform medium Green's function, in the k representation it can be expressed in the same way as in Eq. (2.13). Thus Eq. (2.33) results in the following

equation for the ballistic Green's function in the k representation:

$$\langle G(\omega, k) \rangle = \frac{1}{\frac{\omega^2}{v_{\text{eff}}^2} - k^2 - \Sigma_{\text{eff}}(\omega, k)}. \quad (2.35)$$

If we use the freedom to set the dummy variable $v_{\text{eff}} = \omega/k$, then Eq. (2.35) reduces to

$$\langle G(\omega, k) \rangle = -\Sigma_{\text{eff}}^{-1}(\omega, k), \quad (2.36)$$

which gives the spectral function

$$S(\omega, k) = -\text{Im} \langle G \rangle = \text{Im} [\Sigma_{\text{eff}}^{-1}(\omega, k)], \quad (2.37)$$

where the self energy is calculated with respect to an effective medium wave velocity.

Since our samples are isotropic on average, the vector dependence of k has been dropped from the ensemble-averaged terms. Thus, all that remains is to calculate the self energy for each (ω, k) point – corresponding to different effective medium velocities, and

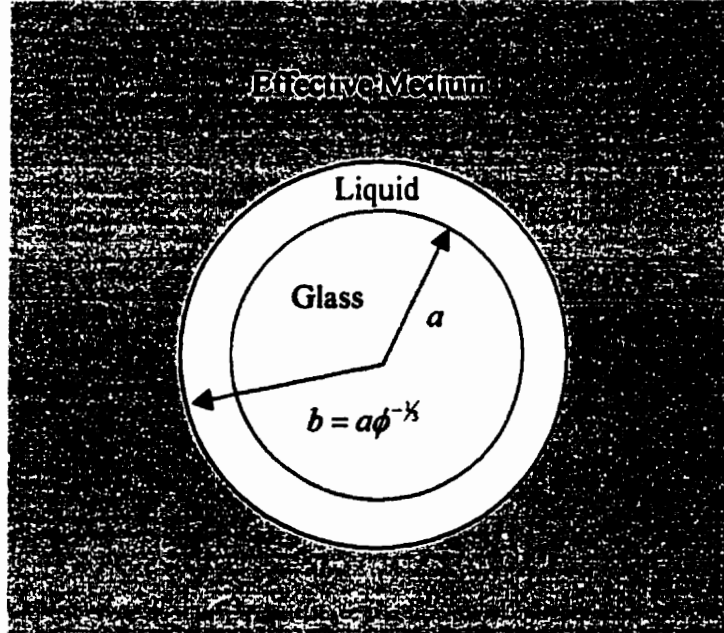


Figure 2.1.2: The coated sphere model.

identify the dispersion curve by finding the peaks in the spectral function.

However, to evaluate the self energy we must first make some approximations. The basic scattering unit in the suspensions will be taken to be a glass sphere, coated by a layer of the liquid, and embedded in the effective medium discussed above [see Fig. 2.1.2]. The thickness of the liquid coating is set by the volume fraction of the scatterers in the sample, to conserve liquid and glass volumes. The infinite effective medium, which surrounds the coated sphere, has a liquid nature (i.e. it only supports longitudinal waves), since the glass does not form a connected network. The density of the effective medium is the average density of the sample. The scattering from this single coated sphere, including the elastic nature of the scatterer, can be calculated in a straightforward manner from the boundary value problem.

If we consider just a single coated sphere scatterer, and call its scattering operator $\mathbf{T}_{\text{eff}}^{(s)}$, then to first order in the number density of scatterers,

$$\langle \mathbf{T}_{\text{eff}} \rangle = n \mathbf{T}_{\text{eff}}^{(s)}. \quad (2.38)$$

This is the widely used independent scattering approximation, which includes all multiple scattering up to infinite order, but ignores any recurrent scattering between particles [Lagendijk & van Tiggelen 1996]. From Eq. (2.34),

$$\Sigma_{\text{eff}} \simeq \langle \mathbf{T}_{\text{eff}} \rangle = n \mathbf{T}_{\text{eff}}^{(s)}. \quad (2.39)$$

To relate $\mathbf{T}_{\text{eff}}^{(s)}$ to the boundary value problem, we can cast Eq. (2.32) into the form

$$\psi(\omega, \vec{r}) = \exp[i\vec{k}_{\text{eff}} \cdot \vec{r}] - \frac{\exp[i\vec{k}_{\text{eff}} \cdot \vec{r}]}{4\pi r} T_{\text{eff}}^{(s)}(\vec{k}_{\text{eff}}, \vec{k}'_{\text{eff}}) \quad (2.40)$$

through the use of Eq. (2.15) and (2.25). Thus, the wave consists of the incident plane wave and scattered spherical waves radiating out from the scatterer. This follows standard scattering conventions, where the scattering amplitude is identified as

$$f(\vec{k}_{\text{eff}}, \vec{k}') = \frac{-T_{\text{eff}}^{(s)}(\vec{k}_{\text{eff}}, \vec{k}'_{\text{eff}})}{4\pi}. \quad (2.41)$$

Combining these equations leads to

$$S(\omega, k) = \frac{1}{n} \text{Im} \left[\frac{1}{T_{\text{eff}}^{(s)}(k_{\text{eff}}, k_{\text{eff}})} \right] = \frac{-1}{4\pi n} \text{Im} \left[\frac{1}{f(k_{\text{eff}})} \right]. \quad (2.42)$$

Here the scattering is evaluated in the *forward direction*, because the ensemble-averaged scattering matrix in Eq. (2.39) depends on only one k . Equation (2.42) explicitly shows that peaks in the spectral function correspond to minima in the scattering. The scattering amplitude can be found from the solution to the boundary value problem, which is discussed in more detail in Cowan *et al.* [1998]. Knowledge of the scattering amplitude also gives the scattering mean free path in the sample.

Figure 2.1.3 shows the results of calculating the spectral function as a function of ω and k in the effective medium for our system of glass beads suspended in a 75% glycerol/water mixture [c.f. Sections 3.3.2 and 3.3.3, and Table 3.2 for material properties]. Here a is the bead radius and c_f is the fluid velocity. Because the experiments consist of measuring the response of the system to input sound with a particular fixed frequency spectrum, peaks in the spectral function are found by holding ω constant and scanning k . The opposite procedure would be appropriate for a Brillouin scattering experiment, which is performed at a constant wave vector. Panel (a) shows $S(\omega, k)$ at a

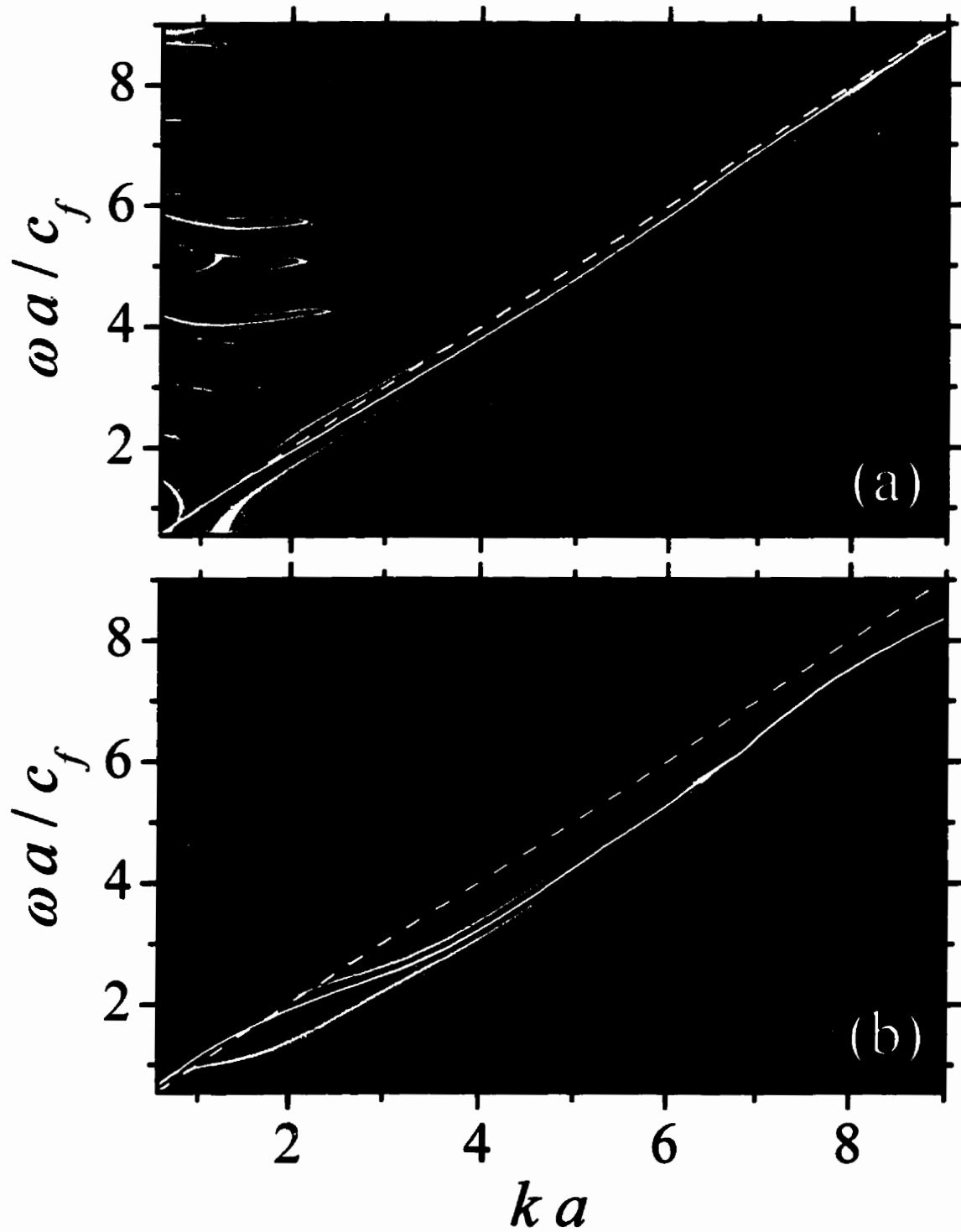


Figure 2.1.3: The calculated spectral function for two volume fractions:

(a) $\phi = 0.20$ and (b) $\phi = 0.61$. The solid line is the dispersion curve, calculated by finding peaks at constant frequency. The dashed line is the dispersion curve in the fluid.

volume fraction of $\phi = 0.20$, where the peaks are quite strong and the dispersion curve (solid line) is fairly close to that in the pure fluid (dashed line). In panel (b), the volume fraction is 0.61; very near the randomly close packed volume fraction of 0.63. Here the peaks are weaker, especially at higher frequencies, and the differences with the fluid dispersion curve are more pronounced – i.e. the dispersion in the sample is stronger than it is at the lower volume fraction.

To find the phase velocity in the sample we take $v_p = \omega/k$ along the dispersion curve. To calculate the group velocity we take $v_g = \frac{d\omega}{dk}$. In both cases, we smooth the dispersion curve to account for the distribution of bead radii in our samples [approximately 5%, see Section 3.3.2]. These calculations will be directly compared to our measured data in Section 5.

Also of interest is the spatial distribution of the energy density of waves in the coated sphere model, which identifies where the wave energy predominately travels, through the liquid or solid. Thus the energy density distribution gives important information about the form of the waves that travel through the material, and about what the possible underlying causes of the observed strong dispersion are. The energy density can also be calculated from the boundary value problem, and is discussed in Cowan *et al.* [1998]. In Section 5, the results of this calculation will be used to develop a qualitative explanation for our experimental results.

2.2 Diffusive Transport

To examine the propagation of the scattered waves in random, inhomogeneous systems, the next moment of the Green's function, $\langle GG^* \rangle$, must be used. This moment gives the transport properties of the ensemble-averaged intensity. In this section, an outline of the derivation of the diffusion equation will be given, with the details left to references. Then the boundary conditions, for a plane slab geometry with partially reflective boundaries, will be presented. Finally, the methods we used to calculate diffusion parameters will be explained.

2.2.1 Diffusion Theory

By considering the intensity, $I = \langle GG^* \rangle$ a transport equation can be developed directly from the wave equation [Sheng 1995 and Lagendijk & van Tiggelen 1996],

$$\frac{dI(\vec{r}, \hat{s})}{ds} = -n\sigma_t I(\vec{r}, \hat{s}) + \frac{n\sigma_t}{4\pi} \int p(\hat{s}, \hat{s}') I(\vec{r}, \hat{s}') d\Omega' + \varepsilon(\vec{r}, \hat{s}). \quad (2.43)$$

Here, \hat{s} is the scattering direction, \hat{s}' is the incident direction, n is the number density of scatterers, $d\Omega$ is a volume element, σ_t is the total scatterer cross section, p is proportional to the square of the scattering amplitude, and ε is a source term. This transport equation is the radiative transfer equation [Ishimaru 1978, Ryzhik *et al.* 1996 and Schriemer 1997], which was originally derived phenomenologically in astrophysics to describe light scattering in atmospheres. In the limit of the path lengths through the sample being much larger than the scattering mean free path, the transport equation can be simplified to a diffusion equation [Ishimaru 1978 and Ryzhik *et al.* 1996]

$$\frac{\partial U}{\partial t} - D \nabla^2 U = \delta(\vec{r} - \vec{r}_o) \delta(t), \quad (2.44)$$

where the right hand side represents a diffuse point source at \vec{r}_o , and U is the diffuse energy density, which is related to the energy flux or acoustic intensity in the z direction (normal to the sample surface) via Fick's law

$$I(t) = -D \frac{\partial U}{\partial z} \quad (2.45)$$

with the diffusion coefficient given by

$$D = \frac{1}{3} v_E l^*. \quad (2.46)$$

Here, l^* is the transport mean free path and v_E is the energy velocity. The transport mean free path is the distance at which the scattering direction becomes randomized, and is equal to the scattering mean free path only if the scattering is isotropic. For anisotropic scattering, the transport mean free path is generally larger than the scattering mean free path, because it takes more than one scattering event to randomize the scattering direction on average. The relationship between the transport and scattering mean free path is given by [Lagendijk & van Tiggelen 1996]

$$\begin{aligned} l^* &= \frac{l_s}{1 - \langle \cos \theta \rangle} \\ &= \frac{l_s}{1 - \frac{\int |f(\theta)|^2 \cos \theta d\Omega}{\int |f(\theta)|^2 d\Omega}} . \end{aligned} \quad (2.47)$$

Within the diffusion approximation, intensity transport can be viewed as a random walk problem between scattering events, with a step size equal to the transport mean free

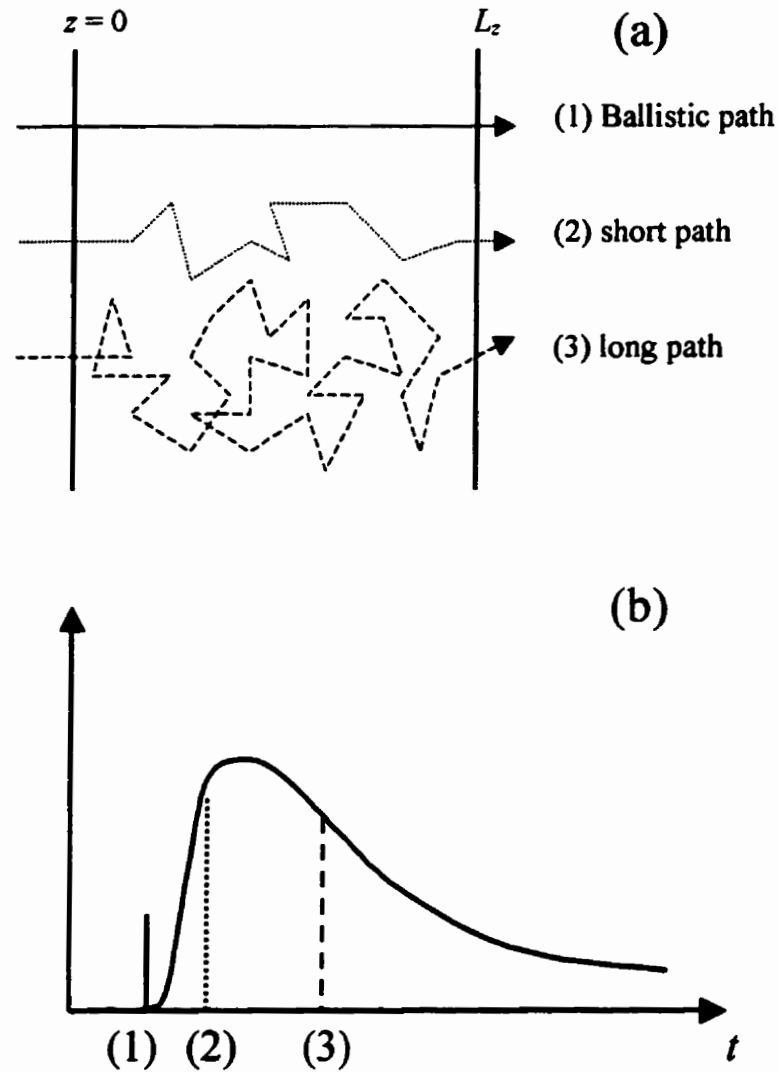


Figure 2.2.1: (a) Different random walk paths through the sample.
(b) Pulsed diffusion approximation for the ensemble averaged intensity.

path and a speed equal to the energy velocity. For a pulsed experiment, diffusion theory predicts the time profile of the ensemble-averaged scattered intensity. This corresponds to predicting the distribution of path lengths through the sample, as is illustrated in Fig. 2.2.1.

2.2.2 Boundary Conditions

Our fluidized bed samples have planar slab geometry, with the transverse dimensions large compared to the thickness, L_z , of the bed [c.f. Section 3.2]. It is therefore reasonable to consider the sample to be an infinite plane slab, with a thickness L_z in the z direction. The walls of the fluidized bed also partially reflect scattered sound back into the sample, causing the sound to remain in the sample longer, thereby shifting the path length distribution to longer scattering path lengths. In general, when measuring diffusive transport in the experiments reported on in this thesis, we used a plane wave source of ultrasound. The appropriate form for these boundary conditions has been worked out, for instance, by Zhu *et al.* [1991]. Only the results will be quoted here; for details refer to the literature.

Reflective boundary conditions are dealt with by equating the reflected diffusive flux to a fictitious flux entering from beyond the sample boundary. If one identifies the average reflection coefficient, R , as the ratio of the incoming to outgoing flux, then the boundary conditions for the energy density can be written

$$\begin{aligned} U - h \frac{\partial U}{\partial z} &= 0 && \text{at } z = 0 \\ U + h \frac{\partial U}{\partial z} &= 0 && \text{at } z = L_z \\ h &= \frac{2L^*}{3} \frac{1+R}{1-R} \end{aligned} \quad (2.48)$$

This is equivalent to extrapolating the energy density to zero at a distance h past the boundaries of the sample.

To find the average reflection coefficient, R , the angular dependence of the

reflected diffusive flux must be considered. By integrating the reflected flux over the incident angle θ , an expression for R can be found:

$$R = \frac{3C_2 + 2C_1}{3C_2 - 2C_1 + 2} \quad (2.49)$$

with

$$\begin{aligned} C_1 &= \int_0^{\pi/2} d\theta R(\theta) \sin \theta \cos \theta \\ C_2 &= \int_0^{\pi/2} d\theta R(\theta) \sin \theta \cos^2 \theta . \end{aligned} \quad (2.50)$$

$R(\theta)$ can be calculated from the material parameters of the wall interfaces, as is shown in Appendix A.

The solution of the diffusion equation [Eq. (2.44) and (2.45)], with the boundary conditions given by Eq. (2.48) and with a plane wave source is given by Carslaw & Jaeger [1959]. In addition, the effects of absorption in the material are accounted for by multiplying $I(t)$ by an exponential time decay, with an absorption time τ_a . For an excitation that is a delta function in time, the result is

$$I(t) = \frac{2De^{-\gamma t}}{L_z^2} \sum_{n=1}^{\infty} A_n e^{-D\beta_n^2 t/L_z^2}, \quad (2.51)$$

with

$$A_n = \frac{\beta_n [\beta_n K \sin \beta_n - \cos \beta_n] [\beta_n K \cos \{\beta_n z_o / L_z\} + \sin \{\beta_n z_o / L_z\}]}{\beta_n^2 K^2 + 1 + 2K}. \quad (2.52)$$

The values of β_n are the positive roots of the transcendental equation

$$\tan \beta = \frac{2\beta K}{\beta^2 K^2 - 1} \quad (2.53)$$

$$K = h/L_z .$$

Here $z_o = l^*$ is the depth into the sample at which the input plane wave becomes equivalent to a diffusive plane wave source; z_o is approximately given by the transport mean free path [Durian, 1994]. As stated above, this solution is for an excitation that is a delta function in time. However, in experimental situations the input pulse has a finite width, so the transmitted flux must be convoluted with the input pulse intensity

$$I_{\alpha}(t) = \int I_{in}(t') I_{delta}(t-t') dt' . \quad (2.54)$$

Therefore the diffusive time profile is completely determined through the knowledge of R , L_z , τ_a , and two of D , v_E , or l^* . Of these, L_z is measurable, and R is known given the material properties of the wall and sample. This leaves the absorption time, diffusion coefficient, energy velocity and transport mean free path to be measured from the time profile, of which only D and τ_a , can be determined accurately from fitting. Thus another method must be developed to calculate at least one of v_E , or l^* .

2.2.3 Calculation of Diffusion Parameters

In this section, relationships between the ballistic and diffusive propagation parameters will be developed. The ballistic parameters can be calculated by applying the spectral function method to our coated sphere model, and from these ballistic parameters, the energy velocity and transport mean free path will be calculated. The model presented here for the energy velocity calculation follows that in Schriemer *et al.* [1997].

Equation (2.47) gives a relationship between the diffusive transport mean free path

and the ballistic scattering mean free path. Entering this equation is the square of the angle-dependent scattering amplitude, which can be calculated within the coated sphere scatterer model.

The energy velocity is the speed at which diffusive energy travels from one random walk step to the next. Thus it can be viewed as the velocity of energy transport in the material, which is given by the ratio of the energy flux to the energy density; however attempts to use Green's function methods to directly calculate this ratio have so far proven intractable in the strong scattering intermediate frequency regime. Therefore, we take a different approach here, starting from the coated sphere embedded in an effective medium model introduced in the ballistic propagation calculations.

Consider a wave of frequency ω incident from the effective medium on a coated sphere. The complex scattering amplitude $f(\theta)$ gives the angular dependence of the phase and amplitude of the resulting scattered wave. For a pulse, made up of a range of frequencies, the frequency dependence of these phase shifts gives the time delay (or advance) relative to the forward direction that the pulse experiences upon scattering. In the forward direction, the velocity of energy transport is given by the group velocity, whereas the energy velocity is defined as the average velocity of energy transport in the material. A simple physical picture of the energy velocity is that it is the average velocity of a wave pulse after many successive scatterings. Since each scattering alters the direction, the average time delay that the wave experiences (Δt_{ave}) is found by performing an angular average, weighted by $f^2(\theta)$, of the scattering delay from a single scatterer.

Thus the energy velocity can be written

$$v_E = \frac{l^*}{\frac{l^*}{v_g} + \Delta t_{ave}} \quad (2.55)$$

or

$$v_E = \frac{v_g}{1 + \frac{\Delta t_{ave} v_g}{l^*}}. \quad (2.56)$$

The result of these transport mean free path and energy velocity calculations agree well with experimental results in our systems, as reported in Schriemer *et al.* [1997], justifying the use of this simple physical model.

2.3 Temporal Autocorrelation

The previous two sections dealt with the ensemble-averaged propagation of waves through strongly scattering samples. In this section, instead of looking at the properties of the scattered waves when averaged over many different arrangements of scatterer positions, we are interested in what happens to the scattered waves as the scatterers move continuously between different arrangements. In the first section we consider singly scattered waves, developing a relationship between the temporal fluctuations in the scattered field caused by the motion of the scatterers, and the mean square displacement of the scatterers. The next sections show how the diffusion approximation can be used to extend this idea to the strong multiply scattering regime. However, here it is the relative motion of scatterers separated by a transport mean free path that is measured. The final sections present theory describing the temporal fluctuations in the phase and intensity of the scattered waves.

2.3.1 Dynamic Sound Scattering (DSS)

By lowering the frequency of the wave so that the wavelength is larger than the size of the particles, the scattering can be weakened to the point where single scattering dominates for a given sample thickness. Dynamic light scattering in the weak scattering limit has been well established [e.g. Berne & Pecora 1976 and Chu 1991], but to the best of our knowledge these techniques have not been used in ultrasonics. The basic idea is to relate the fluctuations in the scattered waves to the motion of the scatterers, using autocorrelation functions. The theoretical relationship is between the field autocorrelation function and the mean square displacement of the scatterers, but for light scattering this

generally must be related to the measured intensity autocorrelation function through the Siegert relation [Sec. 2.3.5]. The ability of ultrasonic detectors to measure the field, as opposed to the intensity, lets us measure the field autocorrelation function directly.

The field autocorrelation function is defined by

$$g_1(\tau) = \frac{\langle \psi(t)\psi^*(t+\tau) \rangle_t}{\langle \psi(t)\psi^*(t) \rangle_t}, \quad (2.57)$$

where ψ is the scattered field and $\langle \rangle_t$ denotes an average over t . The field can be written as a sum over all of the different paths through the sample (or equivalently as a sum over all of the scatterers in the scattering volume)

$$\psi(t) = \sum_p \psi_p(t) = A \sum_p \exp[i\phi_p(t)] \quad (2.58)$$

where A is the single scattering amplitude, and ϕ_p is the phase of the scattering path p .

This leads to

$$g_1(\tau) = \frac{\left\langle \sum_{p,p'} \exp[i\{\phi_p(t) - \phi_{p'}(t+\tau)\}] \right\rangle_t}{\left\langle \sum_{p,p'} \exp[i\{\phi_p(t) - \phi_{p'}(t)\}] \right\rangle_t}. \quad (2.59)$$

For scatterers that are randomly distributed in space, only the terms with $p = p'$ will survive the time average in the numerator and denominator [see Tong *et al.* 1988]. To show this explicitly, we write

$$\begin{aligned} \phi_p(t) &= \vec{q} \cdot \vec{r}_p(t) \\ \phi_{p'}(t+\tau) &= \vec{q} \cdot [\vec{r}_{p'}(t) + \vec{r}_{p'}(t+\tau) - \vec{r}_{p'}(t)] \\ &= \vec{q} \cdot [\vec{r}_{p'}(t) + \Delta\vec{r}_{p'}(\tau)] \end{aligned} \quad (2.60)$$

where $\vec{q} = \vec{k}' - \vec{k}$ is the scattering wave vector (the difference between the scattered (\vec{k}') and incident (\vec{k}) wave vectors), \vec{r}_p is the position of the p^{th} particle and $\Delta\vec{r}_p(\tau)$ is its change in position from time t to time $t + \tau$. Then the numerator in Eq. (2.59) becomes

$$\left\langle \sum_{p,p'} \exp[i\vec{q} \cdot \{\vec{r}_p(t) - \vec{r}_{p'}(t)\}] \exp[-i\vec{q} \cdot \Delta\vec{r}_{p'}(\tau)] \right\rangle_t. \quad (2.61)$$

For random particle positions, and assuming that the average motion of the particles is independent of position, the first exponential will fluctuate and cause the average to be zero, unless the term in curly brackets is identically equal to zero for all times t . This will only happen for all times if $p = p'$. A similar argument holds for the denominator as well.

Returning to Eq. (2.59), we can now write it as

$$g_1(t) = \frac{\left\langle \sum_p \exp[-i\Delta\phi_p(\tau)] \right\rangle}{N} = \frac{\sum_p \langle \exp[-i\Delta\phi_p(\tau)] \rangle}{N}, \quad (2.62)$$

$$= \langle \exp[-i\Delta\phi(\tau)] \rangle$$

where $\Delta\phi(\tau)$ is the change in the phase of a single path over a time τ , due to the motion of the scatterer. The average of an exponential can be expanded in a cumulant expansion

$$g_1(\tau) = 1 - i\langle \Delta\phi \rangle - \frac{1}{2!} \langle \Delta\phi^2 \rangle + \dots$$

$$= 1 - \frac{1}{2} \langle \Delta\phi^2 \rangle + \dots \quad (2.63)$$

$$\approx \exp\left[-\frac{1}{2} \langle \Delta\phi^2(\tau) \rangle\right].$$

As indicated in Fig. 2.3.1, the phase change of a path can be written in terms of the scattering wave vector and the displacement of the scattering particle

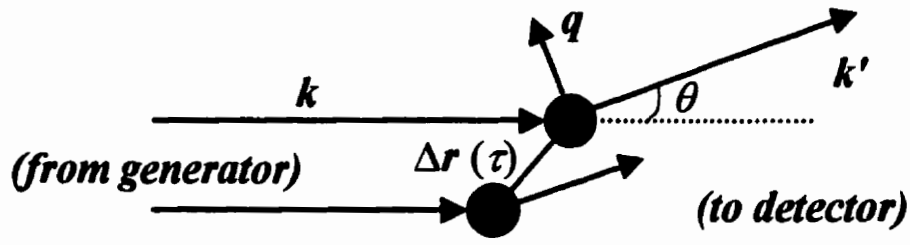


Figure 2.3.1: Single scattering from a moving particle.

$$\begin{aligned}
 \Delta\phi_p &= [\vec{k}' \cdot \vec{r}(t+\tau) - \vec{k} \cdot \vec{r}(t+\tau)] - [\vec{k}' \cdot \vec{r}(t) - \vec{k} \cdot \vec{r}(t)] \\
 &= [\vec{k}' - \vec{k}] \cdot [\vec{r}(t+\tau) - \vec{r}(t)] \\
 &= \vec{q} \cdot \Delta\vec{r}(\tau)
 \end{aligned} \quad . \quad (2.64)$$

Combining this with Eq. (2.63) leads to

$$\begin{aligned}
 g_1(\tau) &= \exp\left[-\frac{1}{2}\langle[\vec{q} \cdot \Delta\vec{r}(\tau)]^2\rangle\right] \\
 &= \exp\left[-\frac{1}{2}q^2\langle\Delta\vec{r}_q^2(\tau)\rangle\right]
 \end{aligned} \quad (2.65)$$

where $\Delta\vec{r}_q$ is the displacement in the direction of the scattering wave vector. Equation (2.65) shows explicitly that DSS is only sensitive to the mean square displacement in the direction of \vec{q} , which is determined by the scattering geometry.

2.3.2 Diffusing Acoustic Wave Spectroscopy (DAWS)

In the intermediate frequency range, scattering can be very strong. The resulting multiply scattered waves can be modeled by the diffusion approximation, which views the propagation as a random walk from one scattering event to the next [c.f. Sec. 2.2]. Within this approximation, an expression relating the field autocorrelation function and the relative motion of the scatterers can be developed [Maret & Wolf 1987, Pine *et al.* 1988, Bicout *et al.* 1993 and 1994]. First, I will derive an approximate relationship between the field autocorrelation function and the relative motion of the scatterers that is appropriate for our non-Brownian fluidized suspensions. Later in this section, a more rigorous relationship that holds for a wider range of dynamical situations will be presented.

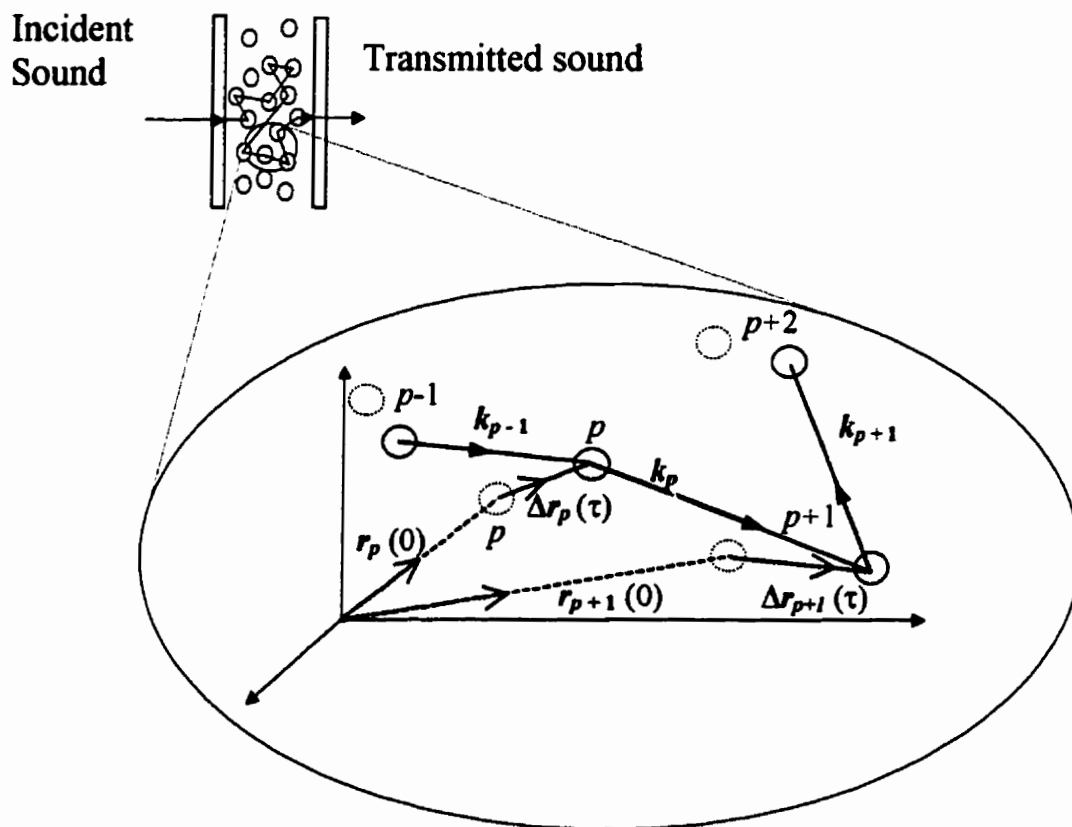


Figure 2.3.2: Segment of a multiple scattering path with moving scatterers. Solid spheres are at $t = \tau$, open spheres are at $t = 0$.

As is evident from Fig. 2.3.2, the phase change of a single scattering path with n scattering events can be written

$$\begin{aligned}\Delta\phi^{(n)} &= \sum_{p=0}^n \vec{k}_p \cdot [\Delta\vec{r}_{p+1}(\tau) - \Delta\vec{r}_p(\tau)] \\ &= \vec{k}_0 \cdot \Delta\vec{r}_1(\tau) - \vec{k}_n \cdot \Delta\vec{r}_n(\tau) + \sum_{p=1}^{n-1} \vec{k}_p \cdot \Delta\vec{r}_{rel,p}(\tau, l^*) ,\end{aligned}\quad (2.66)$$

where the sum splits into three terms because the source ($p = 0$ term) and detector ($p = n$ term) are not moving, and $\Delta\vec{r}_{rel,p}$ gives the relative motion of the p^{th} and $p+1^{\text{th}}$ scatterers, which are on average a distance l^* apart.

In a manner similar to that in the last section, the field autocorrelation function can be written as a sum of contributions from paths with n scattering events,

$$g_1(\tau) = \sum_n g_1^{(n)}(\tau) = \sum_n P(n) \langle e^{-i\Delta\phi^{(n)}(\tau)} \rangle . \quad (2.67)$$

Here $P(n)$ is the fraction of sound in paths of length n , as given by diffusion theory. For a continuous wave input, all path lengths contribute and the sum in Eq. (2.67) must be performed. However for a pulsed input, the average path length is selected by measuring the field fluctuations at a fixed sampling time $t_s = s/\nu_E$ after the input pulse is incident on the sample, and the summation is restricted to include only those paths whose length s differs from the average by the pulse length ($\Delta t/\nu_E$). In particular, for a narrow pulse, $P(n)$ is essentially constant in the summation over n and the normalized field correlation function takes on the relatively simple form

$$g_1(\tau) = \langle e^{-i\Delta\phi^{(n)}(\tau)} \rangle . \quad (2.68)$$

For large n it is a good approximation to assume that successive phase shifts in Eq. (2.66)

are uncorrelated,

$$g_1(\tau) = \left\langle e^{-i\vec{k} \cdot \Delta\vec{r}_{rel}(\tau, l^*)} \right\rangle^{n-1} \left\langle e^{i\vec{k} \cdot \Delta\vec{r}_{rel}(\tau, L)} \right\rangle. \quad (2.69)$$

The second term gives the relative motion of the first and last particles in the scattering path, which are approximately separated by the sample size, L , in a transmission experiment. Equation (2.69) can be further simplified by using the cumulant expansion,

$$g_1(\tau) = \exp \left[-\frac{n-1}{2} \left[\left\langle [\vec{k} \cdot \Delta\vec{r}_{rel}(\tau, l^*)]^2 \right\rangle + \frac{1}{n-1} \left\langle [\vec{k} \cdot \Delta\vec{r}_{rel}(\tau, L)]^2 \right\rangle \right] \right]. \quad (2.70)$$

The three dimensional average of the square of the dot products can be written in terms of α , the angle between the wave vector and the relative displacement.

$$\begin{aligned} \left\langle [\vec{k} \cdot \Delta\vec{r}_{rel}]^2 \right\rangle &= k^2 \left\langle \Delta r_{rel}^2 \cos^2 \alpha \right\rangle = k^2 \left\langle \Delta r_{rel}^2 \right\rangle \left\langle \cos^2 \alpha \right\rangle \\ &= \frac{k^2}{3} \left\langle \Delta r_{rel}^2 \right\rangle \end{aligned} \quad (2.71)$$

The average was split because, for a multiply scattered path, the directions of the wave vector and relative displacement are not correlated (or at least not strongly, as will be discussed later). Substituting Eq. (2.71) into (2.70),

$$g_1(\tau) = \exp \left[-\frac{nk^2}{6} \left[\left\langle \Delta r_{rel}^2(\tau, l^*) \right\rangle + \frac{1}{n} \left\{ \left\langle \Delta r_{rel}^2(\tau, L) \right\rangle - \left\langle \Delta r_{rel}^2(\tau, l^*) \right\rangle \right\} \right] \right]. \quad (2.72)$$

The term in curly brackets will be zero if the motion of particles separated by a distance of more than l^* is uncorrelated. Furthermore, $\left\langle \Delta r_{rel}^2(\tau, l^*) \right\rangle = \left\langle \Delta r_{rel}^2(\tau, L) \right\rangle = 2 \left\langle \Delta r^2(\tau) \right\rangle$ in this case, leading to the standard result used in light scattering experiments in strongly scattering random colloidal suspensions (DWS) [Pine *et al.* 1988]. However, for

millimeter-sized beads in a fluidized bed, the motions of neighbors in the scattering path can be correlated, but even so, for large n this term can be neglected. This is especially true because particles near the walls tend to move more slowly due to viscous drag effects. In our experiments, n is always greater than (usually much greater than) 20, giving an effect which is always less than 5% [Sec. 5.2.1], which means that to a good approximation the field autocorrelation function is given by the simple relationship

$$g_1(\tau) = \exp\left[-\frac{nk^2}{6}\langle\Delta r_{rel}^2(\tau, l^*)\rangle\right]. \quad (2.73)$$

The number of scattering events can be related to the path length (s), and thus the travel time (t_s) in the sample.

$$s = t_s v_E = [n + 1]l^* \quad (2.74)$$

which leads to

$$g_1(\tau) = \exp\left[-\frac{k^2 v_E}{6l^*}\left\{t_s - \frac{l^*}{v_E}\right\}\langle\Delta r_{rel}^2(\tau, l^*)\rangle\right]. \quad (2.75)$$

This equation can be simply inverted to find the relative mean square displacement of particles separated by a distance l^* , given the measured field autocorrelation function and diffusion parameters.

For non-Brownian particles, the early time behavior of the particles should be ballistic, meaning that each particle travels at a (different) constant velocity, without interacting with its neighbors. The mean square displacement from single scattering [Eq. (2.65)] should then be

$$\langle\Delta r^2(\tau)\rangle = V_{rms}^2 \tau^2, \quad (2.76)$$

allowing the root mean square velocity of the particles to be determined. Similarly, the relative mean square displacement will be given by

$$\langle \Delta r_{rel}^2(\tau, l^*) \rangle = \Delta V_{rel}^2(l^*) \tau^2. \quad (2.77)$$

In general, the relative mean square displacement of particles separated by l^* can be expressed as

$$\begin{aligned} \langle \Delta r_{rel}^2(l^*) \rangle &= \left\langle [\Delta \vec{r}(\vec{x} + \vec{l}^*) - \Delta \vec{r}(\vec{x})]^2 \right\rangle \\ &= 2 \langle \Delta r^2 \rangle - 2 \langle \Delta \vec{r}(\vec{x} + \vec{l}^*) \cdot \Delta \vec{r}(\vec{x}) \rangle. \end{aligned} \quad (2.78)$$

Using Eq. (2.76) and (2.77), at early times Eq. (2.78) can be further simplified to

$$\begin{aligned} \Delta V_{rel}^2(l^*) &= 2V_{ms}^2 - 2 \langle V(\vec{x} + \vec{l}^*) \cdot V(\vec{x}) \rangle \\ \Delta V_{rel}^2(l^*) &= 2V_{ms}^2 \left[1 - \frac{\langle V(\vec{x})V(\vec{x} + \vec{l}^*) \rangle}{\langle V(\vec{x})V(\vec{x}) \rangle} \right]. \end{aligned} \quad (2.79)$$

This shows that the length scale dependence of the relative mean square velocity of particles is intimately related to the instantaneous spatial velocity correlation function, and that by varying l^* this correlation function can be probed [Cowan *et al.* 2000].

In Eq. (2.71), it is the dot product of the relative mean square displacement and the wave vector that enters the field autocorrelation function. Since the wave vector points from the center of one particle in the path to its neighbor, this means that DAWS is not sensitive to rotational motion (i.e. $\Delta \vec{r}_{rel} \perp \vec{k}$) of the beads. Therefore the measured relative mean square displacement does not include any rotational contributions. To rigorously describe the measured relative motions, we follow the derivation by Bicout *et*

al. [1993 & 1994], which considers the strain rate tensor of the particle velocity field

$$\varepsilon_{ij}(\tau) = \frac{1}{2} \left(\frac{\partial u_i(\tau)}{\partial r_j} + \frac{\partial u_j(\tau)}{\partial r_i} \right). \quad (2.80)$$

Here $\vec{u}(\tau) = \Delta\vec{r}(\tau)$ is the change in position of the p^{th} particle located at position \vec{r} , and i, j , and k represent Cartesian coordinates. The relative displacement of particles separated by a scattering mean free path can be approximated by the leading order term in a Taylor series expansion,

$$\begin{aligned} \Delta\vec{r}_{\text{rel}, p} &= \Delta\vec{r}_{p+1} - \Delta\vec{r}_p \\ &= l_s [\hat{e}_p \cdot \nabla] \vec{u} \end{aligned} \quad (2.81)$$

where \hat{e}_p is a unit vector in the direction of \vec{k}_p . The phase change of a path then becomes

$$\begin{aligned} \Delta\phi(\tau) &= kl_s \sum_p \sum_{i,j} e_i^{(p)} e_j^{(p)} \varepsilon_{ij}(\vec{r}_p, \tau) \\ &= nkl_s \sum_{i,j} e_i^{(p)} e_j^{(p)} \varepsilon_{ij}(\vec{r}_p, \tau) . \end{aligned} \quad (2.82)$$

For isotropic scattering the \hat{e}_p are randomly distributed, so $\langle \Delta\phi \rangle$ can be found by averaging each term in (2.82) over the unit sphere. For anisotropic scattering, it can be shown that the same holds true, if l_s is replaced everywhere by l^* [Bicout *et al.* 1993].

$$\langle \Delta\phi(\tau) \rangle = \frac{1}{3} n k l^* \left\langle \sum_i \varepsilon_{ii} \right\rangle \quad (2.83)$$

Therefore only the diagonal terms of the strain rate tensor survive the ensemble average, showing that $\langle \Delta\phi \rangle = 0$ unless there is a uniform dilation or compression of the medium. Thus for incompressible media g_1 is determined by the second moment of the phase

change,

$$\langle \Delta\phi^2(\tau) \rangle = \frac{2n(kl^*)^2}{15} \left[\left\langle \left\{ \sum_i \varepsilon_{ii} \right\}^2 \right\rangle + 2 \sum_{i,j} \langle \varepsilon_{ij}^2 \rangle \right]. \quad (2.84)$$

The first term in (2.84) describes the effect of fluctuations in the density of the medium, due to local variations in the number of particles per unit volume, while the second term is simply the sum of all the mean square tensor strains. Therefore the relative mean square displacement measured by DAWS can be written

$$\langle \Delta r_{rel,meas}^2(\tau) \rangle = \bar{\varepsilon}^2 l^*{}^2, \quad (2.85)$$

with the average measured strain rate given by

$$\bar{\varepsilon}^2 = \frac{2}{5} \left[\left\langle \left\{ \sum_i \varepsilon_{ii} \right\}^2 \right\rangle + 2 \sum_{i,j} \langle \varepsilon_{ij}^2 \rangle \right]. \quad (2.86)$$

2.3.3 Continuous Wave DAWS

For a continuous wave input all scattering paths through the cell are sampled, therefore Eq. (2.73) must be averaged over path length, with the weighting given by diffusion theory. This has been worked out in detail by Zhu *et al.* [1991], and results in the following expression:

$$g_1(\tau) = \frac{\left[\sinh[l^* \sqrt{w}] + h\sqrt{w} \cosh[l^* \sqrt{w}] \right]}{\left[1 + h^2 w \right] \sinh[L\sqrt{w}] + 2h\sqrt{w} \cosh[L\sqrt{w}]} \cdot \frac{\left[1 + h^2 \{D\tau_a\}^{-1} \right] \sinh\left[L\sqrt{\{D\tau_a\}^{-1}}\right] + 2h\sqrt{\{D\tau_a\}^{-1}} \cosh\left[L\sqrt{\{D\tau_a\}^{-1}}\right]}{\left[\sinh[l^* \sqrt{\{D\tau_a\}^{-1}}] + h\sqrt{\{D\tau_a\}^{-1}} \cosh[l^* \sqrt{\{D\tau_a\}^{-1}}] \right]}, \quad (2.87)$$

where

$$w = \frac{2k^2 \langle \Delta r_{rl}^2(\tau) \rangle}{l^*} + \frac{1}{D\tau_a}.$$

Here, h includes all of the effects of reflection at the sample boundaries, and is given by Eq. (2.48). Because of its effect on the distribution of path lengths, the absorption time enters continuous wave DAWS, whereas in pulsed DAWS a particular path length is explicitly chosen, so the absorption time is not directly important. The equation can be numerically inverted to find the relative mean square displacement of the particles, given all of the diffusion parameters.

2.3.4 Phase Difference Statistics

The ability of ultrasonic detectors to measure the wave field directly makes it fairly straightforward to measure the phase of the scattered waves. The transmitted phase that we measure in a pulsed experiment, is the result of the interference of many different paths of length n . In order to extract information from these phase measurements, it is necessary to develop a theory of the underlying statistics of the phase of waves scattered in a random medium. This theory has been developed in collaboration with B. A. van Tiggelen.

We begin by assuming circular Gaussian statistics for the complex field, i.e. that

the real and imaginary parts of the field are independent random variables with Gaussian statistics [van Tiggelen *et al.* 1999]. Then, consider the change in the phase of the wave, due to the motion of particles, over a time τ :

$$\Delta\Phi(\tau) = \Phi(t + \tau) - \Phi(t). \quad (2.88)$$

The joint probability distribution for the field, $\psi_t = A_t e^{i\Phi_t}$, at two times, can be written in terms of the amplitude and wrapped phase $[-\pi, \pi]$ at those two times [Goodman 1985 and van Tiggelen *et al.* 1999]:

$$\begin{aligned} P(A_t, A_{t'}, \Phi_t, \Phi_{t'}) \\ = \frac{\mu^2}{\pi^2} A_t A_{t'} \exp \left[-A_t^2 - |z|^2 A_{t'}^2 - \mu^2 A_{t'}^2 + 2|z|\mu A_t A_{t'} \cos[\Phi_t - \Phi_{t'} + \vartheta] \right] \end{aligned} \quad (2.89)$$

with the complex number $z = |z|e^{i\vartheta}$ defined by

$$\frac{\langle \psi \psi^* \rangle}{\langle \psi \psi^* \rangle} = g_1(\tau) = \frac{z^*}{\sqrt{1+|z|^2}} \quad (2.90)$$

and with

$$\begin{aligned} \mu^2 &= 1 + |z|^2 \\ \tau &= t - t' \\ \Delta\Phi &\in [-\pi : \pi]. \end{aligned} \quad (2.91)$$

The two amplitudes, A_t and $A_{t'}$, can be integrated out of Eq. (2.89), and one of the phases can be integrated out at constant $\Delta\Phi$, giving

$$P(\Delta\Phi) = \left[\frac{2\pi - |\Delta\Phi|}{4\pi^2} \right] \frac{1 - g_1^2}{1 - g_1^2 \cos^2[\Delta\Phi]} \left[1 + \frac{g_1 \cos[\Delta\Phi] \cos^{-1}[-g_1 \cos[\Delta\Phi]]}{\sqrt{1 - g_1^2 \cos^2[\Delta\Phi]}} \right] \quad (2.92)$$

with the field autocorrelation function

$$g_1 \approx \exp\left[-\frac{1}{2}\langle\Delta\phi^2(\tau)\rangle\right], \quad (2.93)$$

where $\Delta\phi$ is the phase change of one path through the sample, as in DAWS. From Eq. (2.75), this phase change is related to the relative mean square displacement by

$$\langle\Delta r_{rel}^2(\tau, l^*)\rangle = \frac{3l^*}{k^2 v_E \left[t_s - \frac{l^*}{v_E}\right]} \langle\Delta\phi^2(\tau, l^*)\rangle. \quad (2.94)$$

Note that in the limit $g_1 \rightarrow 0$ the probability distribution is given by the triangle function

$$P(\Delta\Phi) = \frac{2\pi - |\Delta\Phi|}{4\pi^2}, \quad (2.95)$$

which is independent of τ . This means that when using this wrapped phase distribution function, all information about the beads is lost when the field correlation function gets small, just as in DAWS.

By measuring the phase fluctuations as a function of time, the probability distribution $P(\Delta\Phi)$ for different τ can be calculated. Then by fitting Eq. (2.92) to the data, information about the motion of the particles can be extracted from the phase fluctuations.

2.3.5 Siegert Relation

The Siegert relation relates the field autocorrelation function to the intensity correlation function in a random system. As such, it is very important in light scattering, since it is generally easier to calculate the field autocorrelation function theoretically, but it is the intensity correlation function that can be measured. With ultrasound, the field can

be measured directly, so it is possible to test the validity of the Siegert relation under different conditions.

The Siegert relation is [e.g. see Zhu *et al.* 1991]

$$g_2(\tau) = \beta |g_1(\tau)|^2, \quad (2.96)$$

where β is a numerical factor which is ideally 1, g_1 is the field autocorrelation function, and

$$g_2(\tau) \equiv G_2(\tau) - 1, \quad (2.97)$$

where

$$G_2(\tau) = \frac{\langle I(t)I(t+\tau) \rangle_t}{\langle I(t) \rangle_t^2} \quad (2.98)$$

is the intensity autocorrelation function. Thus this relation allows intensity autocorrelation functions to be related to field autocorrelation functions, which are much more easily handled in theoretical models. However, Eq. (2.96) is not exact, and despite its widespread use, there have only been limited studies of its applicability to different experimental situations [Voigt & Hess 1993 and references therein]. In this section we look at the approximations required in the derivation of the Siegert relation, both for singly and multiply scattered waves.

To derive the Siegert relation in the context of singly scattered waves, we start by writing down the intensity autocorrelation function in terms of a sum of field contributions from all of the paths through the sample,

$$\begin{aligned}
G_2(\tau) &= \frac{\langle \psi(t)\psi^*(t)\psi(t+\tau)\psi^*(t+\tau) \rangle}{\langle \psi(t)\psi^*(t) \rangle^2} \\
&= \frac{\left\langle \sum_{i,j,k,l} \exp[i\{\phi_i(t) - \phi_j(t) + \phi_k(t+\tau) - \phi_l(t+\tau)\}] \right\rangle}{\left\langle \sum_{i,j} \exp[i\{\phi_i(t) - \phi_j(t)\}] \right\rangle^2} . \quad (2.99)
\end{aligned}$$

In a random system, the positions of the particles are random, thus the relative phases of different paths are uncorrelated and will average to zero. Therefore, in the denominator only terms with $i = j$ will survive the averaging process, and in the numerator only terms with

$$\phi_i(t) - \phi_j(t) + \phi_k(t) - \phi_l(t) = 0 \quad (2.100)$$

will survive [e.g. Tong *et al.* 1988 and Section 2.3.1]. The two possible choices which will always satisfy Eq. (2.100) for all times are

$$i = j \text{ with } k = l \quad (2.101)$$

and

$$i = l \text{ with } j = k . \quad (2.102)$$

This leads to

$$\begin{aligned}
G_2(\tau) &= \frac{N^2 + \sum_{i,j} \langle \exp[-i\{\Delta\phi_j(\tau) - \Delta\phi_i(\tau)\}] \rangle}{N^2} \\
&= 1 + \frac{1}{N^2} \sum_{i,j} \langle \exp[-i\{\Delta\phi_{rel,ij}(\tau)\}] \rangle , \quad (2.103)
\end{aligned}$$

$$G_2(\tau) = 1 + \beta \langle \exp[-i\{\Delta\phi_{rel}(\tau, R)\}] \rangle_{t,R} . \quad (2.104)$$

Here the last average is over both time and scatterer separation R , in the scattering

volume. $\Delta\phi_{rel}(\tau, R)$ is the relative phase change over a time τ , of paths separated by a distance R . N is the number of scatterers in the scattering volume. The factor β is of order 1, and depends on the geometry and size of the scattering volume, but is primarily determined by how many speckles are averaged by the detector. The phase change can be expressed in terms of the relative displacement of particles, as in Section 2.3.1,

$$G_2(\tau) = 1 + \beta \exp \left[-\frac{q^2}{2} \langle \Delta r_{rel,\vec{q}}^2(\tau, R) \rangle_{i,R} \right] \quad (2.105)$$

$$g_2(\tau) = \beta \int_V h(R) \exp \left[-\frac{q^2}{2} \langle \Delta r_{rel,\vec{q}}^2(\tau, R) \rangle_i \right] dR$$

where, in the last line, the average over R has been explicitly written as an integral over the scattering volume V . The function $h(R)$ gives the fraction of particles in the scattering volume that are separated by a distance R . The relative mean square displacement can be expressed in terms of the mean square displacement and a spatial correlation function [c.f. Sec. 2.3.2],

$$g_2(\tau) = \beta \int h(R) \exp \left[-\frac{q^2}{2} 2 \langle \Delta r_{\vec{q}}^2(\tau) \rangle \left\{ 1 - \frac{\langle \Delta r_{\vec{q}}(\tau, \vec{x}) \cdot \Delta r_{\vec{q}}(\tau, \vec{x} + \vec{R}) \rangle}{\langle \Delta r_{\vec{q}}^2(\tau, \vec{x}) \rangle} \right\} \right] dR \quad (2.106)$$

$$= \beta |g_1(\tau)|^2 \left[\int dR h(R) \left[|g_1(\tau)|^2 \right] \frac{\langle \Delta r_{\vec{q}}(\tau, \vec{x}) \cdot \Delta r_{\vec{q}}(\tau, \vec{x} + \vec{R}) \rangle}{\langle \Delta r_{\vec{q}}^2(\tau, \vec{x}) \rangle} \right].$$

If the motion of the particles in the sample is uncorrelated (or at least for those which are most strongly weighted by $h(R)$), then (2.106) reduces to the Siegert relation [Eq. (2.96)]. However, if the motion of the particles is correlated, there will be deviations from the Siegert relation given by deviations in the following ratio from one:

$$\frac{g_2(\tau)}{\beta |g_1(\tau)|^2} = \int dR h(R) \left[|g_1(\tau)|^2 \right]^{-\frac{\langle \Delta r_{\vec{q}}(\tau, \vec{x}) \cdot \Delta r_{\vec{q}}(\tau, \vec{x} + \vec{R}) \rangle}{\langle \Delta r_{\vec{q}}^2(\tau, \vec{x}) \rangle}} \quad (2.107)$$

In order to use Eq. (2.107) to model deviations from the Siegert relation, we need to approximate the distribution of scatterer separations, $h(R)$. For a finite scattering volume in three dimensions, $h(R)$ will have a peak value at a particular value of the separation distance, R_p . Thus, the simplest approximation is to only consider the contribution to the integral at this peak, i.e. to take $h(R)$ to be a delta-function centered at R_p . Within this approximation, Eq. (2.107) can be solved for the spatial correlation function of the particle displacements:

$$\frac{\langle \Delta r_{\vec{q}}(\tau, \vec{x}) \cdot \Delta r_{\vec{q}}(\tau, \vec{x} + \vec{R}_p) \rangle_x}{\langle \Delta r_{\vec{q}}^2(\tau, \vec{x}) \rangle_x} = 1 - \frac{\ln [g_2(\tau)/\beta]}{\ln [|g_1(\tau)|^2]}. \quad (2.108)$$

For multiply scattered waves, the analysis is essentially the same up to Eq. (2.103), except that the $\Delta\phi$ are interpreted as the phase changes for paths with n scattering events, and N is now the number of scattering paths through the sample. As n increases from 1, the situation is similar to the single scattering case; the motion of particles in adjacent paths might be correlated, leading to deviations from the Siegert relation. But as n gets larger, the scattering path samples a larger and larger volume of the sample, and so the phase changes of different paths of the same length are likely to become more and more decorrelated. Therefore, one may expect that the Siegert relation will hold for long scattering paths, but may not hold for shorter paths in the presence of significant particle velocity correlations.

2.4 Suspended Particle Motion

In this section, the current state of the theory underlying the motion of non-Brownian particles that are suspended in fluidized beds is presented. The first section develops the analogy between sedimentation of particles in a fluid and fluidization. An expression for the average sedimentation velocity, or equivalently the average flow velocity of the fluid in a fluidized bed is derived for low volume fractions of particles, and a phenomenological form is presented for high volume fractions. Section 2.4.2 presents some of the competing theories that have arisen in the attempt to describe the root mean square fluctuations in the particle velocity, and their dependence on the size of the system.

2.4.1 Sedimentation and Fluidization

In the simplest view of sedimentation and fluidization, they are simply related through a change in reference frames. Sedimentation refers to the frame where the average velocity of the fluid is zero, and the particles sediment down under the influence of gravity. Fluidization refers to the frame where the average velocity of the particles is zero, and it is the fluid that is moving up. Therefore a fluidized bed is a convenient way to study sedimentation in the lab, since in the lab frame the particles have an average velocity of zero, so that the particles' motion can be studied as long as desired without having them sediment. However this view is likely to be overly simplistic, in particular if one considers a finite system with solid walls as a boundary. In the sedimentation case, the walls are stationary with respect to the average velocity of the fluid, but in the fluidization case the fluid moves with respect to the walls. Given a finite viscosity, this effect is bound to result in some subtle, and perhaps not so subtle, differences between sedimentation and

fluidization, but nonetheless the basic analogy between sedimentation and fluidization is likely to be approximately valid.

To derive an expression for the average fluid velocity needed to suspend particles in a fluidized bed at a volume fraction of ϕ , we follow the approach outlined by Russel *et al.* [1989] to derive the average sedimentation velocity. Considering a single sphere of radius a in an infinite fluid, the terminal Stokes velocity V_o , can be found by simply balancing the force due to gravity with the viscous drag force, leading to the equation

$$V_o = \frac{2[\rho_p - \rho_f]a^2g}{9\eta}. \quad (2.109)$$

Here, ρ_p is the density of the particles, ρ_f is the density of the fluid, η is its viscosity, and g is the acceleration due to gravity. This equation is valid for low particle Reynolds number, corresponding to creeping flow conditions,

$$Re = \frac{2a\rho_f V_o}{\eta} < 1. \quad (2.110)$$

However, even for low Re , when more spheres are added, giving a finite concentration or volume fraction of particles, the situation becomes much more complex.

At finite volume fractions, hydrodynamic interactions between particles can lead to a reduction in the sedimentation velocity, as compared to that of a single particle. For particles with large diameters, these hydrodynamic forces dominate Brownian motion, with the relative strengths of these effects measured by the Peclet number

$$Pe = \frac{8\pi a^2 \Delta \rho g}{3kT} \frac{\Delta V}{V_o}, \quad (2.111)$$

where ΔV is the velocity variance for sedimentation, which is equal to the rms particle velocity, $V_{rms} = \langle V^2 \rangle^{1/2}$, for fluidization. When $Pe \gg 1$, hydrodynamic forces determine the spatial distribution of particles, and the particle velocity distribution. In our samples $Pe \sim 10^{11}$, meaning that the particles are decidedly non-Brownian.

Hydrodynamic interactions are caused by viscous effects, mediated by the fluid flow fields induced by the motion of each particle; they are long range, varying as r^{-1} . Using the Stokes equation, an exact form for the interaction between pairs of particles can be derived, and the sedimentation (or fluidization) velocity (V_f) can be expressed as an expansion in ϕ ,

$$\frac{V_f}{V_o} = 1 - K_2\phi + O(\phi^2) \quad (2.112)$$

with $K_2 = 6.55$ for hard colloidal spheres. In the derivation of this equation, the particles were assumed to be randomly distributed in space. However, when the particles are non-Brownian there is no reason to expect that all configurations of the particles are equally probable. Nonetheless, for large particles and also for larger ϕ , it has been found that the phenomenological form

$$\frac{V_f}{V_o} = [1 - \phi]^{\kappa_2} \quad (2.113)$$

characterizes the experimentally observed behavior, although K_2 is no longer equal to 6.55 [Russel *et al.* 1989 and references therein].

2.4.2 Velocity Fluctuations and Correlations

There is a basic analogy between studying the statistics of the particles' velocity

distribution in a fluidized bed, and the statistics of wave propagation in a random system. In both cases, we look at the first two moments of the probability distribution, with each moment illuminating a different aspect of the physics of the system. The average particle velocity $\langle \vec{V} \rangle$ is analogous to the Green's function of the average field $\langle G \rangle$. In a fluidized bed the average velocity of the particles is equal to zero (but the average velocity in sedimentation is equivalent to the average fluid flow rate in fluidization), and the next moment of the velocity distribution holds most of the physics of interest. This moment is the mean square velocity fluctuation $\langle \vec{V}(\vec{r}) \cdot \vec{V}(\vec{r}) \rangle$, or more generally the velocity correlation $\langle \vec{V}(\vec{r}) \cdot \vec{V}(\vec{r} + \vec{r}') \rangle$, and is analogous to the Green's function representation of the average intensity $\langle GG^* \rangle$, or the field correlation $\langle G(\vec{r})G^*(\vec{r} + \vec{r}') \rangle$. The mean square velocity fluctuations give information about the average speed of the particles in the fluidized bed, while the velocity correlation function gives information about flow patterns and regions of correlated motion that form spontaneously in fluidized suspensions.

Under the same conditions used to derive Eq. (2.112) for the sedimentation velocity, a scaling theory can be developed for the mean square velocity fluctuations [Caflisch & Luke 1985]. Owing to the long-range nature of hydrodynamic interactions, particles at large separations continue to strongly interact, and, if the particles are assumed to be randomly distributed, this results in an ensemble-averaged velocity variance of

$$\langle V^2 \rangle = \int V^2 dP \sim \phi \int V^2 d^3 r \quad (2.114)$$

where $dP = \phi d^3 r / [4\pi a^3 / 3]$ represents the uniform probability distribution. Since the

velocity field caused by a particle decays as r^{-1} , $V \sim r^{-1}$ in the integral above, which leads to a linear dependence of $\langle V^2 \rangle$ on the system size L .

$$\langle V^2 \rangle^{\frac{1}{2}} = \phi^{\frac{1}{2}} L^{\frac{1}{2}} \quad (2.115)$$

Thus the velocity fluctuations diverge with sample size, becoming infinite for an infinite sample. Evidence for this seemingly unphysical result has been mixed, with some experiments and simulations [Ladd 1996] agreeing with (2.115), but others showing a saturation of the velocity variance at larger sample sizes [Nicolai & Guazzelli 1995, Segrè *et al.* 1997]. Segrè *et al.* [1997] also found experimental evidence for a velocity correlation length, or screening length ξ , above which velocity fluctuations are cut-off. Using this screening length, Segrè *et al.* [1997] proposed that the conflicting experimental results could be reconciled. For sample sizes larger than ξ , the velocity fluctuations will not increase with further increases in the sample size, whereas for smaller sample sizes, the magnitude of the velocity fluctuations will decrease as the sample size is reduced. However, the exact nature of this screening length, its underlying causes, and how it scales with system size, are still not understood.

To attempt to explain the origin of the screening length several theoretical models have been proposed. These models fall into two basic types; the first explores the consequences of relaxing the assumption of random particle distributions and the second explicitly investigates the effects of boundary conditions (i.e. solid motionless walls).

If the particles in the suspension preferentially arrange themselves in configurations which screen the hydrodynamic force from distant particles, then the velocity fluctuations

will saturate at this screening distance, ξ (i.e. there will be no dependence on the system size for systems larger than ξ). Koch & Shaqfeh [1991] proposed a specific choice of the average particle configuration that leads to a finite result for the velocity variance. The particle configuration used corresponds to a net deficit of one particle in a volume of radius ξ surrounding any given particle in the suspension. This leads to a screening for distances larger than ξ , and to a saturation in the velocity variance. The predicted screening distance, and the velocity variance at length scales larger than ξ , are of order

$$\begin{aligned}\xi &\sim \phi^{-1} \\ \langle V^2 \rangle^{\frac{1}{2}} &\sim V_0\end{aligned}\tag{2.116}$$

while for length scales less than ξ the velocity variance follows Eq. (2.115). The screening distance ξ is equivalent to the velocity correlation length of the velocity correlation function, $\langle \vec{V}(\vec{r}) \cdot \vec{V}(\vec{r} + \vec{r}') \rangle$. The justification for choosing this particular form for the average particle configuration is not particularly strong, but if one considers the effects of 3 particle hydrodynamic interactions on the structure of the suspension, there is a tendency towards a particle deficit, with a probability which decays as r^{-1} .

Levine *et al.* [1998] applied renormalization group methods to coarse grain the hydrodynamic equations of motion for the suspension. Coarse-grain equations are the result of local averaging of the microscopic equations of motion, and are expressed in terms of a local volume fraction and a local particle velocity. The equations are coarse grained at a length scale $l \gg a$, and the fluctuations at length scales smaller than this are included in the equations phenomenologically. This study leads to the possibility of two

“phases”, a screened and unscreened phase, with the unscreened phase occurring when Brownian motion dominates the hydrodynamic interactions. The unscreened phase follows the Caflisch & Luke [1985] result, with a diverging velocity variance. The screened phase is similar to the Koch & Shaqfeh [1991] result, with the velocity variance following the Caflisch & Luke [1985] result for length scales less than ξ , and saturating at larger length scales. However, the resulting average particle distribution of the suspension is significantly different. Also, the predictions for the volume fraction dependence of the screening length and velocity variance differ,

$$\begin{aligned}\xi &\sim \phi^{-\frac{1}{3}} \\ \langle V^2 \rangle^{\frac{1}{2}} &\sim L^{\frac{1}{2}} \quad L < \xi \\ &\sim \xi^{\frac{1}{2}} \quad L > \xi .\end{aligned}\tag{2.117}$$

Brenner [1999] takes a different angle on the problem, by considering the effects of the boundary conditions that are imposed on a suspension by the solid walls of its container. Figure 2.4.1 shows the container, with height L_y , width L_x , and smallest dimension L_z . Near walls the r^{-1} hydrodynamic interactions decay more quickly, at least as fast as r^{-2} . This means that the nature of the flow field caused by a single particle depends on its distance from the nearest wall of the container. Thus a particle which is a distance z from the nearest wall has an interaction volume of $v_o \sim z^3$, within which the strong r^{-1} law holds. Particles that are outside of this interaction volume only interact weakly, and can be ignored.

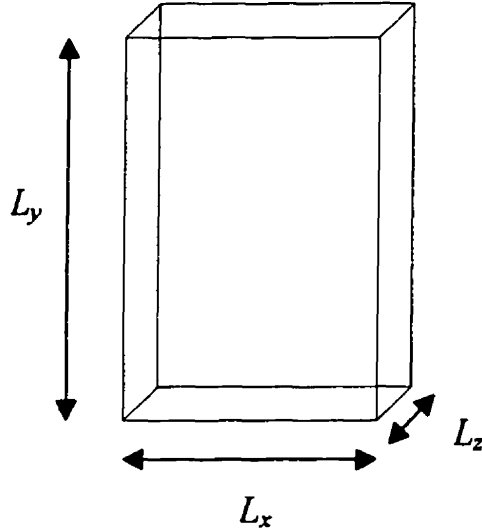


Figure 2.4.1: Sample cell dimensions for Brenner's arguments.

The idea of an interaction volume means that there are two regimes, a strongly interacting one where the interaction volumes of particles overlap, and a weakly interacting one where they do not. In the weakly interacting regime the particles do not interact, so one would expect a random distribution of particles to remain random, leading to a result similar to the predictions of Caflisch & Luke [1985],

$$\langle V^2 \rangle^{\frac{1}{2}} \sim L_x L_z^{\frac{1}{2}} \phi^{\frac{1}{2}}. \quad (2.118)$$

Above a critical volume fraction, or above a critical L_z , the suspension will enter the strongly interacting regime. In this regime

$$\begin{aligned} \xi &\sim L_z^{\frac{2}{3}} \phi^{-\frac{1}{3}} \\ \langle V^2 \rangle^{\frac{1}{2}} &\sim V_o L_z^{\frac{1}{3}} \phi^{\frac{1}{3}} . \end{aligned} \quad (2.119)$$

Note that Brenner's theory only considers the screening effects of the walls, and does not take into account any intrinsic screening in suspensions due to possible correlations in the

positions of particles.

All of the previous theories assumed that the Reynolds number was small, $Re < 1$, and therefore ignored any inertial effects. Inertial effects may lead to other mechanisms that screen long-range hydrodynamic interactions [Koch 1993 and Brenner 1999]. Koch [1993] considers the wake of a particle with intermediate ($Re \sim 1$, inertial effects begin to appear) to high Reynolds number ($Re \sim 10$, inertial effects become important). This causes a net deficit of particles in the center of the wake behind a particle, as they are pushed out of the wake by the fluid flow field. This leads to a screening length

$$\xi \sim \phi^{-1} \quad (2.120)$$

and beyond this screening length the velocity variance is

$$\langle V_y^2 \rangle^{\frac{1}{2}} \sim \phi^{\frac{1}{2}} V_o. \quad (2.121)$$

This theory uses approximations which are only valid for intermediate Reynolds numbers, and fails at both low and high Re .

Brenner [1999] also addresses Reynolds number dependence. In his argument, he assumes that the divergent Caflisch & Luke [1985] result holds, and considers a system that is large enough that the particle diffusivity D_p , due to the velocity fluctuations, is of the same order as the momentum diffusion constant, given by the kinematic viscosity $\nu = \eta / \rho_f$. Then the particles diffuse faster than the momentum they release into the fluid, so that momentum transport away from the particles is no longer effective. Thus the velocity field caused by a particle is no longer long range, and the r^{-1} particle interactions break down, i.e. they are effectively screened out by inertial effects. By balancing ν with

$D_p \sim \langle V^2 \rangle^{\frac{1}{2}} \xi$, the following scaling laws are obtained:

$$\begin{aligned}\xi &\sim a [Re]^{-\frac{1}{3}} \phi^{-\frac{1}{3}} \\ \frac{\langle V^2 \rangle^{\frac{1}{2}}}{V_o} &\sim [Re]^{-\frac{1}{3}} \phi^{\frac{1}{3}} .\end{aligned}\quad (2.122)$$

In Brenner's arguments, these laws apply when the sample is large enough that wall effects no longer dominate, i.e. if the screening length due to inertial effects is smaller than the screening length due to wall effects. This inertial screening will cut off the divergent velocity fluctuations in an infinite system, without invoking a special spatial distribution of particles. This theory is not quantitatively applicable at very large Reynolds numbers, where the Stokes velocity of a single particle is no longer simply given by Eq. (2.109), although the general qualitative predictions should still hold true.

All of the above theories apply only in the low volume fraction limit, but our experimental techniques are readily applicable to intermediate and high volume fractions. At these volume fractions, the basis of the above theories, which is to only consider the sum of all two particle hydrodynamic interactions, begins to fail. Therefore, the behavior of velocity fluctuations and correlation lengths in the high volume fraction regime has not been studied extensively, either experimentally or theoretically.

3. Apparatus

This chapter describes the apparatus used to perform the experiments reported in this thesis. The mechanical apparatus, such as water tanks, temperature control systems, and pumping systems are described first. The details of the construction and composition of the fluidized bed samples is presented in the next section. Then the properties of our ultrasonic transducers and hydrophones are discussed, and the electronics used to generate and detect the ultrasonic pulses are introduced.

3.1 Mechanical Apparatus

3.1.1 Water Tanks

All of these experiments were performed with the sample immersed in a large tank of water. Water is an efficient transmitter of ultrasound, and it provides a convenient way to couple ultrasound from the generating and receiving transducers to our samples, without the need for direct contact and bonds. Immersion in a water bath also gave a simple and effective way to stabilize and control the temperature of our samples.

Two aquariums were used in these experiments. The smaller of the two, which was used for the initial measurements of ballistic transport, was made out of glass, and measured 33 x 75 x 40 cm deep. To reduce the amount of sound reflected back from the glass walls of the tank, it was lined with an absorbing cork sheet. In order to break up any remaining reflections into many directions, 2 x 2 x 40 cm vertical polystyrene foam strips were glued around the inside of the tank at approximately 15 cm intervals. Sheets of 1.4-

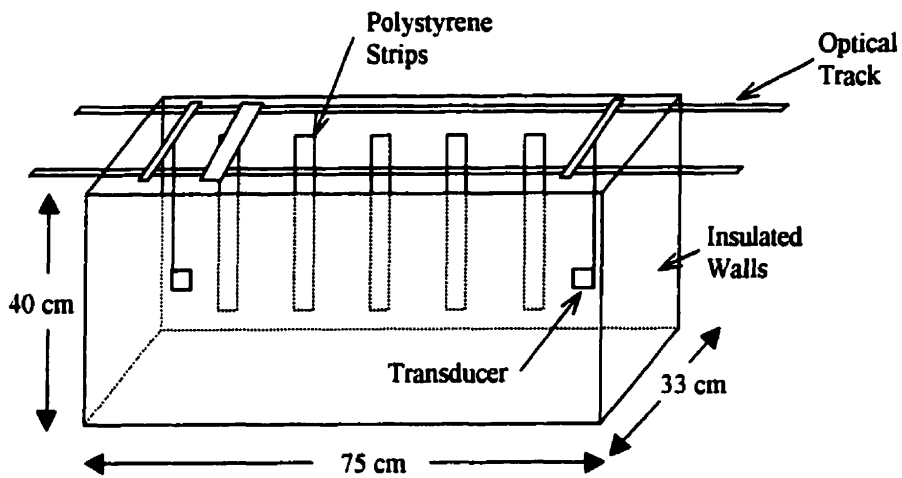


Figure 3.1.1: Small water tank geometry.

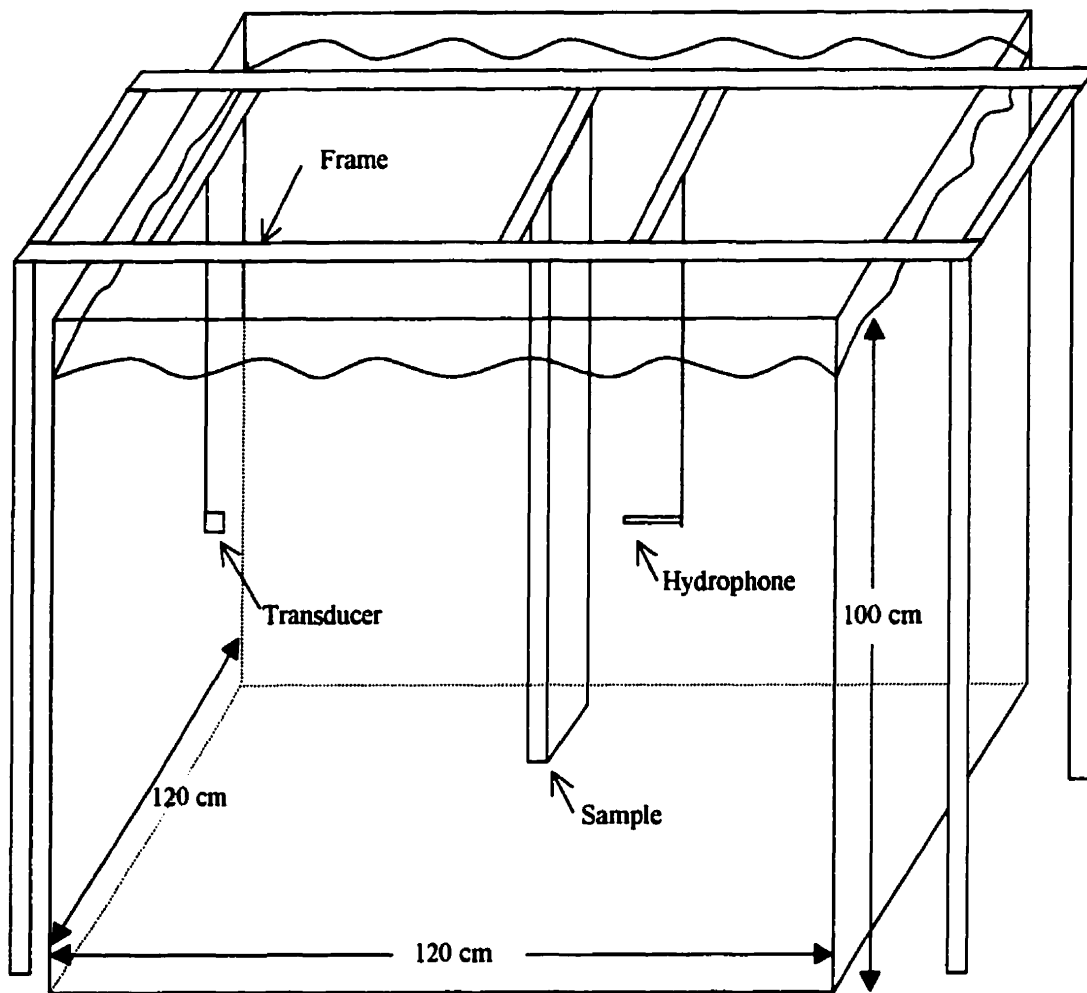


Figure 3.1.2: Large tank geometry.

inch blue foam insulation ($R = 7$) were placed around the outside of the tank, to help control the temperature of the water. An optical track was placed above the tank, and the transducers were attached to stainless steel rods, which were suspended from the track and into the water [Fig. 3.1.1].

The larger of the two tanks was made of reinforced fiberglass, and measured 120 x 120 x 100 cm deep [Fig. 3.1.2]. The tank was insulated by placing sheets of blue foam insulation around its sides, and sheets of plastic bubble wrap were placed on the surface of

the water, both to insulate and to reduce evaporation. To mount equipment in this tank we built a large steel frame above the tank, and suspended the transducers and samples down into the water.

3.1.2 Temperature Control Systems

It was important to keep the temperature of our system stable for several reasons. The velocity of sound in water depends slightly on temperature, varying from $1.48 \text{ mm}/\mu\text{s}$ at 20°C to 1.50 at 27°C , i.e. by about $0.2\%/\text{ }^\circ\text{C}$. The travel time between the receiving and generating transducers in the tank is generally several hundred μs , which means that a one degree change in temperature during a data run can lead to a shift in timing of about half of a microsecond. This is approximately one period at a frequency of 2.25 MHz , and it is about 2% of what was generally the earliest sampling time used in DAWS measurements. More importantly, it can lead to a drift in the ballistic offset, which can be difficult to remove from the field autocorrelation measurements, particularly for single scattering measurements, where the ballistic signal can be relatively large. Thus, this magnitude of temperature drift can make it difficult to analyze some temporal autocorrelation data. In addition, the viscosity of the glycerol and water solution in the fluidized bed is also temperature dependent, and therefore the flow rate needed to attain a particular volume fraction of beads, as well as the particle Reynolds number in the fluidized bed, are both sensitive to the temperature.

To reduce the possible effects of temperature fluctuations to a manageable level, we insulated the tank, and used a heater, mixer and temperature controller to stabilize the temperature at 27.0°C , with variations of less than $\pm 0.05^\circ\text{C}$ for the small tank, and $\pm 0.1^\circ\text{C}$

for the large tank. In the smaller tank, we used a 100 W stainless steel immersion heater, with a Tronac Model PTC-41 controller. For the large tank we used a 6 kW over-the-side copper immersion heater, controlled by an Omega CN3251 Fuzzy Logic PID temperature controller.

3.1.3 Pumping System

To pump water through the fluidized bed we constructed two basic pumping systems, one for the small tank and one for the large tank, as pictured in Fig. 3.1.3 and 3.1.4 respectively. The small tank system used a glass jar for a fluid reservoir, which was insulated to control the fluid temperature, and was sealed to control the differential evaporation of water out of the glycerol/water solution used in the bed. There was also a thermometer mounted in the reservoir to provide a measure of the fluid temperature. The fluid was moved by a medium sized centrifugal drill pump, driven by a 1/8-hp DC electric motor, that was geared down to provide larger torque at slow speeds. The motor was controlled by a custom built DC motor controller. Quarter-inch-diameter plastic vacuum tubing was used to connect the pump, reservoir, and sample together. A thermistor was mounted in one of the fluidized bed's outlet tubes, giving another measurement of the fluid temperature. To measure the flow rate in this system, we closed valve #2 and opened valve #1 [Fig. 3.1.3], and then, with the reservoir unsealed, we measured the rate at which fluid filled a one-liter graduated cylinder.

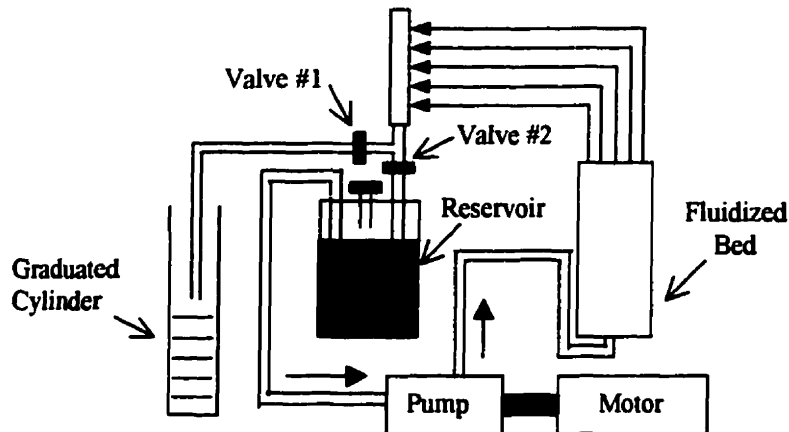


Figure 3.1.3: Pumping system for the small tank.

For the large tank, the pumping system was somewhat different [Fig. 3.1.4].

Instead of using a glass reservoir outside of the tank, a copper reservoir was submerged in the water filled tank, in order to keep the temperature of the fluid as stable as possible. The fluid was pumped out of the reservoir by a rotor pump, with a top flow rate of about 40 l/min., and driven by one of two variable speed motors. The first motor was the same as the one used for the small tank's pumping system, and it was controlled by the same custom built controller. This motor was used to drive the pump smoothly at lower speeds. The second motor was more powerful, at $\frac{1}{2}$ -hp, and it was not geared down, allowing it to drive the larger pump at high speeds, and giving us faster flow velocities in the fluidized bed. Another custom built controller, consisting of a Variac and rectifier mounted in a metal case, was used to drive this motor. Flow rates were measured using essentially the same method outlined above for the smaller tank's pumping system. Temperature measurements in this system were performed using a thermistor mounted in an outtake pipe of the fluidized bed.

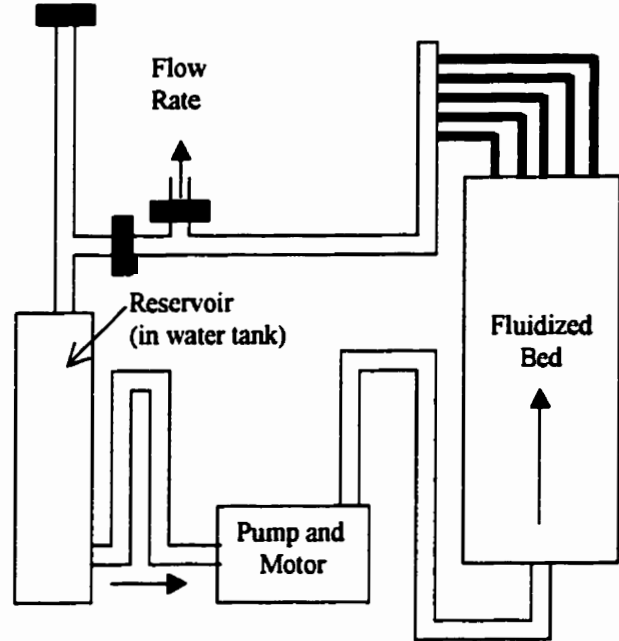


Figure 3.1.4: Pumping system for the large tank.

3.2 Sample Preparation

3.2.1 Fluidized Bed Construction

The fluidized beds were rectangular in cross-section, consisting of a central metal spacer, with two plastic walls attached with an o-ring seal, and held in place by screws and metal plates [Fig. 3.2.1]. Three beds were made, using two basic designs. For the original ballistic propagation measurements, and initial DAWS & DSS measurements, the meta

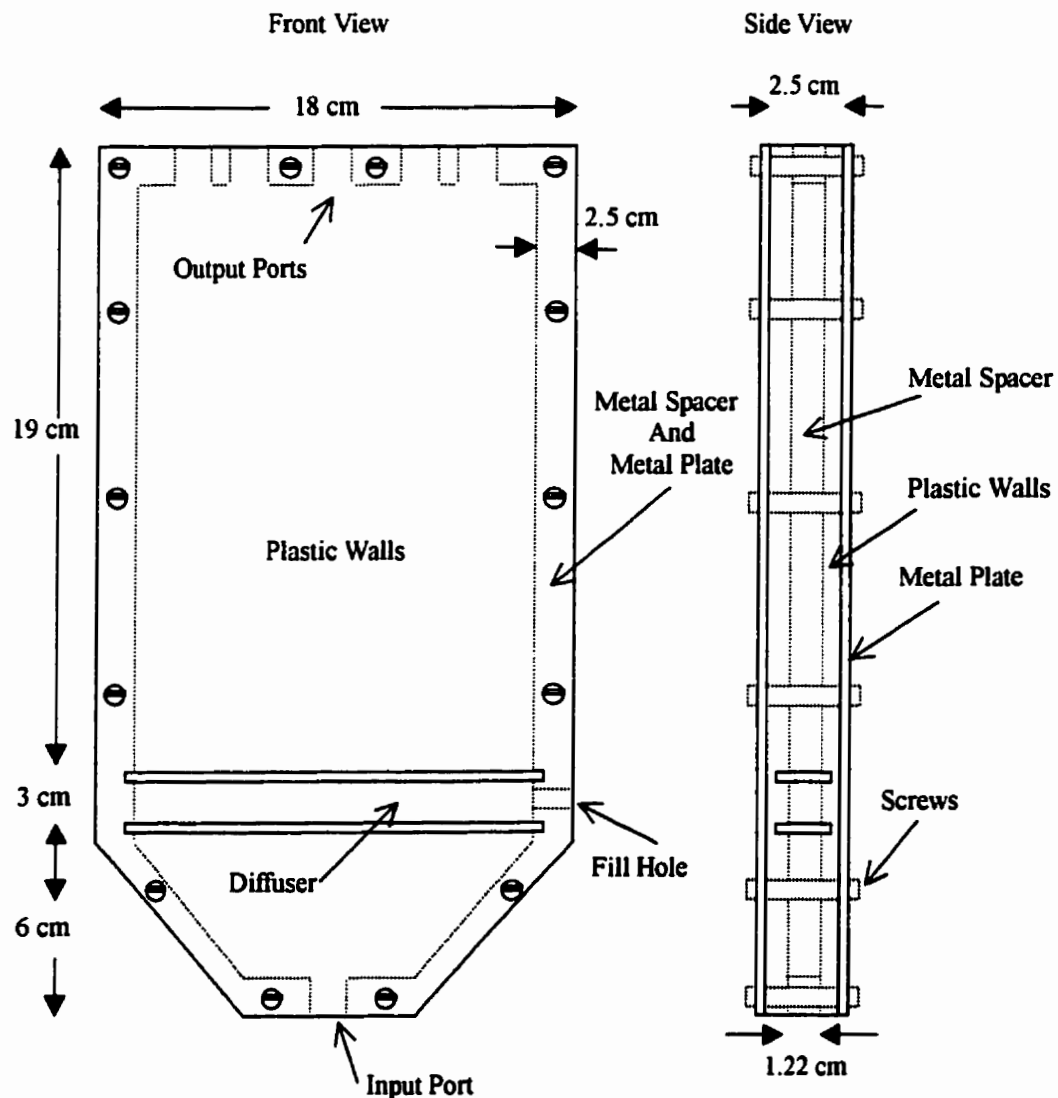


Figure 3.2.1: Small fluidized bed design.

spacer was 12.20 mm thick, the inner height was 17 cm, and the width was 12.6 cm. Two sets of walls were made. One was flat and 6.33 mm thick, giving a sample thickness of 12.20 mm. The other walls were 9.50 mm thick and inset into the sample, reducing the thickness of the bed to 7.76 mm.

The next generation of beds was larger [Fig. 3.2.2]; inside the bed, the height was about 60 cm and the width was 17.8 cm. Two metal spacers were constructed, with thicknesses of 18.6 and 36.5 mm. Flat, half-inch-thick (12.7 mm) flat plastic walls were used with the larger bed, giving a bed thickness of 36.5 mm. Inset, 9.50 mm thick plastic walls were used with the thinner divider, giving a sample thickness of 12.8 mm. Another set of inset, half-inch-thick walls were used with the thinner bed, to give us a third sample thickness, 5.40 mm. The bottom of the both bed designs was formed into a v-shape, which spread out the fluid flowing into the bed from the single hole that was drilled into the bottom of the bed. The fluid was then forced through a diffuser, which generated a uniform flow profile as the fluid entered the main part of the fluidized bed. Two diffuser designs were used for the original bed. The first design consisted of close packed, static, 5-mm-diameter glass beads, held in place by a plastic sheet with small holes drilled into it. The improved design had 1-mm-diameter glass beads close packed in a 3 cm thick layer. For the next generation of beds, the diffuser consisted of two stainless steel screens with 100 μm holes, sandwiching a 10 cm long section of close packed, static, 1 mm glass beads [Fig. 3.2.2]. In all cases, the pressure drop across the diffuser was larger than the pressure drop across the fluidized section, which has been suggested as a necessary condition for attaining uniform flow at the bottom of the bed [Davidson 1985]. At the top of the cell

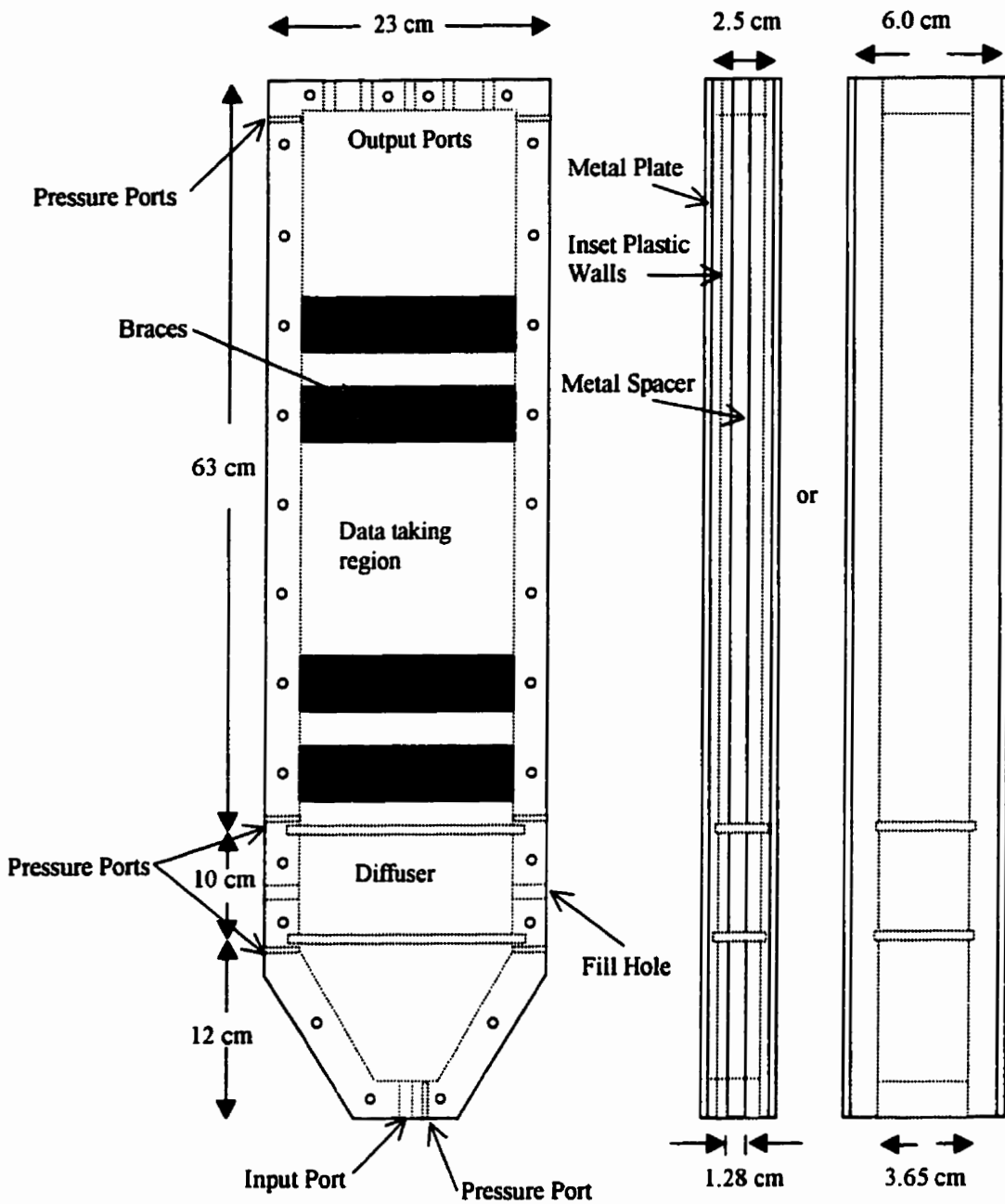


Figure 3.2.2: Large fluidized bed design.

there were five $\frac{1}{4}$ -inch pipes attached to the bed to collect the fluid as it left the cell.

The larger beds were designed with pressure ports [Fig. 3.2.2], to which differential pressure transducers were attached to measure the pressure drops across the

diffuser and the fluidized section, on both sides of the bed. The large pressures involved in the attaining low volume fractions in thickest bed made it advisable to brace the plastic walls, in order to avoid bowing and deformations. In the fluidized section, this was done by using easily removable brass bars, mounted horizontally and spaced at intervals as indicated in Fig. 3.2.2. In the diffuser section the outer metal plates extended across the whole width of the fluidized bed, to give additional support.

It was important to ensure that the velocity of the fluid was as uniform as possible when it left the diffuser and entered the bottom of the fluidized section of the bed. If the flow pattern is not uniform, large-scale instabilities can result. These instabilities often take the form of swirls with a size that is the same as the system size [Davidson 1985]; an example of which is drawn in Fig. 3.2.3(a). One measure of the flow profile into the bottom bed is the pressure difference across the diffuser at different locations. In Fig.

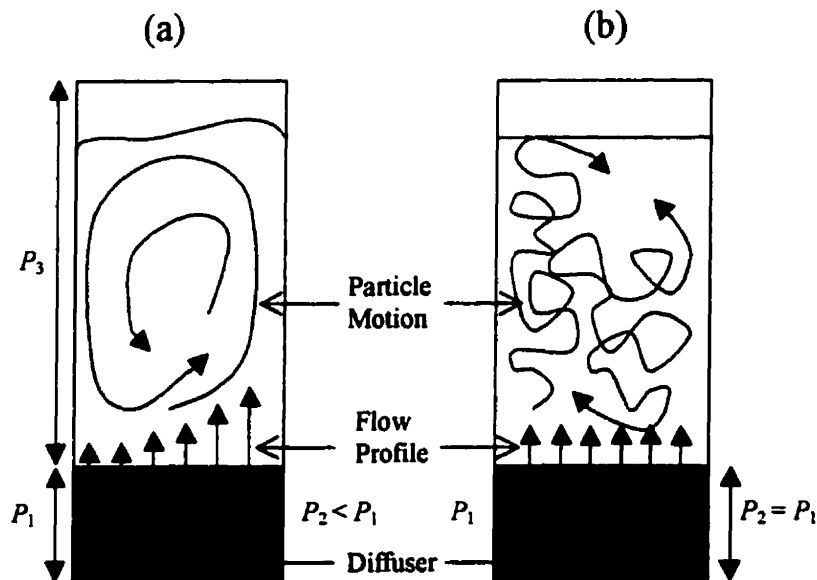


Figure 3.2.3: (a) Non-uniform flow from the diffuser.
(b) Uniform fluidization.

3.2.3(a), the pressure on the right side of the bed is lower than that on the left. This sets up a tendency for fluid and particles to flow to the right at the bottom of the bed, which leads to a large swirling pattern in the particles motions. Figure 3.2.3(b) shows the case where the pressures on either side of the bed are equal. This means that the flow profile into the bed is uniform, which eliminates the large-scale instabilities that can arise in the non-uniform case.

As was mentioned earlier, to ensure a uniform flow from the diffuser, the pressure difference across it (P_1 or P_2) should be equal to, or larger than, the pressure difference across the rest of the bed (P_3) [Davidson 1985]. In our experiments, depending on the volume fraction and Reynolds number, P_3 is at most 3 kPa, while the smallest diffuser pressures were 3.1 kPa, and in this extreme case, P_1 and P_2 were equal to within 1%. It is also important to ensure that the exit holes of the diffuser are spaced no more than a particle diameter apart, and that the diffuser is uniform. This was ensured by carefully packing glass beads that were the same size as the fluidized particles into the diffuser, and capping them with a fine mesh. By building the diffuser using these prescriptions, we were able to achieve uniform motion of the particles throughout the fluidized bed, without large-scale flow patterns.

3.2.2 Glass Beads

The particles used in the fluidized beds were approximately spherical glass beads. They came in a fairly polydisperse package, with diameters spanning the range between 0.70 and 1.18 mm. To further narrow the range of bead diameters in our fluidized bed we used two brass sieves, with filter sizes of 0.850 and 0.900 mm, which gave us a bead

radius of 0.438 ± 0.012 mm. The glass beads have a bulk longitudinal sound velocity of 5.6 mm/ μ s, a shear velocity of 3.4 mm/ μ s, and a density of 2.5 g/ml. The glass beads with diameters outside of the 0.850 to 0.900 mm range were used in the packed section of the fluidized bed diffuser.

A hole in the side of the metal spacer of the fluidized bed was used to add beads to the diffuser section. One of the outlet holes was used to add the sieved glass beads to the fluidized section of the bed. The beads were added slowly, in order to reduce the number of air bubbles introduced to the system. After an appropriate number of glass beads were added, the fluidized bed was sealed and attached to the pumping system, which was then turned on and left to run for several hours in order to remove any remaining air bubbles.

3.3.3 Fluids

Three different fluids, each with a different viscosity, were used to fluidize the glass spheres. The fluids were all stable solutions of glycerol and water, with 60%, 75% and 94% glycerol by weight. Each fluid had a different viscosity, which we could measure by timing the fall of a single sphere down the center of a large diameter container, giving the Stokes velocity [Eq. (2.109)], and thus the viscosity. The measured viscosities compared well with accepted values [DOW 1989] and are listed in Table 3.1, along with the particle Reynolds number [Eq. (2.110)], which ranges from low ($\sim 10^{-2}$) to intermediate (~ 10). The 75% fluid was used at two temperatures, 23°C in the small tank and 27°C in the large tank. All other fluids were used at 27°C.

Table 3.2 gives a summary of the ultrasonic properties of the glass beads and fluids used in all of the samples. Because of the large impedance mismatch between the glass

and all of the various fluids, there is very strong scattering of ultrasound in the intermediate frequency regime, where the wavelength is comparable to the particle size.

Fluid	V_o (mm/s)	η (cP)	Re
94%	2.0	261	7e-3
75%	22 or 13	25 or 41	.9 or .3
60%	60	8.3	7

Table 3.1: Fluid parameters at 27 or 23°C.

Fluids	ρ (g/ml)	c_l (mm/μs)
94% Glycerol/Water	1.25	1.86
75% Glycerol/Water	1.19	1.84
60% Glycerol/Water	1.15	1.66

Particles	Radius, a (mm)	ρ (g/ml)	c_l (mm/μs)	c_T (mm/μs)
Glass Beads	0.4375	2.5	5.6	3.4

Table 3.2: Summary of the ultrasonic properties of the sample constituents.

Height (L_y) (mm)	Width (L_x) (mm)	Thickness (L_z) (mm)
~ 120	127	7.76
~ 120	127	12.2
~ 450	178	5.40
~ 450	178	12.8
~ 450	178	36.5

Table 3.3: Summary of the dimensions of the fluidized suspensions.

3.3 Generation and Detection of Ultrasound

3.3.1 Piezo-Electric Effect

The transducers used in these experiments generate and receive ultrasound by using a material that exhibits the piezo-electric effect. The piezo-electric effect is a coupling of deformations in the crystal lattice of a material to its polarization, and thus to the electric field. Thus, when a sound wave impinges on the material, the periodic pressure fluctuations deform the crystal lattice, and produce an oscillating electric field that is proportional to the average pressure across the surface of the crystal. This coupling works in both directions, which means that through the application of an oscillating electric field, piezo-electric crystals can also be used to generate ultrasound.

3.3.2 Plane Wave Immersion Transducers

The immersion ultrasonic transducers used in the experiments, utilize PZT (lead-zirconium-titanate), a piezo-electric material, to transform electrical energy into an ultrasonic wave, or visa versa. The basic design of the Panametrics plane wave transducers used is outlined in Fig. 3.3.1. The active element is a thin disk of piezo-electric crystal, and that is where ultrasound is produced or detected, through its coupling with the electric field. The active layer has a high acoustic impedance, so that if it was immersed in the water alone, the generated ultrasound would be strongly reflected off of both of its surfaces. This would lead to a very sharp frequency response, centered at a wavelength corresponding to twice the layer thickness (plus harmonics); and the waveform would be drawn out in time, an effect known as transducer ringing.

To reduce ringing, a backing layer is placed behind the active layer. The backing layer is a strong absorber of ultrasound, and has an acoustic impedance which is just slightly less than that of the active layer. It therefore absorbs energy incident on it, either directly, or after reflection from the front surface of the active layer. This broadens the frequency response of the transducer, which allows for a more accurate reproduction of pulsed waveforms. However, the impedance of the active layer is much larger than that of water, so that if it was immersed directly in water, most of the energy would be reflected back into the transducer for a generated wave, or back out of the transducer for an incoming wave. To increase the amount of transmitted energy, a coupling layer with an impedance that is between that of the active element and water, is attached to the front face of the transducer. The thickness of the coupling layer is set to be one quarter of the design wavelength, which, when combined with the phase shift of π upon reflection from the active layer, means that multiple reflections interfere constructively with the transmitted wave. The coupling layer also serves the purpose of water proofing the transducer, and protecting it from wear and tear.

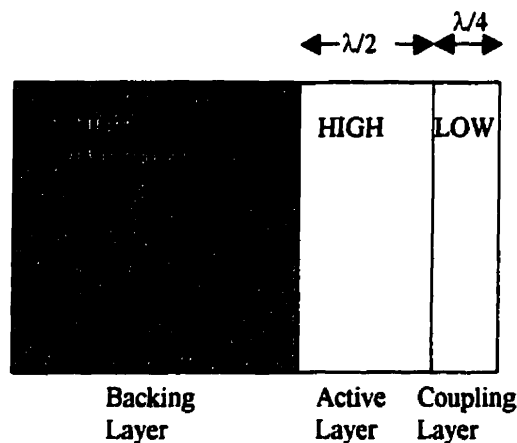


Figure 3.3.1: Plane wave transducer design.

For the purposes of calculating the spatial pattern of the transducer beam, the transducer can be modeled as a thin disk radiator. The surface of the disc is excited by a uniform sinusoidal velocity (directed towards the fluid), $v(t) = \exp[i\omega t]$. The resulting pressure wave is given by the Rayleigh expression [Ristic 1983],

$$\begin{aligned} p(t, \vec{r}) &= \frac{\rho}{2\pi} \iint_A \frac{\frac{\partial}{\partial t} v\left(t - \frac{R}{c}\right)}{R} dA \\ &= \frac{i\omega\rho}{2\pi} \exp[i\omega t] \iint_A \frac{\exp\left[-i\frac{\omega R}{c}\right]}{R} dA \end{aligned} \quad (3.1)$$

where ρ is the fluid density, c is its longitudinal velocity, A is the disk area, and R is the distance between dA and the field point \vec{r} [Fig. 3.3.2].

The intensity of a pressure wave can be written

$$\begin{aligned} I &= \operatorname{Re} \left\{ \frac{pv^*}{2} \right\} \\ &= \operatorname{Re} \left\{ \frac{-i}{2\omega\rho} p \frac{\partial p^*}{\partial z} \right\}. \end{aligned} \quad (3.2)$$

Equations (3.1) and (3.2) can be solved explicitly for the intensity along the z -axis, giving

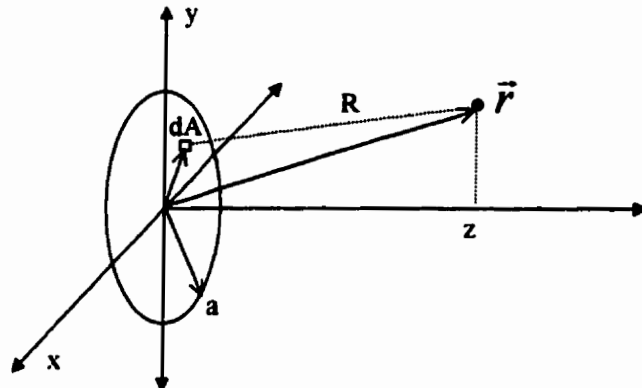


Figure 3.3.2: Geometry for a thin disk radiator.

$$I(z) \propto \sin^2 \left\{ \frac{\pi}{\lambda} \left[\sqrt{z^2 + a^2} - z \right] \right\} \left[1 + \frac{z}{\sqrt{z^2 + a^2}} \right], \quad (3.3)$$

which is plotted in Fig. 3.3.3 for a half-inch-diameter transducer at 1 MHz. Here a is the radius of the disk. Close to the transducer, in the near-field, there are many rapid variations in intensity. However, when $z \gg a$, Eq. (3.3) reduces to a smooth z^{-2} dependence, indicating a spherical wave in the far-field. The maxima in Eq. (3.3) are approximately given by

$$z_n = \frac{a^2 - \frac{\lambda^2}{4} \{2n+1\}^2}{\{2n+1\}\lambda}, \quad (3.4)$$

where $n = 0, 1, 2, \dots$. The last maximum along the z -axis gives the near-field distance, and it is

$$z_F = \frac{a^2 - \frac{\lambda^2}{4}}{\lambda} \approx \frac{a^2}{\lambda}. \quad (3.5)$$

The final approximation used in Eq. (3.5) is that $a^2 \gg \lambda^2$, which held true for all of the plane wave transducers that were used. For $z > z_F$, the intensity varies smoothly with z , and the region is called the far-field, or Fraunhofer zone. In the near-field, or Fresnel zone ($z < z_F$), waves emanating from the source points on the disc interfere strongly, giving many rapid fluctuations in the intensity as a function of x and y as well as z . For this reason, it is desirable to place our samples in the far-field of the transducer [Table 3.4].

In the far-field, the Fraunhofer approximation can be used to solve for the off-axis intensity, giving a spherical wave modulated by a spherical Bessel function in $\sin\theta$ [Ristic

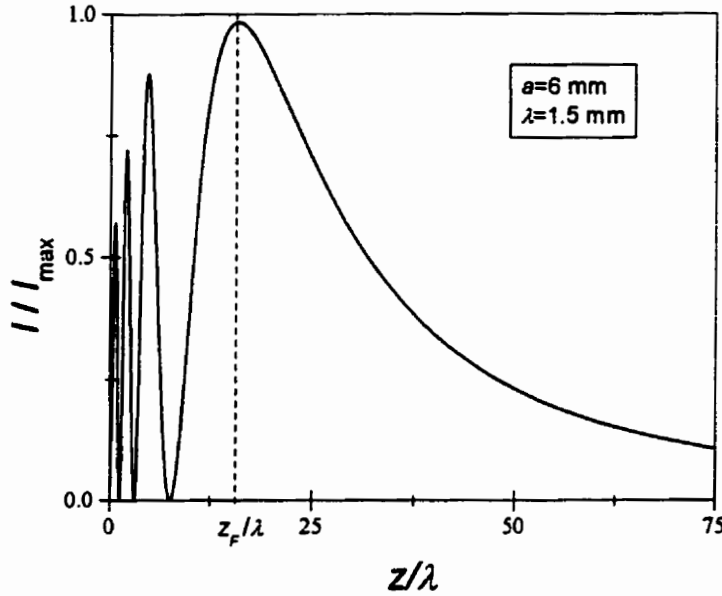


Figure 3.3.3: Thin disk radiator intensity on the z -axis.

1983].

$$I \propto \frac{1}{r^2} \left[\frac{2J_1\left(2\pi \frac{a}{\lambda} \sin \theta\right)}{2\pi \frac{a}{\lambda} \sin \theta} \right]^2 \quad (3.6)$$

This can be used to define a -6 dB beam divergence angle

$$\sin \theta_D = \frac{0.257\lambda}{a} \quad (3.7)$$

as indicated in Fig. 3.3.4.

To simplify the analysis of boundary conditions in our experiments, it is desirable to have an approximately plane wave incident on the sample. In Table 3.4, the near-field distance, divergence angle, and beam diameter B at the sample position (40 cm for the small tank and 60 cm for the large tank) are shown for the transducers used in these experiments. As is evident from the beam diameters, the smallest transducer for a given frequency is best suited to producing a quasi-plane wave at the sample. The larger

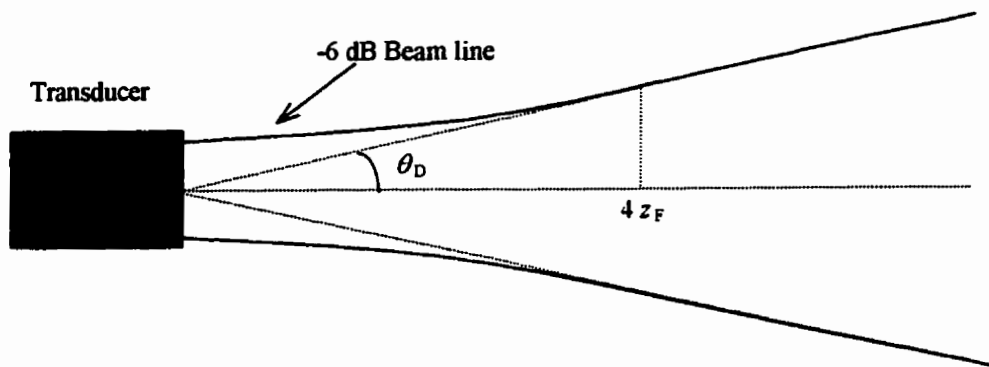


Figure 3.3.4: Transducer beam pattern.

diameter transducers were used as detectors in ballistic measurements, where their larger size increased the spatial averaging of the detected field.

$D = 2a$	Frequency	z_F (cm)	θ_D ($^{\circ}$)	$B@40\text{cm}$	$B@60\text{cm}$
$0.25'' = 6 \text{ mm}$	2.25 MHz	1.4 cm	3.3 $^{\circ}$	4.6 cm	6.9 cm
$0.5'' = 12 \text{ mm}$	1.0	2.4	3.7	5.2	7.8
$1'' = 25 \text{ mm}$	0.5	5.2	3.5	4.9	7.3
25	1.0	10.4	1.8	$\cong 2.5$	3.8
25	2.25	23.4	0.79	$\cong 2.5$	$\cong 2.5$
$1.5'' = 37 \text{ mm}$	0.25	5.7	4.8	6.7	10

Table 3.4: Beam parameters for plane wave transducers in water.

3.3.3 Focusing Immersion Transducers

Transducers can also be made with a plano-concave spherical lens as the coupling layer, which, if the velocity in the lens is greater than that in water, generates a converging, or focusing wave. For a tightly focused beam, the size of the spot at the focal point of the lens can be viewed to a good approximation as a point source, which is another convenient boundary condition. The Panametrics focusing immersion transducers that were used, focused down to a -6 dB beam diameter of [Panametrics 1991]

$$B_F = \frac{1.028F\lambda}{D} \quad (3.8)$$

where F is the focal length of the lens and D is the diameter of the transducer. The length of the focal zone is given by

$$F_z = \frac{F^2}{z_F} \left[\frac{2}{1 + \frac{F}{z_F}} \right] \quad (3.9)$$

where z_F is the near-field distance [Eq. (3.5)].

In practice, it is desirable to have the transducer focused on the surface of the

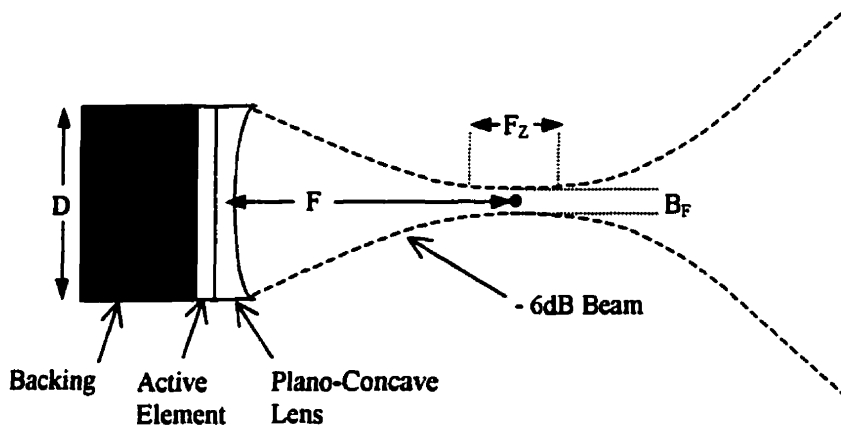


Figure 3.3.5: Focusing transducer design and beam pattern.

sample. When the sample is held between plastics walls, the effects of the different sound velocities in water and plastic must be taken into account when determining where to position the transducer. The distance the transducer must be from the wall is given by

$$x = F - L_{\text{wall}} \left[\frac{c_{\text{wall}}}{c_{\text{water}}} \right], \quad (3.10)$$

where F is the focal length in water and L_{wall} is the wall thickness.

3.3.4 Hydrophones

In the near-field of the sample, all of the scattered waves interfere to give a random speckle pattern, with a correlation area on the order of λ^2 [Fig. 1.1.1]. Due to these rapid spatial fluctuations in the phase and amplitude of the scattered field, and because a transducer measures the average field across its face, the detector must be smaller than a wavelength in order to avoid phase cancellations and measure the scattered field accurately. Miniature hydrophones from Specialty Engineering were used to perform this task [Fig. 3.3.6]. The hydrophones were well backed, with a strongly absorbing material whose impedance was closely matched to that of the PZT element. The PZT element had a diameter of 400 μm , giving it an area of λ^2 when the frequency is ~ 4 MHz, well above our highest frequency of 2.25 MHz. The PZT element was also very thin, which gave it a resonant frequency well above those of interest. Because the hydrophone was strongly damped and well below resonance, it was able to accurately detect ultrasonic waveforms over a large frequency range with almost constant sensitivity, albeit with a much weaker response than it would have at resonance. For this reason, the hydrophone also came with an attached 15 dB preamplifier to boost the detected signal amplitude.

3.4 Generating Electronics

3.4.1 Overview

This section gives a general overview of the basic functions that need to be performed in order to generate radio frequency pulses that are suitable for driving our ultrasonic transducers. An introduction to some of the equipment that we used to perform these tasks will also be given. The specific ways these devices were setup for all of the different experiments will be left to later sections in the next chapter.

To generate radio frequency electronic pulses to send to the transducers, we need equipment that can perform the basic functions outlined in Fig. 3.4.1. First a continuous wave RF signal must be generated at the desired carrier frequency, and then this signal needs to be modulated, to give the desired pulse shape. Note that the pulse modulation and the RF source have to be synchronized, so that the phase of the pulse does not drift with respect to the pulse envelope. This is accomplished by triggering the pulse generator using the RF source. The pulse then has to be amplified to a voltage appropriate for the generating transducer. Finally, we need to be able to repeat the pulse at the desired repetition rate.

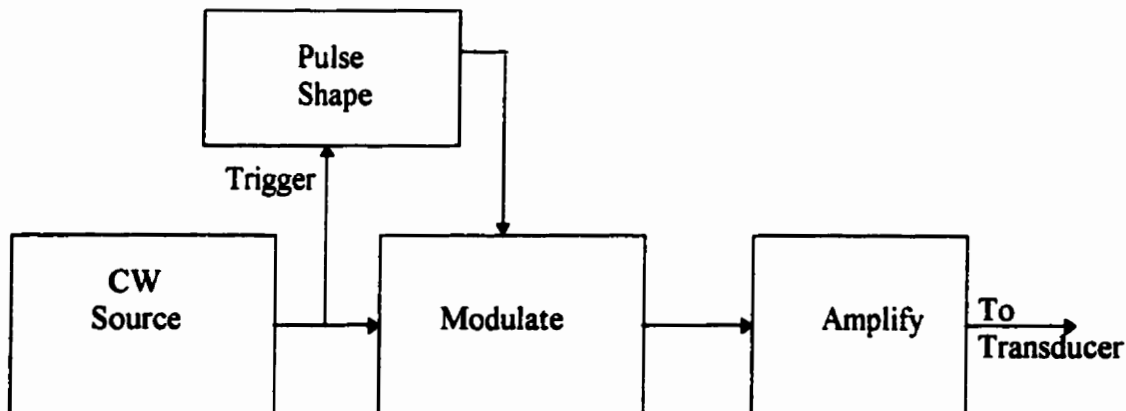


Figure 3.4.1: Generating electronics flowchart.

3.4.2 Fluke Frequency Synthesizer

The Fluke 6060B is a highly stable, digital RF frequency synthesizer. Its frequency range spans 0.01 to 1050 MHz, and it can output at a power level up to +13 dBm. It uses a internal 10 MHz crystal oscillator, in a temperature controlled oven, as a frequency reference, and it supplies a clock output to allow one to synchronize other digital equipment to this stable clock. Due to its excellent stability, this was the preferred generator. However, when it was unavailable, a General Radio Company I269-A analogue frequency generator was used in its place.

3.4.3 Stanford Delay Generator

Up to two model DG535 Stanford Research Systems digital delay generators were used to supply various trigger pulses and to generate the pulse envelope. Each delay generator has four individually adjustable output channels, A to D. Each channel switches from a low to a high voltage at an adjustable and precise (to 5 ps) time, allowing for the production of delayed triggers for other equipment. There also are outputs which give: A XOR B, A AND B, C XOR D, and C AND D. By setting the individual channels appropriately, the XOR output could be set up to give a square pulse with an adjustable length [e.g. Fig. 3.4.2], which was the method used to produce pulse envelopes.

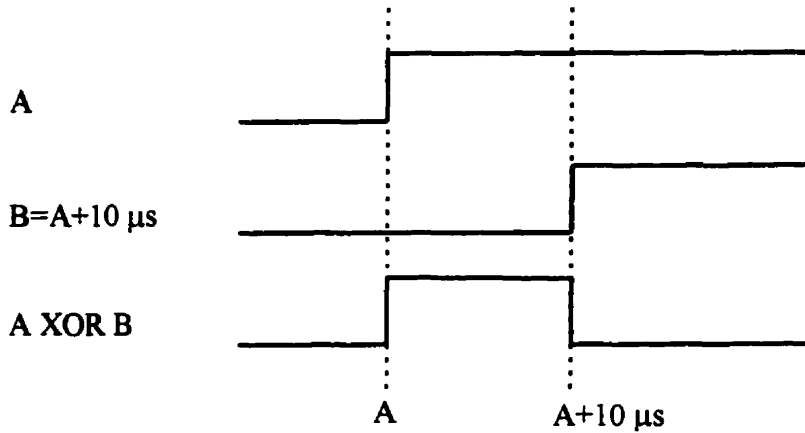


Figure 3.4.2: Setting the pulse width using the Stanford delay generator.

The Stanford delay generator can use the 10 MHz clock supplied by the Fluke as its time-base, ensuring that there is no digitization jitter between the pulse envelope and cw-source. It also can be triggered off the cw-output of the Fluke, ensuring that the phase of the signal does not drift with respect to the pulse envelope. The repetition rate of the Stanford is controlled by its longest time delay, i.e. it does not accept a new trigger until all of the delays have counted down.

3.4.4 Mixers

Mini-Circuits ZAY-3 mixers were used to modulate the cw-output of the Fluke frequency synthesizer. The pulse output of the Stanford delay generator was used as the modulating signal. In order to minimize leakage of the cw-signal, three mixers were connected in series.

3.4.5 AR Power Amplifier

The Amplifier Research 250L power amplifier was used to amplify the output of the Fluke and mixers to a level large enough to fully excite the generating transducer. In

continuous mode, its maximum power output is 250 watts, with a frequency range of 0.01 to 220 MHz.

3.4.6 Alan and Telonic Attenuators

To make fine adjustments to the output level of the Amplifier Research power amplifier, we found it convenient to use a low power, adjustable, precision Telonic attenuator to adjust the input level. The attenuation of the Telonic model 8143S is adjustable from 0 to 110 dB in steps of 1 dB. We also used a 3 dB fixed attenuator on the output of the high power amplifier. This was done to decouple the amplifier from the RF reflections back from the transducer, whose electrical impedance was not perfectly matched to the 50Ω output impedance of the amplifier and coaxial cables.

3.4.7 Power Splitters

A power splitter, with a 50Ω input and output impedance, was used to cleanly split the output of the Fluke frequency synthesizer. One output of the splitter continued on to the mixers and then to the Amplifier Research power amplifier. The other output was used to trigger the Stanford delay generator, which then produced the pulse envelope. The power splitters were also necessary in the measurement of sound reflected back from the generating transducer, as will be discussed in detail in a later section. Two models of power splitters were used, Mini-Circuits ZMSC-2-18 and Merrimac PDM-20-250.

3.5 Receiving Electronics

3.5.1 Overview

This section gives an overview of the electronics that were used to detect and process the electrical signal coming from the receiving transducer or hydrophone. The specifics will be left to the descriptions of each different experiment, in the next chapter.

The basic functions that needed to be performed by the receiving electronics system are outlined in Fig. 3.5.1. The signal coming from the transducer was amplified, but, since our samples can have a large range of transmission coefficients, the level of the signal had to be adjusted so that it was appropriate for the amplifier. This adjustment was done by using a Telonic low power adjustable attenuator, which was described in the previous section. To improve signal to noise ratio, filters were used to remove unwanted high and low frequencies. We then used one of two digital oscilloscopes to measure the signal. The oscilloscope was triggered by the Stanford delay generator, thereby ensuring that it was synchronized with the sound pulse. The oscilloscope was connected to a computer, which was used to save the data.

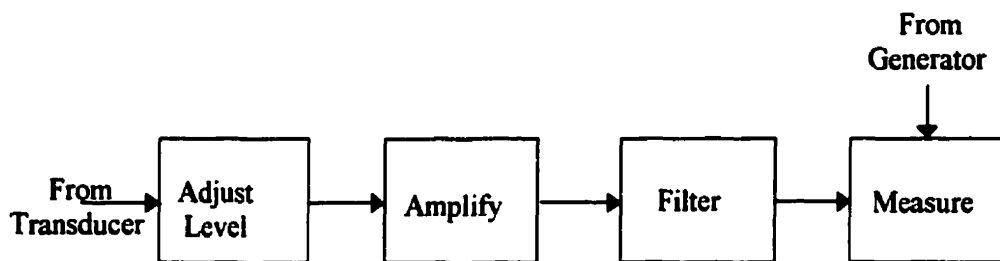


Figure 3.5.1: Receiving electronics flowchart.

3.5.2 Matec Receiver Amplifier

The Matec Receiver Amplifier Model 605 is a three-stage amplifier, usable in the frequency range of 100 kHz to 25 MHz. For the first stage, there is a choice of one of two pre-amplifiers. One of the preamplifiers (Model 253) is a 20 dB broadband (100 kHz-30 MHz), low noise amplifier. The other preamplifier (model 252) is an adjustable bandpass filter, with 30 dB of gain. After the pre-amplification stage, there is an additional adjustable gain (10 to 60 dB) amplifier, which we did not use. Instead we used the final, 24 dB, amplification stage, since it has better noise characteristics than the adjustable stage, and provided sufficient gain.

The Matec Receiver also functions as an amplitude detector. This stage of the receiver uses a diode detector to measure the amplitude envelope of the RF signal. It was used to directly measure the wave amplitude, in the experiments that tested the Siegert relation.

3.5.3 LC Filters

To remove unwanted frequencies, several high and low-pass Butterworth LC-filters were constructed. An example of a low pass filter, with a 3-pole, 50Ω output impedance design is illustrated in Fig. 3.5.2. We used 0.4, 1.5, 3.0 MHz low pass filters and 0.13, 0.5, 1.0, 1.5 MHz high pass filters.

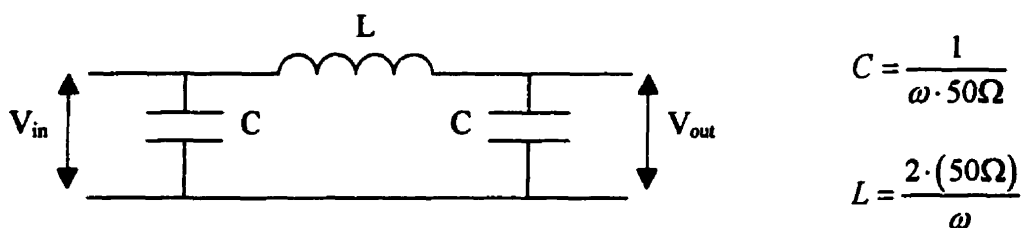


Figure 3.5.2: LC Butterworth filter design.

3.5.4 Tektronics Digital Oscilloscope

The model 544A Tektronics Digital Oscilloscope is an 8 bit, 1 Giga-Sample per second, digitizing oscilloscope, with a maximum record length of 50,000 points. It has an averaging mode, which can average up to 10,000 consecutive signals. When used in averaging mode, the effective voltage resolution is increased to 12 bits.

The Tektronics scope also has a GPIB interface, which allows a computer to control it, and to download data from it. Computer programs were written in Visual C++ to perform needed control functions.

3.5.5 Gage Digital Oscilloscope

The Gage CompuScope 6012 is a 12 bit, 60 MS/s, oscilloscope on an internal computer card. It has a maximum record length of 1 million points (actually 1 MB of points), and since it is directly connected to the computer's internal bus, data transfer is much faster than over a GPIB interface. There also is a gated digitization input, which allows an external signal to turn the acquisition of data on and off as desired.

One problem with this oscilloscope was the triggering, which jittered randomly by several points. This required the use of various tricks to compensate for the problem, which will be discussed in detail in the appropriate sections. Because of this problem, the Tektronics scope was used to acquire ballistic and scattered data, while the Gage CompuScope was only used to acquire the temporal fluctuation data that required its large record length.

The CompuScope was controlled by a computer program, written using Visual C++, which gave a level of control that could not be achieved with the software that Gage

supplied.

3.5.6 Boxcar Integrators

To sample the received signal at a specific time after the input pulse, we used a Stanford Fast Gated Integrator and Boxcar Averager Model SR250. This device reads the average voltage over an adjustable time window, and then outputs this voltage until the next trigger is received; at this point it samples the input again and resets the output. By setting the time window to be much less than a period (~30 ns), the boxcar lets us repeatedly sample the wave field at a particular time for each pulse. The boxcar also supplies different coarse gain settings (much like an oscilloscope), and an exponential moving averaging module, which averages several consecutive triggers together. The boxcar has a high input impedance, but a direct signal output is supplied, which lets us measure the RF-signal and terminate it at 50Ω on the Tektronics oscilloscope. The boxcar also supplies an output of the gate it uses as a time window, allowing us to view it directly on the Tektronics oscilloscope.

4. Experiments

This chapter presents the details of how all of the experiments were performed, and gives an explanation of how some of the data were analyzed. It starts with an explanation of how pulsed transmission experiments were performed and analyzed, for both the ballistic and scattered components. The next section deals with DAWS, discussing the various geometries and techniques used and developed. The following two sections describe the two DSS methods that were developed. Finally, the methods used to record and analyze phase data, as well as an experiment to test the Siegert relation under various conditions, are explained.

4.1 Pulsed Transmission Measurements

This section deals with the experimental methods used to measure the propagation parameters of ultrasonic pulses transmitted through fluidized suspensions. First, the details of the electronics used in these experiments will be discussed. Then we will discuss the experimental techniques used to measure and extract information about the ballistic and scattered propagation.

4.1.1 Setup

The electronics used to generate and receive ultrasonic pulses are shown in Fig. 4.1.1. The Fluke Synthesizer acts as the RF source, and supplies the Stanford Delay Generator with its external clock. The continuous wave output of the synthesizer was split, with one branch triggering the delay generator, and the other continuing on to a set of three mixers attached in series. As discussed in Section 3.4.3, the delay generator was used to produce the pulse envelope, which was fed into all three of the mixers as the modulating signal. To ensure that the power amplifier was not saturated, the RF-pulse output of the mixers was generally reduced in amplitude by 15 dB, using a Telonic attenuator. The signal was then amplified, and sent to the transducer, where it was converted into an ultrasonic pulse.

The sample was placed well into the far-field of the plane-wave generating transducer, as discussed previously in Section 3.3.2 (see Table 3.4). For scattering measurements, a hydrophone detector was placed about 3 mm away from the surface of the sample, in the near-field of the sample. When the sample was thin and the scattering was relatively weak, the hydrophone was also used for ballistic measurements. When the

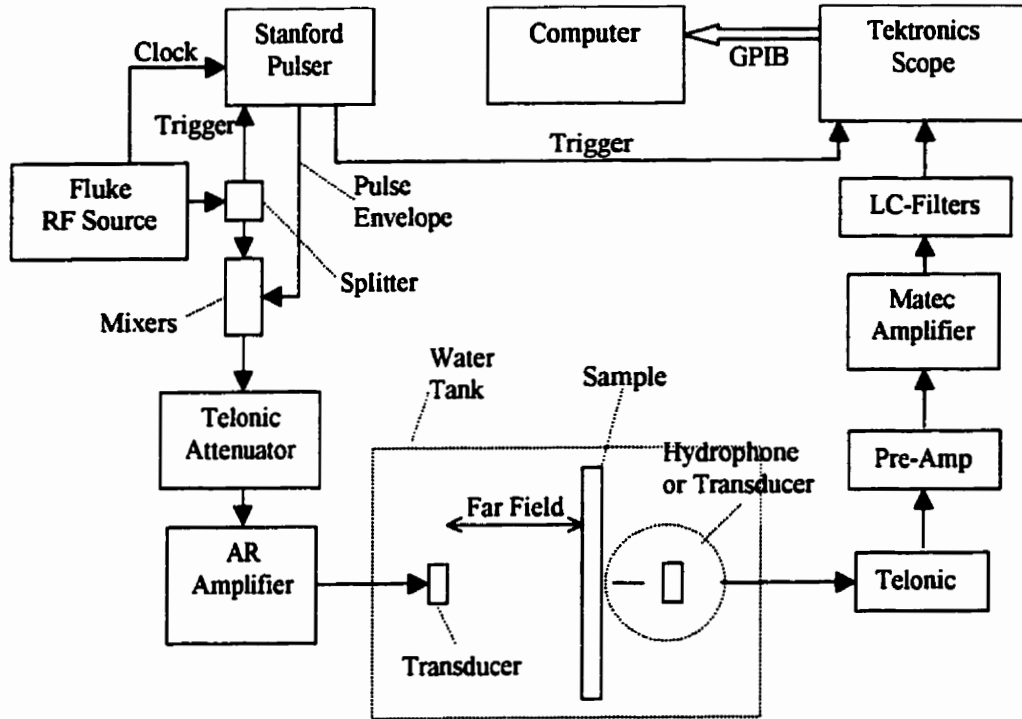


Figure 4.1.1: Electronics setup for pulsed sound propagation.

ballistic signal was much smaller than the scattered signal, a plane wave transducer was used in place of the hydrophone to improve averaging.

Another Telonic attenuator was used to adjust the amplitude of the detected signal to a level that was appropriate for the detection amplifiers. The signal was then connected to either the broadband or bandpass Matec pre-amplifiers. The broadband amplifier allowed us to use just one pulse to measure the ballistic parameters over the full bandwidth of the transducer, as will be described in the next section. The bandpass pre-amplifier improved signal to noise, and let us use a much narrower range of frequencies, as was sometimes necessary when the scattering was very strong and the scattering mean free path was strongly frequency dependent. The signal was then amplified, filtered using LC-filters, and recorded using the Tektronics oscilloscope and a computer.

4.1.2 Ballistic Measurements

The volume-fraction dependence of ballistic transport was investigated experimentally using pulsed ultrasonic techniques. When the scattering is strong the transmitted waveform detected by the receiving transducer can be split into two components. There is a small ballistic pulse, which consists of the unscattered or forward-scattered waves, and a larger scattered component. This is evident from Fig. 4.1.2(a) and (b), which shows the transmitted field for several different ensembles of the scatterers, at two different volume fractions. At both volume fractions, one can see the phase and amplitude fluctuations of the scattered component superimposed on the ballistic pulse at early times, and extending to much longer times as progressively longer and longer

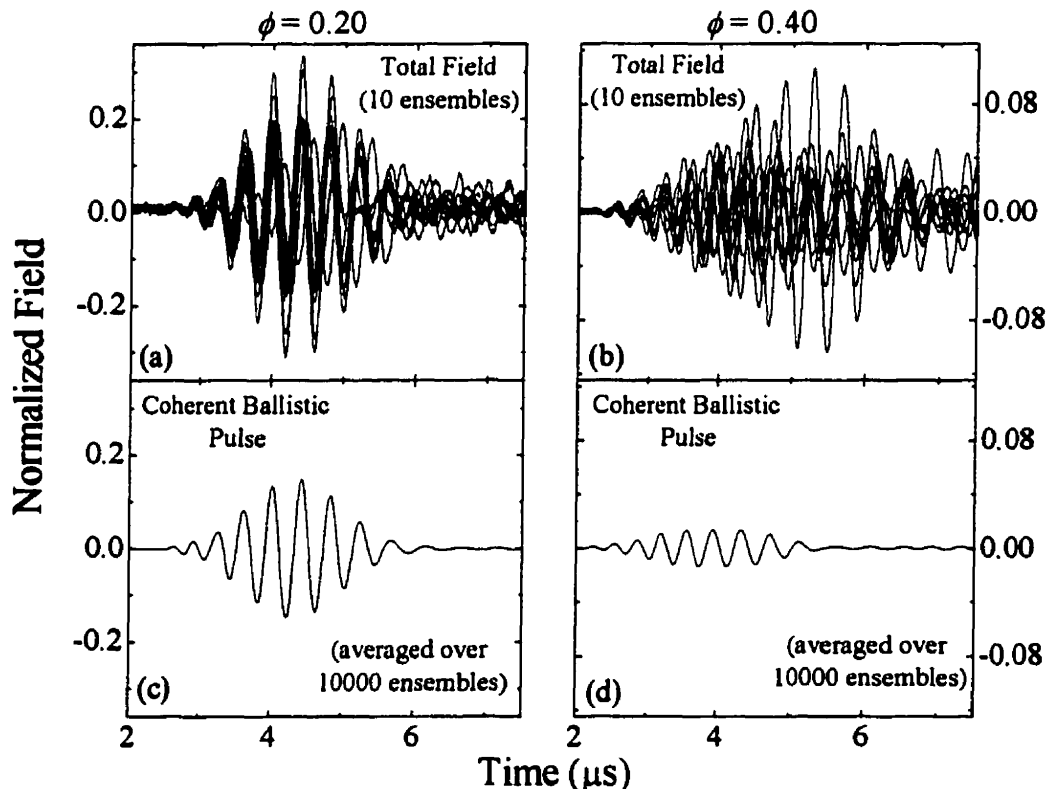


Figure 4.1.2: Extracting the ballistic pulse from the transmitted field. (a) & (b) The measured transmitted field for 10 different ensembles at $\phi = 0.2$ and 0.4 . (c) & (d) The results of averaging the field over 10,000 ensembles.

multiple scattering path lengths are traversed.

To measure the group and phase velocities, the ballistic pulse must be extracted from the dominant multiply scattered waves. The beads in the fluidized bed were in continuous motion, moving a mean distance which was negligibly small over the time the pulse takes to travel through the sample, but which was significant (appreciable compared to the wavelength) over the time between repetitions of the input pulse. Thus by averaging the transmitted field over many such repetitions, we can in effect average over many different ensembles of the scatterers. This leads to phase cancellations in the scattered component, since the phase and amplitude of the scattered waves change randomly from one pulse to the next, while the ballistic pulse remains unchanged. This effect is demonstrated in Fig. 4.1.2, which shows the full transmitted ultrasonic field, measured using the miniature hydrophone. In Fig. 4.1.2(a) and (b), we compare the detected fields at two volume fractions by overlaying the transmitted wave for 10 different ensembles of the scatterers. At the lower volume fraction of 0.20 where the scattering is weaker, evidence of the coherent component of the field can be seen by eye, as a substantial fraction of the detected field at early times (the first 6 or 7 oscillations in the pulse) arrives in phase for each ensemble of the beads. The ballistic signal that is extracted by ensemble averaging the transmitted signal over 10000 realizations of the random configurations of the beads at this volume fraction is shown in Fig. 4.1.2(c). When the volume fraction is increased to 0.40, the true power of this configuration averaging technique becomes apparent. As a result of the increased scattering, the relative amplitude of the ballistic to scattered sound is decreased, and a coherent component is not readily

apparent. However, after ensemble averaging the field, the scattered fields are effectively eliminated and the small ballistic signal clearly emerges with an excellent signal-to-noise ratio.

If required, further cancellation of the scattered component can be achieved by using a large diameter piezoelectric transducer as the detector, in place of the hydrophone. Since the transducer detects the average instantaneous field of the transmitted wave over the front face of the piezoelectric element, much of the scattered ultrasound is canceled in the detector due to the random phase fluctuations of the scattered waves across the transducer face. In the near-field of the sample, the speckle size, or coherence area, of the scattered waves is of order of the square of the wavelength [Fig. 1.1.1]. Thus, at a typical frequency ~ 1 MHz, several hundred speckles interfere at the face of a one-inch-diameter transducer, when it is placed in the near-field, about 5 centimeters away from the sample. This gives good cancellation of the scattered component of the wave field and leaves the spatially coherent ballistic pulse unaffected.

To measure the frequency dependence of the scattering mean free path, we first digitized a reference pulse, which traveled through the sample cell without the beads being in the sound beam. Then the ballistic pulse was recorded, and the magnitudes of the Fast Fourier Transforms (FFTs) of the pulses were compared, as shown in Fig. 4.1.3(a) for a sample with a volume fraction of 0.45 and a thickness of 7.76 mm. Fig. 4.1.3(b), shows the ratio of the two FFTs, in this case over a bandwidth from about 1.0 MHz to 3.5 MHz. This ratio gives the transmitted amplitude, by compensating for the frequency-dependent response of the transducers and the reflections and absorption in the cell walls. At low

frequencies, the ratio is almost unity, showing there is very little attenuation of the ballistic pulse, corresponding to the upper end in frequency of the weak Rayleigh scattering regime. However, as the frequency is increased above 1 MHz, the ratio drops, reaching a deep minimum at about 2 MHz as a result of the strong scattering in the sample. The square of this ratio gives the frequency-dependent reduction in the transmitted intensity of the ballistic signal, from which the scattering mean free path, l_s , was determined by using Eq. (2.7).

Many of the ballistic measurement experiments were performed using short input

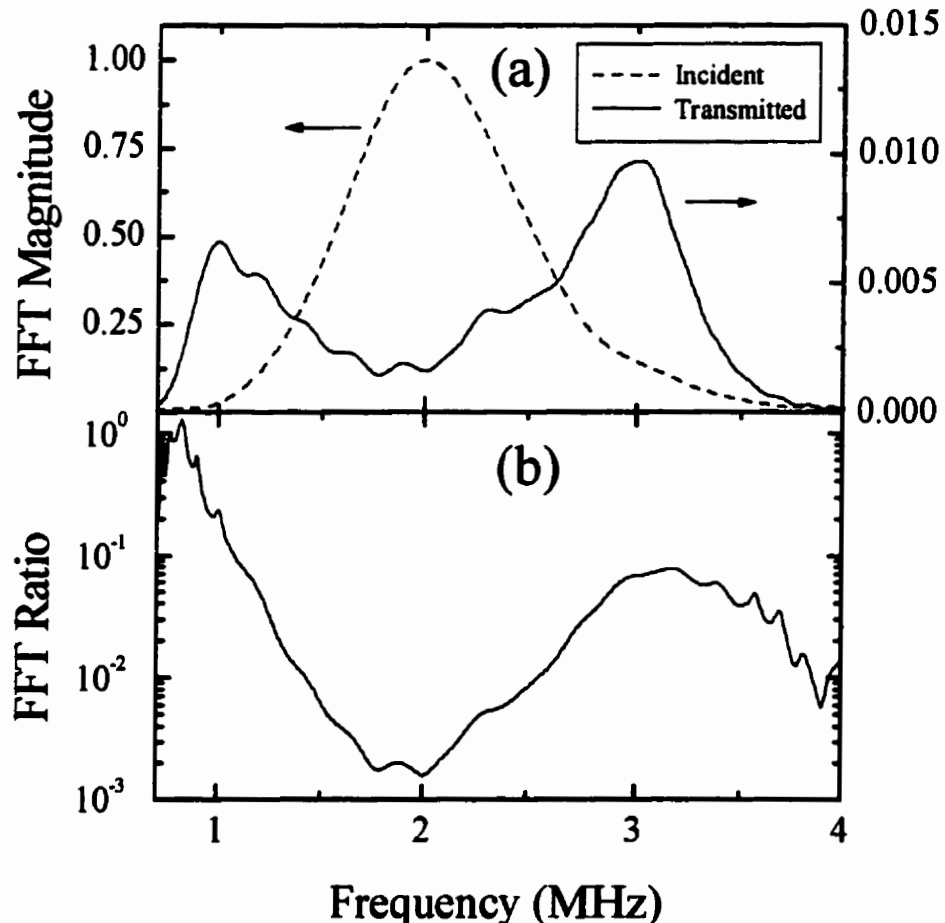


Figure 4.1.3: Measurement of the scattering mean free path. (a) The measured FFT amplitude of the incident and transmitted sound pulses as a function of frequency. The arrows indicate the appropriate vertical scale. (b) The ratio of the transmitted to incident FFT amplitudes.

pulses, so that the frequency content of the pulse extended over the entire frequency spectrum of the generating transducer (FWHM was approximately 50% of the central frequency). For the thicker samples, the corresponding FFT ratio disappeared into the noise level near the scattering maximum, forcing the use of a different approach. In order to take ballistic data in this region, a series of longer pulses were used, each with a narrow frequency bandwidth centered on the frequency of interest, thereby excluding from the pulse any large high or low frequency components that would have saturated the detection electronics at the increased sensitivity needed to measure these weak signals.

To measure the group and phase velocities, FFTs are used to digitally filter the detected pulses to form Gaussian pulses with a relatively tight bandwidth (<10%), centered at several frequencies spanning the bandwidth of the pulse. An example of this technique is shown in Fig. 4.1.4 for data taken at a volume fraction of 0.45, some of which is identical to that used to generate the FFTs shown in Fig. 4.1.3. The unfiltered short pulses in the first column show very strong dispersion effects, with a clear separation of faster high frequency components in the pulse from slower low frequency components. This effect becomes more pronounced as the sample thickness increases and the transmitted pulses become broader and more distorted. The propagation of this short distorted pulse cannot be described by a single value of the group velocity. However, the frequency dependence of both the group and phase velocities can be accurately determined from these data by using a Gaussian filter function to narrow the frequency bandwidth of the pulse, so that dispersive distortion of the pulse is reduced and the group velocity description of pulse propagation is appropriate [c.f. Section 2.1.1]. The results of this

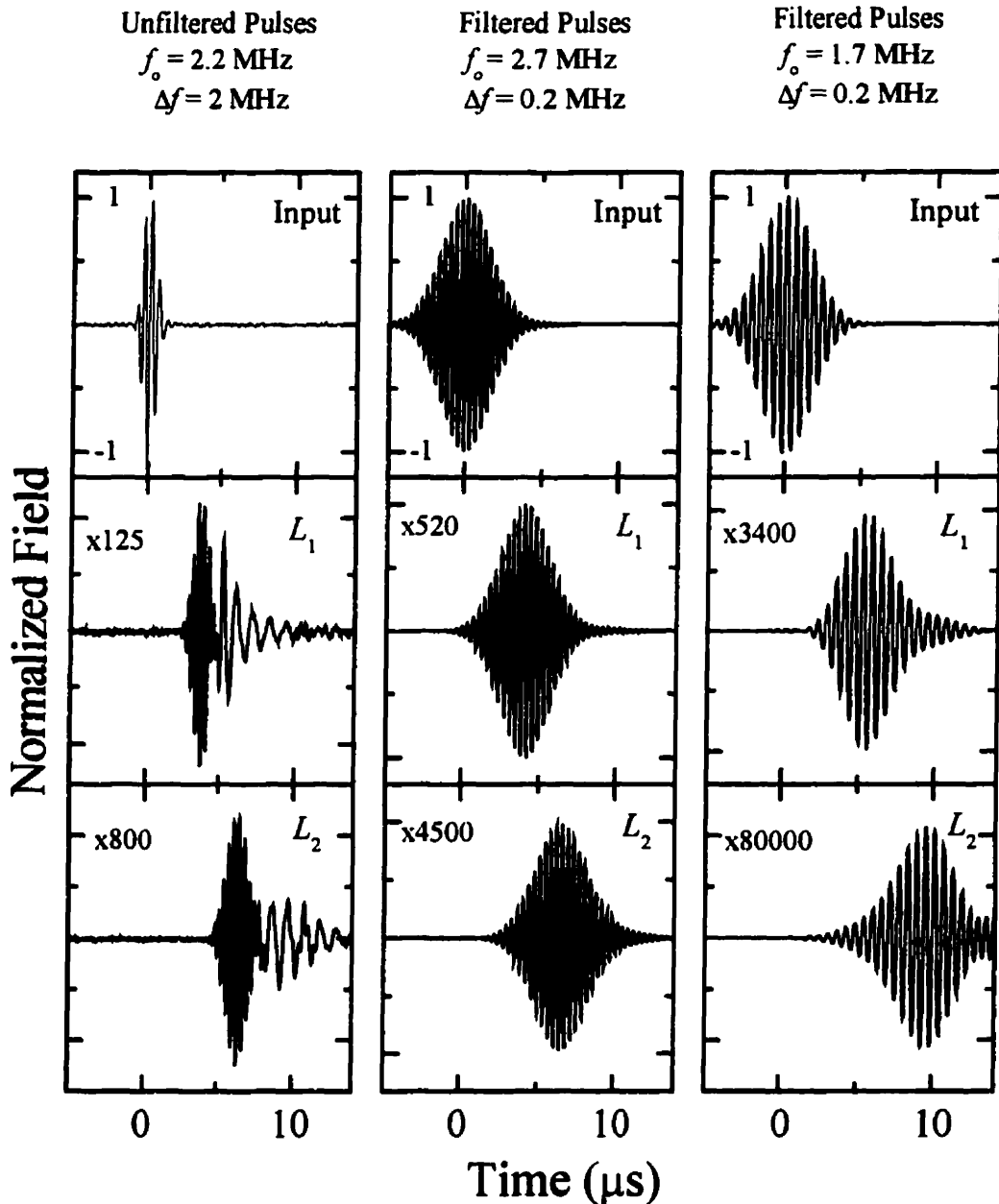


Figure 4.1.4: Digitally filtering the detected waveforms. The column of three graphs at the far left shows the unfiltered measured input waveform and the waveforms transmitted through samples of thickness $L_1 = 7.76$ and $L_2 = 12.2$ mm. The other two columns show pulses filtered at two different frequencies. The numbers (e.g. x125) give the change in the vertical scale of the data relative to the input waveform scale.

filtering process for two central frequencies of 2.7 and 1.7 MHz are shown in the second and third columns of Fig. 4.1.4 respectively. Although small dispersion effects can still be seen in the slight broadening of the pulses with increasing sample thickness, the filtered pulses have a well defined central frequency and have symmetric peaks, so that both the phase and group velocities can be determined. The phase velocity was measured from the time taken by the carrier frequency oscillations to travel through both of the samples, using the condition that the velocity must be independent of sample thickness to resolve the possible ambiguity of one or more multiples of 2π in the total phase shift of the transmitted pulse. Simple inspection of Fig. 4.1.4 indicates that the pulses at 2.7 MHz travel faster than the 1.7 MHz pulses, confirming that the group velocity is slower at the lower frequency. The group velocity was measured quantitatively by determining the amplitude envelopes of the incident and transmitted pulses, measuring the time interval between the peaks of the two pulse envelopes, and calculating the velocity from the ratio of sample thickness to pulse envelope propagation time.

4.1.3 Diffusive Measurements

The technique used to measure the scattered field is essentially the reverse of that used to isolate the ballistic component in the previous section. Using the miniature hydrophone, the full transmitted field was detected and digitized, for approximately 121 different ensembles of scatterers. Then the ballistic component was measured using the same 10000 pulse averaging function on the Tektronics oscilloscope that was used in Section 4.1.2. At this point, it was useful to digitally filter the scattered and ballistic data, in order to focus on a tighter bandwidth around the frequency of interest, and to reduce noise. This ballistic component was then subtracted from each of the 121 digitized ensembles, leaving only the scattered component of the transmitted field behind. The amplitude envelope of the scattered field was found and squared, giving the intensity as a function of time for each ensemble. Then the intensity envelopes of the ensembles were averaged together, resulting in the ensemble-averaged scattered intensity profile. The 121 ensembles used gives reasonable statistics, with fluctuations in the average intensity of less than 10%. This process is illustrated in Fig. 4.1.5 for data filtered with a 10% bandwidth, in a quite strongly scattering sample.

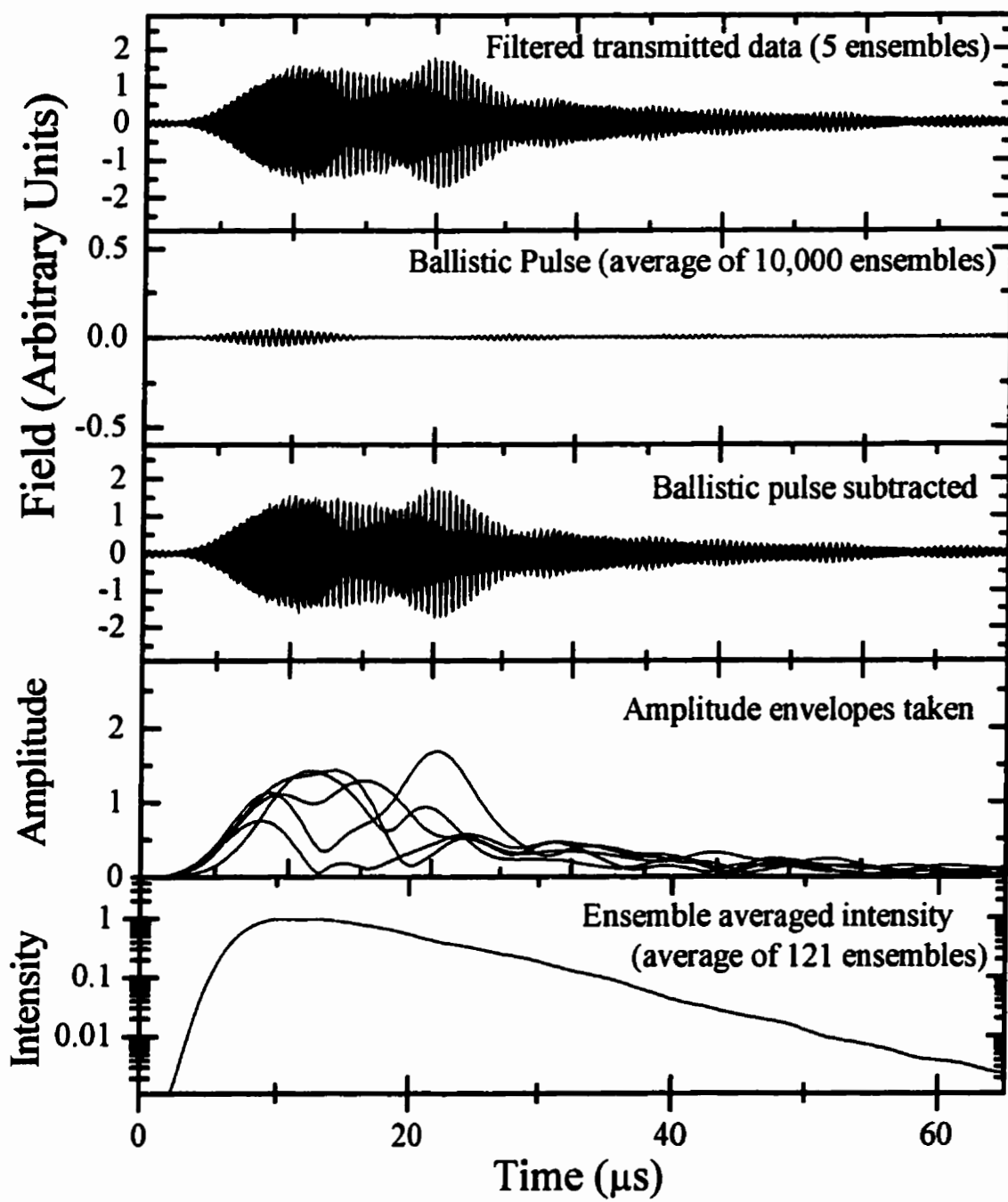


Figure 4.1.5: Extracting the ensemble averaged scattered intensity. Each graph shows representative results from each stage in the analysis, as indicated above.

To test the accuracy of the diffusion approximation, and to extract diffusion parameters, the predictions of diffusion theory were fitted to the ensemble-averaged scattered intensity. The appropriate boundary conditions were discussed in Section 2.2.2; there is a plane wave incident on an effectively infinite slab of thickness L_z , sandwiched by walls with an angle averaged reflection coefficient R . The resulting expression is given by Eq. (2.51), with the addition of an overall amplitude factor, A , which takes into account small cancellations in the scattered field over the face of the hydrophone, and additional losses in the absolute transmission not accounted for in the boundary conditions used. The reflection coefficient, R , can be calculated [c.f. Appendix A], given the measured wall and sample velocities and densities. In our systems, the energy velocity and transport mean free path are approximately equal to their ballistic analogues, to within small correction factors which can be calculated theoretically [Section 2.2.3 and Schriemer *et al.* 1997]. The fitting parameters are the diffusion coefficient D , the absorption time τ_a , and the amplitude A . The diffusion coefficient largely determines how quickly the intensity profile rises and peaks, with larger coefficients corresponding to faster rise times. Conversely, the absorption time has its largest effect at long times, where it helps determine the behavior of the tail of the intensity profile. To include the effects of the finite width of the input pulse, the measured input intensity envelope was convoluted with the theoretical expression during the fitting process.

4.2 DAWS Field Measurements

4.2.1 Pulsed Measurements

In the pulsed DAWS technique, a regular train of pulses was sent through the sample, with a repetition time τ . Either a plane wave transducer in the far-field, or a point source at the face of the sample (from a focusing transducer) could be used as the input wave. For each pulse, the transmitted field was sampled at a fixed time, t_s , after the input wave arrived at the sample. This sampling time sets the path length, and through the diffusion approximation, it can be related to the number of scattering events undergone. This leads to a simple relationship between the mean square relative displacement of the particles and the field autocorrelation function, as given by Eq. (2.75).

The electronics needed to generate the input pulses and to sample the field at a fixed time are illustrated in Fig. 4.2.1. The method used to generate the ultrasonic pulse train was the same as that used for the transmission measurements of the last section, only now two Stanford delay generators were needed to produce all of the required triggers. As discussed in Section 3.4.3, the pulse repetition rate was controlled by the longest delay setting on the delay generator (to within one period of the carrier frequency), which, depending on the speed of the bead dynamics, was set somewhere in the range of 0.5 to 50 ms. The detection electronics were also the same through the amplification and filtering stages, up to the detection stage. To sample the field at one particular time we used the Boxcar Integrator, triggered using the delay generator. In cases where the signal-to-noise ratio was small, the repetition rate was increased and the adjacent averaging function of the boxcar was used to smooth out the sampled field. When doing

this it was important to ensure that the pulse repetition rate was fast enough that the underlying field did not change significantly over the averaging time window. The integrated and averaged output of the boxcar was read by the Gage CompuScope, using its gated digitization option. The gate for the CompuScope was supplied by one of the delay generators, and was an 8 μ s long square TTL pulse. When the gate pulse was high, the CompuScope recorded 8 data points, the minimum allowed width of the gate. It did this once for each ultrasonic pulse until the memory on the CompuScope was full, after 1,047,040 data points or 130,880 pulses. The data were then saved to the computer hard drive, and the process repeated 5 to 50 more times, depending on the statistics desired.

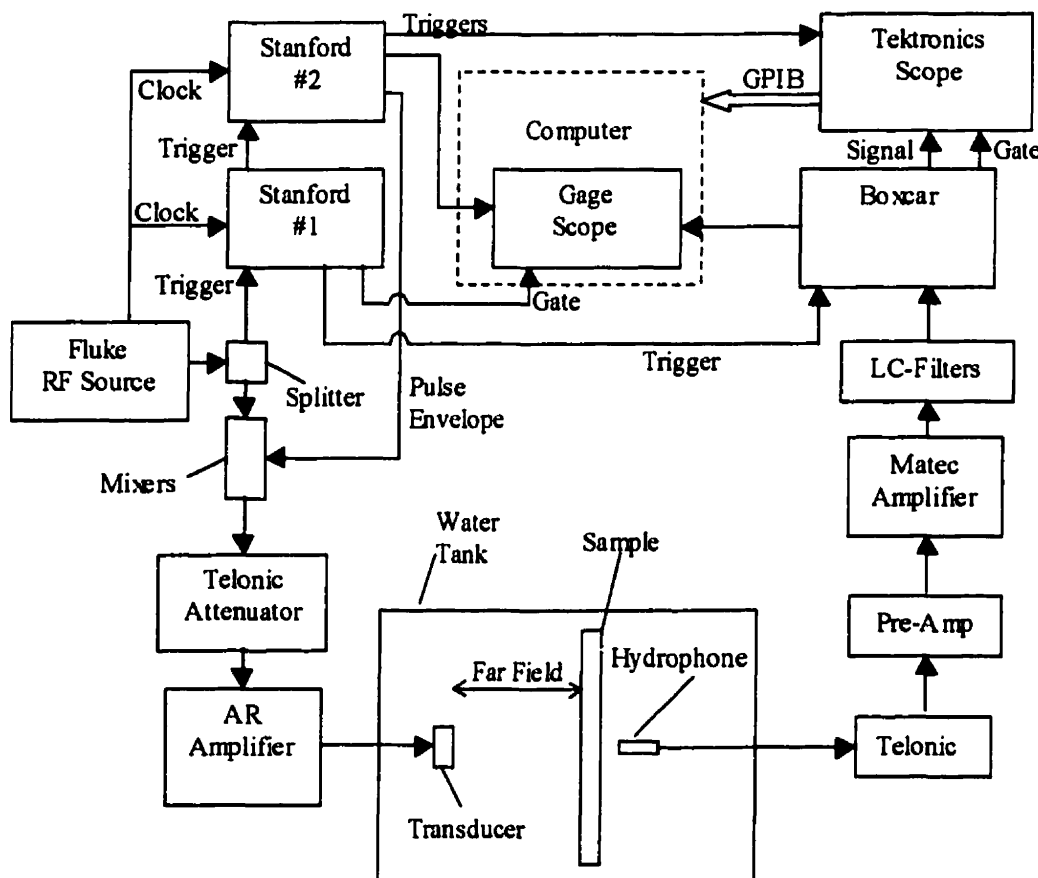


Figure 4.2.1: Electronics setup for DAWS/DSS measurements.

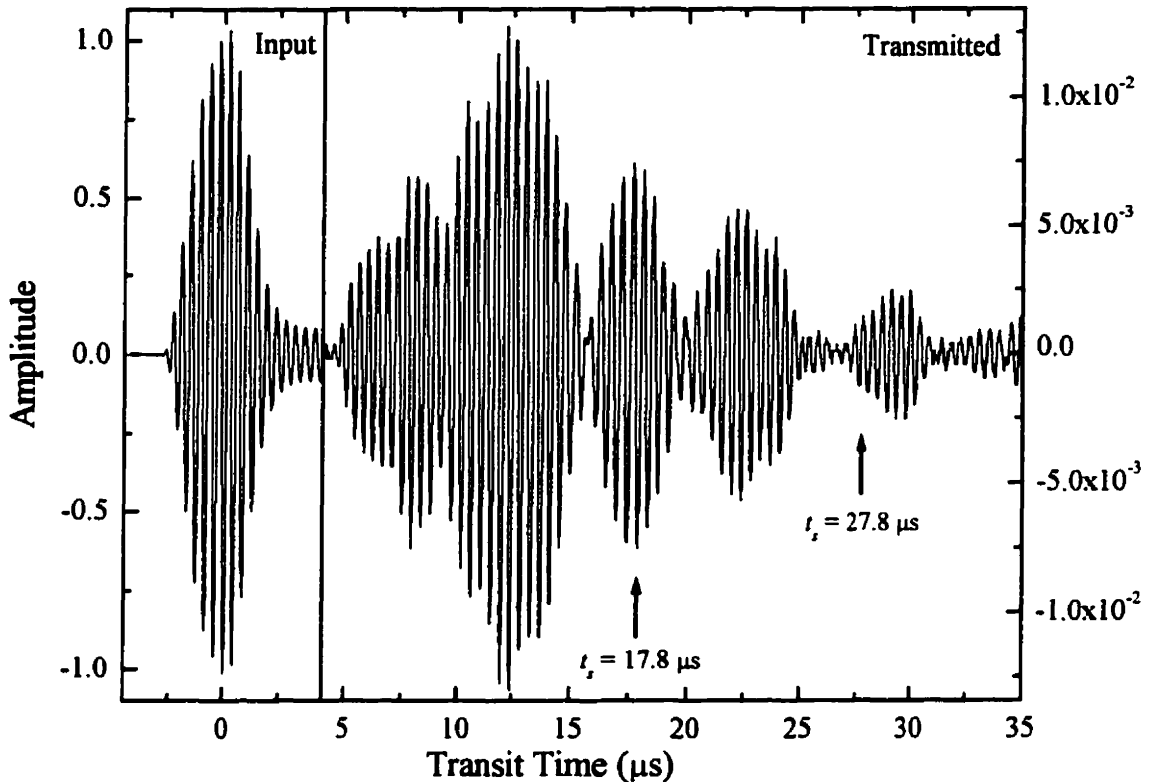


Figure 4.2.2: Sampling the transmitted field. In the left panel a typical input pulse is shown. In the main panel a typical transmitted pulse is shown, and two sampling times are indicated by arrows.

Figure 4.2.2 shows a typical input pulse, and the resulting scattered field. By changing the trigger time of the boxcar, the field could be sampled at any arbitrary time, two of which are indicated by arrows. The corresponding field fluctuations are plotted in Fig. 4.2.3(a). The field at the later sampling time fluctuates much more quickly than that from the earlier sampling time, since the waves have had a longer path through the sample, and have undergone more scattering events. Each bead in the scattering path moves by a small amount between pulses, and so the total phase change of the whole path through the sample will, on average, be proportional to the number of scattering events, as indicated in Eq. (2.73). This is borne out by the autocorrelation functions and relative mean square

displacements [Fig. 4.2.3(b) and (c)]. The autocorrelation functions are calculated from the field fluctuations by using FFTs and the correlation theorem [Press *et al.* 1992]

$$\Im[f \otimes g] = \Im[f] \Im[g^*]. \quad (4.1)$$

The electronics, and small amplitude stray ballistic sound, can give the field fluctuations a

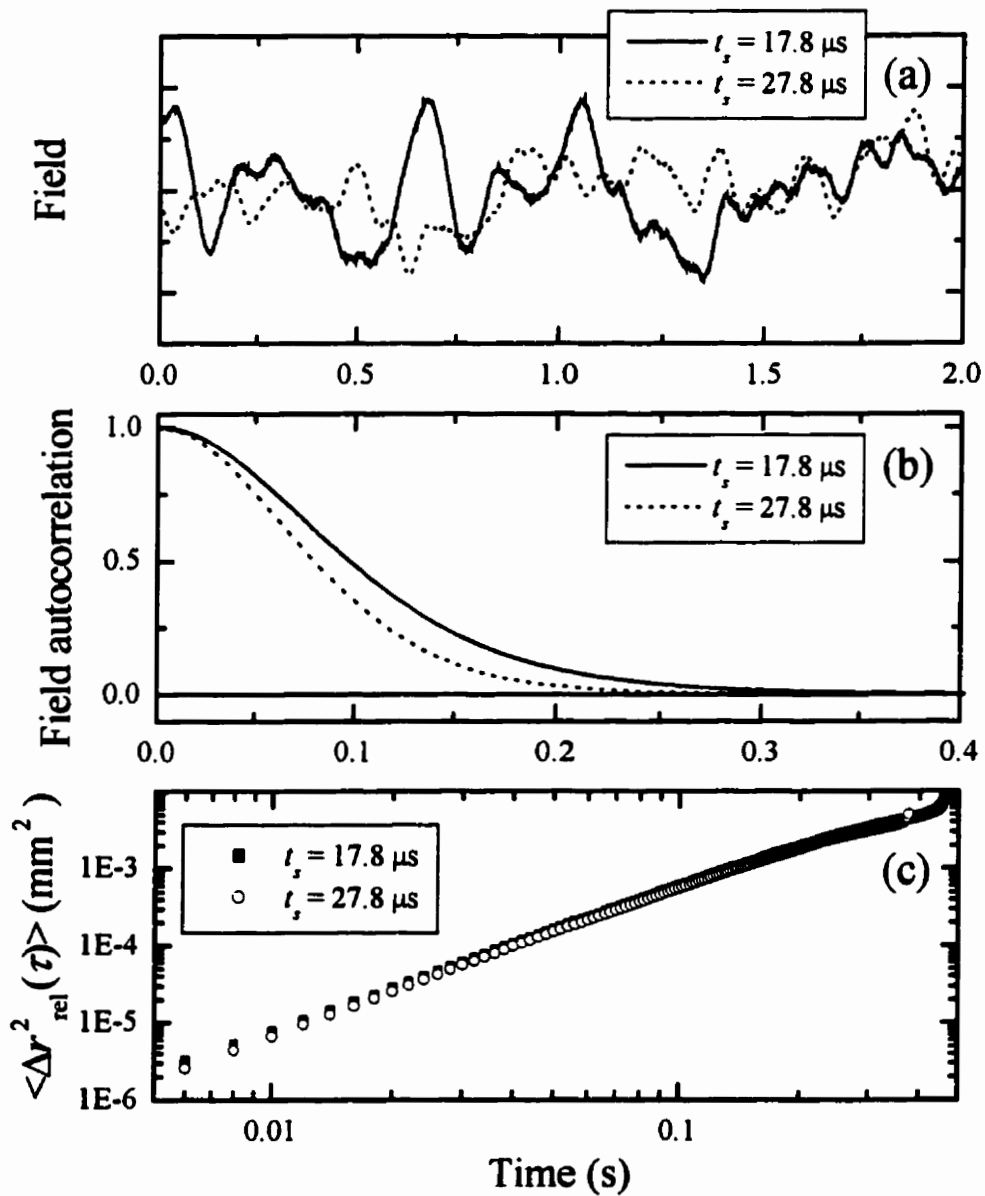


Figure 4.2.3: (a) Field fluctuations measured at the two sampling times in Figure 4.2.2. (b) The corresponding field autocorrelation functions. (c) The resulting relative mean square displacements.

DC-offset. The offset was found by calculating the average value of the field from all of the data files, and then it was subtracted from each file. The unnormalized autocorrelation functions were found for each data file separately, averaged together, and finally, the result was normalized to be equal to 1 at $t = 0$. Processing the data from all of the separate files in this fashion leads to an autocorrelation function which is equivalent to that which would have been found by taking one very long data file; however the correlation function will not extend to as large a time difference as could be measured from a long file.

Using Eq. (2.75), the relative mean square displacement of particles separated by a distance l^* can be calculated from the field autocorrelation functions. The transport mean free path and energy velocity can be estimated from the measured ballistic group velocity and scattering mean free path [c.f. Sec. 2.2.3]. The wave vector k is determined by the carrier frequency of the pulse and the ballistic phase velocity in the sample. All that remains is to determine the average time that the sampled wave has spent traveling through the suspension (t_{ref}). Using the Stanford delay settings, it is straightforward to determine the time at which the boxcar samples the field. We then recorded a reference pulse through the sample cell, with the beads out of the transducer beam, and found the center of the pulse. This reference time can be written

$$t_{ref} = \frac{L_{T \rightarrow S}}{c_{water}} + 2 \frac{L_{wall}}{c_{wall}} + \frac{L_z}{c_{liq}} + \frac{d}{c_{water}}, \quad (4.2)$$

where the various terms are defined in Fig. 4.2.4(a). Similarly, the time at which the boxcar samples the transmitted field is:

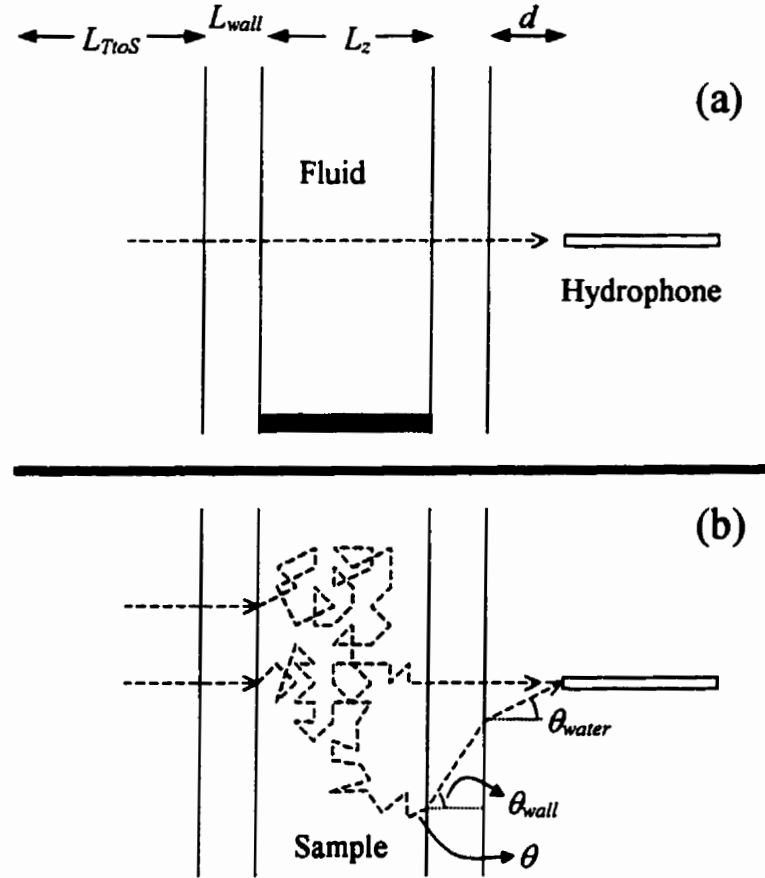


Figure 4.2.4: Wall corrections for DAWS. (a) The reference path (L_{TiOS} is the distance between the transducer and sample wall.) (b) Two scattering paths with different exit angles θ .

$$t_B = \frac{L_{TiOS}}{c_{water}} + \frac{L_{wall}}{c_{wall}} + t_s + \frac{L_{wall}}{c_{wall} \cos\{\theta_{wall}\}} + \frac{d}{c_{water} \cos\{\theta_{water}\}}, \quad (4.3)$$

where θ is the exit angle from the sample, which changes for different paths, as indicated in Fig. 4.2.4(b). Combining Eq. (4.2) and (4.3), solving for t_s , and taking an average over angle results in

$$\langle t_s \rangle_\theta = t_B - \left\{ t_{ref} - \frac{L}{c_{liq}} \right\} - t_w. \quad (4.4)$$

Here, t_w is a correction factor due to the spread of different path lengths through the final

wall, and is given by

$$t_w = \left\langle \frac{L_{wall}}{c_{wall}} \left\{ \frac{1}{\cos[\theta_{wall}]} - 1 \right\} + \frac{d}{c_{water}} \left\{ \frac{1}{\cos[\theta_{water}]} - 1 \right\} \right\rangle_g . \quad (4.5)$$

This average is calculated and listed in Appendix B, for all of the different sample velocities and wall thicknesses, but it is generally about 3 to 4 μs for our samples. This compares to sampling times of 15 to 30 μs for the thin samples, and 50-100 μs for the thick samples. Using Eq. (4.4) we can determine the time the detected sound has spent in the sample, and thus calculate the mean square displacements of the particles.

Figure 4.2.5 shows some examples of the relative mean square displacements measured for several volume fractions in the $L_z = 7.76 \text{ mm}$ sample. At early times, the mean square displacement has a τ^2 dependence, which indicates that the particles are each moving at constant, but different, velocities, without interacting. Thus

$$\langle \Delta r_{rel}^2(t^*) \rangle = \tau^2 \Delta V_{rel}^2(t^*), \quad (4.6)$$

where $\Delta V_{rel}^2(t^*)$ is the relative mean square velocity. At later times, the particles begin to interact with their cage of nearest neighbors, and their speed and direction changes, leading to a slower increase in the mean square displacement at a crossover or correlation time τ_c . To model this crossover, we use the following simple phenomenological equation, with τ^2 dependence at early times and a weaker power law time dependence (m) at times later than τ_c :

$$\langle \Delta r_{rel}^2 \rangle = \frac{\{\Delta V_{rel} \tau\}^2}{1 + \left\{ \frac{\tau}{\tau_c} \right\}^{2-m}}. \quad (4.7)$$

Using this model, both the mean square relative particle velocity and a measure of the local correlation time can be extracted from the data. To estimate the uncertainty in the

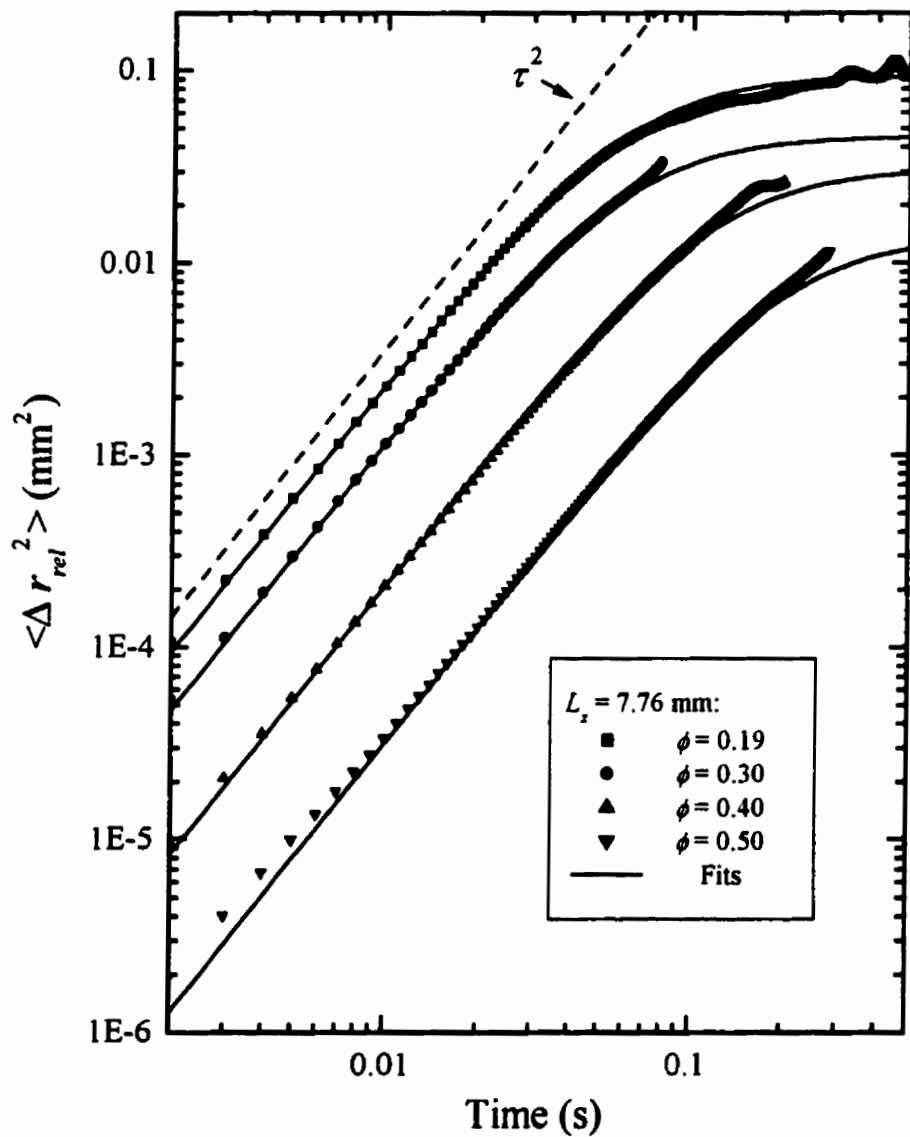


Figure 4.2.5: Mean square displacement of the beads relative to their neighbors at several ϕ , along with fits of Eq. (4.7) to the data.

fitting parameters, fits were performed holding $m = 0$ and letting m vary. The differences were generally less than 5% in the velocities, but could be much larger in τ_c for some measurements.

It must be reemphasized that DAWS measures the relative mean square displacement of particles *separated by a distance l^** . The transport mean free path can be varied by changing the frequency of the ultrasound, and by doing this we were able to measure the instantaneous spatial velocity correlation function, as discussed in Section 2.3.2.

When the signal to noise ratio is small and the adjacent averaging in the boxcar is not sufficient to alleviate the problem, the effects on the field correlation functions can be significant. In extremely bad cases, the measured field fluctuations looked like those shown in Fig. 4.2.6(a), where the dotted line corresponds to the measurement without any boxcar averaging. The noise shows up as rapid, uncorrelated fluctuations superimposed on the slower, correlated field fluctuations that we wish to measure. This is made clear by calculating the autocorrelation function of the data, as is illustrated in Fig. 4.2.6(b) and (c). Figure 4.2.6(c) shows the effect at small τ , where there is a sharp drop in the correlation function, caused by the decorrelation in the field due to the randomness of the noise from one pulse to the next. The effect of this drop in the correlation function on the measured values of the mean square displacement is to cause them to be larger than the actual values at short times. This effect can be seen in the 50% data in Fig. 4.2.5, where the mean square displacements at early times are above the τ^2 line.

The thin line and circles in Fig. 4.2.6 show the result of adjacent averaging with an

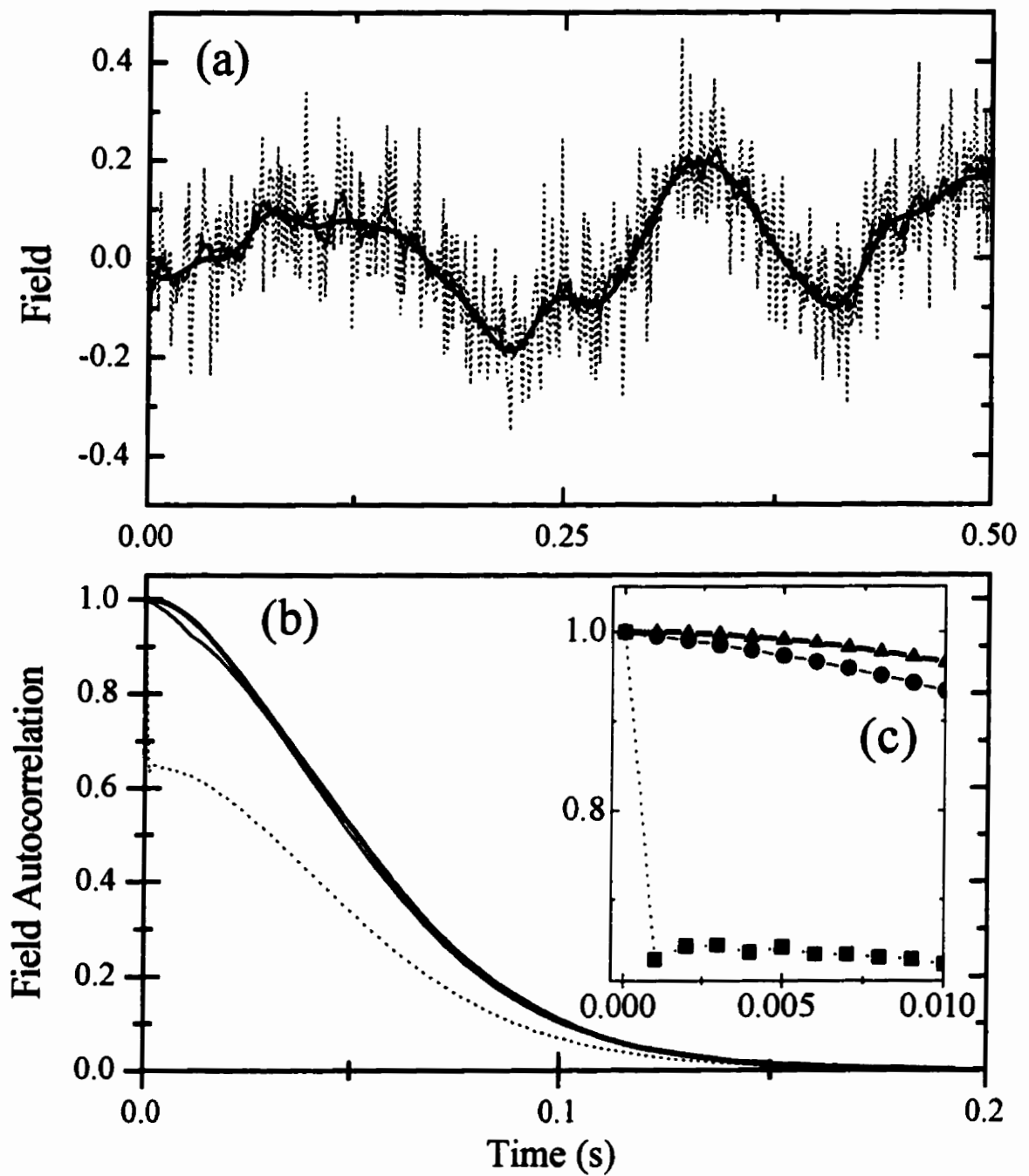


Figure 4.2.6: Noise problems with DAWS data. (a) The raw data (dotted line), the results of adjacent averaging with an 11-point window (thin line) and the results of low pass FFT filtering the data (thick line). (b) The corresponding field autocorrelation functions. The inset, (c), shows the early time behavior of the autocorrelation functions.

11 point window. The fluctuations are now much smoother, while leaving the underlying oscillations intact. A more sophisticated method for reducing the noise is to FFT-filter the field fluctuation data. All that is needed is a filter function that cuts off high frequency components corresponding to the noise, while leaving the lower frequency components that correspond to the particle motions. A convenient choice is the Fermi-Dirac distribution function

$$h(f) = \frac{1}{\exp\left[\frac{f - f_o}{\sigma}\right] + 1}, \quad (4.8)$$

which is equal to 1 below f_o , and quickly drops to zero above f_o . The result of FFT filtering the field with this function is shown by the thick line and triangles, were it can be seen that this method works quite well at removing the effects of noise. The FFT filtering method also has the advantage that it can be used to remove extremely low frequency components, which correspond to drifts in the DC offset.

4.2.2 Continuous Wave Measurements

Diffusing Acoustic Wave Spectroscopy can also be performed using continuous wave ultrasound, as was discussed in Section 2.3.3. This allows for the measurement of much faster dynamics than the pulsed method is capable of, since the shortest measurable time difference in the field fluctuations is now on the order of the period of the ultrasound, and not the pulse repetition rate. However, in the experiments reported in this thesis, pulsed measurements were sufficiently fast to measure the particle dynamics, and therefore continuous wave measurements were primarily performed as a proof of method.

To produce a quasi-continuous wave input pulse we used the same electronics as

were used for the pulsed DAWS measurements [Fig. 4.2.1]. The pulse length was set using the Stanford delay generator #2, and was of the order of several hundred seconds, depending on the sampling rate of the boxcar. We waited for one second before taking data, in order to ensure that all paths in the sample had been sampled, and that we were in the cw limit. Then the GageScope was triggered, and it recorded the boxcar output. The boxcar was set up to sample the field at a time that is synchronized with the input sound, which was accomplished by triggering it using delay generator #1, which was triggered by the input wave. This means that we measure the field fluctuations minus the $\exp[-i\omega_0 t]$ fluctuations due to the input pulse carrier oscillation, which gives the appropriate field autocorrelation function for use in Eq. (2.87).

For pulsed data, the sampling time sets the path length in the sample, and thus the mean number of scattering events, whereas for continuous wave data all path lengths are sampled, and an weighted integration over path length must be performed. This integral has been worked out previously, and is given by Eq. (2.87), which must be inverted to find the relative mean square displacement. This is done numerically by solving the non-linear algebraic equation for each time point, using the previous time point as an initial guess for the solution.

The results of the numerical inversion are plotted in Fig. 4.2.7, along with the corresponding pulsed measurements of the relative mean square displacement. Note that the continuous wave data are much more sensitive to the early time behavior of the particles and are less effected by noises limitations. The results of the two methods are in good agreement, especially for times between 2×10^{-2} and 2×10^{-1} , where they give

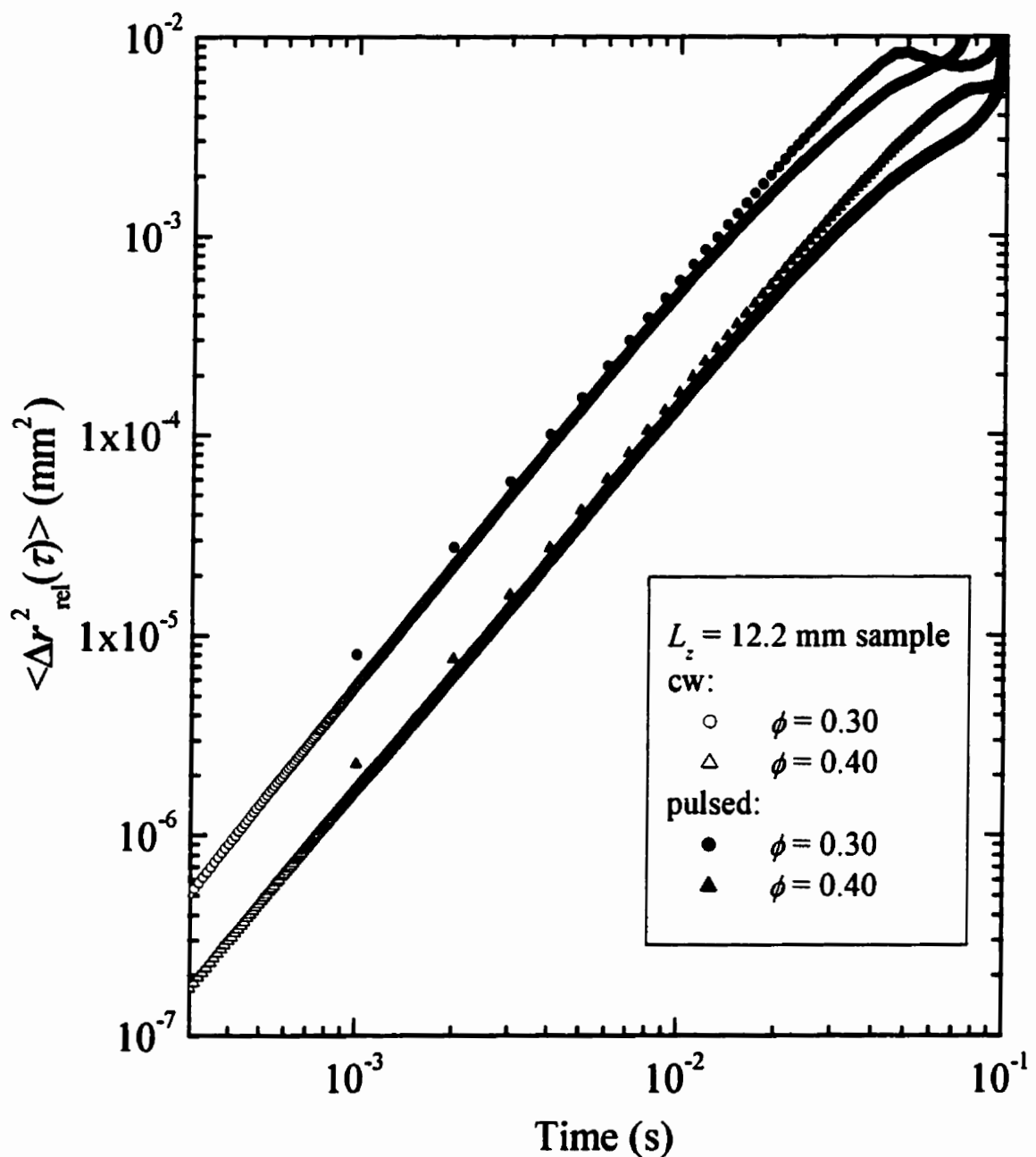


Figure 4.2.7: Comparison of pulsed and cw methods in the $L_z = 12.2 \text{ mm sample}$ at two volume fractions.

essentially the same rms relative velocity. At later times the agreement is not as good, most likely due to the increased contribution to $g_1(\tau)$ of short paths through the sample at large correlation times ($g_1(\tau)$ for short paths decorrelates more slowly than for longer paths), since these paths are not as well modeled by the diffusion approximation [e.g. MacKintosh & John 1989]. Another possible source of the small inconsistency is the background in the cw experiment, caused by reflections off the sides of the water tank. This background does not affect the pulsed experiment, and while it was subtracted out of the cw data, small changes in the offset of the correlation function will have a comparatively large effect on the mean square displacement as the correlation function approaches zero. Nonetheless, continuous wave DAWS can be used in place of pulsed techniques to measure the relative velocity, if the particle dynamics are fast enough to warrant the extra complexities in analysis.

4.3 DSS Near-Field Measurements

In Section 2.3.1, a relationship was derived between the mean square displacement of the scattering particles and the single scattering field autocorrelation function. In order to evaluate Eq. (2.65), the average value of the scattering wave vector must be determined for the geometry used. In this section, we will discuss the situation where the hydrophone is used as a detector, and is placed in the near-field of the sample.

The electronics setup is the same as that used for pulsed DAWS [Fig. 4.2.1]. For these experiments, a one-inch-diameter 0.5 MHz plane wave transducer was used to generate the input pulse, giving a scattering mean free path that was greater than 30 mm, which ensured that the scattering was dominated by singly scattered sound, at least in the 7.76- and 12.2-mm-thick samples that were used. The scattered field is sampled at one particular time, and by determining the corresponding set of single scattering paths of length t_s , the average scattering angle can be found. This is discussed in detail in Appendix C, which includes an analysis of the effects of the range of input angles from the transducer, the scattering volumes, the angle-dependant scattering amplitude, the angle-dependent wall transmission, and the small shear wave component in the walls. The basic result of this analysis is that we measure an average of all of the components of the mean square displacement with the magnitude of $\langle \bar{q} \rangle$ accounting for the variation of the scattering angle with sampling time, such that

$$g_i(\tau) = \exp[-\bar{C}\langle \Delta r^2(\tau) \rangle], \quad (4.9)$$

where \bar{C}/k^2 is a parameter that incorporates all of the effects mentioned above. The

factor \bar{C}/k^2 is plotted in Fig. 4.3.1 for the two samples used (k is the wave vector in the sample). Once the mean square displacements are found, the root mean square velocities and the correlation times can be extracted by using the same fitting function as was used to analyze the DAWS data [Eq. (4.7)]. From the crossover or correlation time we can determine the dynamic correlation length ($d_c = \tau_c V_{rms}$), which is the average distance traveled by a particle before its velocity is significantly changed.

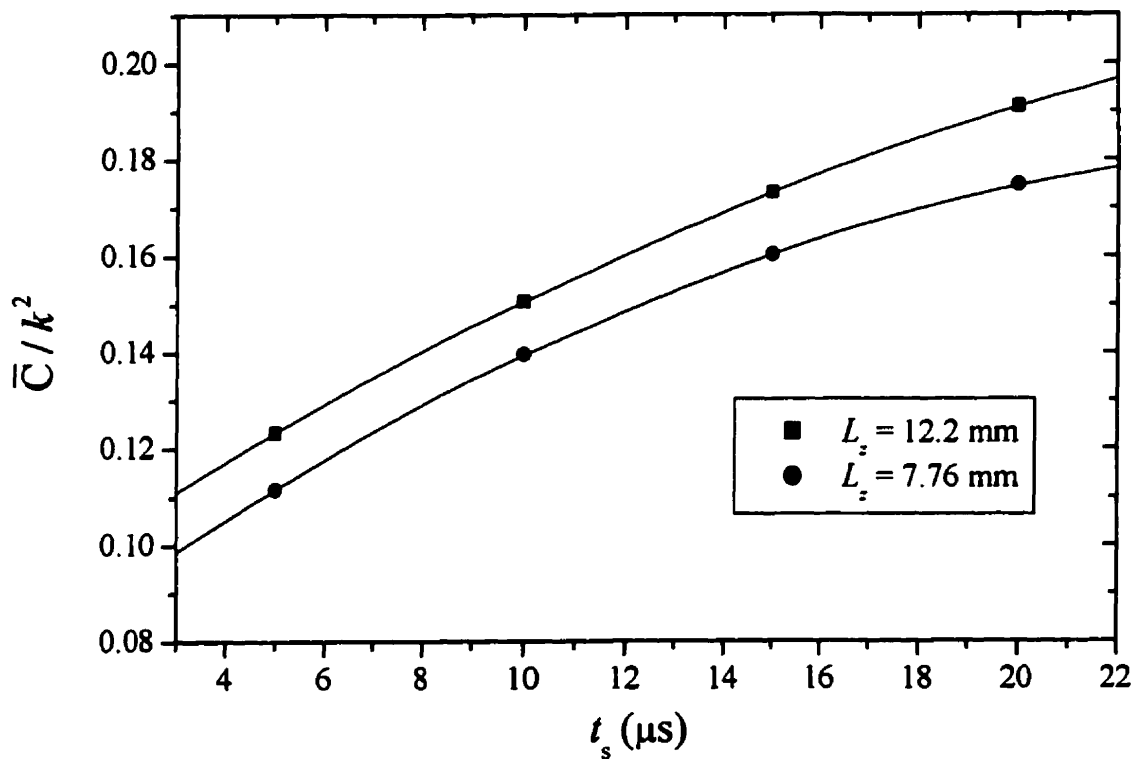


Figure 4.3.1: Near-field single scattering calculation showing the value of the constant \bar{C} for the two sample thicknesses as a function of sampling time. The lines are interpolated fits to the calculated values (points).

4.4 DSS Far-Field Measurements

The far-field single scattering geometry is more useful than the near-field setup that we originally used, but it is somewhat more difficult to arrange because of the large path lengths that are needed in the water tank. For this reason, we were only able to use this geometry once the large tank was acquired. The usefulness of this geometry comes from the fact that by changing the positions of the generating and receiving transducers, different directions of \vec{q} can be selected, and thus the different spatial components of the rms velocity can be measured independently. This is illustrated in Fig. 4.4.1, where the scattering geometry used to isolate each component of V_{rms} is shown. By choosing θ_{water} such that the angle in the sample medium is 45° , the scattering angle for the horizontal and vertical setups is 90° , and \vec{q} lies along the x and y -axis respectively. The reflection geometry uses the same transducer to generate and detect ultrasound, giving a scattering

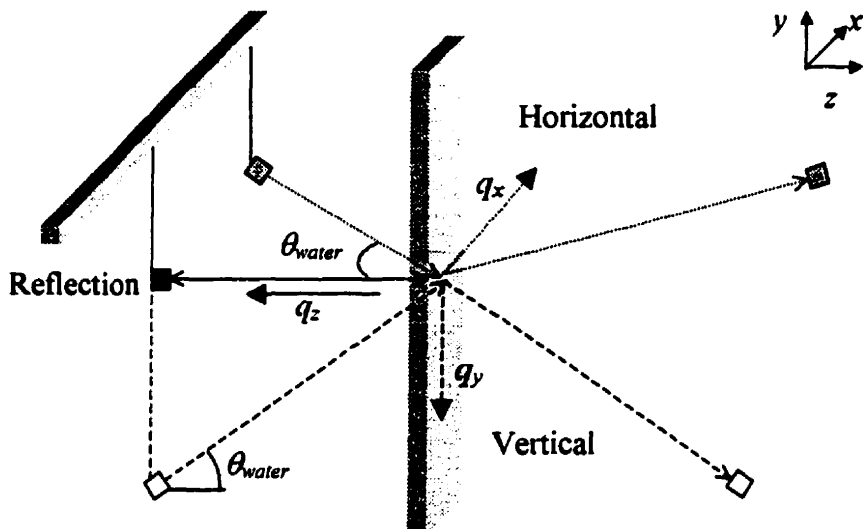


Figure 4.4.1: Far-field single scattering geometry. The solid lines show the reflection geometry (V_z), the dashed lines show the vertical geometry (V_y) and the dotted lines show the horizontal geometry (V_x).

angle of 180° , and \vec{q} parallel to the z -axis.

Plane wave transducers were used, with a central frequency of 250 kHz and a diameter of 1.5". This low frequency ensured that single scattering was dominant even in our thickest samples. The pulses used were 20 μ s long and square, giving a reasonable balance between time and frequency widths. The field was sampled at one particular time, in the middle of the spread of arrival times for the scattered waves. The electronics setup for the horizontal and vertical experiments was the same as that shown in Fig. 4.2.1. For the reflection geometry the electronics had to be adjusted [Fig. 4.4.2], so that the same transducer could be used as both generator and receiver.

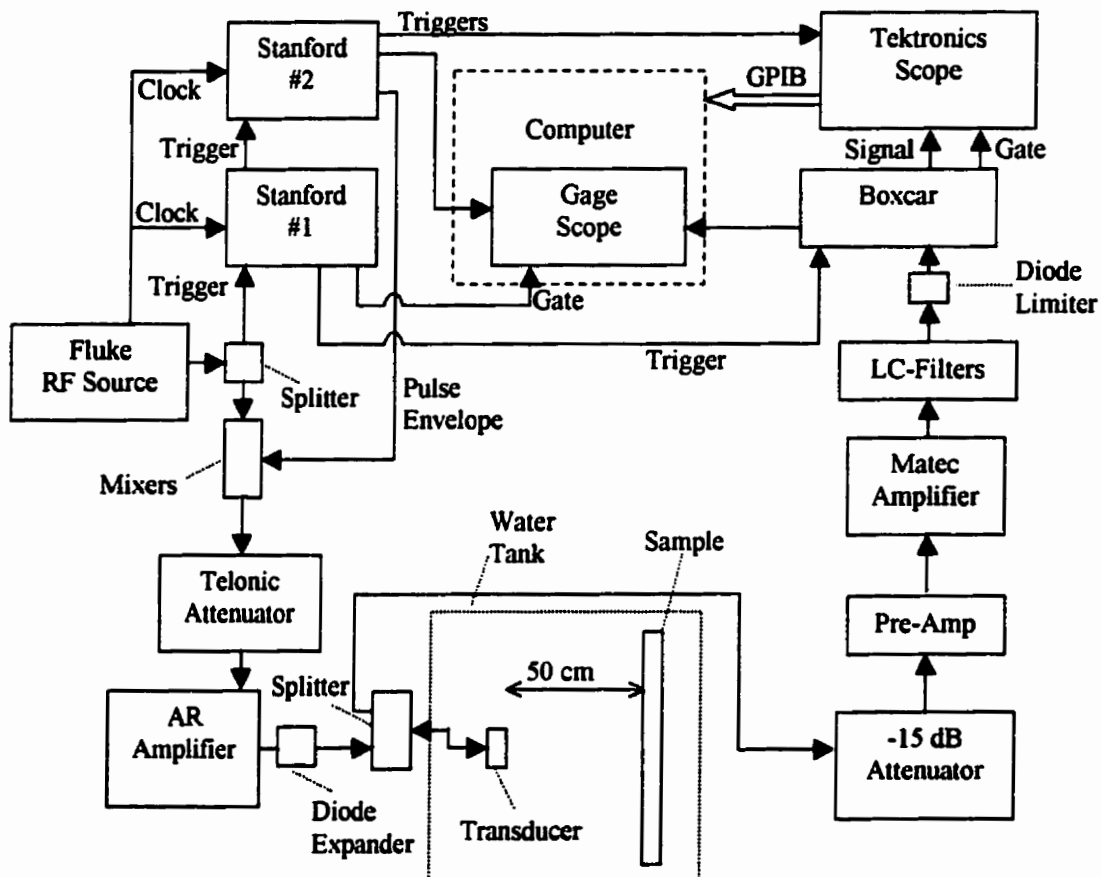


Figure 4.4.2: Electronics setup for reflection DSS measurements.

Because of the finite distance between the sample and the transducers, there is a range of possible scattering angles that are detected at the sampling time, depending on both the geometry and the time width of the input pulse. The situation for the horizontal and vertical geometry is shown in Fig. 4.4.3. The transducers are placed 50 cm away from the sample (in a direction perpendicular to the sample face), and are angled towards the sample at about 35° (depending on the sample's phase velocity), which gives an angle inside the sample of 45° , and a scattering angle that is twice this. The beam spread angle is about 5° , which results in a range of scattering angles from 74° to 104° . However, in this case the geometry is not the limiting factor, because we are sampling at one particular arrival time. This limits the range of paths which can reach the detector at the sampling time to those whose travel time is equal to the time of the central path, plus or minus half of the time width of the input pulse. It is here that the long path lengths in the water tank help to reduce the spread in the scattered angle, as illustrated in Fig. 4.4.4, which plots the change in the travel time versus scattering angle. The spread in the scattering angle, $\Delta\theta$, is reduced to about $\pm 1.5^\circ$ for the input pulse width of $20 \mu\text{s}$. It must be noted that for all

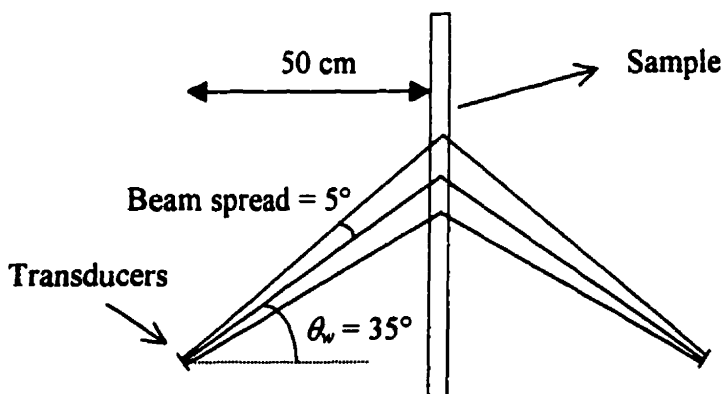


Figure 4.4.3: Beam spread for vertical and horizontal geometries.

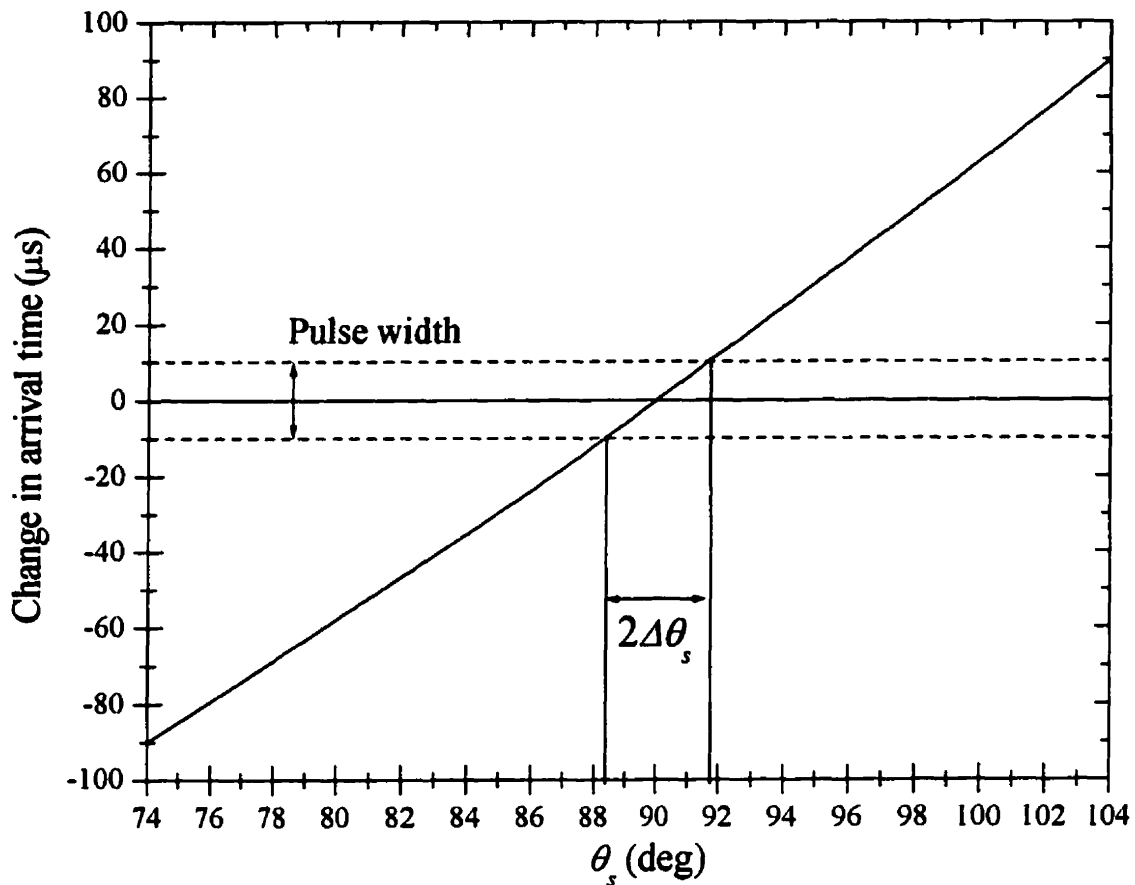


Figure 4.4.4: Effect of the finite pulse width on the spread of scattering angles. The change in arrival time is plotted versus the scattering angle, with the spread in pulse width indicated by dotted lines and the resulting spread in scattering angles indicated by vertical solid lines.

of these scattering angles, \vec{q} has essentially the same direction, it is only the finite size of the transducer and the finite thickness of the sample that have an effect on the direction. In practice, the direction of \vec{q} is limited by the accuracy with which the transducers were aligned, $\Delta\theta_q = 1^\circ$.

For the reflection geometry, the situation is different. Here the limiting factor on the spread of scattering angles is the angular size of the transducer as seen from the sample, as is shown in Fig. 4.4.5. For a 1.5" diameter transducer placed 50 cm from the

sample, the spread in water angles is $\pm 1.7^\circ$, giving a spread in the scattering angle of $\Delta\theta_s = 2^\circ$. However, the direction of \bar{q} varies by as much as 5° , because of the beam divergence angle of the transducer, although once again this is limited by the timing and pulse width factors to $\Delta\theta_{\bar{q}} = 4^\circ$ in this case.

Once the field autocorrelation function has been measured, the appropriate \bar{q} can be substituted into Eq. (2.65), and the mean square displacements can be found. The resulting expression is

$$\langle \Delta r_i^2(\tau) \rangle = -\frac{1}{2k^2 \sin^2 \left\{ \frac{\theta_s}{2} \right\}} \ln [g_1(\tau)], \quad (4.10)$$

where k is the wave vector in the scattering medium and i represents the appropriate Cartesian coordinate. This in turn gives the three spatial components of the root mean square velocity, and the dynamic correlation length in each of the three directions.

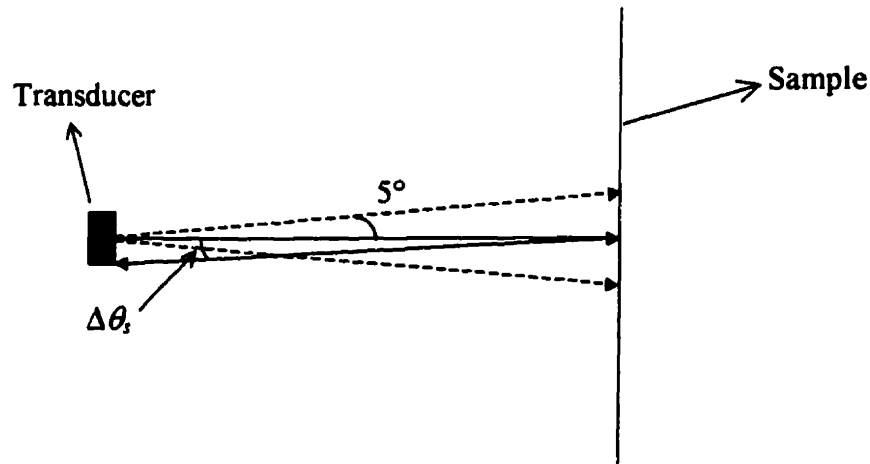


Figure 4.4.5: Reflection geometry scattering angles, showing both the range of scattering angles $\Delta\theta_s$ due to the finite size of the transducer and the beam spread (5°).

The small spread in the direction of \vec{q} leads to a slight mixing of the different components of the mean square displacement, especially in the reflection geometry, where the effect is exacerbated by the fact that $V_{z,rms}$ turns out to be the smallest component of the rms velocity (by as much as a factor of 4). This mixing effect is of order $\sin^2[\Delta\theta_{\vec{q}}]$, which at its worst gives a weighting of the order of 0.5% to the mixed in components.

4.5 Phase Measurements

4.5.1 Setup

When using ultrasound, the fluctuations in the phase of the scattered signal can be measured in a straightforward manner. This was done by recording short segments of the scattered wave field, instead of just sampling the field at one time, allowing the phase and amplitude of the wave to be measured. The Gage CompuScope was used to do this, by setting it up in gated digitization mode with the gate length set to 63 points and a sampling rate of 30 MS/s, giving a 2.1 μ s time window (4.7 periods at 2.25 MHz). These experiments were performed at DAWS frequencies, on the 12.2-mm-thick fluidized bed, placed in the large tank, using the 60% glycerol/water mixture as the fluid.

The electronics used are pictured in Fig. 4.5.1. The setup is essentially the same as that used for the pulsed field DAWS measurements on the generation side, but differs slightly on the detection side. Instead of using the boxcar, the amplified and filtered hydrophone signal was put into channel A of the CompuScope, which then recorded a 2.1- μ s-long segment of the signal when the gate was high. This 2.1 μ s segment started at a sampling time of 17 μ s, corresponding to about 34 scattering events in the $\phi = 0.40$ sample used. However, as alluded to earlier, the CompuScope has very poor triggering which jitters by up to 3 points. In order to correct for the poor triggering of the CompuScope, a triangle ramp function, generated in sync with the input pulse, was fed into channel B. This ramp function lasted about 3 μ s, and started just before the time at which the gate should have begun. By measuring both the scattered waveform, which changes from one pulse to the next, and this steady ramp function, the waveform could be

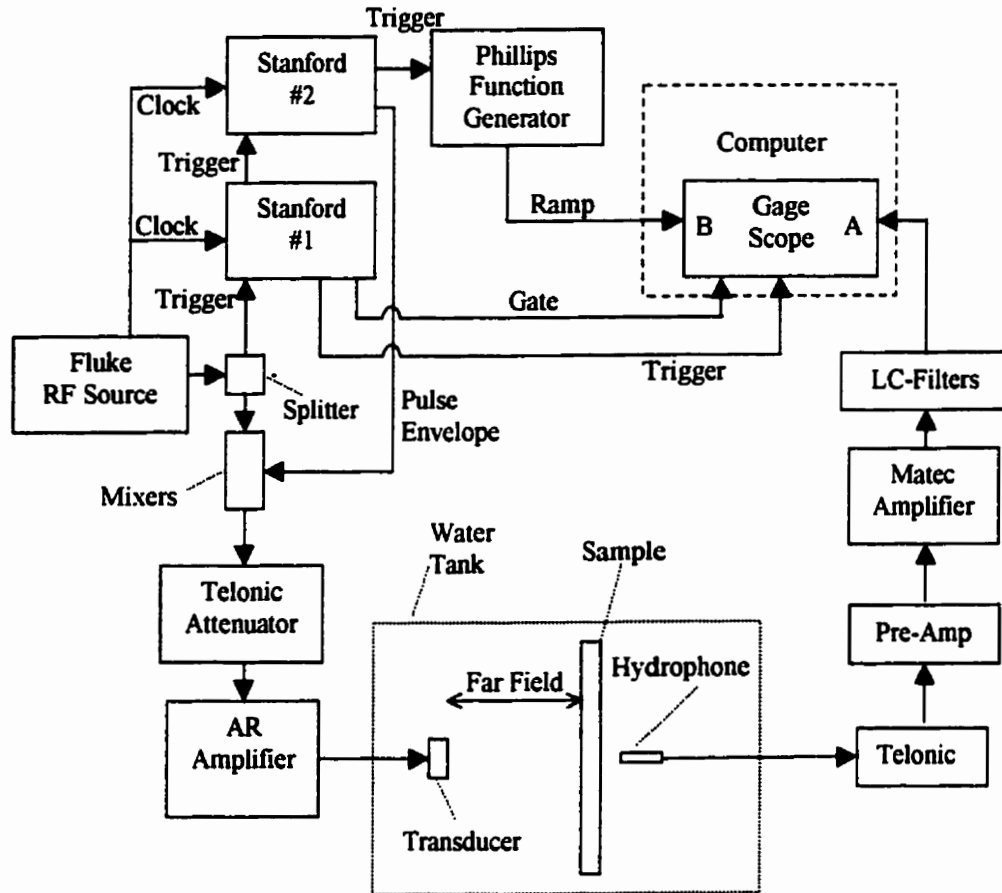


Figure 4.5.1: Electronics setup for phase measurements.

corrected for the sloppy triggering in the CompuScope. The fact that both channels had to be used, means that only about 8300 consecutive pulses could be recorded before the memory buffer of the CompuScope was full. This corresponds to about 16 seconds of data when the pulse repetition rate is 2 ms. The series of pulses was repeated at least 10 times to improve the measurement statistics.

4.5.2 Phase and Amplitude Extraction

Once the segments of field have been recorded and corrected for trigger jitter, the phase and amplitude of each record must be found. This is done by using a standard

numerical technique, which has been previously used in our group [Jones 1996], and is described below.

The wave field of the recorded segment can be written as $\psi(t) = A(t)\cos[\omega t + \Phi(t)]$, where A is the amplitude and Φ is the phase. This is multiplied by a reference signal $R_s = \sin[\omega t]$, where ω is the central frequency of the ultrasonic pulse:

$$\begin{aligned}\psi(t)R_s(t) &= A(t)\cos[\omega t + \Phi(t)]\sin[\omega t] \\ &= A\{\cos\omega t\cos\Phi - \sin\omega t\sin\Phi\}\sin\omega t \\ &= A\{\cos\omega t\sin\omega t\cos\Phi - \sin^2\omega t\sin\Phi\} \\ &= A\left\{\frac{1}{2}\sin 2\omega t\cos\Phi - \frac{1}{2}[1 - \cos 2\omega t]\sin\Phi\right\} \\ &= \frac{A}{2}[\sin 2\omega t\cos\Phi + \cos 2\omega t\sin\Phi - \sin\Phi]\end{aligned}\quad (4.11)$$

Similarly, it is also multiplied by a cosine reference signal, $R_c = \cos[\omega t]$:

$$\begin{aligned}\psi(t)R_c(t) &= A(t)\cos[\omega t + \Phi(t)]\cos[\omega t] \\ &= \frac{A}{2}[\cos 2\omega t\cos\Phi - \sin 2\omega t\sin\Phi + \cos\Phi]\end{aligned}\quad (4.12)$$

Then Eq. (4.11) and (4.12) are digitally filtered with a low pass filter, to remove the $2\omega t$ signals, leaving only

$$\begin{aligned}\psi(t)R_s(t) &\equiv S = -\frac{A(t)}{2}\sin\Phi(t) \\ \psi(t)R_c(t) &\equiv C = \frac{A(t)}{2}\cos\Phi(t)\end{aligned}\quad (4.13)$$

Thus, the amplitude and phase of the segment are given by

$$A(t) = 2\sqrt{C^2 + S^2}$$

$$\Phi(t) = \tan^{-1} \left[\frac{-S}{C} \right] . \quad (4.14)$$

This method gives the phase and amplitude of the recorded segments as a function of time in the segment. Then, by selecting a particular time in the segments at which to sample the phase and amplitude, the fluctuations in the scattered wave due to the motion of the beads can be measured.

An example of measured amplitude fluctuations at three different sampling times is plotted in Fig. 4.5.2. The three times correspond to times which are 0.25, 0.5, and 0.75 of the way across the acquired waveforms. These sampling times are far enough away from each other that the amplitudes are not the same, however they are still very strongly

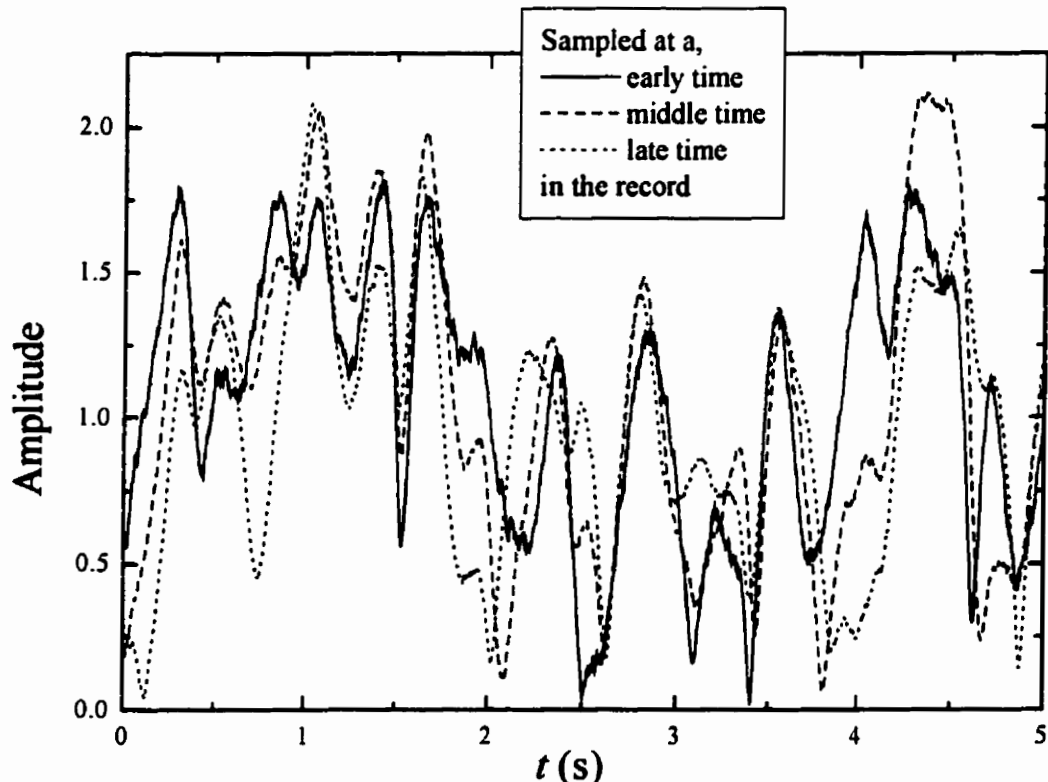


Figure 4.5.2: Amplitude fluctuations at 3 sampling times in the record.

correlated with one another. The amplitude gets extremely close to zero 2-3 times in the 5 seconds shown, which is typical for this data set; on average this occurs about once every 2 seconds.

The wrapped phase variations for the same three sampling times are shown in Fig. 4.5.3. As was discussed in Section 2.3.3, the phase can be unwrapped by removing any jumps in the phase which are larger than π radians. This gives the cumulative phase, which is plotted in Fig. 4.5.4. The behavior of the cumulative phase at the three sampling times is very similar, except for differences of 2π , which creep in due to slight differences

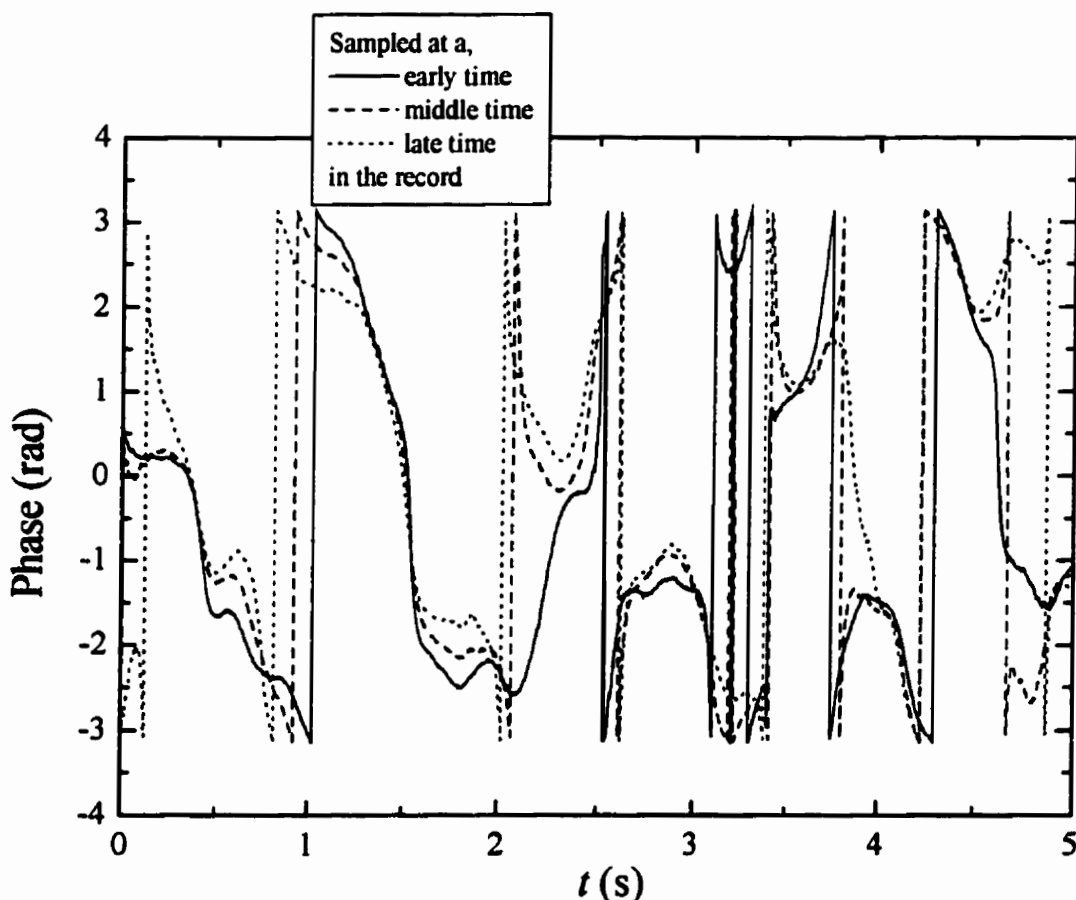


Figure 4.5.3: Fluctuations in the wrapped phase at three sampling times in the record.

during the rapid variations/jumps of $\pm\pi$ in the phase when the amplitude is close to zero.

In most cases the ballistic or electronic DC offset is negligible, but on the occasions when it is not, it must be corrected for. This is done by writing the measured fluctuations in the transmitted wave as a sum of the average (or ballistic) and the scattered components,

$$\psi(t) = A(t)e^{i\Phi(t)} = A_B e^{i\Phi_B} + A_S(t)e^{i\Phi_{S(t)}}. \quad (4.15)$$

Then a time average of Eq. (4.15) is taken, giving the ballistic component in terms of averages (over the different ensembles/segments) of the measured phase and amplitude

$$A_B e^{i\Phi_B} = \langle A(t)e^{i\Phi(t)} \rangle_t. \quad (4.16)$$

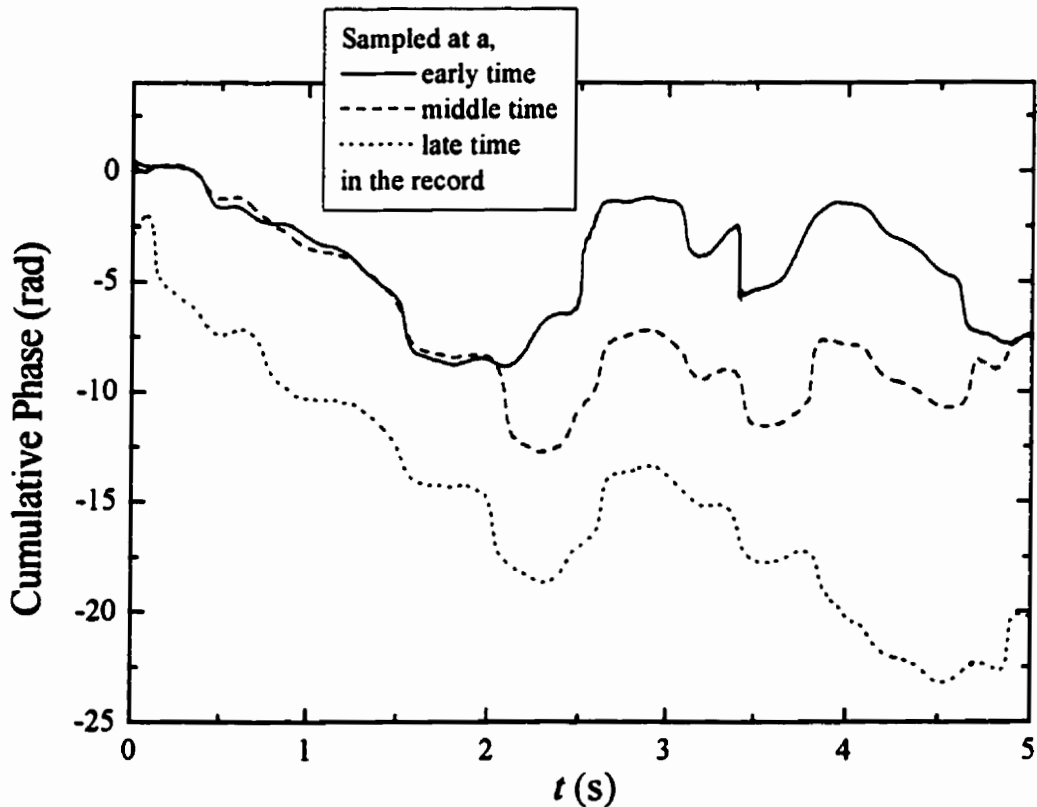


Figure 4.5.4: Fluctuations in the cumulative phase at the same three sampling times in the record.

This equation can be solved for the ballistic amplitude (A_B) and phase (Φ_B)

$$A_B = \sqrt{\langle A(t) \cos \Phi(t) \rangle_t^2 + \langle A(t) \sin \Phi(t) \rangle_t^2} \\ \Phi_B = \tan^{-1} \left[\frac{\langle A(t) \sin \Phi(t) \rangle_t}{\langle A(t) \cos \Phi(t) \rangle_t} \right] . \quad (4.17)$$

And finally, Eq. (4.15) and (4.17) can be solved for the scattered component of the transmitted field

$$A_s(t) = \sqrt{[A(t) \cos \Phi(t) - A_B \cos \Phi_B]^2 + [A(t) \sin \Phi(t) - A_B \sin \Phi_B]^2} \\ \Phi_s(t) = \tan^{-1} \left[\frac{A(t) \sin \Phi(t) - A_B \sin \Phi_B}{A(t) \cos \Phi(t) - A_B \cos \Phi_B} \right] , \quad (4.18)$$

which gives the phase and amplitude fluctuations, corrected for the ballistic offset.

In cases where noise was a problem, smoothing analogous to that discussed in Section 4.3.1 was undertaken. This smoothing was done on the real and imaginary parts of the wave (i.e. Eq. (4.13)) instead of on the phase and amplitude directly. This method avoids problems of smoothing out the zeros in the amplitude and the corresponding jumps in the phase.

From the wrapped and cumulative phases, we can calculate the probability distribution and moments of the phase change for different time differences τ :

$$\Delta \Phi(\tau) \equiv \Phi(t + \tau) - \Phi(t) . \quad (4.19)$$

This probability distribution will be compared to the theoretical predictions discussed in Section 2.3.4.

4.6 Simultaneous Intensity and Field Measurements

To test the Siegert relation [Section 2.3.5], it is convenient to be able to measure the scattered intensity (or amplitude) at the same time as the scattered field. By measuring the two simultaneously, we ensure that any deviations from the Siegert relation can not be attributed to changes in the sample, thereby giving a very accurate test of Eq. (2.96). The Siegert relation was tested under three conditions. First we tested it in a cw DAWS experiment, and then we moved to a pulsed DAWS setup. Finally, it was tested in a single scattering DSS far-field experiment. In all cases the electronics setup was essentially that shown in Fig. 4.6.1. The amplitude was detected by splitting the amplified signal, and

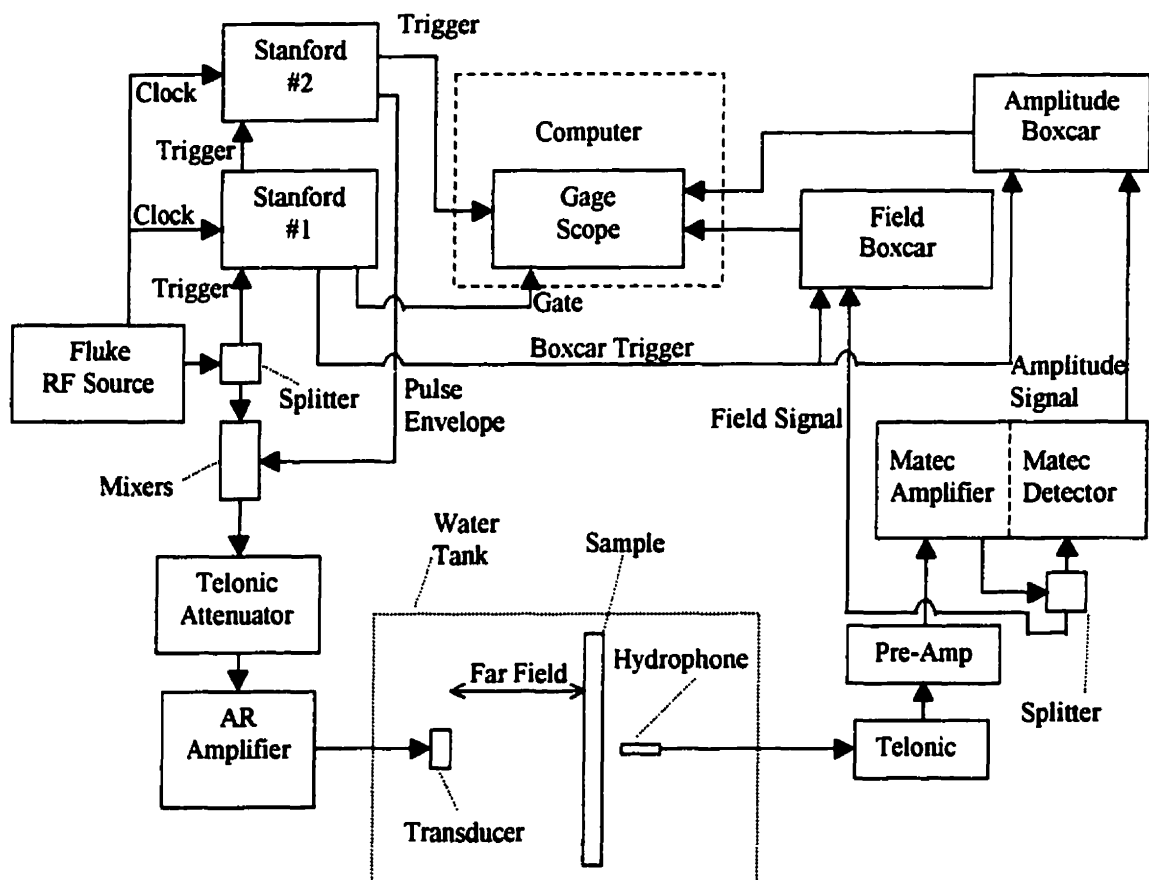


Figure 4.6.1: Electronics setup for simultaneous amplitude and field measurements.

sending half to the Matec Amplifier amplitude detector stage [c.f. Sec. 3.5.2]. Two separate boxcar integrators were used, one to sample the field, and one to sample the amplitude, both triggered at the same sampling time. The output of the boxcars were fed into channels A and B in the GageScope, giving a simultaneous record of the amplitude and field fluctuations as the particles moved.

Some typical field and amplitude fluctuation data are plotted in Fig. 4.6.2, where the amplitude data have been corrected for the different gain introduced by the Matec detector. As expected, the absolute value of the field stays within the amplitude envelope,

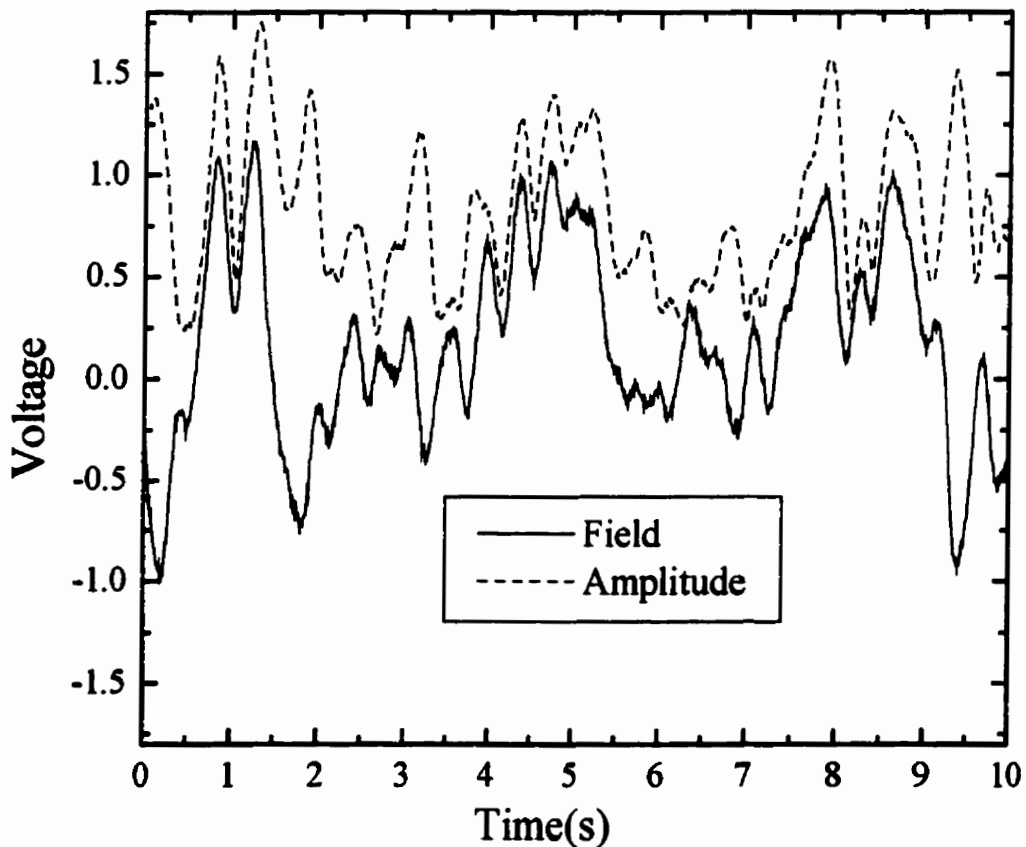


Figure 4.6.2: Amplitude and field fluctuations due to the motion of the scattering particles.

and fluctuates between negative and positive values as the phase fluctuates. There is some correlation between the two, but the fluctuations in the phase of the scattered wave cause the field to have different peaks and dips. In this case there is no noticeable DC offset, but when there was, it could simply be subtracted off of the field, while the amplitude could be corrected by using the method that was discussed in Section 4.5.2. The intensity was found by squaring the amplitude, and the field and intensity autocorrelation functions were then calculated. The factor of β that enters the Siegert relation [Eq. (2.96)], is found by using the fact that $g_1(0) = 1$, giving a direct test of the Siegert relation.

4.7 Non-Linearity Tests

All of the analysis and theory in this thesis assumes that the scattering medium is linear, i.e. that the ultrasonic propagation properties of the material do not depend on the amplitude of the wave. While the ultrasonic amplitudes were small enough that non-linearities were negligible in water, it is conceivable that the samples are more susceptible to non-linearity. The assumption of linearity in the samples was explicitly tested in two ways. First, we varied the amplitude of the input wave over a range of about 40 dB, and looked for differences in the measured ballistic parameters. Second, we looked for transmitted signal at frequencies which were twice that of the input wave, caused by the effect known as frequency doubling, which is expected if there is non-linear propagation.

An example of the first kind of test, for an input pulse at 0.5 MHz, is shown in Fig. 4.7.1. The top panel shows the phase velocity as a function of the input amplitude, expressed as dB down from the maximum that the transducer can generate. The velocity is quite flat, with all variations within the error bars. However, there is evidence of a slight trend towards slower velocities at the higher amplitudes. In panel (b), the transmission is plotted as a function of wave amplitude. Here the result is even flatter, with all of the measurements the same within error bars. Again there is the hint of a trend, this time towards higher transmission at the highest amplitude. However, if there were non-linearity, one might expect that the transmission at the original frequency would be reduced at larger amplitudes, since energy is being converted into higher frequency modes. Therefore, if there is any non-linearity, it is so small that it is at the limit of what can be measured by using this technique.

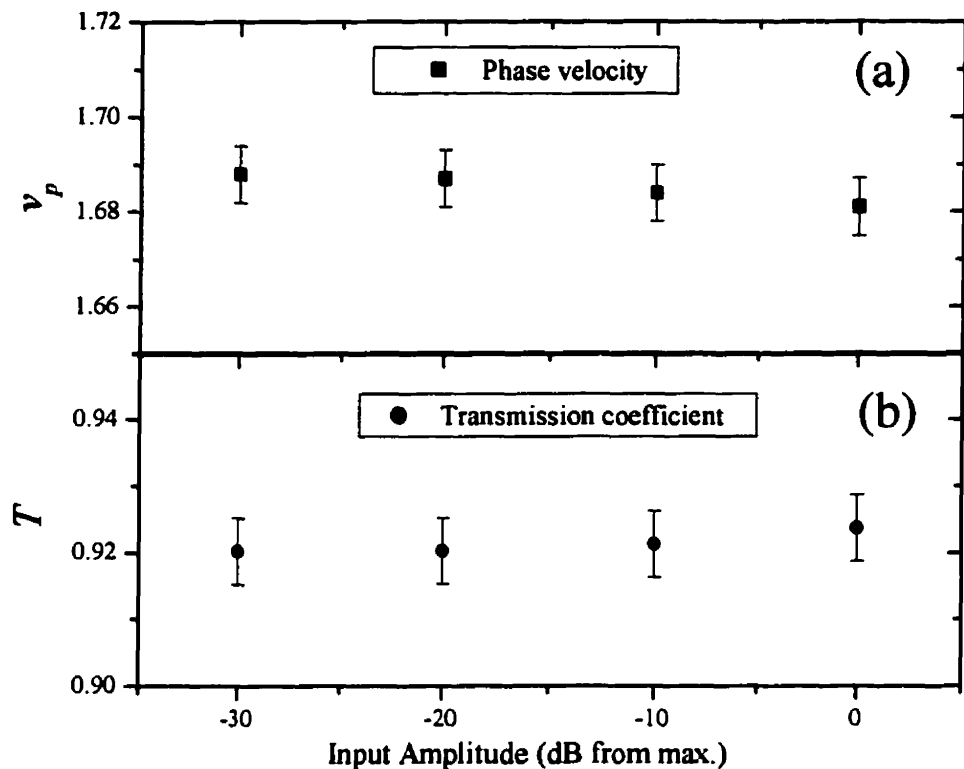


Figure 4.7.1: Dependence of (a) the phase velocity and (b) the transmission on the input amplitude.

The second method is perhaps a more sensitive probe. In practice this technique is somewhat complicated by the fact that the transducer has its first harmonic at this same double frequency. This means that there is some input sound at the doubling frequency, although its amplitude is smaller than at the main frequency by about 45dB. Therefore we must measure both the input pulse and the pulse transmitted through the sample, as a function of input amplitude, and look for an anomalous peak in the transmission at the doubling frequency. This is done in Fig. 4.7.2 for the same 0.5 MHz input pulse. If there were a frequency doubling peak, we would expect it to be at about 1.0 MHz, and to have

a width about twice that of the input pulse, or 0.06 MHz. There is no compelling evidence of such a peak in the data at the large amplitudes; if there is frequency doubling, it is at a level below -50 dB. Therefore, neither procedure was able to detect a significant non-linearity in the samples.

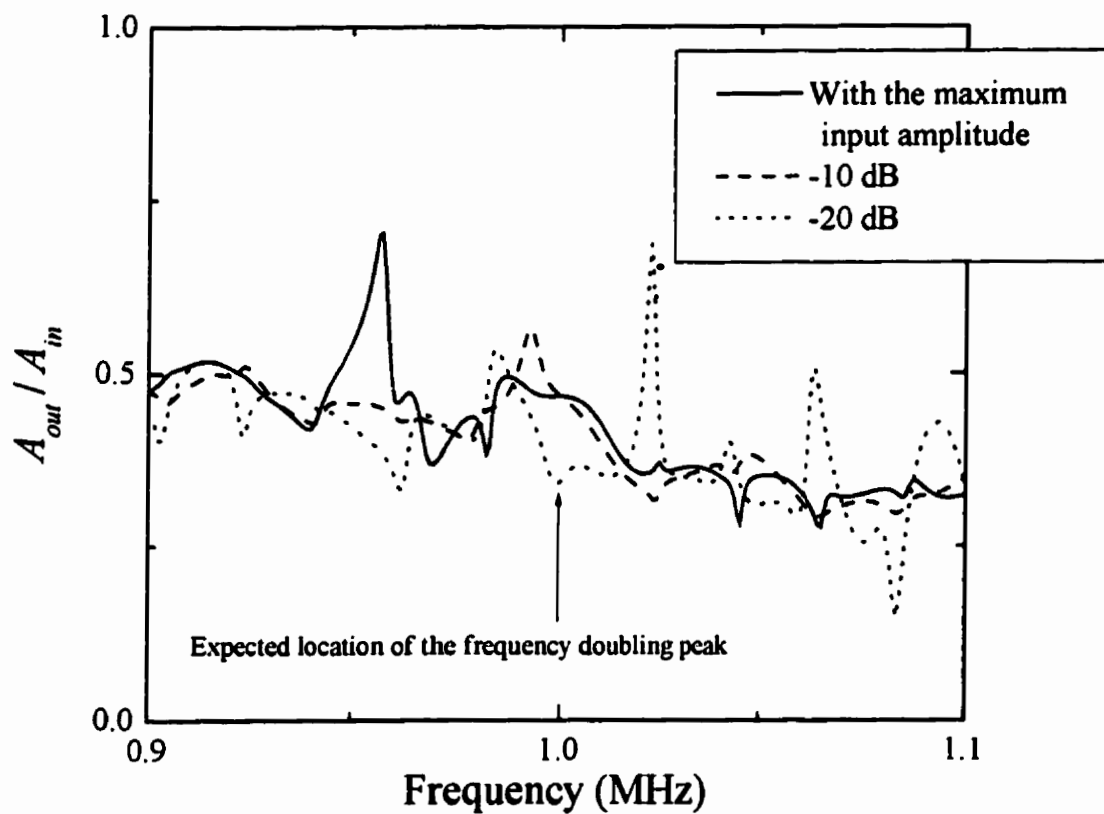


Figure 4.7.2: Ratio of the input and transmitted amplitudes near 1.0 MHz, for a primary excitation at 0.50 MHz. A_{in} at 1.0 MHz is 45 dB smaller than A_{in} at 0.50 MHz.

5. Results and Discussion

This section is split into three main parts. In the first part, the results of our wave propagation experiments, both ballistic and scattered, are discussed. In the second part, the ultrasonic correlation techniques (DAWS and DSS) are discussed in more detail, and various methods are tested and compared. The final part presents the results of the fluidized bed study, and discusses our interpretation of the data.

5.1 Wave Propagation

In this section, the results of our pulsed wave propagation experiments are presented, and discussed in light of the theory from Section 2. Section 5.1.1 deals with the ballistic measurements, while Section 5.1.2 presents the results of the measurements of the ensemble-averaged scattered intensity through our glass bead suspensions.

5.1.1 Ballistic Propagation in Glass Bead Suspensions

Using the experimental techniques described in Section 4.1.2, we investigated the ballistic propagation of ultrasound through samples with volume fractions of glass beads ranging from 0.045 to 0.61. We made a detailed study of the suspensions in the 75% glycerol/water mixture, measuring the velocities and mean free paths over a large range of frequencies and volume fractions, with the goal of stringently testing the spectral function approach used to calculate ballistic parameters [as reported in Cowan *et al.* 1998]. For the suspensions using the other two fluids, we only measured the ballistic properties needed for the DAWS and DSS experiments. Therefore, this section will focus on the system with the 75% glycerol/water solution, while the ballistic properties used in the DAWS/DSS study of the other two systems are listed in Appendix D, in Table D.1.

Some of our measurements of the phase velocity at four volume fractions are shown in Fig. 5.1.1, plotted as a function of reduced frequency. At the lowest volume fraction, the phase velocity is very close to the velocity of sound in the bulk fluid, indicated by the dashed line, over the entire frequency range. However as the volume fraction is increased, a stronger frequency dependence develops, reaching a maximum

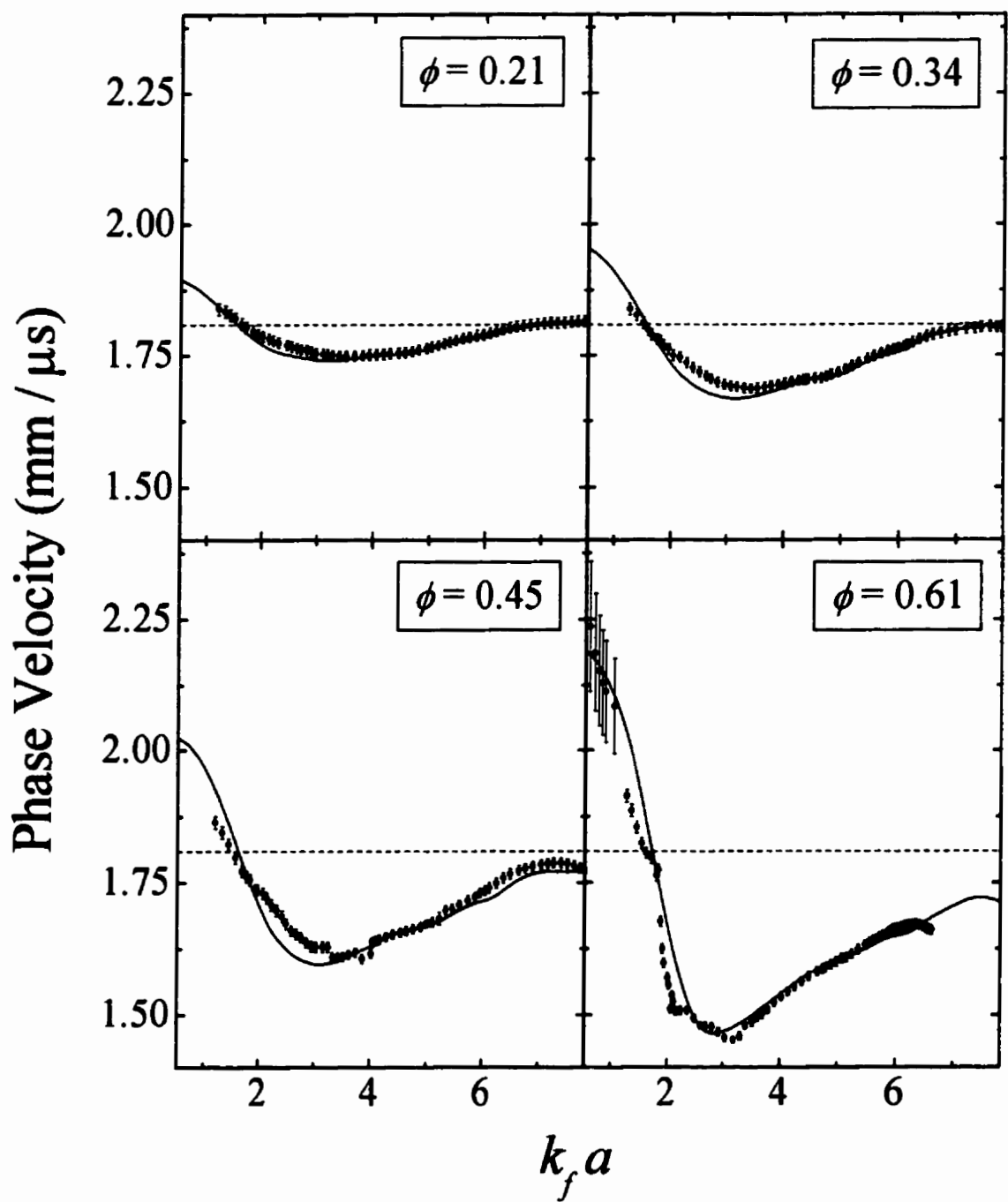


Figure 5.1.1: Phase velocity (points), and theory (lines), for a 75% glycerol/water glass bead suspension. k_f is the wave vector in the fluid, and a is the bead radius.

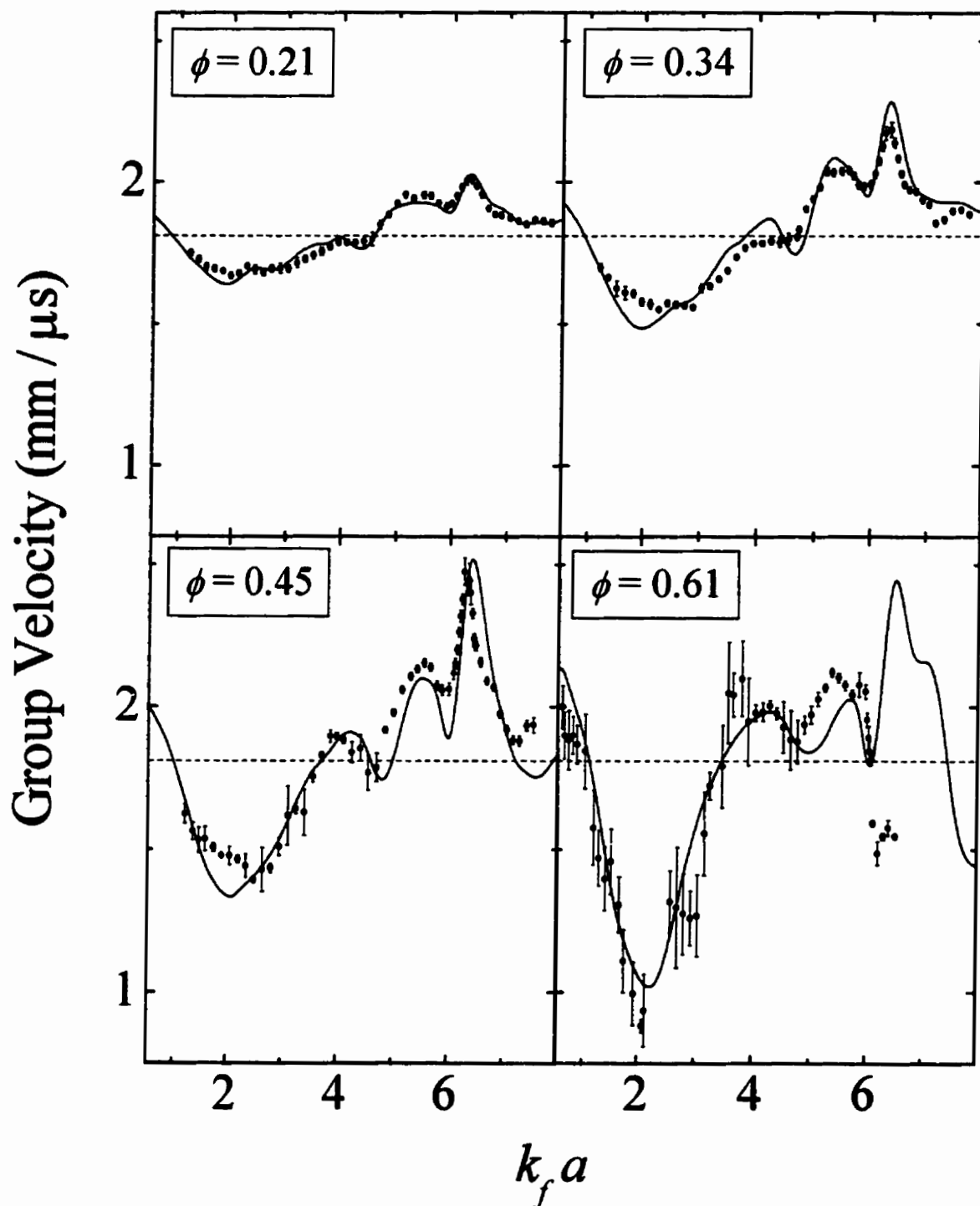


Figure 5.1.2: Group velocity (points), and theory (lines), for a 75% glycerol/water glass bead suspension. k_f is the wave vector in the fluid and a is the bead radius.

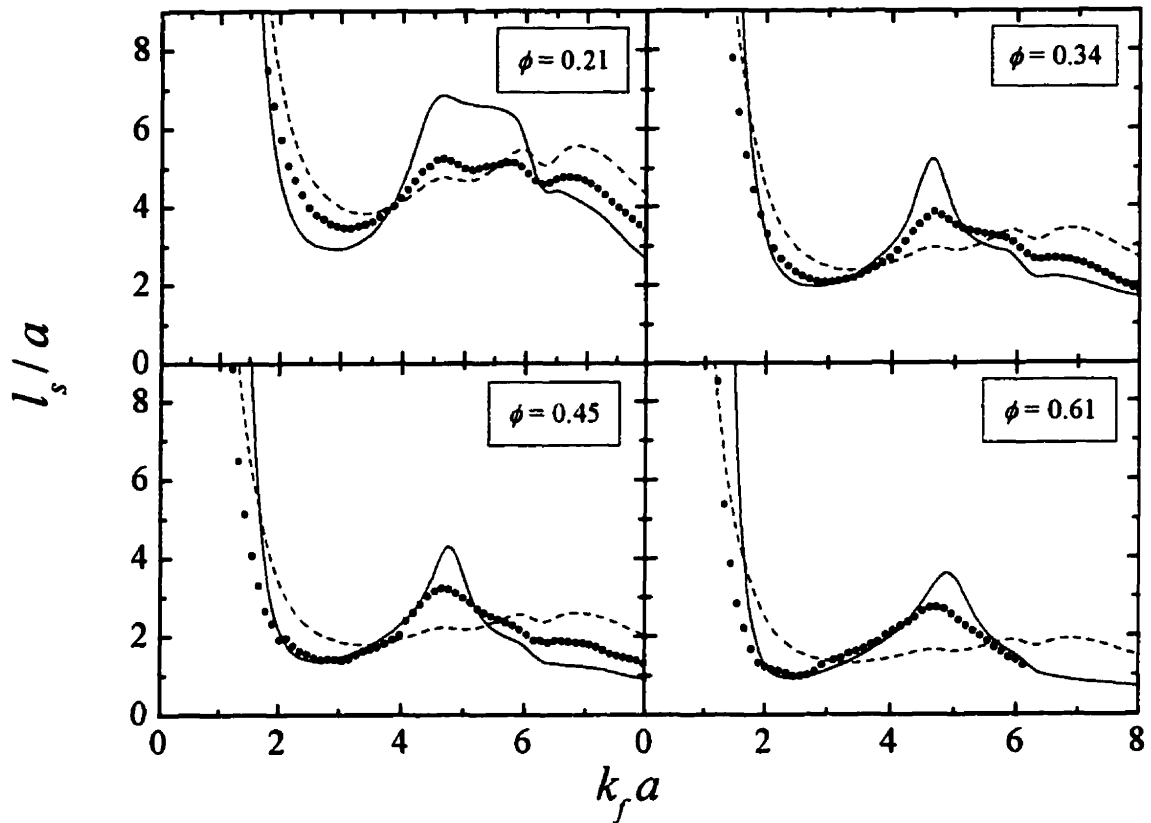


Figure 5.1.3: Scattering mean free path data (points), with effective medium theory (solid lines) and an isolated glass sphere in fluid calculation (dashed lines).

variation with frequency of about 40% at $\phi = 0.61$, which is about 7 times greater than at $\phi = 0.21$. Our group velocity data [Fig. 5.1.2] show the same volume fraction trends, with relatively little dependence on frequency at the lowest volume fraction but with progressively larger variations in the frequency dependence of the velocity as the volume fraction increases. The variation of the group velocity is in general much larger than that of the phase velocity; for the most concentrated sample the group velocity changes by more than a factor of two, reaching values less than 1 mm/ μ s near the rather sharp minimum at $k_f a \approx 2 - 2.5$. Near this minimum, the group velocity is well below all the bulk velocities of both the solid and fluid constituents of the sample, suggesting that the

scattering is having a strong effect on the ballistic propagation at the higher volume fractions. Measurements of the scattering mean free path [Fig. 5.1.3] shed further light on the connection between strong scattering and the propagation velocities. The scattering mean free path has a pronounced dip for $k_f\alpha$ between 2 and 3, which corresponds to the dips seen in both the phase and group velocities. This means that when scattering is at its strongest, the wave speeds of the ballistic pulse are greatly reduced. Careful inspection of the Fig. 5.1.3 shows that the position of the minimum in the mean free path moves to slightly lower frequencies as ϕ increases; the positions of the minima in the phase and group velocities also show the same trend, confirming that the reduction in the wave velocities is caused by scattering. The scattering mean free path data also indicate that the scattering in this system becomes very strong in this frequency range, as demonstrated by the fact that at the minimum in l_s for $\phi = 0.61$, the mean free path becomes smaller than one-half the wavelength of sound in the sample.

The results of these experiments show that despite the strong scattering, the group velocity is well behaved, exhibiting no anomalous properties such as negative nor infinite values, over the entire range of frequencies and volume fractions investigated. One of the most striking features of our experimental results is the strong volume fraction dependence of both velocities. At low volume fractions there is weak dispersion, i.e. the velocities have little frequency dependence, but as the volume fraction is increased the dispersion increases dramatically. At high volume fractions this strong dispersion is similar to that found in earlier experiments [Page *et al.* 1996] on randomly close packed ($\phi = 0.63$) glass beads in water. Our current results show clearly that the volume fraction

dependence of the dispersion seen in acoustic systems is opposite to that predicted for electromagnetic waves [Sheng *et al.* 1995, Busch *et al.* 1995 and Busch *et al.* 1996]. Thus the idea that the most dramatic dispersion effects should be observed at low volume fractions of scatterers does not apply in typical acoustic systems such as ours, a result which we now explain theoretically using the spectral function approach.

Using the model described in Section 2.1.3, we determined the phase velocity $v_p = \omega/k$ for each volume fraction of beads from the ratio of frequency to wave vector along the dispersion curve, giving the solid curves shown in Fig. 5.1.1. To account for the small 5% variation in the size of the glass beads, the theory dispersion curves were also averaged over the bead size distribution, which was essentially flat between the two sieve sizes used to sort the beads. Excellent quantitative agreement with the data is found at all volume fractions, with the theory correctly predicting the magnitude of the phase velocity, as well as both the frequency and volume fraction dependence. The group velocity $v_g = d\omega/dk$ is calculated by differentiating, with a small amount of smoothing to remove numerical noise, the dispersion curve to obtain the solid curves plotted in Fig. 5.1.2. Again very good agreement with the data is found, with the considerable structure in the frequency dependence of the group velocity being correctly predicted at all frequencies and volume fractions investigated.

The same theoretical model can be used to estimate the scattering mean free path, which is calculated from the scattering cross section of the coated elastic sphere [see Cowan *et al.* 1998]. This was determined in two equivalent ways, either from the peak of the spectral function (which is equal to the imaginary part of the reciprocal of the self

energy) through the use of the optical theorem, or by integrating the square of the scattering amplitude over all angles. Here the model is not as successful, as it underestimates the magnitude of the scattering because it assumes a uniform environment around each sphere, in contrast with the actual physical situation in which there are additional contributions to the scattering from the random configurations of the neighboring spheres. We account for this effect empirically by dividing the theoretical predictions by a phenomenological scaling parameter p_σ , which is taken to be independent of frequency and is obtained by fitting theory to experiment. This fitting parameter p_σ is found to range from 1.6 to 2 as ϕ increases from 0.2 to 0.6, consistent with exact multiple sphere scattering calculations that account explicitly for this additional scattering effect [Jing *et al.* 1992]. As shown by the solid curves in Fig. 5.1.3, reasonable agreement with the data is obtained, especially at high volume fractions, where the theory does an excellent job of predicting the location of the first minimum in the scattering mean free path. It is worth noting that the coated sphere calculation is much more successful in predicting the location of this minimum in l_s than is a calculation based on the scattering cross section of single bare glass sphere in water, shown by the dashed curves. This demonstrates the power of our effective medium technique in accounting for the multiple scattering effects that are very important at high volume fractions.

To explain the strong volume fraction dependence of the velocities seen in the experiments, we calculated the average energy densities as a function of frequency both inside the glass beads and in the fluid coating. This calculation is described in Cowan *et al.* [1998], and the results at $\phi = 0.61$ are shown in Fig. 5.1.4. The average energy

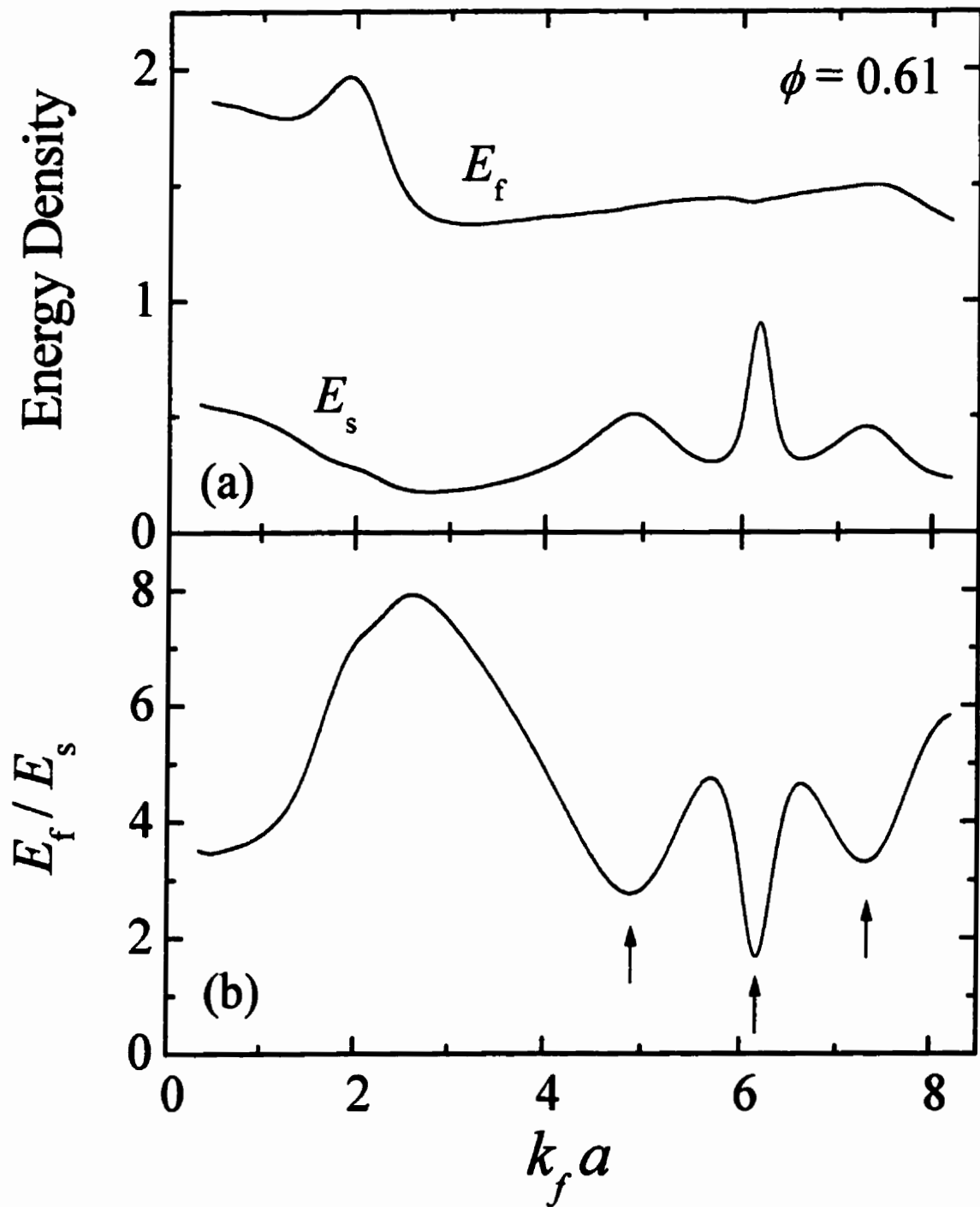


Figure 5.1.4: (a) Average energy density in the solid and fluid.
(b) The ratio of the fluid to solid energy density. The arrows correspond to the three minima in the group velocity.

densities, normalized by the energy density of the incident wave, are plotted in Fig. 5.1.4(a). This figure clearly demonstrates that the energy density in the fluid layer is much higher than in the solid spheres at all frequencies, and delineates the structure in the frequency dependence that results from the scattering. While the normalized energy density in the fluid layer shows only a weak dependence on frequency at high frequencies, E_f is seen to exhibit a maximum near $k_f a \approx 2$, corresponding to the resonant condition that the wavelength in the fluid layer λ_f equals half the circumference of the solid sphere. As expected, this resonance weakens as the volume fraction decreases, and the size of the fluid pockets between the beads increases. By contrast, the energy density in the glass beads E_s exhibits three peaks at higher frequencies, which correspond to resonant scattering by the solid spheres. By comparing Fig. 5.1.4(a) with Fig. 5.1.2, it can be seen that the peaks in E_s correspond to the high frequency minima of the group velocity, indicating that strong resonant scattering can indeed slow down the propagation of acoustic waves. However, it should also be noticed that there is no resonant scattering in the spheres associated with the first and the largest dip in the group velocity. Instead, the energy density ratio E_f/E_s exhibits a strong peak at that frequency, seen in Fig. 5.1.4(b), indicating that most of the wave energy is trapped in the fluid layer. This is clearly delineated in Fig. 5.1.5, where the energy density in a liquid-coated solid sphere, embedded in the renormalized effective medium, is plotted as a function of position for $k_f a = 2.6$. In this frequency regime, the trapping of wave energy in the fluid causes wave propagation to slow down via a different physical mechanism: here the slowdown is due to the tortuosity of the connected fluid pathways rather than resonant scattering by the solid

spheres.

This microscopic picture of wave propagation in our acoustic system also provides the basis for understanding why the volume fraction dependence of the dispersion is opposite to that found for electromagnetic waves [Sheng *et al.* 1995, Busch *et al.* 1995 and Busch *et al.* 1996]. For electromagnetic waves, the velocity inside the solid scatterers is normally lower than in the surrounding medium, since the scatterers usually have the higher dielectric constant. Consequently, in the vicinity of Mie resonances the electromagnetic energy density is very large inside the scatterers and small outside. At low ϕ , this leads to a long dwell time of the waves inside the scatterers, and large dispersion effects. However, as ϕ increases, the resonances become smeared out, as the wave energy that is predominantly concentrated in the scatterers couples from one scatterer to the next, and the dispersion is reduced [Sheng *et al.* 1995, Busch *et al.* 1995 and Busch *et al.* 1996]. By contrast, in our acoustic experiments the velocities of the elastic waves inside the solid scatterers are higher than in the surrounding medium, causing most of the wave energy to be concentrated in the fluid, as seen in Fig. 5.1.4 and 5.1.5. Consequently, the two mechanisms that lead to wave dispersion in the acoustic case, tortuosity slowdown and resonant scattering in the spheres, are both more effective at high volume fractions of scatterers. It should be clear that the tortuosity effect is most pronounced at larger values of ϕ , since the tortuosity of the fluid pathways increases with the volume fraction of scatterers as the pockets of fluid surrounding the scatterers shrink in size. Moreover, the effect of the resonant scattering in the spheres is to divert some of the wave energy from the fluid into the spheres, where the waves become partially

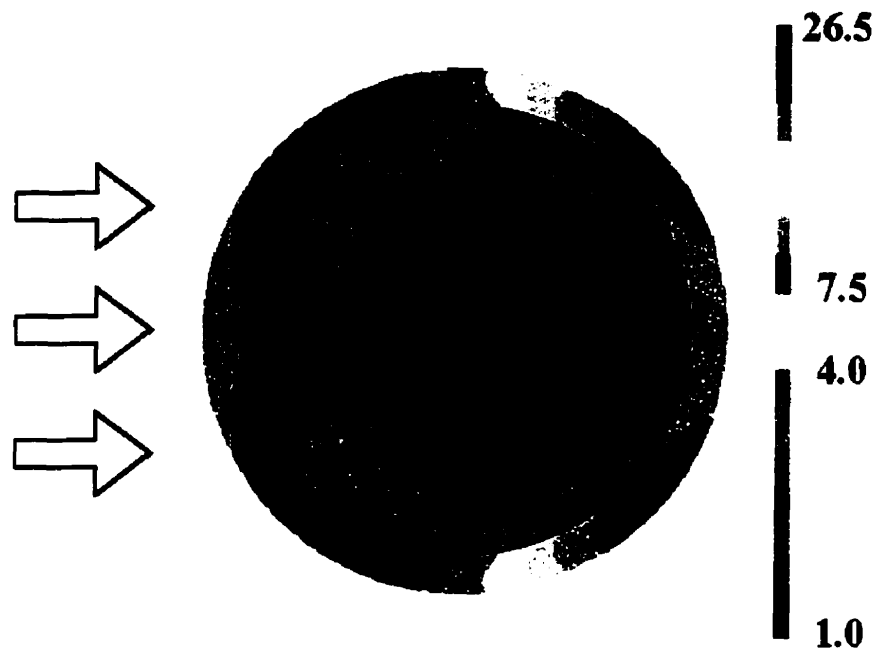


Figure 5.1.5: Spatial distribution of the sound energy density in a coated sphere scatterer embedded in the effective medium.

trapped, thus also slowing the propagation. However, for acoustic waves the majority of the wave energy still remains in the fluid, and as a result the resonances do not become washed out at high volume fractions. As ϕ increases, the waves spend a greater fraction of their time partially trapped in the spheres simply because there are more of them; thus the magnitude of the dispersion increases correspondingly, in agreement with our experiments.

5.1.2 Scattering in Glass Bead Suspensions

The main goal of our measurements of the ensemble-averaged scattered intensity was to extract diffusion parameters for use in the interpretation of DAWS. To relate the field autocorrelation function to the relative mean square displacement of the beads, the transport mean free path and one of either the diffusion coefficient or energy velocity must be known. As mentioned previously, pulsed transmission measurements give information about the diffusion coefficient and the absorption time in the sample, but do not yield accurate information about the transport mean free path or energy velocity. The transport mean free path can be measured directly through total transmission measurements as a function of sample thickness; however this is difficult in ultrasonics, although it has been done by Schriemer *et al.* [1997] for randomly close packed glass beads in water. These experiments agree well with the theory discussed in Section 2.2.3, which relates the transport mean free path to the ballistic scattering mean free path, and the energy velocity to the group velocity. Therefore, the approach we take in this thesis is to use this theoretical model to calculate the transport mean free path and energy velocity, given the measured ballistic parameters. In this section I will present the results of independent measurements of the diffusion coefficient, and check if the results of the calculations and measurements are consistent with Eq. (2.46), which relates the three quantities.

The ratio of the transport mean free path to the scattering mean free path at two volume fractions has been calculated and plotted in Fig. 5.1.6, for the frequency range over which DAWS data was taken. The differences between the scattering and transport mean free paths arise due to anisotropic scattering. Depending on the volume fraction, the

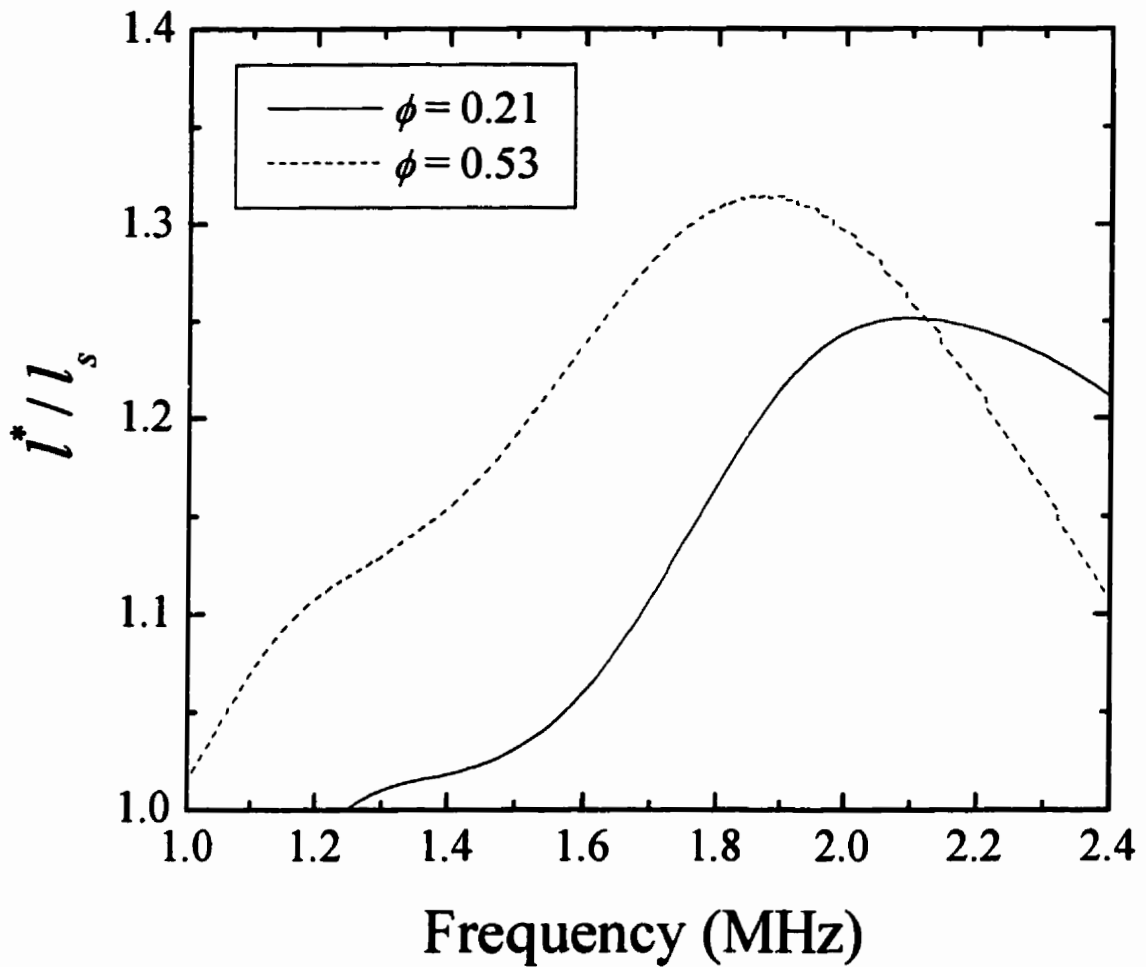


Figure 5.1.6: Calculated ratio of the transport to scattering mean free paths.

ratio approaches 1, corresponding to essentially isotropic scattering, at frequencies lower than about 1.0 to 1.2 MHz, and has a peak value of 1.2 to 1.3 near a frequency of 1.8 to 2.2 MHz. Using this calculated ratio, and the scattering mean free path measured in our ballistic experiments, the transport mean free path in our samples can be estimated. Figure 5.1.7 shows the calculated ratio of the energy velocity to the group velocity at the same two volume fractions. Again, the ratio approaches one at low frequencies (~ 1.0 MHz), but at higher frequencies the velocity ratio is less than one. The ratio also approaches one

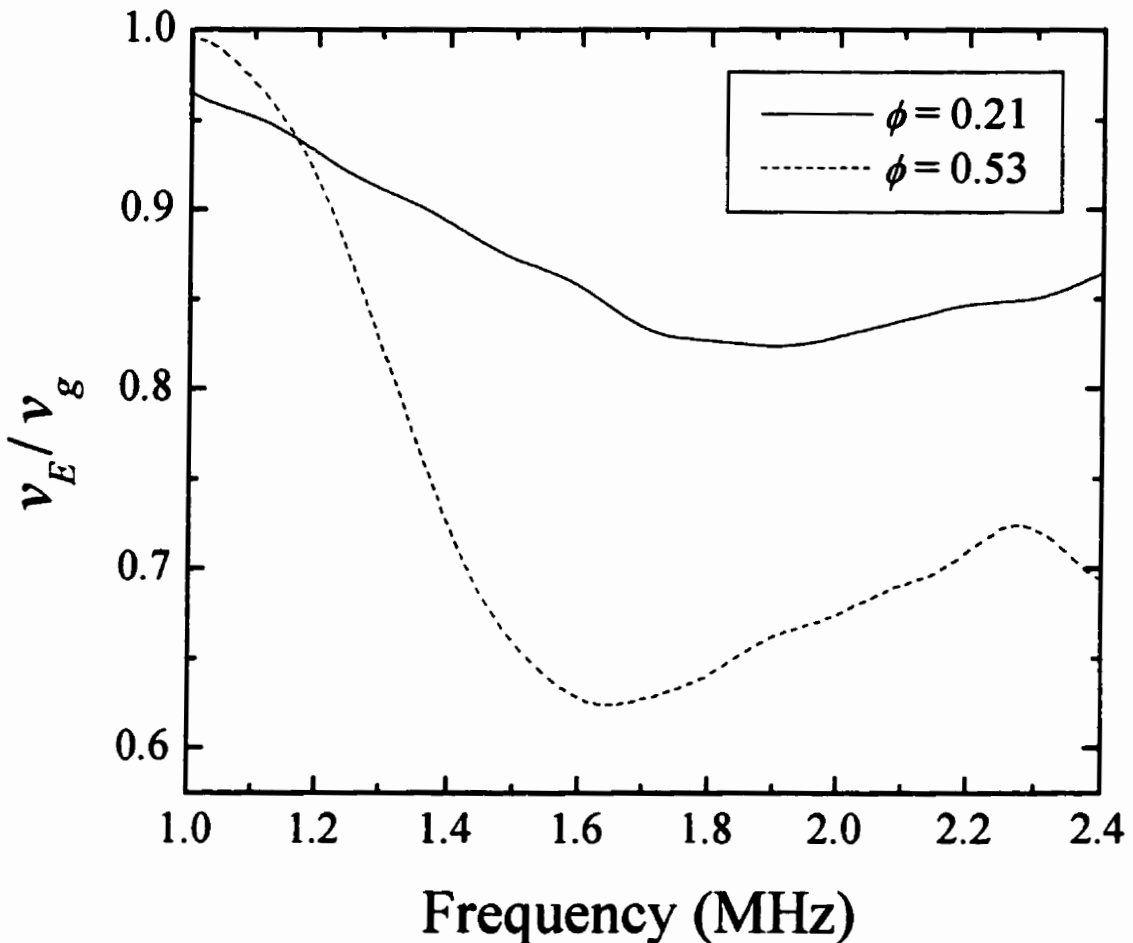


Figure 5.1.7: Calculated ratio of the energy to group velocities.

as the volume fraction gets smaller, because the transport mean free path is larger, reducing the importance of the scattering delay (which does not depend strongly on volume fraction) relative to the travel time between the scattering events [c.f. Eq. (2.56)].

The ensemble-averaged scattered intensity transmitted through our suspensions was measured over a wide range of frequencies and volume fractions using the technique discussed in Section 4.1.3. To illustrate the main results, I will focus on the experiments on the samples with a 75% glycerol/water fluid, and with thicknesses of $L_z = 12.8$ and 36.5

mm. The data for each sample and frequency were fit using diffusion theory and the appropriate boundary conditions [Section 2.2.2]. In these fits, we used the calculated values of the transport mean free path and group velocity in the determination of the boundary conditions, i.e. $z_o \sim l^*$, the distance into the sample at which diffusion begins, and the time at which diffusion begins, z_o / v_g . However, the fits were quite insensitive to the values of the transport mean free path and group velocity that were used. The fitting parameters were the diffusion coefficient, the absorption time, and the overall amplitude factor. Some examples of the data and fits for the samples with $L_z = 12.8$ mm are plotted in Fig. 5.1.8, while examples with $L_z = 36.5$ mm are plotted in Fig. 5.1.9. All of the data rise to a peak intensity at fairly early times, and then exponentially decay with time constants that depend on both the diffusion coefficient, absorption time and sample thickness. For the $L_z = 12.8$ mm sample, the data for two volume fractions are plotted at several different frequencies. The peak scattered intensity ranges from about 10^{-2} to 10^{-4} times the input intensity, with the intensity of the scattered sound getting smaller as either the frequency or the volume fraction is increased. This occurs because the scattering is stronger (i.e. the mean free path is smaller), which leads to the input intensity spreading out more in both space and time. The time corresponding to the peak intensity generally increases as the mean free path gets smaller, because the diffusion coefficient also gets smaller. However, in the presence of absorption the peak time is no longer $\propto L_z^2/D$, but is strongly dependant on τ_s , which decreases with frequency and volume fraction. This is

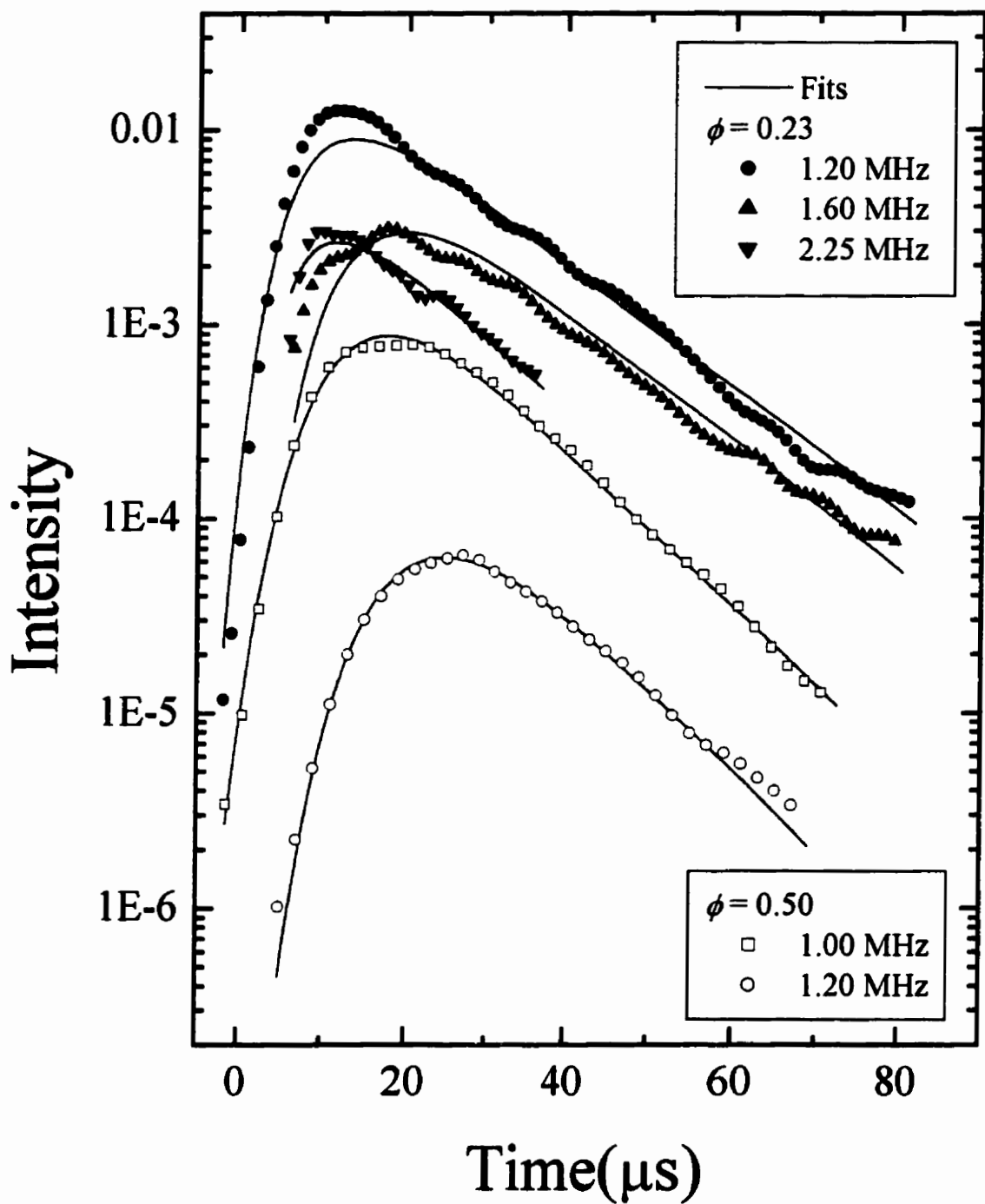


Figure 5.1.8: Measured ensemble-averaged scattered intensity (symbols) and fits of diffusion theory (lines) for $L_z = 12.8$ mm.

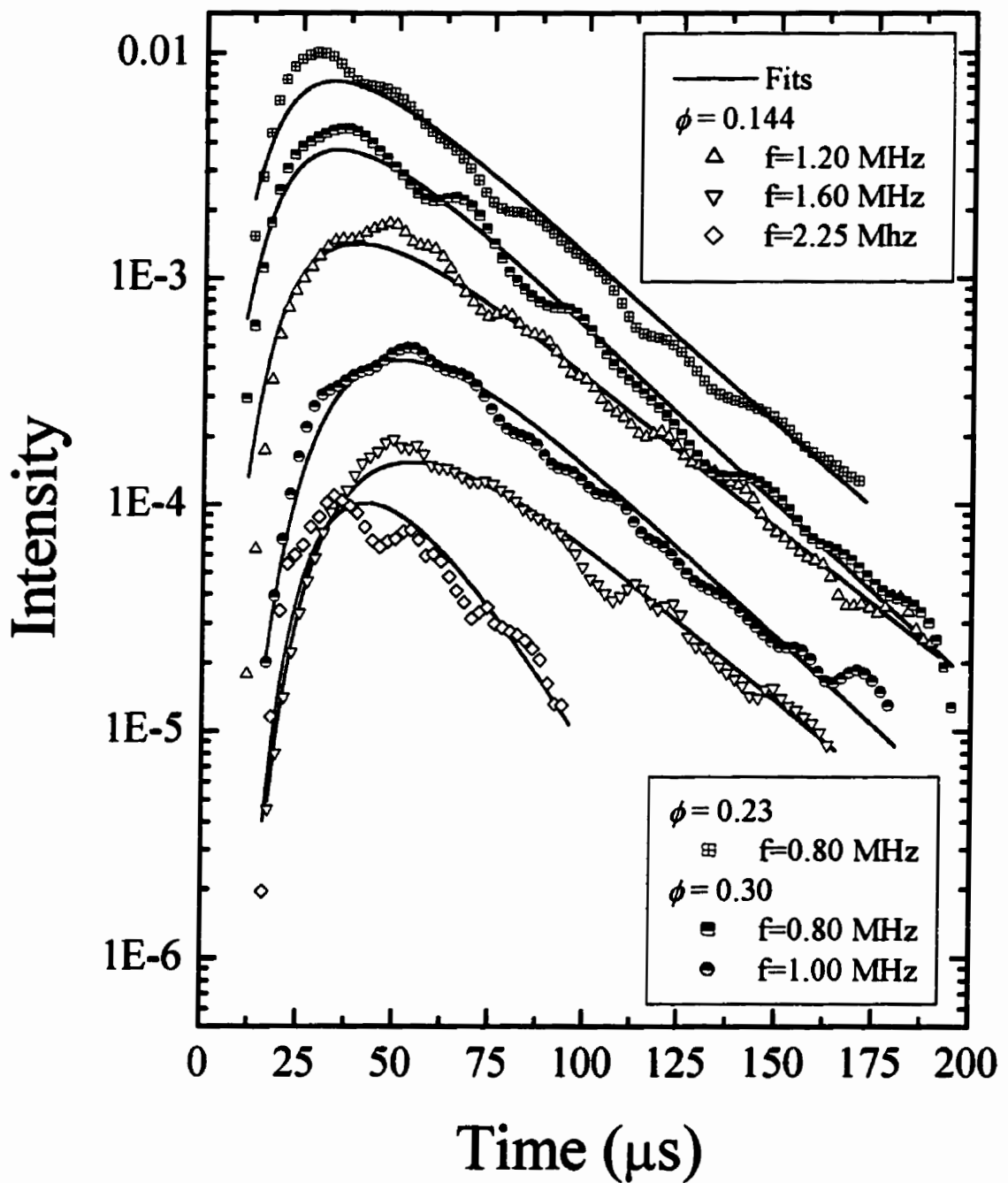


Figure 5.1.9: Measured ensemble-averaged scattered intensity (symbols) and fits of diffusion theory (lines) for $L_z = 36.5$ mm.

why the $f = 2.25$ MHz data peak so soon and decay so quickly relative to the 1.6 MHz data, even though D is similar at the two frequencies. The $L_z = 36.5$ mm data show the same basic trends, but now the peak intensity arrives at a later time, and the time it takes the intensity to decay is also longer. Diffusion theory captures the data quite well, with the weighted $\chi^2 \sim 1$ for most of the fits; however the theory does have some problems accurately fitting the initial rise and peak for some of the data sets. Nonetheless, the diffusion coefficients are accurately determined from the fits to the time profiles. Note that in these fits we have only considered data from effectively thick samples ($L_z/l^* > 4$), where the diffusion approximation is expected to work [Zhang *et al.* 1999].

The diffusion coefficients are shown in Fig. 5.1.10, with the measured diffusion coefficients (from the fits) plotted against the theoretical diffusion coefficient expected from the calculated values of the transport mean free path and energy velocity. The calculated values are based on the measured scattering mean free paths and group velocities, which lead to the error bars shown. The measured diffusion coefficients have uncertainties from the fits, which are estimated to be 15%. The measured and theoretical values agree quite well within error bars over a large range of D , with only a few anomalous points lying significantly above the line for $D < 1$ mm²/μs. In the region where the data from the thick and thin samples overlap ($D \sim 0.7$ to 2 mm²/μs), the measured diffusion coefficients are in agreement with each other.

Figure 5.1.11 shows the measured absorption lengths ($l_a = \tau_a v_E$) as a function of volume fraction, for several frequencies. The absorption length decreases (i.e. the absorption becomes stronger) as the volume fraction is increased, suggesting that the

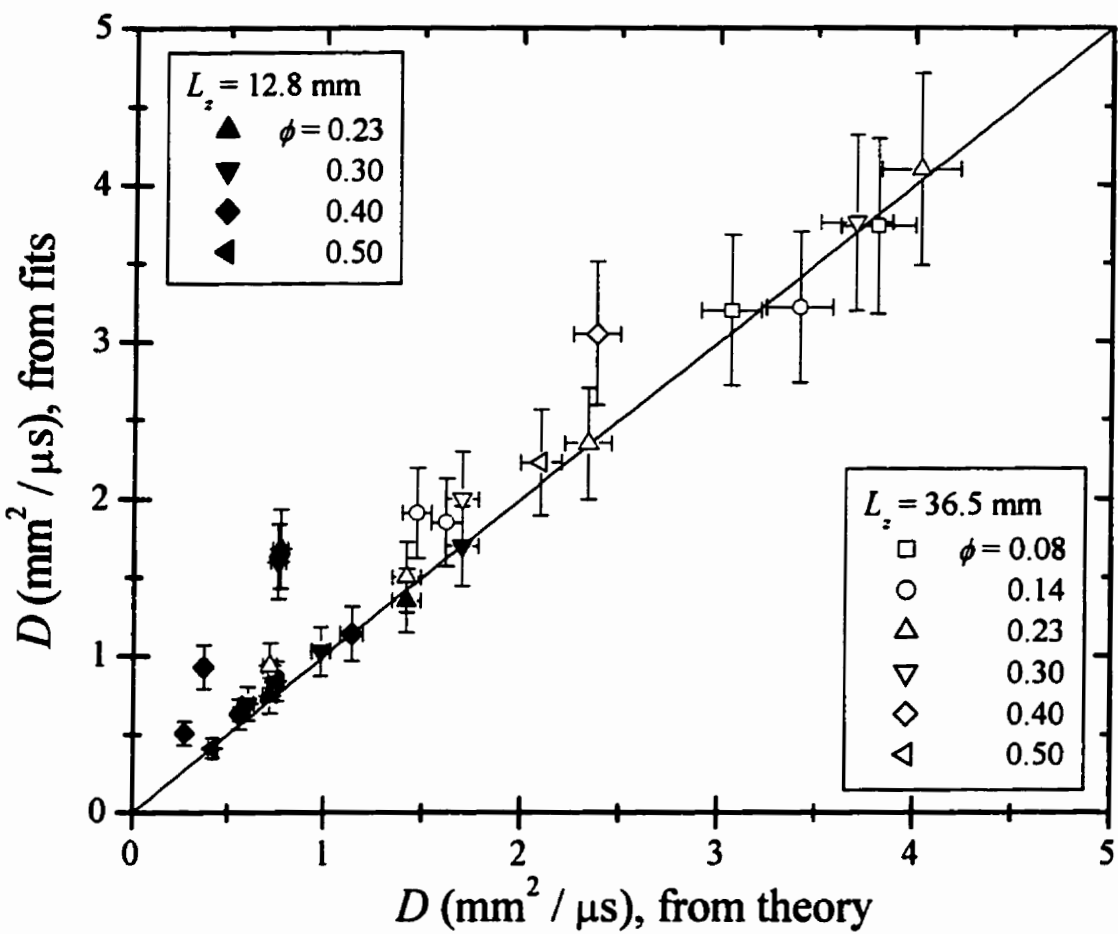


Figure 5.1.10: Diffusion coefficients from the fits plotted versus the theoretical calculations.

absorption is largely interfacial, since we expect that the bulk absorption in the fluid is actually larger than it is in the glass. The other possible explanation, i.e. that the bulk absorption in the glass beads dominates, is discounted by the fact that we find that the absorption in the suspensions with less viscous fluids is weaker than that in higher viscosity suspensions. Since interfacial absorption will be stronger at higher viscosity, while the bulk absorption in glass does not depend on the fluid properties to first order, this means that the observed viscosity dependence is consistent with the dominance of

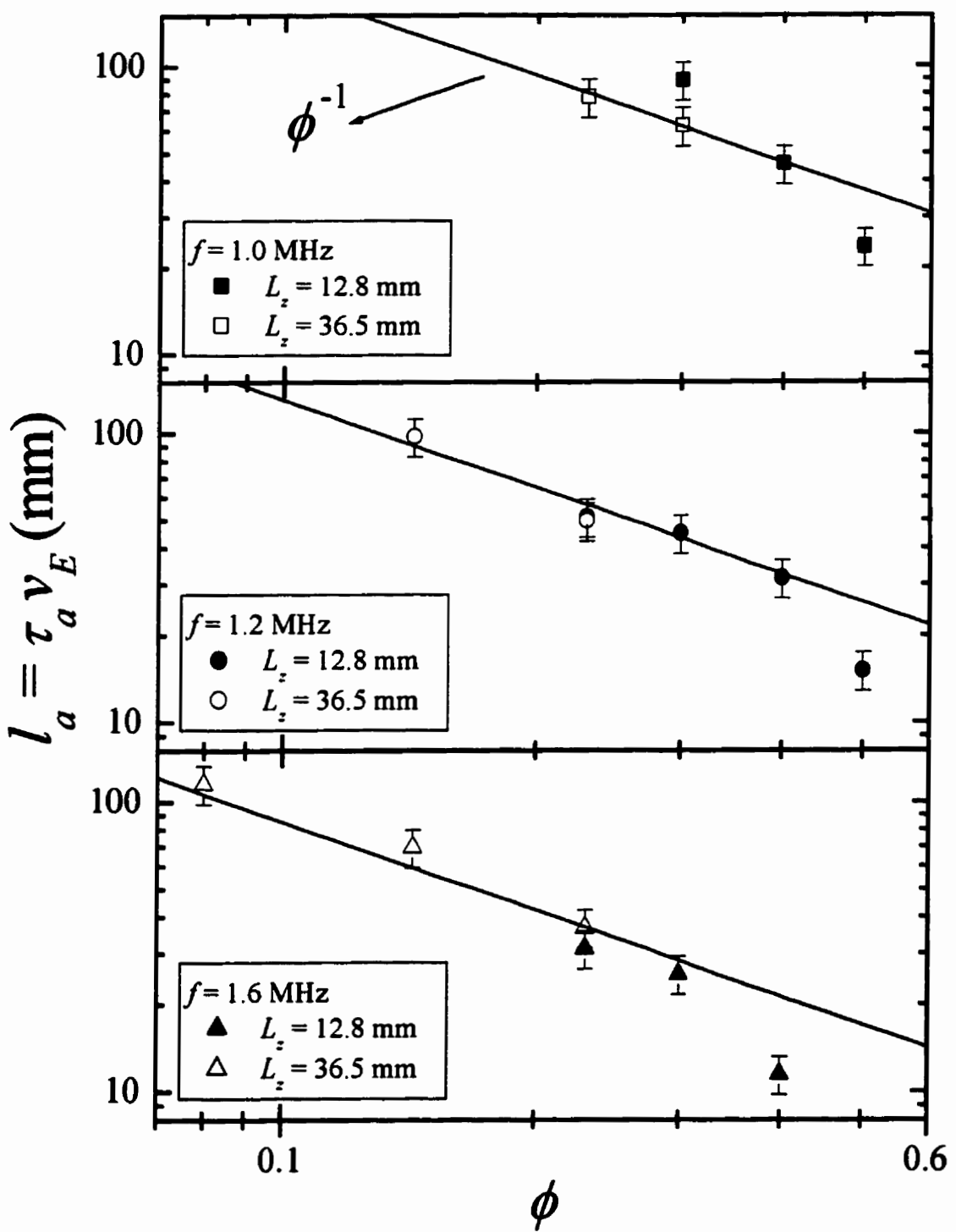


Figure 5.1.11: Absorption lengths vs. volume fraction at three different frequencies along with fits of ϕ^{-1} to the data.

interfacial effects. Also, note that the absorption in the suspension is substantially stronger than the absorption in the bulk fluid ($l_f > 200$ mm). The absorption lengths have an approximately ϕ^{-1} dependence on the volume fraction at lower volume fractions, while they decrease more quickly at the highest volume fractions. The ϕ^{-1} dependence is consistent with an interfacial absorption mechanism, since the strength of the absorption should be proportional to the amount of surface area in the sample, which is proportional to the number of particles and thus to ϕ . At larger ϕ other mechanisms may be introduced, due to the narrow channels and rubbing contacts between the glass beads, leading to the observed increase in the absorption. For completely rigid spheres in a fluid, Temkin [1996] predicts that in the low frequency and volume fraction limit the absorption length has a f^{-2} dependence on frequency. For elastic spheres, Hinders [1991] derives theoretical expressions for the absorption length by solving the boundary value problem, including the damped shear waves in the surrounding fluid, resulting in a f^{-1} dependence in the low frequency ($k_f a \ll 1$) and volume fraction limit. However, our data are in the intermediate frequency regime ($k_f a \sim 1$), as shown in Fig. 5.1.12, where the coefficients of the low volume fraction ϕ^{-1} fits from Fig. 5.1.11 are plotted versus normalized frequency. In this frequency regime, resonant modes in the elastic spheres could in general have a strong effect on the absorption [Hinders 1991]. We find a frequency dependence which lies between f^{-1} and f^{-2} in our suspensions with $\phi < 0.40$, whereas for randomly close packed glass spheres in water, a $1/f$ dependence has been found over a similar frequency range [Page *et al.* 1995, Weaver & Sachse 1995], indicating once again that the character of the absorption changes at high volume fractions.

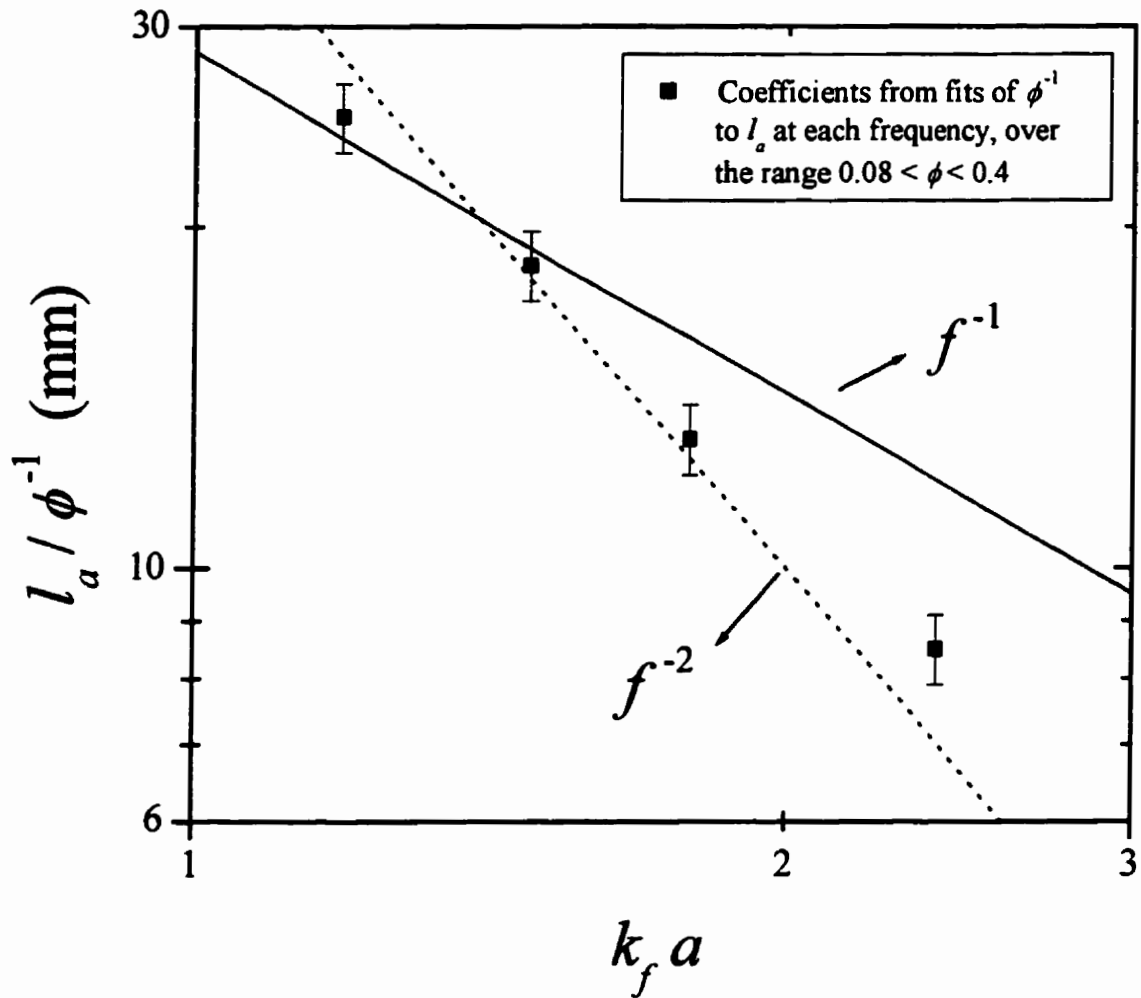


Figure 5.1.12: Absorption lengths vs. frequency.

Diffusion theory describes propagation through our samples well, provided that they are thick compared to I^* ($L_z/I^* > 4$) [Zhang *et al.* 1999]. Further, the model used to relate the ballistic parameters to the diffusive parameters works quite well over a large range of volume fractions. This justifies the use of the calculated energy velocity and transport mean free path in the interpretation of DAWS data.

5.2 Spectroscopy Techniques

The results of tests of the self consistency of DAWS and DSS are presented, and different methods are compared. The phase probability measurements are compared to theory, and the results are discussed. Finally, the Siegert relation is tested for pulsed and continuous wave inputs, and for singly and multiply scattering paths through the sample.

5.2.1 Diffusing Acoustic Wave Spectroscopy

In this section, the results of tests of the approximations used in DAWS are discussed, and a comparison is made between plane wave and point source input wave geometry.

5.2.1.1 Test of the Approximations

To test the approximations made in the derivation of Eq. (2.75), (the basic equation used to find the relative mean square displacement from the field correlation function) we measured the field correlation function at different sampling times or path lengths. By comparing the relative mean square displacements calculated from our data using Eq. (2.75), we can test whether the term introduced by the first and last scattering events is negligible [Eq. (2.72)]. This also allows us to test the basis of pulsed DAWS, namely that the field correlation time varies linearly with the number of scattering events.

Figure 5.2.1 shows two examples of test data, taken in our thinnest sample at two different volume fractions. The data sets with large numbers of scattering events (n) agree quite well with one another at early times. Also note that each data set agrees with

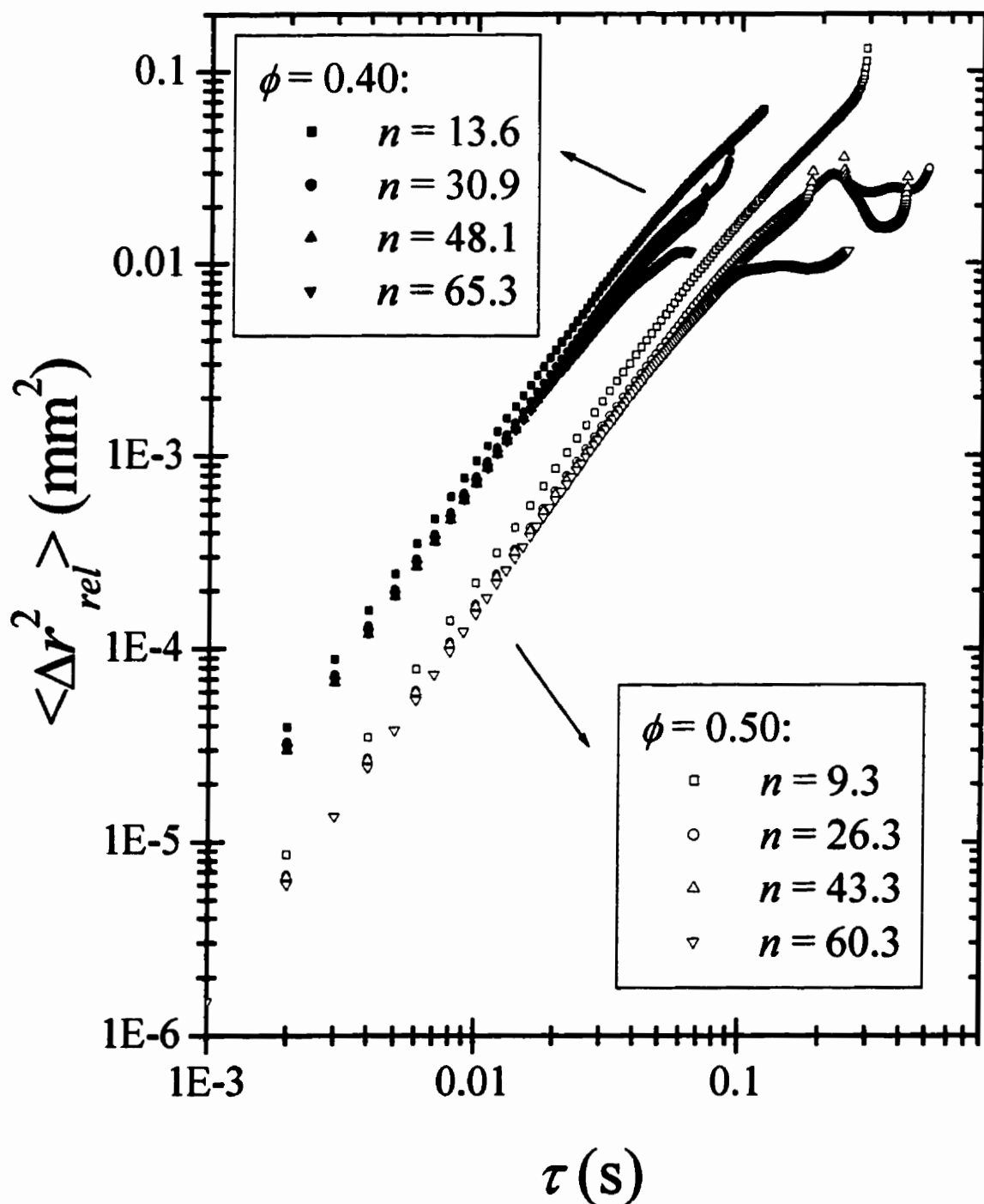


Figure 5.2.1: Comparison of DAWS measurements at different sampling times (or number of scattering events n) for two volume fractions.

the others at late times, up until the time at which the data set reaches its own particular noise threshold, where it levels off. However, as the number of scattering events gets to be less than about 20, there is a noticeable deviation from the data sets with larger n . This is explored in more detail in Fig. 5.2.2, where the relative mean square velocities extracted from the curves in Fig. 5.2.1 are plotted versus the number of scattering events. For $n > 20$ the differences caused by the $1/n$ correction term in Eq. (2.72) are small (< 5%) and not overly important when compared to other sources of uncertainty (e.g. the transport mean free path and energy velocity). However as n gets smaller, the influence of the correction term becomes clear. To check the magnitude of the correction term we fit the data with the form expected from Eq. (2.72). For the 50% volume fraction data, the relative velocity on the length scale of the sample (the average distance between the first and last scatterings) from the fit was 5.0 mm/s, compared to the independently measured values of 3.1 mm/s at a separation of $L = 5.4$ mm, and $\sqrt{2} V_{ms} = 7.6$ mm/s for separations larger than 22 mm (the correlation length). Thus the value extracted from the fit is reasonable, since the average distance between the first and last scattering events should be somewhat larger than L_z .

All of the DAWS data used in this thesis consist of at least two data runs, measured at two different sampling times. Both of the sampling times used were late, corresponding to long paths, thereby improving the approximations. The results from the two sampling times were compared, and generally were in quite good agreement with each other. By taking data at two different (late) times for all of our data, we ensured that the DAWS approximations held, and therefore that the data are meaningful. We were also

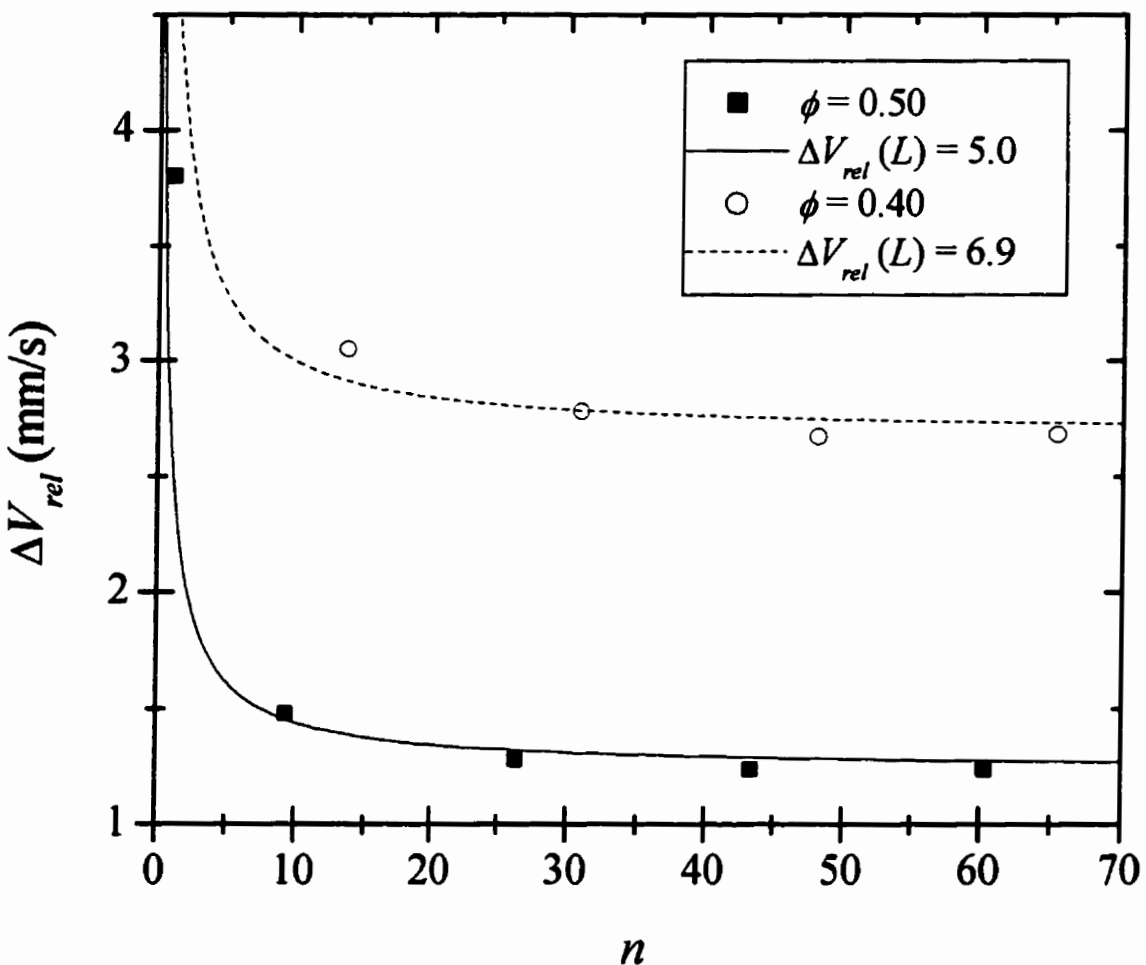


Figure 5.2.2: Measured rms relative velocity versus number of scattering events n . The fits shown are from Equation (2.72).

able to use the agreement between the two sampling times to help in calculating the component of the error bars due to the $1/n$ correction term. It also should be noted that these results mean that it is straightforward to use pulsed DAWS on samples that are less thick than the four mean free paths that are needed for the diffusion approximation to accurately determine the distribution of path lengths. One need only set the sampling time,

or equivalently the path length, to be long enough that the sound that is detected has undergone more than 20-25 scattering events. This is in contrast to the situation with continuous wave DAWS or DWS, where in order to examine thin samples one must go beyond the diffusion approximation, by using radiative transfer theory or the telegrapher equation to take the short paths into account [MacKintosh & John 1989 and Lemieux *et al.* 1998].

5.2.1.2 Comparison of Transmission Techniques

Most of the DAWS data taken in the experiments reported in this thesis used plane wave input pulses. However, occasionally a focusing transducer was focused on the sample face, giving a point source input wave. The advantage of a point source is that there is more signal, since all of the input energy is focused down on a small spot, instead of spread out in a quasi-plane wave. Therefore, when the signal to noise ratio was too small with a plane wave transducer, a point source transducer could be used to record more reliable data. In addition to demonstrating the feasibility of extending the signal to noise by using a point source, by comparing the results from the two different input geometries, we are testing the robustness of the DAWS technique itself. Note that ideally the analysis of the pulsed DAWS technique does not depend on the input geometry; all that is needed is the average length of the scattering paths the are being measured.

In Fig. 5.2.3, the relative mean square displacements calculated from point source and plane wave DAWS data are compared. Three different volume fractions are shown, and there is quite good agreement in all three cases. The primary differences are at early times, where noise may be more of a problem and can lead to the bending over of

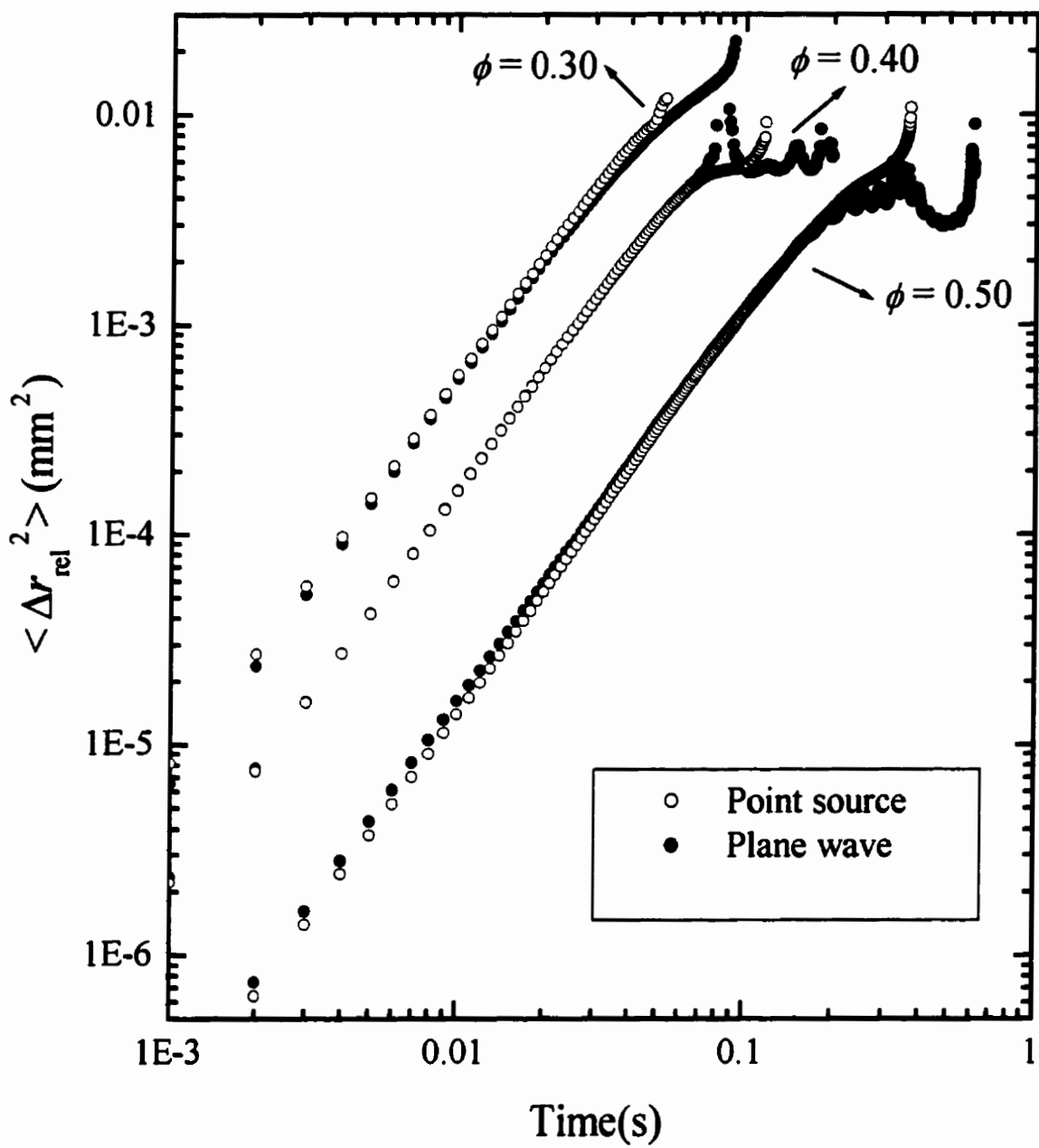


Figure 5.2.3: Comparison of DAWS experiments that used point source (open) and plane wave (closed) inputs.

the mean square displacement that is evident in the 50% plane wave data [Sec. 4.3.1].

These data show that focusing transducers can be used to increase the signal to noise ratio in DAWS, if necessary. The data also provide another test of the theory and approximations that underlie the technique, by showing that the pulsed DAWS technique does not depend on the input geometry in practice as well as in theory.

5.2.2 Dynamic Sound Scattering

5.2.2.1 Test of the Far-Field Technique

To test the self consistency of the far-field DSS techniques, we measured the root mean square velocity for several intermediate directions of \vec{q} , and compared the results to those calculated from the measurements of the three principle components. An example of the result is plotted in Fig. 5.2.4; the measurements were done with \vec{q} lying in two

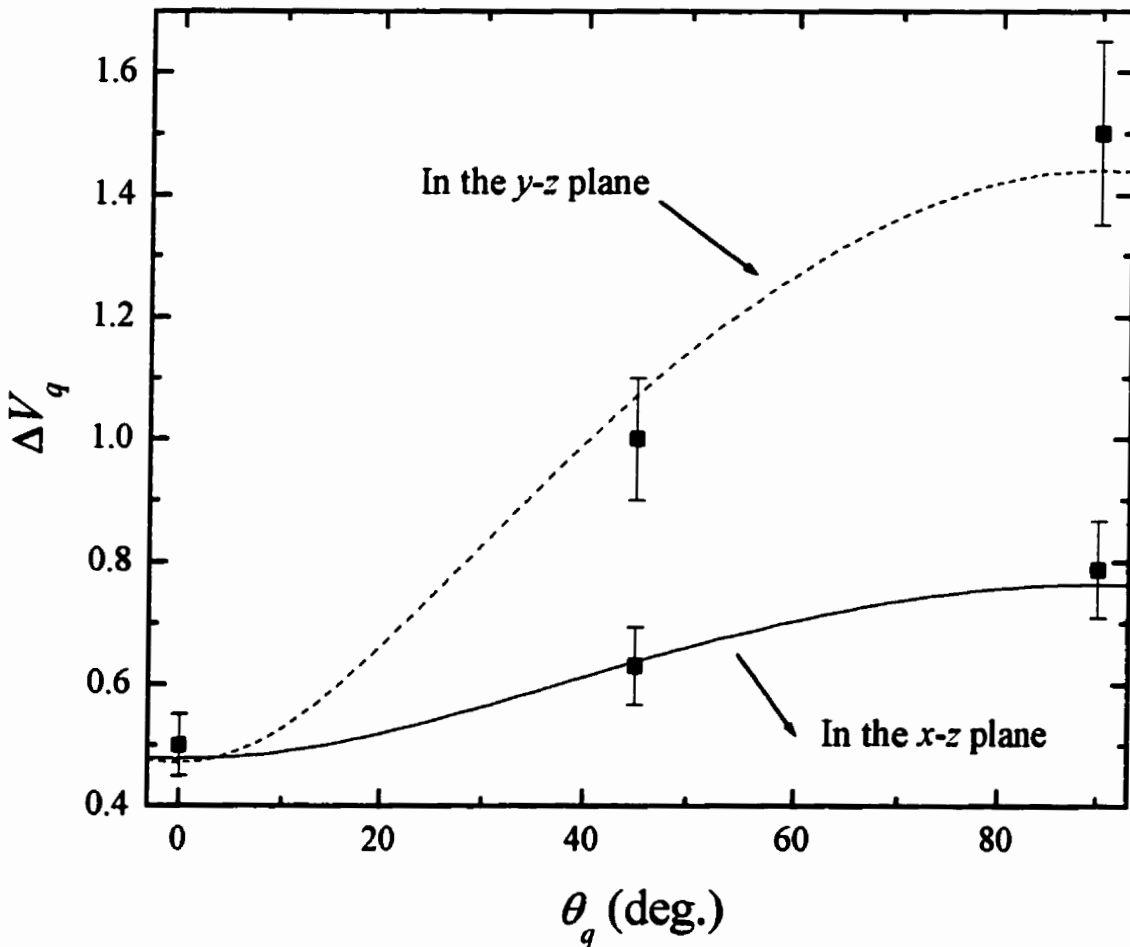


Figure 5.2.4: Test of the far-field technique at a low volume fraction. The lines indicate the expected behavior in the two planes.

planes, the x - z plane and the y - z plane. The lines in the graph are fits of,

$$\Delta V_{\vec{q}} = \sqrt{\Delta V_{x \text{ or } y}^2 \sin^2 \theta_{\vec{q}} + \Delta V_z^2 \cos^2 \theta_{\vec{q}}} \quad (5.1)$$

to the measured data, with $\theta_{\vec{q}}$ being the angle between \vec{q} and the z -axis. The error bars are a combination of errors from the fitting of the phenomenological function [Eq. (4.7)] to the mean square displacement, and from the uncertainty in k caused by the finite pulse width. The results are consistent with our interpretation, and in fact the two fits give the same value for the z -component of the root mean square velocity.

We also tested the reflection geometry, which was used to measure the z -component of the velocity. In this geometry, the same transducer is used to generate and to measure the ultrasound scattered back from the sample with a scattering angle of 180° . To test this technique, we placed two transducers on the same side of the sample, one inclined towards the sample at $-\theta_w$ and the other at $+\theta_w$. The \vec{q} resulting from this setup points along the z -axis, and has a magnitude that depends on the scattering angle:

$$|\vec{q}| = 2k \sin \left[\frac{\theta_s}{2} \right] \quad (5.2)$$

$$\theta_s = 180^\circ - 2 \sin^{-1} \left[\frac{v_p}{c_w} \sin \theta_w \right]. \quad (5.3)$$

The mean square displacements measured at three different scattering angles are compared in Fig. 5.2.5. They agree quite well over most of the time range, with only a slight difference in the $\theta_s = 110^\circ$ as it rolls-over. These measurements also check that the mean square displacement does not depend on the magnitude of q , at least over the limited range of values that we used (all of our data has $90^\circ < \theta_s < 180^\circ$). This means that any

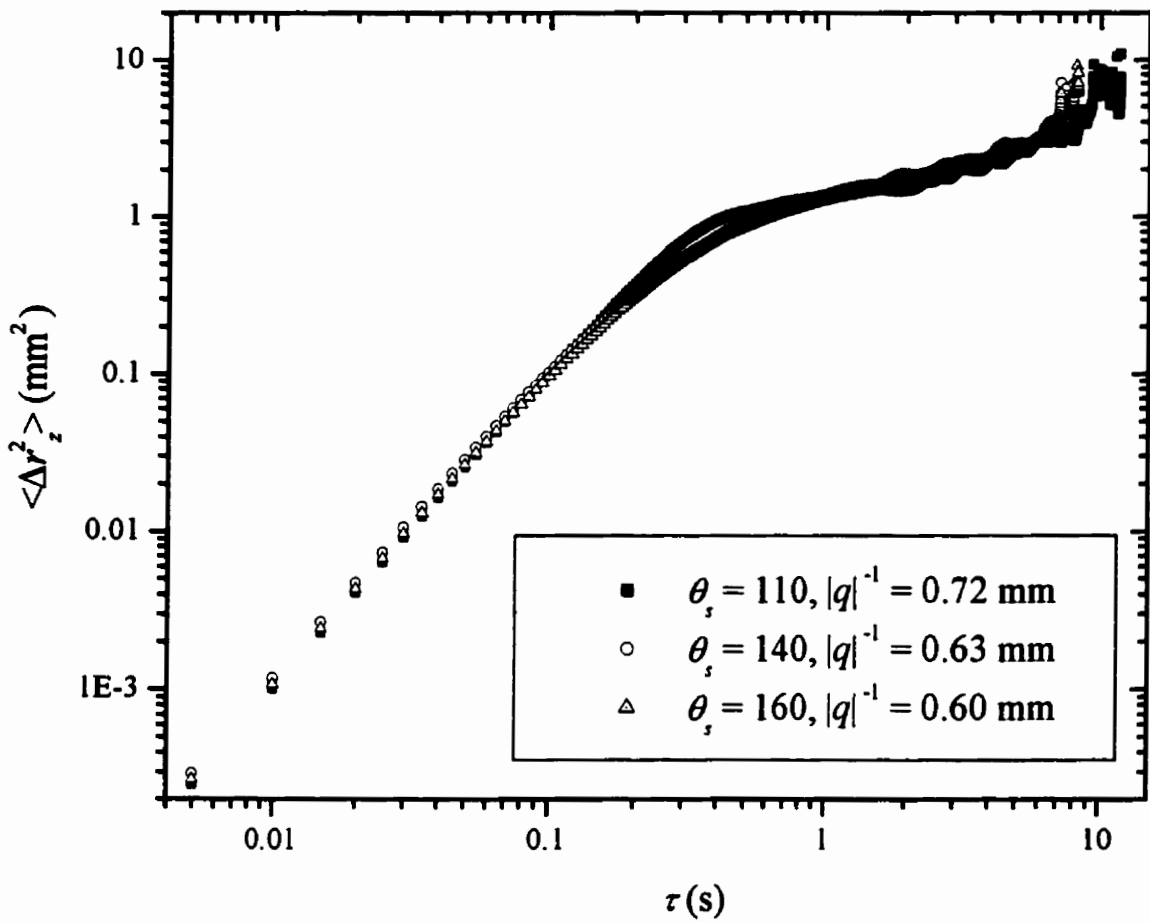


Figure 5.2.5: Test of the far-field reflection geometry. The measured mean square displacement of the beads along the z direction is shown for three different scattering angles.

possible structure factor effects are not important on the length scales (q^{-1}) at which the measurements are performed. This is reasonable, because q^{-1} is less than a bead diameter, and therefore we are measuring the motion of individual beads.

5.2.2.2 Comparison of DSS Techniques

The far-field DSS technique can give more information about the scatterers and the analysis is more straightforward; therefore once we had acquired the large water tank,

we abandoned the near-field DSS technique. However, my original data were taken using the near-field technique, and thus it is important to compare the results of the two techniques to test their self-consistency. By using two methods and comparing the results, we are also testing the accuracy of both of the measurement techniques.

The results of two tests are shown in Table 5.1. In the first column, the near-field measurement of the approximate three-dimensional root mean square velocity is shown. The next column is the full three-dimensional root mean square velocity, found by combining the far-field measurements of all three components. The last two columns show the expected near-field measurement value calculated from the far-field measurements [Eq. (C.12)], and the percent difference from what was actually measured (i.e. between columns one and two). The two techniques agree to within $\pm 5\%$, which is also within the expected error bars on each (about 15% on the near-field calculation, and 10% on the far-field measurements). Therefore, the two techniques are consistent with each other, providing a check on the validity of the near-field technique and the accuracy of DSS in general.

Near-Field		Far-Field		% diff.
	V'_{rms}	V_{rms}	$V'_{rms} = \sqrt{V_{rms,x}^2 + V_{rms,y}^2 + 2V_{rms,z}^2 \tan^2 \alpha}$	
#1	1.74	1.86	1.81	+3.9
#2	2.18	2.12	2.06	-5.8

Table 5.1: Comparison of the values of V_{rms} measured using the near- and far-field DSS techniques.

5.2.3 Phase Measurements

5.2.3.1 Wrapped Phase Statistics

The temporal evolution of the phase of the transmitted wave was measured in a strongly scattering sample (i.e. under DAWS conditions), as was described in Section 4.5. The wrapped $[-\pi, \pi]$ phase probability distribution, $P(\Phi)$, is plotted in Fig. 5.2.6. As expected for a random sample, it is flat within statistical error bars. This flat phase distribution is consistent with Gaussian statistics for the complex field, which is the basis of the theory that was presented in Section 2.3.4.

Of greater interest are the probability distributions of the change in the phase over

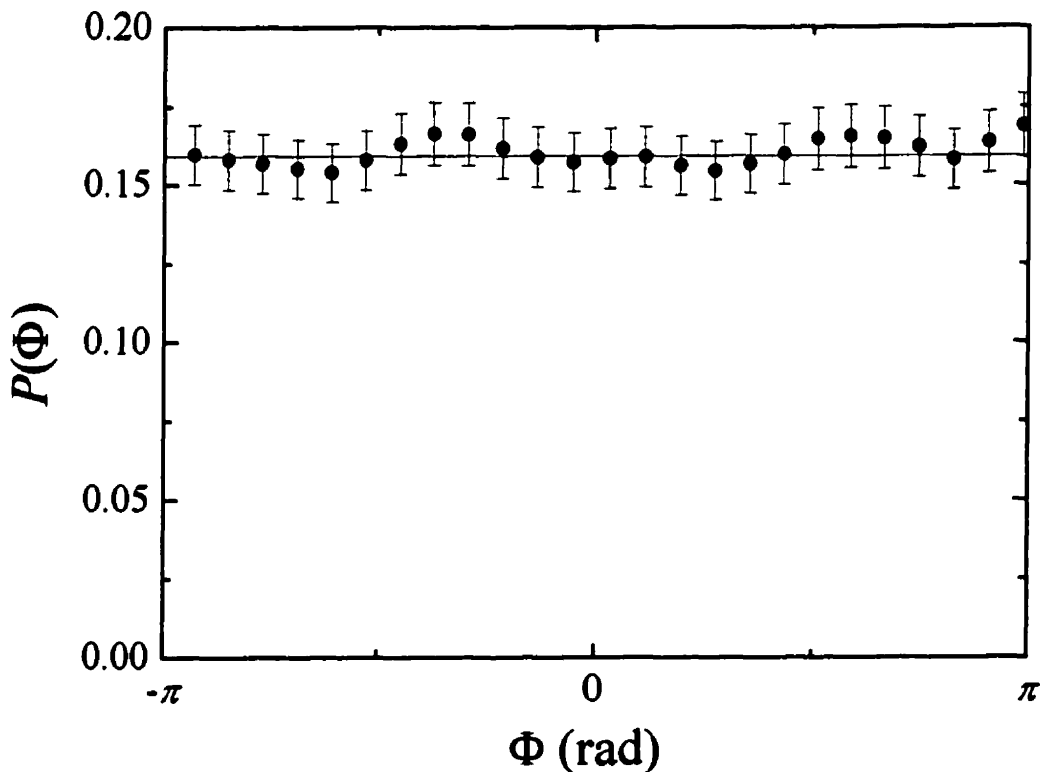


Figure 5.2.6: Transmitted phase probability distribution in a random multiply scattering sample. The solid line is a uniform probability distribution between $-\pi$ and π .

time τ , $P(\Delta\Phi(\tau))$. These distributions should contain information about the motion of the scatterers in the suspension, which can be extracted by fitting the theoretical form that was derived in Section 2.3.4. Note that the only fitting parameter is $\langle \Delta\phi^2 \rangle$, the mean square phase change of one path through the sample, which is averaged over the same phase distribution that enters the DAWS formalism. Therefore, one approach to extracting information about the motion of the particles is to fit the theoretical form of $P(\Delta\Phi)$ to our data at different τ , which yields $\langle \Delta\phi^2 \rangle$ as a function of τ . Then $\langle \Delta\phi^2 \rangle$ can be directly related to the relative mean square displacement of the particles, as was done in the DAWS derivation.

In Fig. 5.2.7, the phase difference probability distribution is plotted for four different values of τ , along with fits of Eq. (2.92). The early times have a fairly narrow peak centered at $\Delta\Phi = 0$, which broadens as the time difference increases and the particles move further from their original positions. There also are peaks near $\pm 2\pi$, which correspond to the jumps in the wrapped phase going from $-\pi$ to $+\pi$ or vice versa. As τ gets larger, the probability distribution approaches a triangle function [Fig. 5.2.7(d)], which is independent of τ . This happens because the correlations have become very small, and the underlying phase distribution is flat in $[-\pi, \pi]$ [Fig. 5.2.6]. Therefore, at the time depicted in Fig. 5.2.7(d) all reliable information about the time evolution of the particles has been lost. The agreement between theory and experiment is excellent over the entire range of phases and τ .

As a further example of the excellent agreement between theory and experiment,

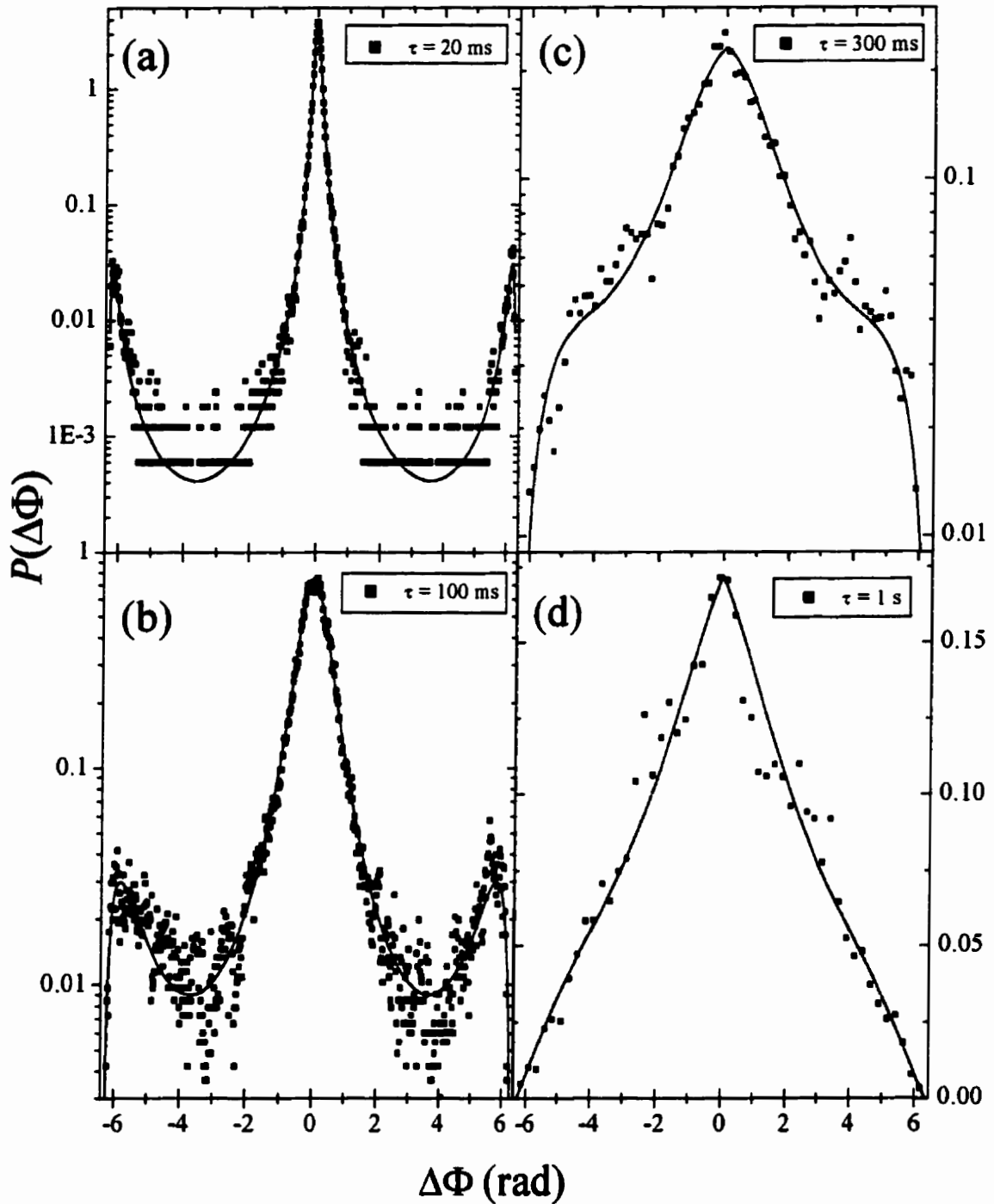


Figure 5.2.7: The wrapped phase-difference probability distribution measured at four different time differences (points), along with the theoretical fits (lines).

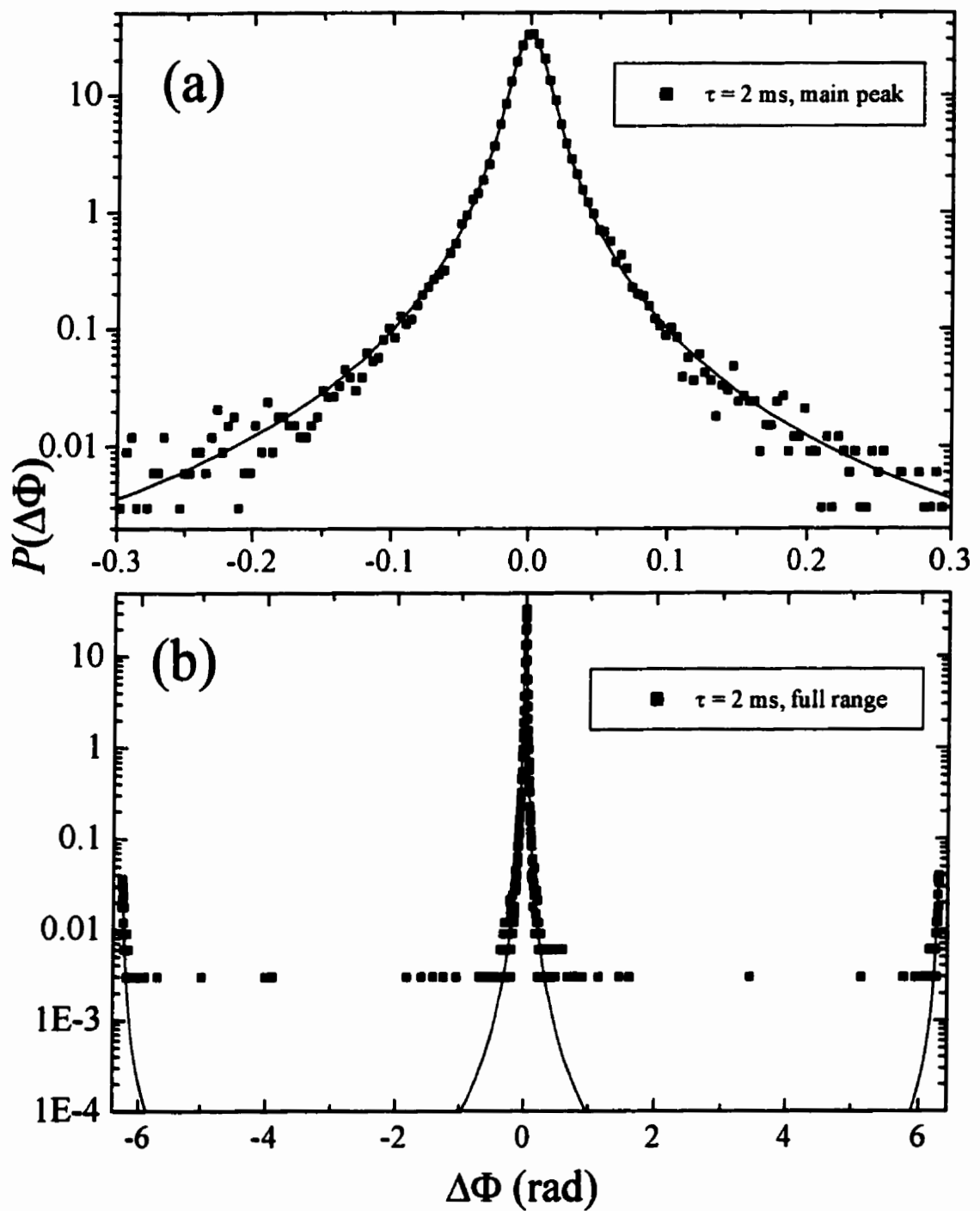


Figure 5.2.8: The wrapped phase-difference probability distribution (measured data (points) and theoretical fits (lines)) at an early time difference. (a) The central peak and (b) the full range of phase differences.

the measured distribution at the earliest time difference, $\tau = 2\text{ms}$, is plotted in Fig. 5.2.8.

Panel (a) shows a zoomed in view of the narrow central peak, along with a fit to the data.

The theory and experiment agree for the central peak in $P(\Delta\Phi)$ extremely well over almost 4 orders of magnitude. Furthermore, in panel (b), the entire range of $P(\Delta\Phi)$ is shown, and the same curve fits the small peaks in the data near $\pm 2\pi$, which are down from the central peak by more than 3 orders of magnitude.

As mentioned previously, one way to extract information about the particle motion

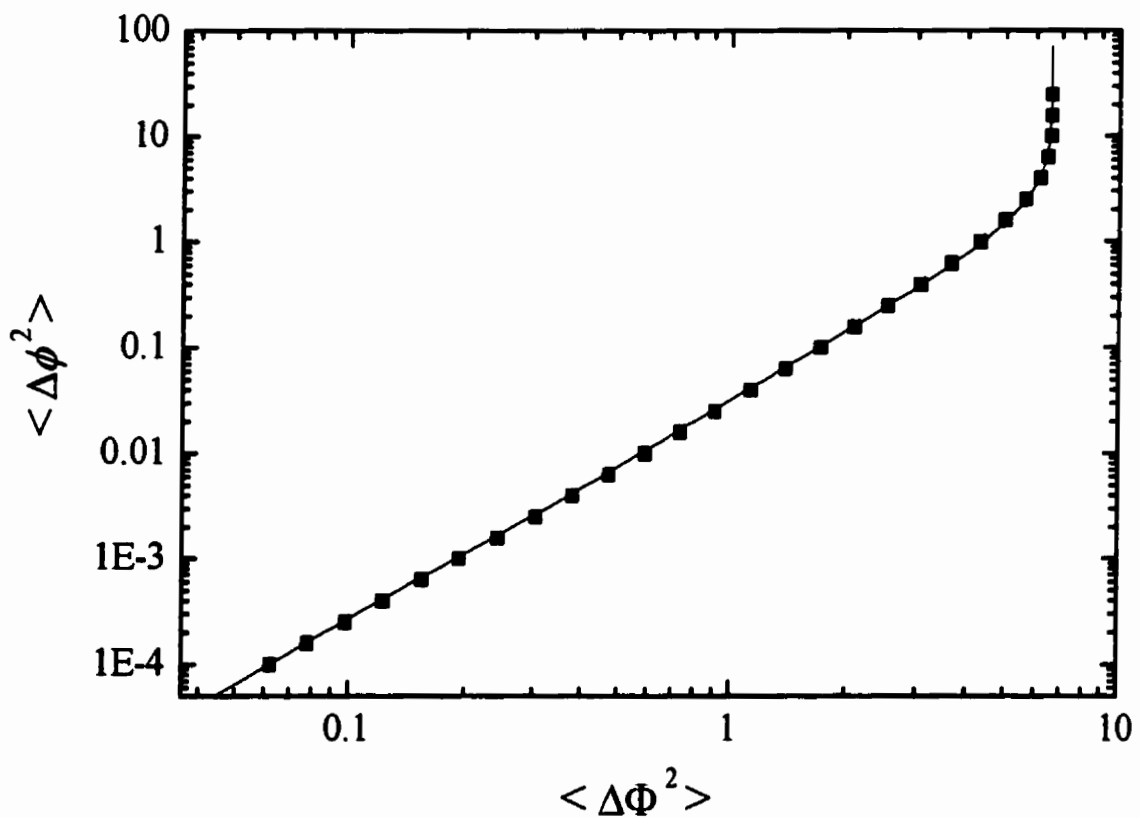


Figure 5.2.9: The relationship between the mean square phase change of the transmitted field and the mean square phase change of a single path through the sample (the line is an interpolating function).

is to fit the measured probability distribution at each time difference of interest. However, this is rather calculation intensive, so a more elegant way is to use Eq. (2.92) to relate $\langle \Delta\Phi^2 \rangle$ to $\langle \Delta\phi^2 \rangle$ directly,

$$\langle \Delta\Phi^2 \rangle = \int P(\Delta\Phi) \Delta\Phi^2 d(\Delta\Phi) = f(\langle \Delta\phi^2 \rangle). \quad (5.4)$$

Then, by calculating $\langle \Delta\Phi^2 \rangle$ from the phase data, and using Eq. (5.4) to calculate $\langle \Delta\phi^2 \rangle$, the relative mean square displacement of the scatterers can be found as a function of τ . Unfortunately, the integral in Eq. (5.4) must be done numerically, leading to the function plotted in Fig. 5.2.9. This plot shows explicitly that accurate information about the

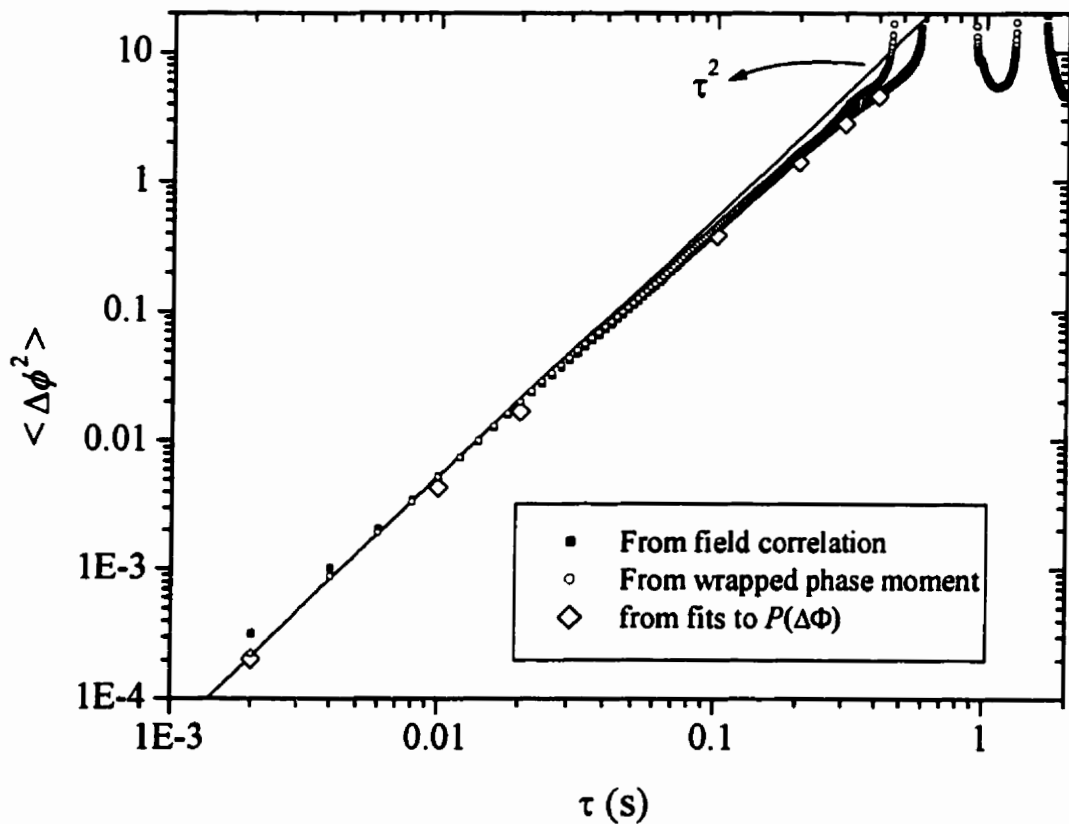


Figure 5.2.10: Comparison of phase (open circles and diamonds) and field (closed square) methods. The line is proportional to τ^2 .

motion of the beads is lost as $\langle \Delta\Phi^2 \rangle$ gets large, in particular at $\langle \Delta\Phi^2 \rangle \sim 6$. This corresponds to a phase change of a single path of $\langle \Delta\phi^2 \rangle^{1/2} \sim 2$ radian, which in turn corresponds to $g_1 \rightarrow 0.1$. Therefore at long times, using the wrapped phase to measure the motion of the beads does not have any obvious advantage over using the field fluctuations to measure the phase; both methods lose accuracy as $g_1 \rightarrow 0$.

The $\langle \Delta\phi^2 \rangle$ resulting from the wrapped-phase method and field fluctuation method are compared in Fig. 5.2.10. The circles are from Eq. (5.4), while the diamonds are from direct fits to the probability distribution. Both phase methods compare well to the field fluctuation data, although the fits to the probability distribution seem to be systematically below the others by a very small factor.

Overall, the theory used to describe the phase probability distribution describes our experimental data remarkably well. The method used to extract information about the motion of the scatterers also works well, and is in agreement with the field fluctuation measurements.

5.2.3.2 Cumulative Phase Statistics

The jumps of 2π can be removed from the time record of the wrapped phase, giving the so-called cumulative phase, as was discussed in Section 4.5. At small τ , the wrapped and cumulative phase difference distributions are essentially the same, except that the cumulative phase does not have peaks at $\pm 2\pi$ because they have been removed by the unwrapping algorithm. Removing the jumps in the phase lets us follow its variations for a longer time, which means that the phase difference probability continues to broaden even

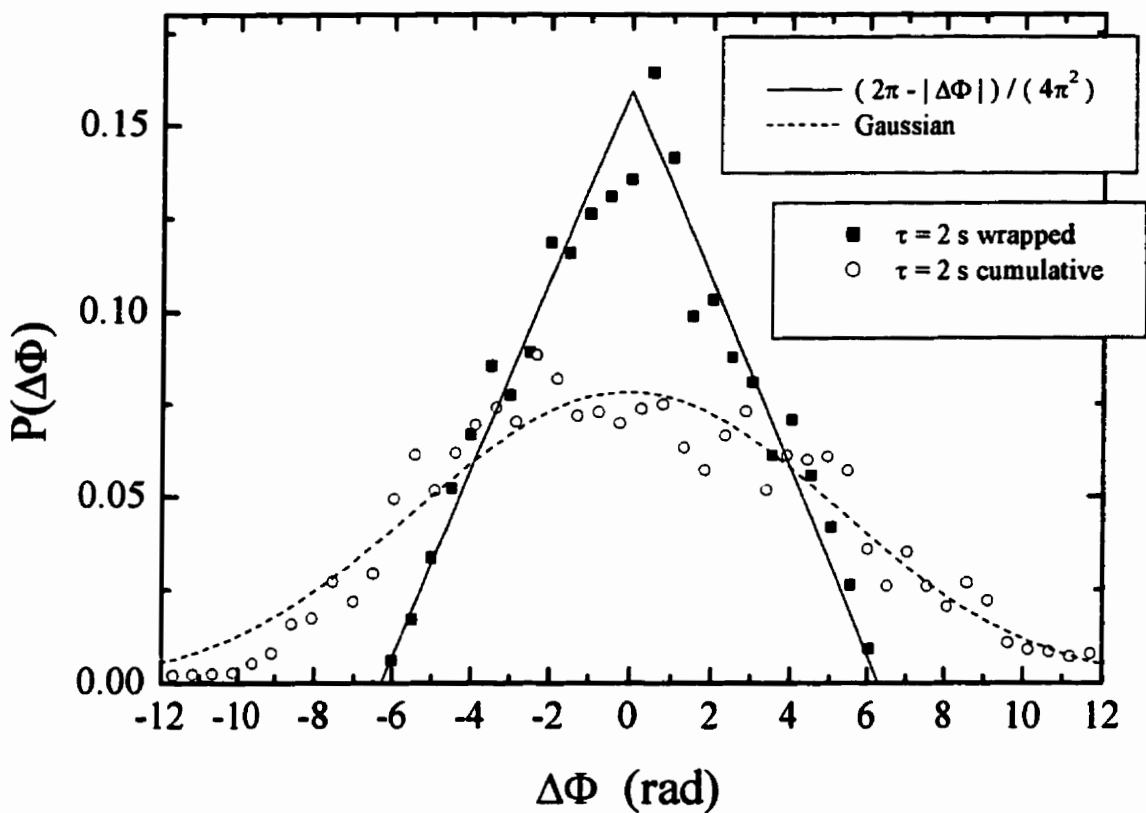


Figure 5.2.11: Comparison of wrapped and cumulative phase-difference probability distributions at a large τ .

after the wrapped distribution has saturated as a triangle function. This is illustrated in Fig. 5.2.11, which shows the wrapped and cumulative phase distributions at a late time τ . The cumulative phase difference distribution is approximately Gaussian, but an explicit theory will have to wait for later work.

5.2.4 Siegert Relation

5.2.4.1 Single Scattering Test

The Siegert relation was tested in the single scattering configuration on a 12.8 mm thick sample with a 40% volume fraction, and with the scattering vector \vec{q} aligned along the vertical direction. The field and amplitude were measured simultaneously by following the procedure outlined in Section 4.6, giving both the field and intensity correlation functions. The intensity correlation function g_2/β , and the square of the field correlation function ($|g_1|^2$) are plotted in Fig. 5.2.12 as a function of time. It is clear that the Siegert relation does not hold for single scattering in our system, which means that the spatial

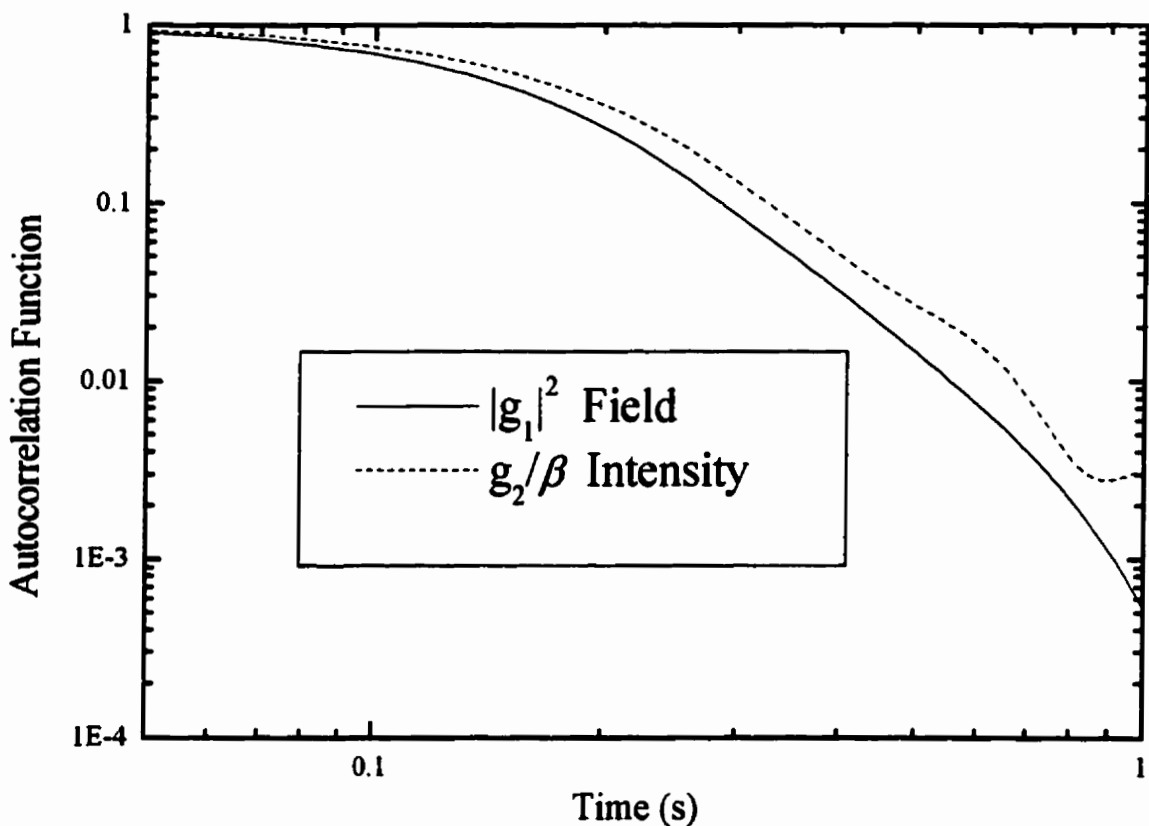


Figure 5.2.12: The field and intensity autocorrelation functions for a single scattering experiment, as a function of time.

correlations between the displacements of particles in the scattering volume are important.

Using Eq. (2.108), the spatial correlation function of the displacements of particles separated by a distance R_p can be calculated from the field and intensity autocorrelation functions. This equation only takes into account contributions from scatterers that are a distance R_p apart, where this distance corresponds to the most probable separation between particles in the scattering volume. In Fig. 5.2.13, the results of this calculation are shown as a function of time τ .

Note that the spatial correlation function in question can also be expressed in terms

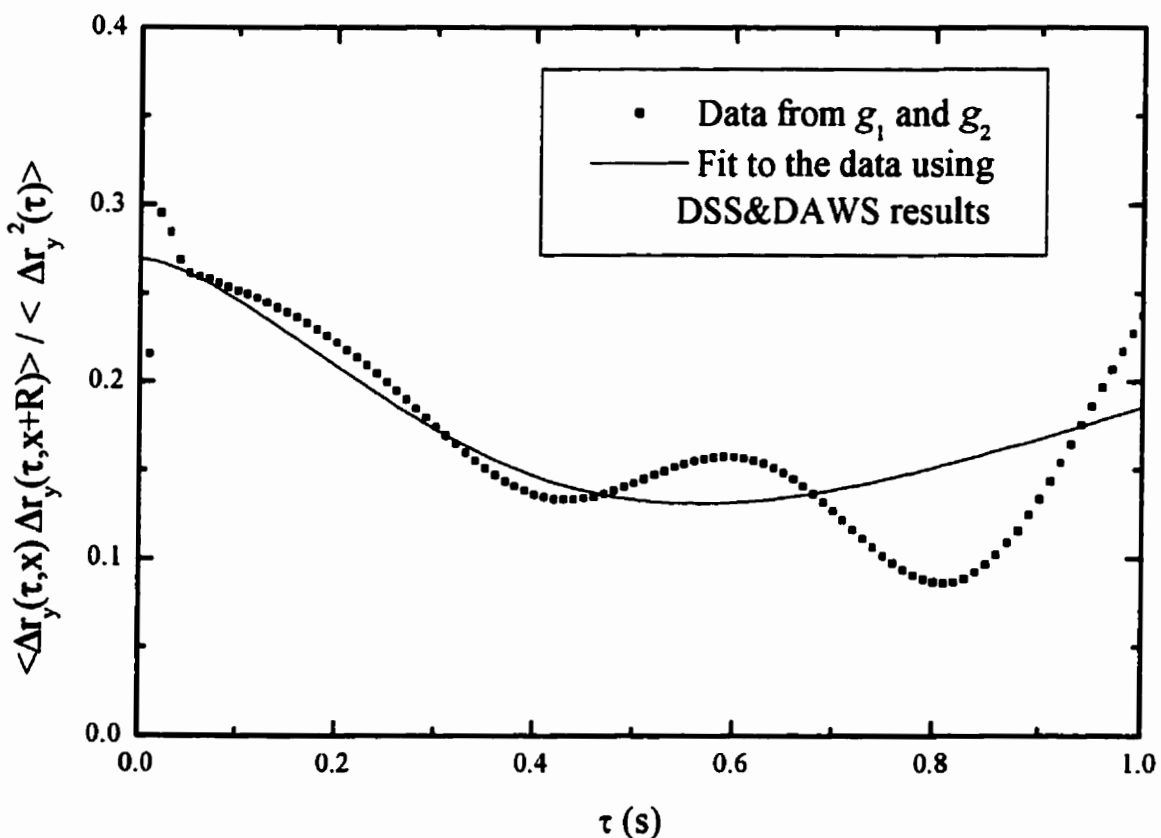


Figure 5.2.13: Spatial correlation function of the displacements of particles separated by R_p , with a fit from DAWS and DSS data giving $R_p = 22$ mm.

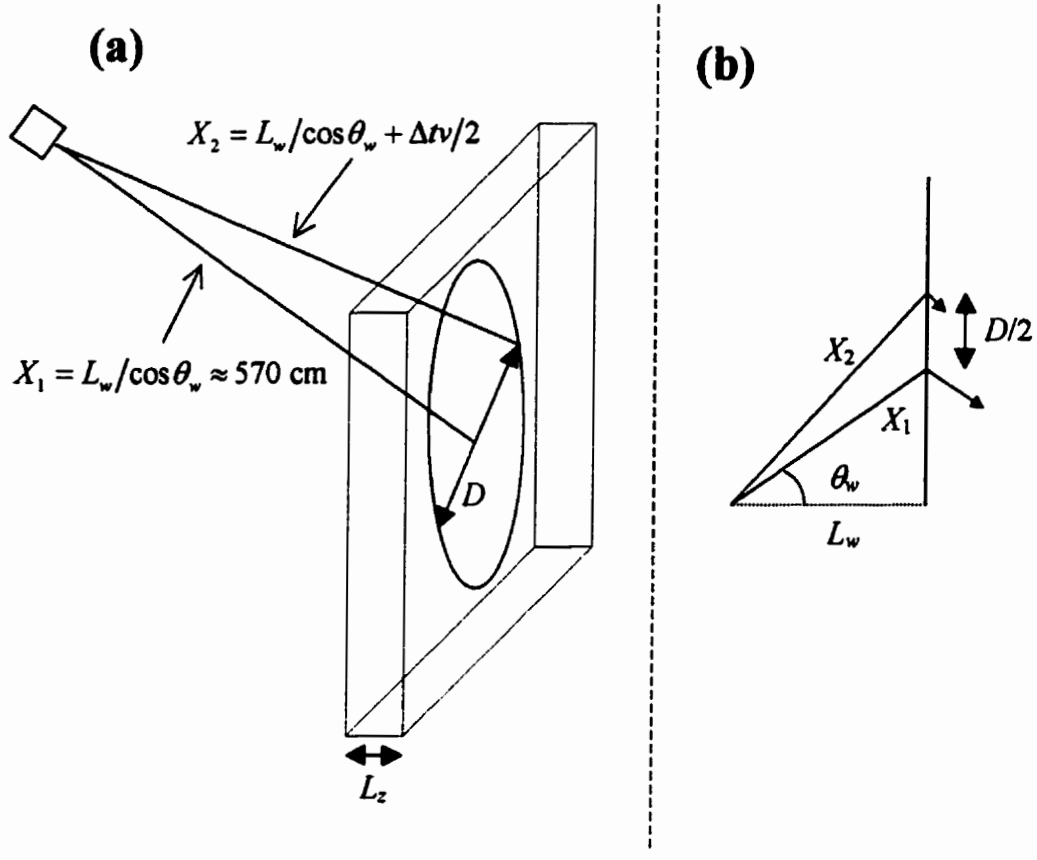


Figure 5.2.14: Far-field, single scattering geometry, showing the size of the scattering volume.

of the temporal particle correlation functions measured by DAWS and DSS (we consider the y -components of the displacements, corresponding to our experimental geometry)

$$\frac{\langle \Delta r_y(\tau, \bar{x} + \vec{R}_p) \cdot \Delta r_y(\tau, \bar{x}) \rangle_x}{\langle \Delta r_y(\tau, \bar{x}) \cdot \Delta r_y(\tau, \bar{x}) \rangle_x} = 1 - \frac{\langle \Delta r_{y,rel}^2(\tau, R_p) \rangle}{2 \langle \Delta r_y^2(\tau) \rangle} = 1 - \frac{\langle \Delta r_{rel}^2(\tau, R_p) \rangle}{2 \langle \Delta r^2(\tau) \rangle}. \quad (5.5)$$

DSS can measure $\langle \Delta r^2(\tau) \rangle$ directly, and DAWS allows us to measure $\langle \Delta r_{rel}^2(\tau, R) \rangle$ for relatively small R . For R that are too large to measure (because l^* would be too large compared to the sample thickness to achieve multiple scattering) the length scale dependence of $\langle \Delta r_{rel}^2(\tau, R) \rangle$ can be extrapolated [c.f. Sec. 5.3.4] to the R of interest. The

fit to the data in Fig. 5.2.13 uses the measured $\langle \Delta r^2(\tau) \rangle$ and an extrapolated estimate of $\langle \Delta r_{rl}^2(\tau, R) \rangle$, with $R_p = 22$ mm. The fit captures the overall trends in the data quite well, although the high frequency oscillations are not reproduced (they are likely caused by insufficient ensemble averaging). To check if the value of R_p obtained from the fit is plausible, a model of the scattering volume must be developed.

The scattering volume can be approximated by a cylinder with a diameter given by

$$D \sim 2 \left[\sqrt{\left[\frac{L_w}{\cos \theta_w} + \frac{\Delta \nu}{2} \right]^2 - L_w^2} - \sqrt{\left[\frac{L_w}{\cos \theta_w} \right]^2 - L_w^2} \right] \sim 60 \text{ mm} \quad (5.6)$$

and a thickness equal to the sample thickness L_z [Fig. 5.2.14]. The size of the scattering volume is primarily set by the input pulse width ($2\Delta t$), in the same way as the angular resolution of far-field DSS was [Section 4.4]. Assuming a uniform distribution of particles in the volume, and ignoring the thickness L_z (since $L_z < D$), $h(R)$ (the fraction of pairs of particles in the scattering volume that are separated by R) can be expressed as an integral over the scattering volume. Consider Fig. 5.2.15, where the cross-sectional area of the scattering volume is drawn, along with a particle at position \vec{r} . The arc length Γ is proportional to the number of particles inside the scattering volume that are a distance R away from this position, and $h(R)$ is proportional to the integral of Γ over all of the particle positions \vec{r} in the scattering volume. Making use of the expressions shown in Fig. 5.2.15, we obtain the following result for $h(R)$:

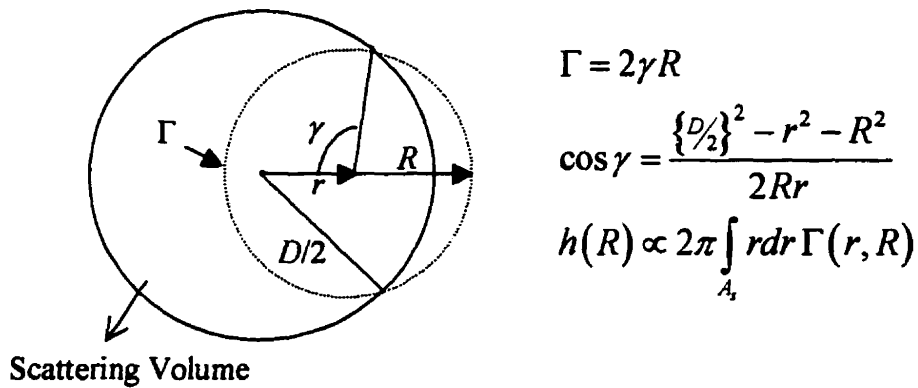


Figure 5.2.15: Diagram showing the location of particles separated by R in the scattering volume.

For, $R = 0$ to $D/2$:

$$h(R) \propto 2\pi^2 R \left[\frac{D}{2} - R \right]^2 + 4\pi R \int_{\frac{D}{2}-R}^{\frac{D}{2}} r dr \left[\pi - \cos^{-1} \left[\frac{\left(\frac{D}{2}\right)^2 - r^2 - R^2}{2Rr} \right] \right] \quad (5.7)$$

For, $R = D/2$ to D :

$$h(R) \propto 4\pi R \int_{R-\frac{D}{2}}^{\frac{D}{2}} r dr \left[\pi - \cos^{-1} \left[\frac{\left(\frac{D}{2}\right)^2 - r^2 - R^2}{2Rr} \right] \right] .$$

The result of numerically evaluating these integrals is shown in Fig. 5.2.16. As mentioned previously, for a finite scattering volume with a dimension greater than one, h has a peak, which in this case is at about $R_p = 25$ mm. The simple model, which just used the peak separation R_p to calculate the deviations from the Siegert relation, gave a value $R_p = 22$ mm when fit to the data. Therefore, our simple model is consistent with the scattering volume estimates, suggesting that our picture of the cause of deviations from the Siegert relation is correct. In this picture, the long-range correlation in the motion of particles in our samples leads to the breakdown of the Siegert relation. If the motion of particles, separated by distances that are comparable to the size of the scattering volume,

was not correlated, then the Siegert relation would hold true. Thus, the single scattering Siegert relation will only be valid under conditions where the scattering volume is large compared to the particle velocity correlation volume.

Given these results, the deviations from the Siegert relation also provide a way to measure the spatial-temporal correlation function in Eq. (5.5). This correlation function measures correlations in the displacements of particles separated by R_p , as a function of time. For example, the data in Fig. 5.2.13 show the correlations in the motion of particles separated by 22 mm, giving a correlation between the early time displacements of the particles of approximately 0.27. As the time is increased, this correlation first decreases, until it reaches a minimum and then surprisingly begins to increase again at later times. As a possible future extension of this work, the most probable particle separation, R_p , could be varied by changing the pulse width or beam size, providing a unique and novel probe into spatial-temporal correlations in the motion of particles.

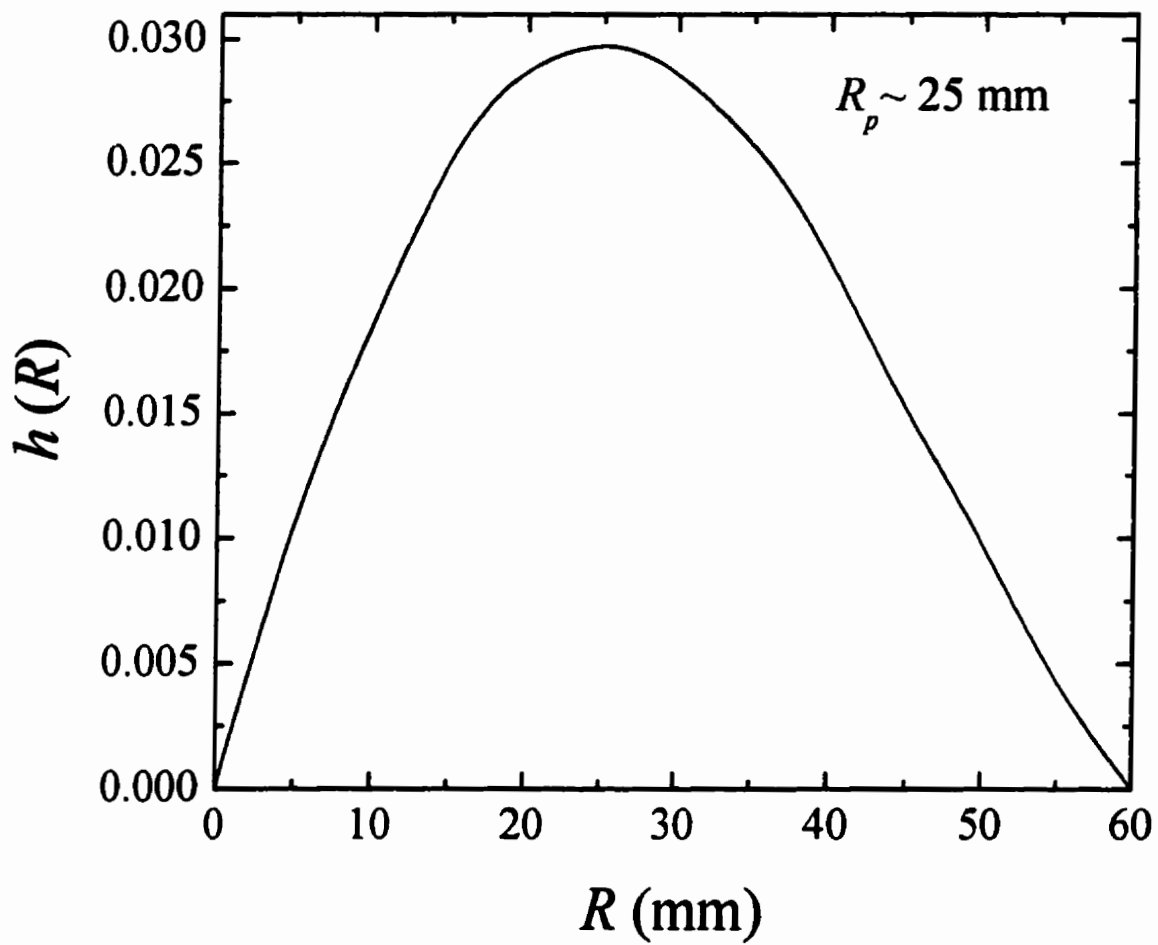


Figure 5.2.16: Fraction of particles separated by a distance R .

5.2.4.2 Pulsed DAWS Test

We have also tested the Siegert relation in a sample and at a frequency where there was strong multiple scattering, meaning that this was a DAWS, not a single scattering measurement. Measurements were done at three different volume fractions, and for different scattering path lengths at each volume fraction. The resulting autocorrelation functions are plotted in Figs. 5.2.17 to 5.2.19.

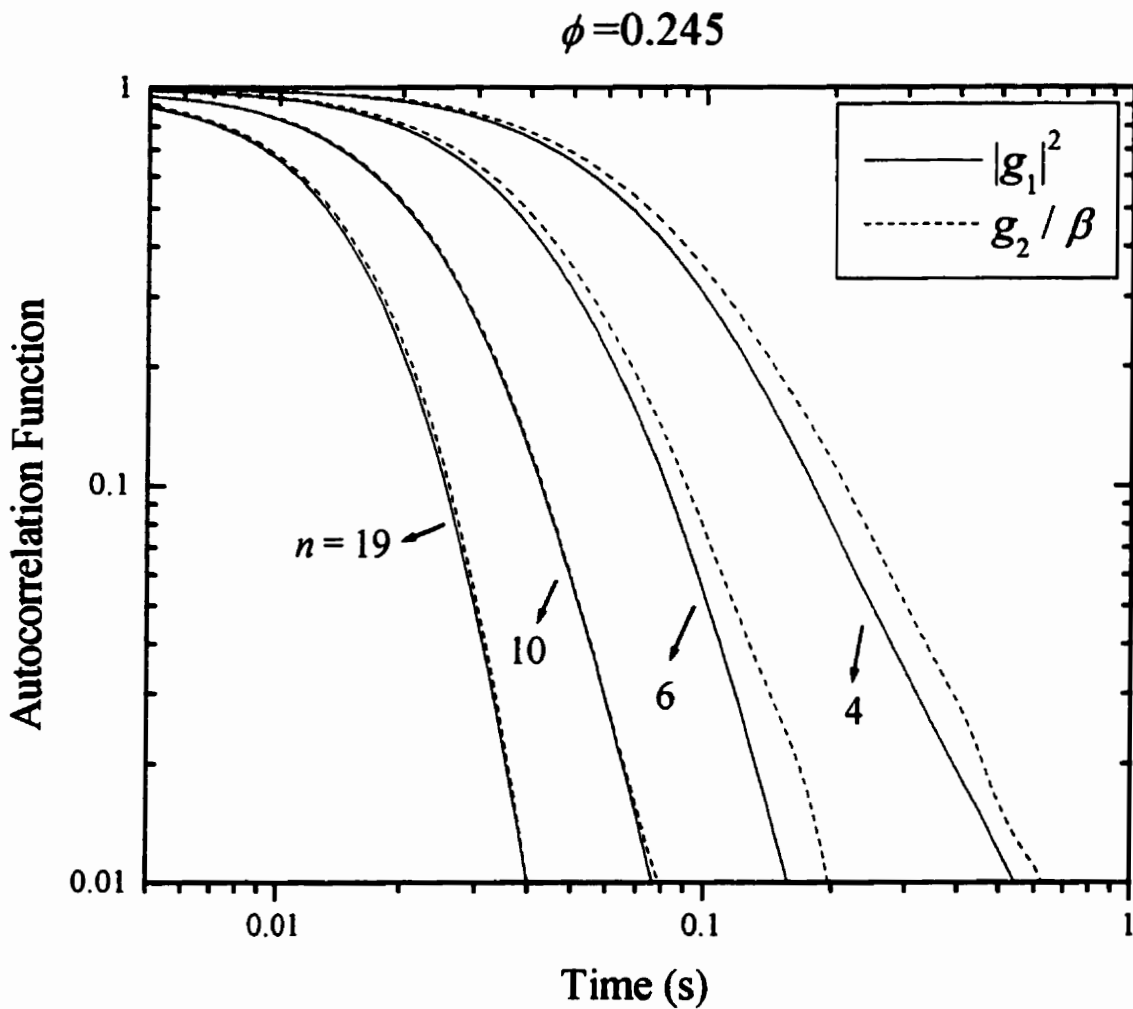


Figure 5.2.17: Test of the Siegert relation in a multiply scattering sample, with a volume fraction $\phi = 0.245$.

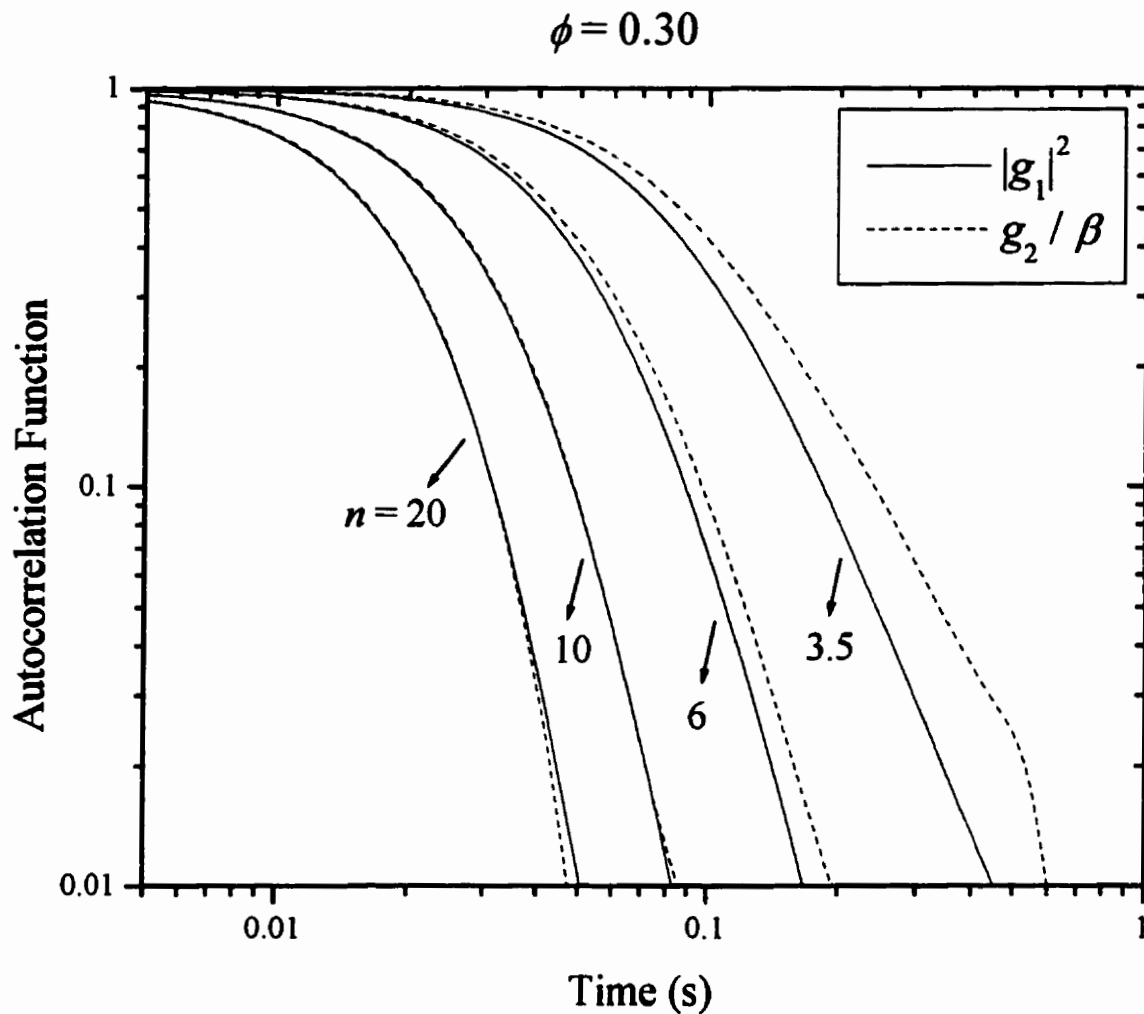


Figure 5.2.18: Test of the Siegert relation in a multiply scattering sample, with a volume fraction $\phi = 0.30$.

Fig. 5.2.17 shows the field and intensity correlation functions for four different path lengths at the lowest volume fraction, $\phi = 0.245$. For the two longest path lengths, the results obey the Siegert relation, but for the two shorter paths they do not. This trend continues for the different path lengths measured in samples with higher volume fractions, shown in Fig. 5.2.18 ($\phi = 0.30$) and 5.2.19 ($\phi = 0.50$). This effect is expected, as was discussed in Section 2.3.5. One possible explanation is that the longer paths include

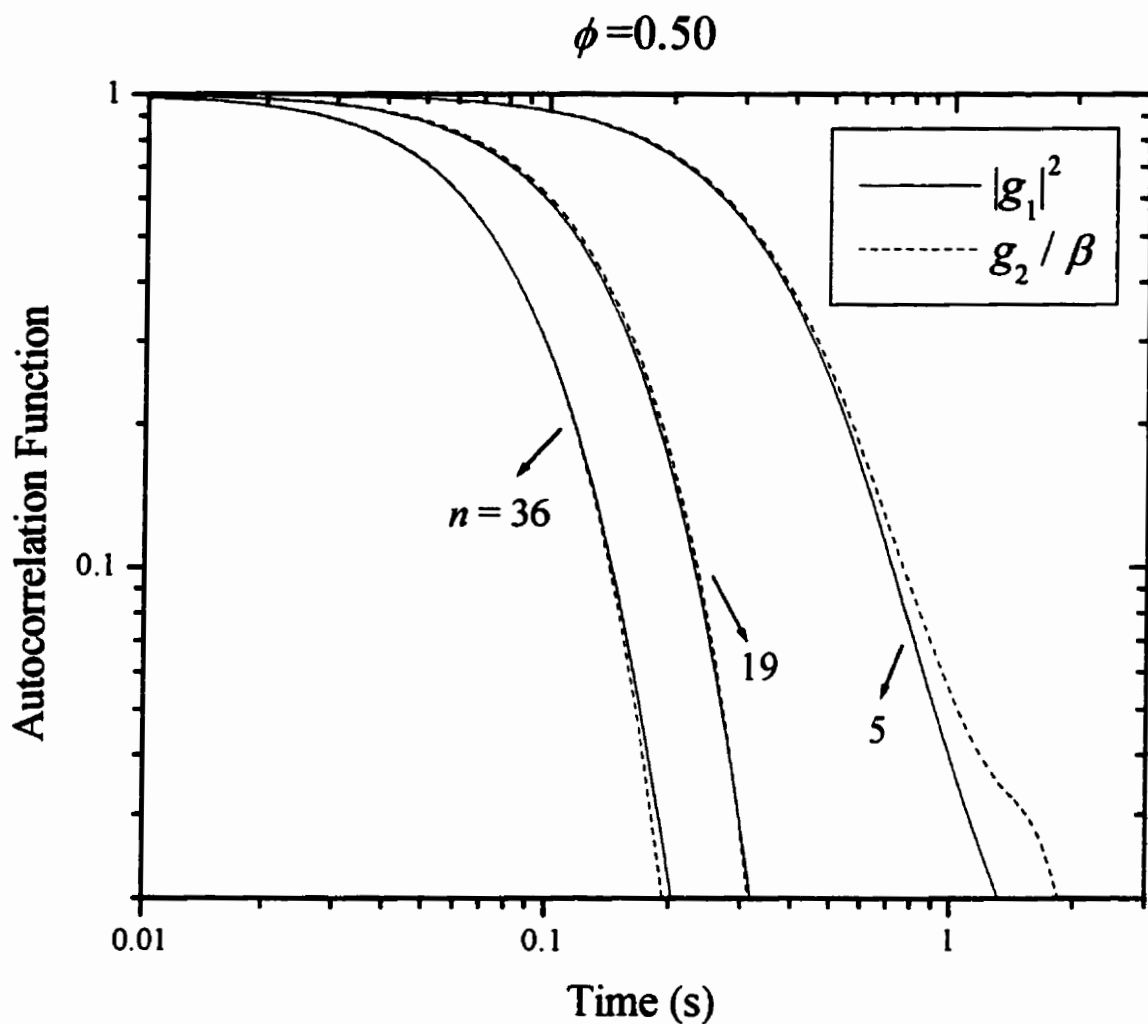


Figure 5.2.19: Test of the Siegert relation in a multiply scattering sample, with a volume fraction $\phi = 0.50$.

particles from a larger volume of the sample. and so the motion of different particles in the scattering paths is largely uncorrelated. This would mean that the phase change of different scattering paths would also be uncorrelated. Another possible explanation for this effect is that when the paths include many scattering events, the direction of the wave vector between scattering events will be randomized. Therefore even if the motion of the particles included in two neighboring scattering paths is strongly correlated, the phase

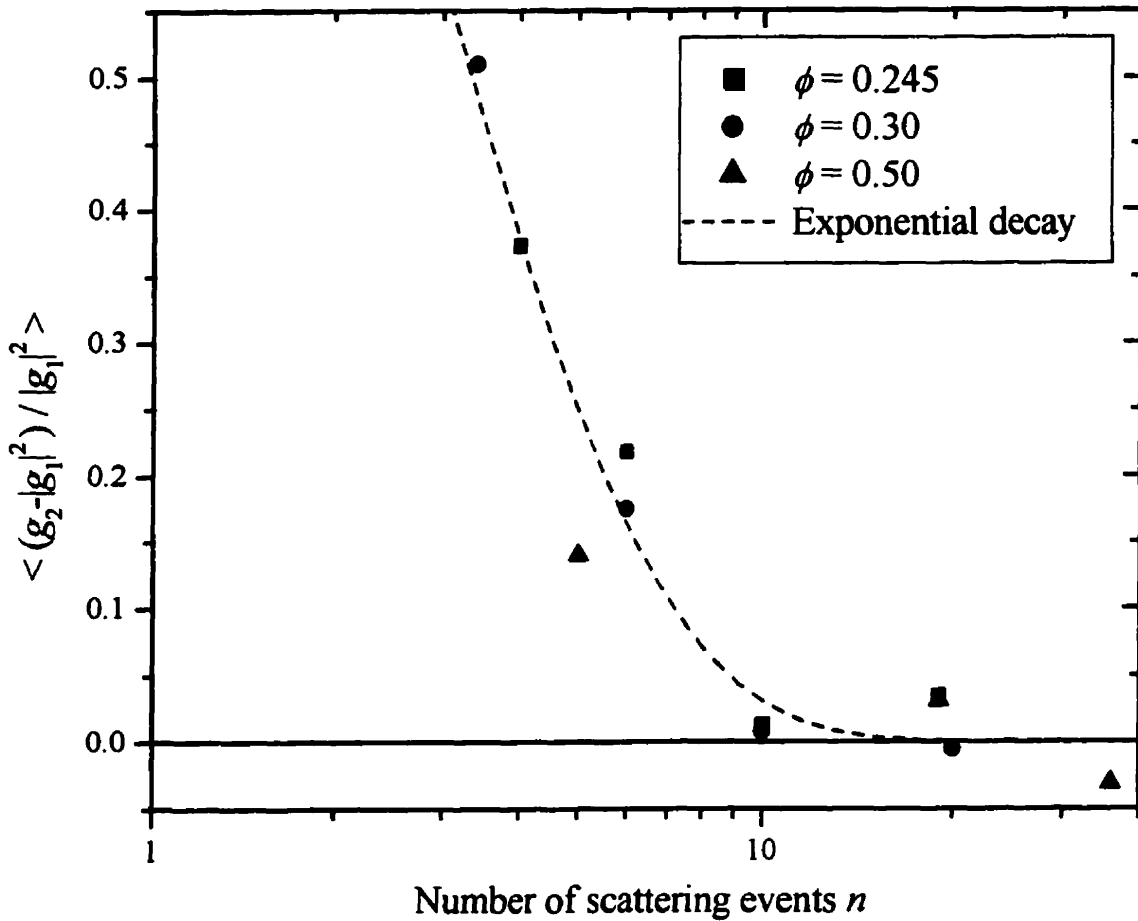


Figure 5.2.20: Deviation from the Siegert relation in multiply scattering samples, with a dashed line drawn as a guide to the eye.

changes introduced into each path by the motion of the particles would not be correlated, because the directions of the scattering wave vectors are uncorrelated. These ideas are explored in more detail in Fig. 5.2.20, which shows the average deviation from the Siegert relation plotted versus the number of scattering events. For the purpose of analysis, the average deviation was defined as the average of

$$\frac{g_2/\beta - |g_1|^2}{|g_1|^2} \quad (5.8)$$

over time, from $\tau = 0$ to the time at which $|g_1|^2$ drops to 0.03. This value of $|g_1|^2$

corresponds to the top of the noise level in the worst of the intensity correlation function data. The average deviations from all three volume fractions are plotted on the graph, and their behavior is remarkably similar. The deviations are essentially zero for $n > 10$, and increase exponentially for smaller n . As will be discussed in Section 5.3.5, the velocity correlation length, ξ , of the particles (which gives the average distance over which particle velocities are correlated) depends on volume fraction, varying from $\xi = 7.9$ mm at $\phi = 0.245$ to 17.5 mm at $\phi = 0.5$. The volume that encloses a path of $n = 10$ steps must have one dimension equal to at least $L_z = 12.2$ mm (since we are measuring transmitted sound). To estimate the other two dimensions, we calculate the root mean square displacement of diffusing sound as a function of path length,

$$\langle \Delta r_s^2 \rangle^{\frac{1}{2}} \sim \sqrt{D\tau} = \sqrt{\frac{Dnl^*}{v_E}} = l^* \sqrt{\frac{n}{3}}. \quad (5.9)$$

Thus the average transverse size of the scattering volume occupied by a single path varies from approximately 3.3 mm at $\phi = 0.245$ to 1.2 mm at $\phi = 0.5$. The scattering volumes (V_s) are compared to the correlation volumes (V_c) in Table 5.2. We find that the scattering

ϕ	$V_s = L_z \langle \Delta r_s^2 \rangle$	$V_c = \xi^3$
0.245	130 mm ³	490 mm ³
0.3	115	670
0.5	17	5300

Table 5.2: Comparison of scattering volumes to correlation volumes for $n = 10$.

volume is much less than the velocity correlation volume, which means that the motion of the particles in a scattering path is significantly correlated for $n = 10$. Thus, even in the presence of significant correlations, the Siegert relation holds for DAWS paths that are longer than 10 steps. This occurs because these paths are long enough that the directions of the wave vectors of the scattered waves are well randomized, so that the phase changes of different paths are not correlated with one another, even if the motion of the particles in the scattering paths is correlated. Thus, in contrast to the single scattering case, where the failure or success of the Siegert relation was determined solely by the correlations in the system, in the multiply scattering case the properties of the diffusing waves themselves overcome the effects of correlations, allowing the Siegert relation to hold true.

5.2.4.3 Continuous Wave Test

We have also tested the Siegert relation with a continuous wave input, using the same experimental techniques discussed previously. The sample and frequency were chosen so that there was strong multiple scattering, meaning that this was also a DAWS measurement. In contrast to a pulsed input, with a continuous wave input a wide range of scattering paths contribute to the transmitted field and intensity fluctuations.

The resulting field and intensity autocorrelation functions are plotted in Fig. 5.2.21

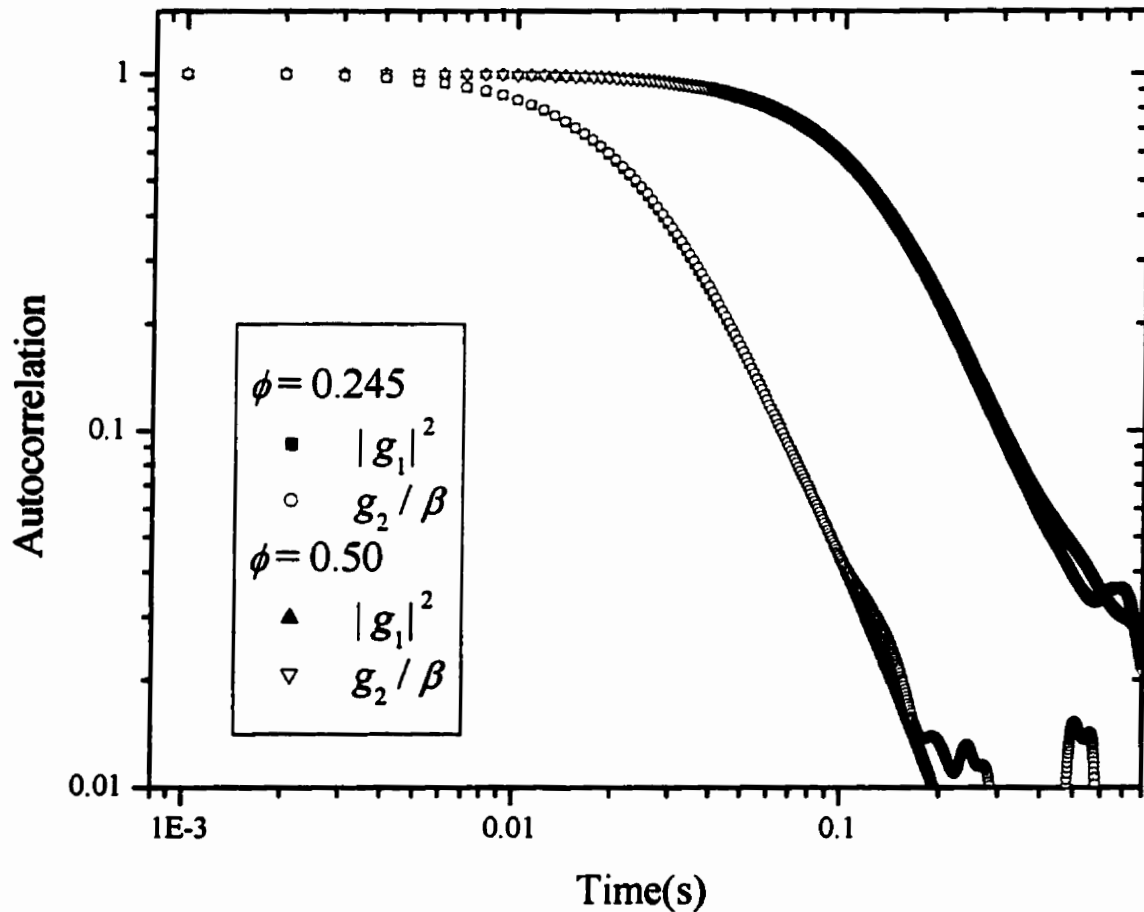


Figure 5.2.21: Test of the Siegert relation in a multiply scattering sample, for a continuous wave input at two volume fractions.

for two volume fractions. The agreement with the Siegert relation is quite good for both volume fractions over the measured time range. This is true because when a strongly scattering sample is thick enough that the diffusion approximation is obeyed, long path lengths dominate the transmission. Since the Siegert relation is obeyed for paths that are longer than 10 scattering events, a relatively short path length ($10l^* \ll L_z^2/l^*$), the continuous wave autocorrelation functions also obey the Siegert relation.

5.3 Fluidized Bed Dynamics

This section presents the results of applying our new experimental techniques to measure some of the properties of fluidized suspensions. I begin by considering the fluidization velocity, or perhaps equivalently the sedimentation velocity, measured for different sample sizes and Reynolds numbers as a function of the average volume fraction of the suspension. Then I discuss measurements of the volume fraction at different heights in the bead column, looking for possible variations in the volume fraction with vertical position in the suspension. After these preliminaries, I go on to discuss the results of the DSS and DAWS measurements, in light of the different competing theories presented in [Section 2.4.2](#).

5.3.1 Fluidization Velocities

We have measured the flow velocity needed to fluidize 0.875-mm-diameter glass bead suspensions of different volume fractions for all of the combinations of sample sizes and fluids that we used. The results are plotted in Fig. 5.3.1, normalized by the single sphere Stokes velocity, which was measured independently. The data scatter around the phenomenological fit discussed in Section 2.4.1, with $K_2 = 4.4$; our data are in agreement with other sedimentation experiments with 0.35 mm beads, which gave $K_2 = 4.65$ [Russel *et al.* 1989]. There are some systematic effects, with the high volume fraction flow velocities for both the high and low Reynolds number samples being consistently higher than the flow velocities at intermediate Reynolds numbers. There is no discernable effect on the fluidization velocity when only the sample size is changed.

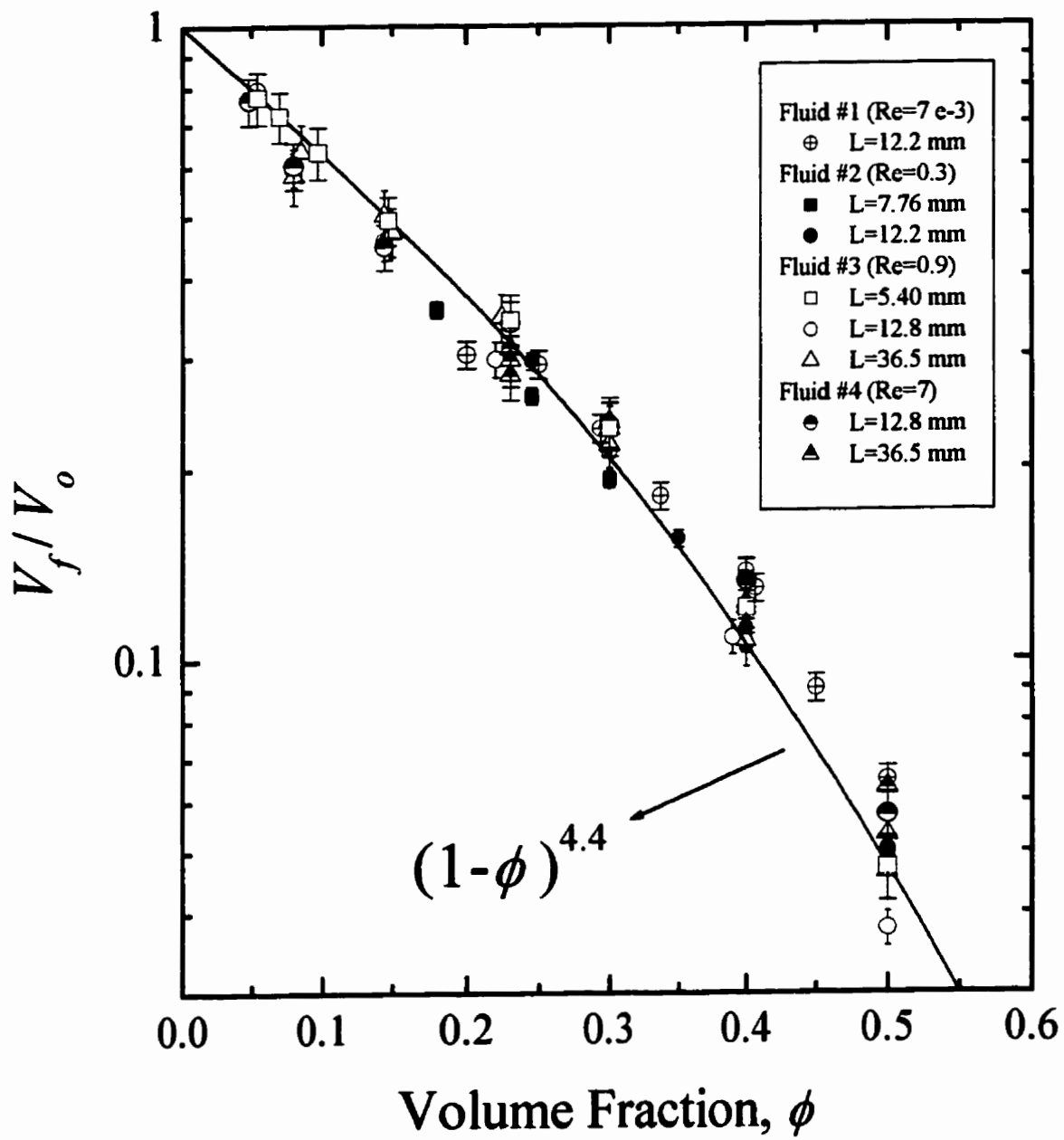


Figure 5.3.1: The fluidization velocity versus volume fraction, for all of our samples.

5.3.2 Cell Uniformity

It is possible that the local time-averaged volume fraction changes with position in the fluidized bed. To check to see if this happens, we measured the ballistic transmission of ultrasound through the suspension at different heights in the fluidized bed. The scattering mean free path is approximately inversely proportional to the volume fraction, and thus is a measure of the local volume fraction. By using a hydrophone placed close to the exit face of the sample, and measuring the ballistic transmission, we are only sensitive to the small region of the sample directly between the hydrophone and transducer.

The results of these measurements at different volume fractions and on different samples are plotted in Fig. 5.3.2. While the overall uniformity of the particle concentration is good, indicating that the fluid flow is well distributed throughout the bed, there is some variation in the volume fraction, especially in the top 30% of the column. However, the volume fraction does not change by more than a few percent in the middle of the column, where we took our measurements. The slight variation in volume fraction means that it is important to make all of the measurements on a sample at the same height in the column, to ensure that the volume fraction remains constant.

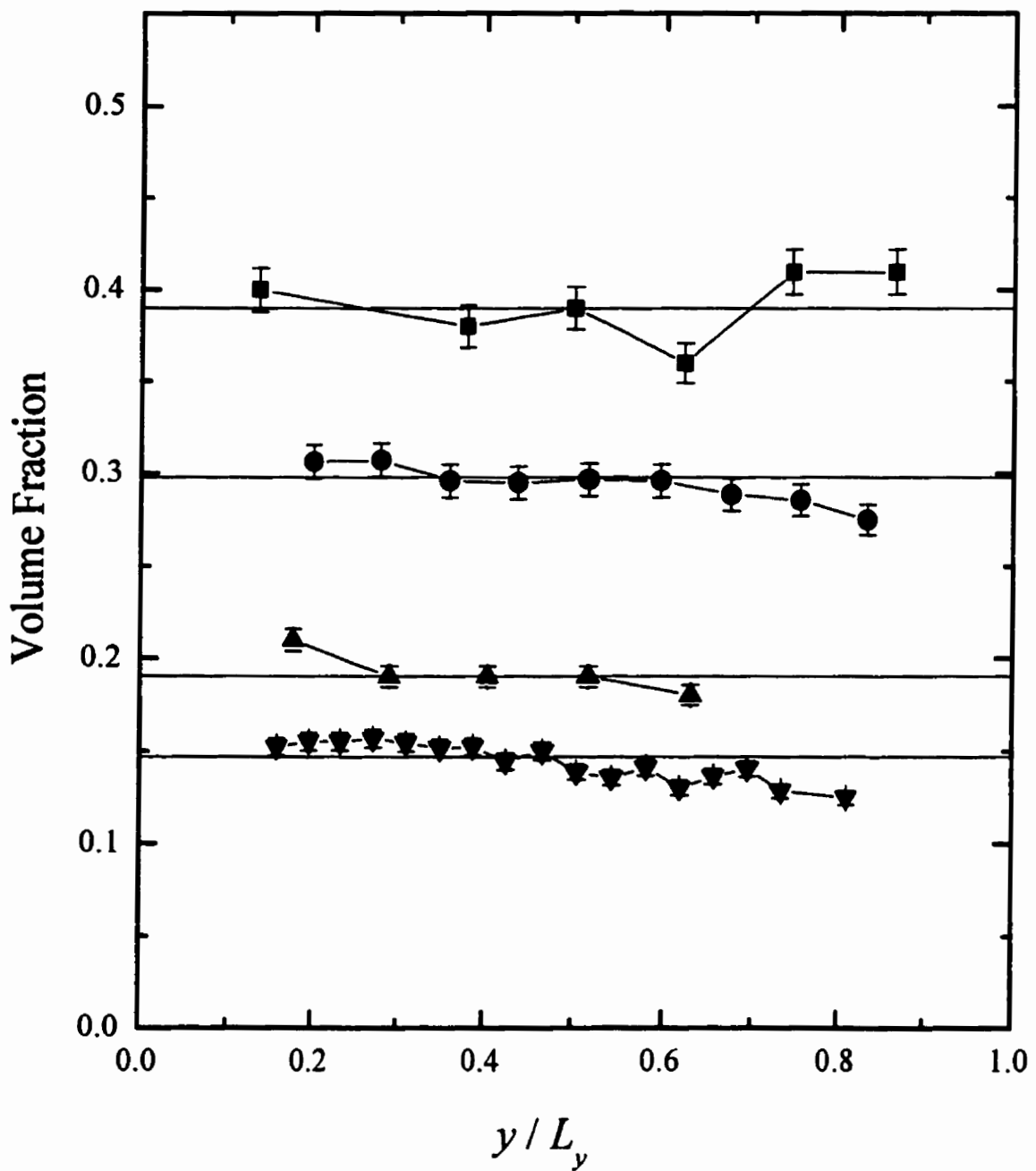


Figure 5.3.2: The variation in the volume fraction with height in the suspended column, for several average volume fractions.

5.3.3 RMS Particle Velocities

The root mean square particle velocities in our fluidized suspensions were measured using the DSS (Dynamic Sound Scattering) technique discussed earlier. The next three sections will focus on the results from the thickest sample ($L_z = 36.5$ mm) at a Reynolds number of 0.9, in order to illustrate the data collected; the sample thickness and Reynolds number dependence will be examined in later sections. For this sample, we used the far-field DSS technique at a frequency of 250 kHz, which allowed us to measure all three components of the rms particle velocity independently. In a fluidized suspension the average velocity of the particles is zero, which means that these rms velocities are equivalent to the rms velocity fluctuations about the mean.

Examples of field autocorrelation functions are plotted in Fig. 5.3.3, for $\phi = 0.40$ and 0.50, in both the x (large horizontal) and y (vertical) directions. The autocorrelation functions in the x direction behave as expected, decaying to zero at times larger than the correlation time. The autocorrelation function in the vertical direction shows the same behavior for the 40% sample; however for the 50% sample the autocorrelation function dips below zero, corresponding to a fairly strong anti-correlation at a time of about 0.84 s. Generally, this kind of behavior in the autocorrelation function is indicative of a periodic fluctuation in the system, with the anti-correlation peaking when the time difference is half of a period. Periodic volume fraction waves have been observed in fluidized beds at high volume fractions [Didwania & Homsy 1981 and Ham *et al.* 1990, for example], and they are also found to break up for volume fractions less than about 50-55% [Didwania & Homsy 1981]. These waves travel in the vertical direction, and therefore

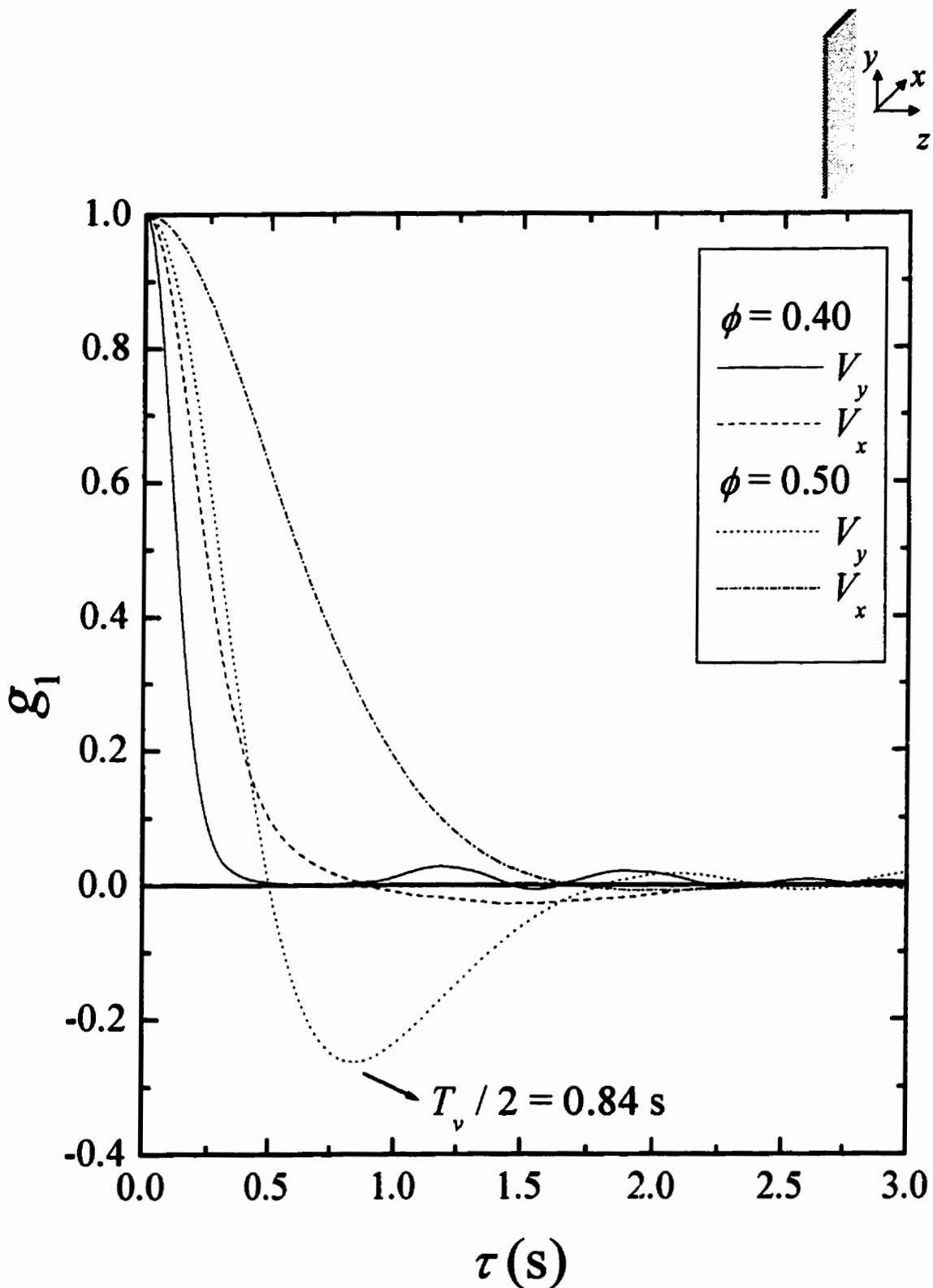


Figure 5.3.3: The measured autocorrelation functions in the vertical and horizontal directions, for $\phi = 0.40$ and 0.50 .

will only show up in the vertical component of the rms particle velocity, as we have observed. The voidage wave frequencies we observe are about 0.59 Hz for the samples with a Reynold's number of 0.9, and 1.8 Hz for the samples with $Re = 7$. These values are of the same order of magnitude as those found in previous experiments on somewhat different suspensions [Ham *et al.* 1990]. Even in the presence of voidage waves, the vertical rms velocity can still be estimated at $\phi = 0.50$, by using the early time behavior of the autocorrelation function, but the dynamic correlation length (the average distance a particle moves in the vertical direction before its vertical velocity is changed) can not be accurately determined.

For all other volume fractions, the determination of the rms velocity components followed the procedure discussed in Section 4.2 and 4.4. The results are plotted in Fig. 5.3.4, normalized by the single particle Stokes velocity. The error bars in the rms velocity represent a combination of several sources of uncertainty. The pulses contain a range of frequencies, and therefore there is an uncertainty in the effective ultrasonic wavelength. There also is uncertainty in the scattering angle as was discussed in Section 4.4. The fits of the phenomenological function discussed in Section 4.2 also introduce an error into the extracted rms velocity. There also is uncertainty in the normalizing velocity (in this case the Stokes velocity, in other cases the fluidization velocity). Finally, there is random statistical error because the fluidized suspension is a random system, and we are measuring a statistical average of its properties. Thus there is a combination of random and systematic errors, some of which are difficult to quantify exactly, and so the error bars shown are conservative, and likely overestimate the uncertainties.

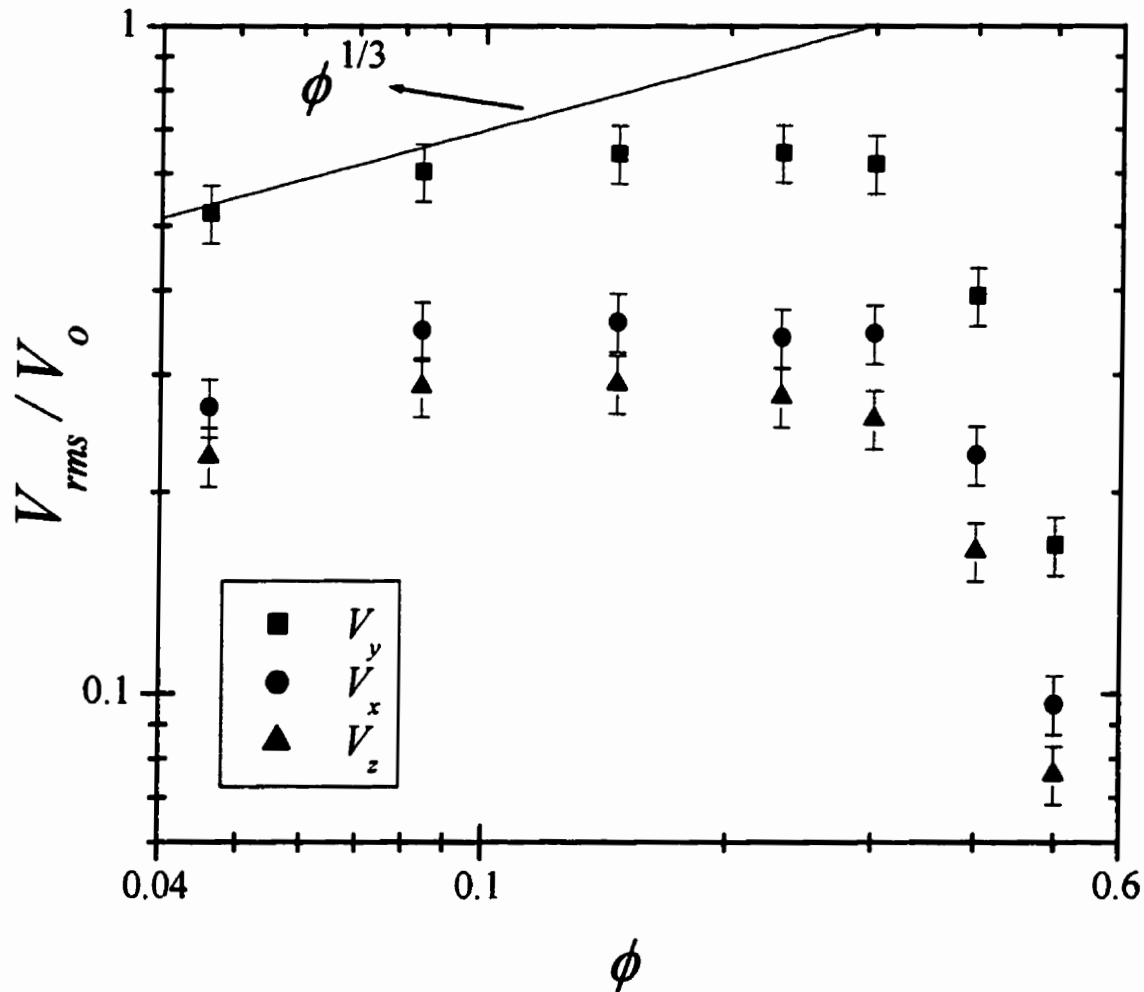
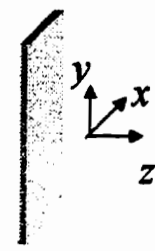


Figure 5.3.4: The measured rms velocity components normalized by the Stokes velocity, plotted as a function of ϕ , for the $L_z = 36.5$ mm sample with $Re = 0.9$.

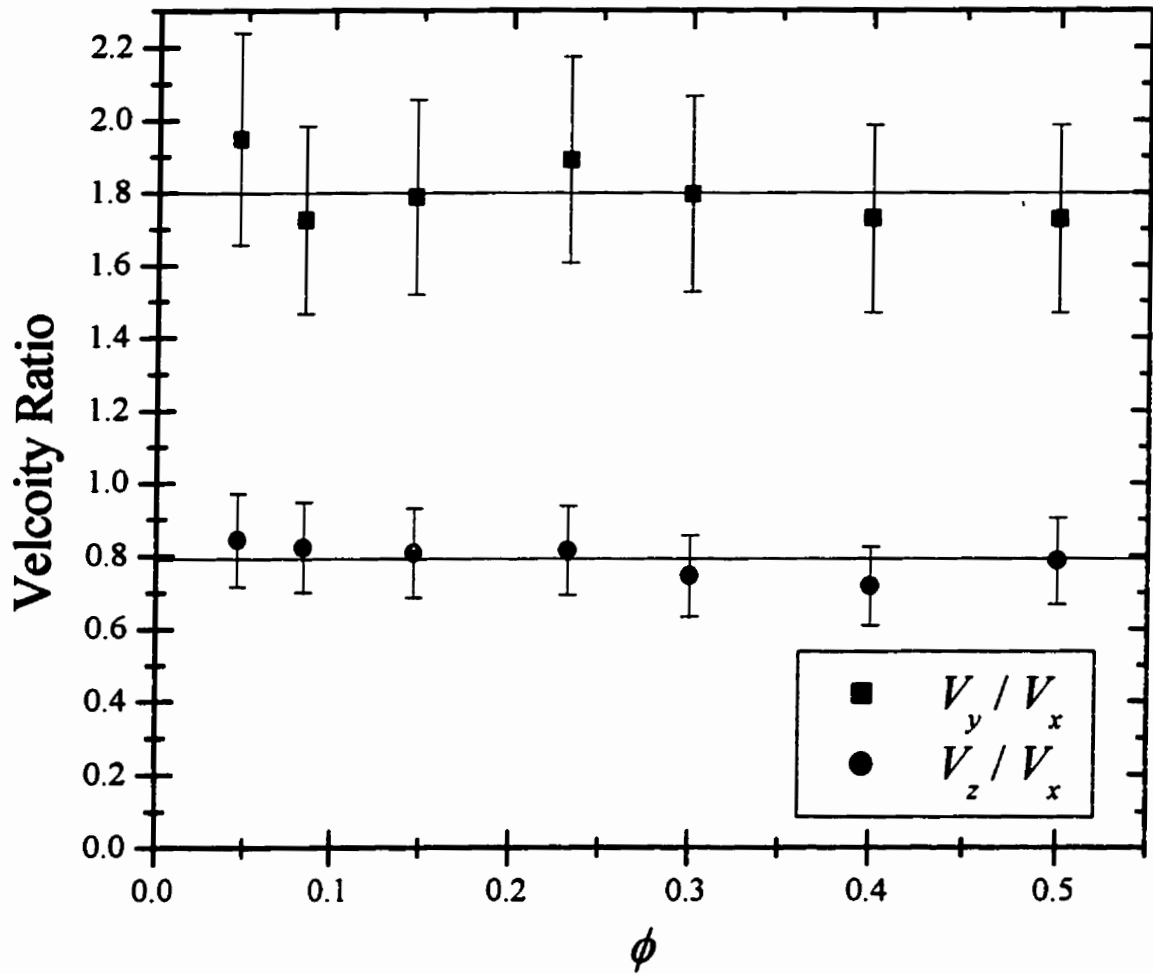
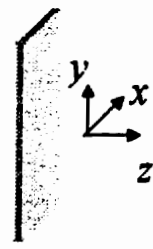


Figure 5.3.5: The ratio of the rms velocity components for $L_z = 36.5$ mm.

In Figure 5.3.4, the vertical component of the rms velocity is larger than both of the horizontal components, and the x -component is larger than the z -component. At low volume fractions, all components of the velocity increase with increasing ϕ , but between 10% and 30% the velocity is fairly constant, and above 30% it begins to drop again. Although we only have at most two data points in what could be considered the low volume fraction limit, the dependence is of order $\phi^{1/3}$ in this region. One of the most striking things about the data is that the ratio of the different components remains remarkably constant over the entire volume fraction range. This is shown in detail in Fig. 5.3.5, where the ratio of V_y to V_x is shown to be 1.8, and the ratio of V_z to V_x to be 0.79.

Rather than normalizing the rms velocity by the Stokes velocity (i.e. the fluidization velocity for a single isolated particle), it is more useful to normalize by the fluidization velocity for the volume fraction in question, as this is the relevant velocity scale in the suspension. This is done in Fig. 5.3.6 for the three components shown previously in Fig. 5.3.4. At low volume fractions, the volume fraction dependence of the vertical component is still approximately $\phi^{1/3}$, although it could be up to $\phi^{1/2}$ for the x and z -components. Both the $\phi^{1/3}$ dependence and the magnitude are in excellent agreement with previous low volume fraction (< 0.05) measurements of the y and x -components, performed on very low Reynolds number sedimenting suspensions by direct video imaging [Segrè *et al.* 1997]. In Fig. 5.3.4, the absolute (i.e. normalized by V_o) rms velocity decreased at large volume. Now, however, the rms velocity fluctuations normalized by the appropriate ϕ -dependent fluidization velocity actually increase as the volume fraction increases. This increase is much faster than $\phi^{1/3}$, in fact it is approximately linear in ϕ , and

it only begins to level off at $\phi \sim 0.50$. This increase has not been observed in recent video imaging of sedimenting suspensions at high volume fractions, where instead the velocity fluctuations were found to be roughly independent of ϕ for $\phi > 0.1$ [Segrè *et al.* 2001].

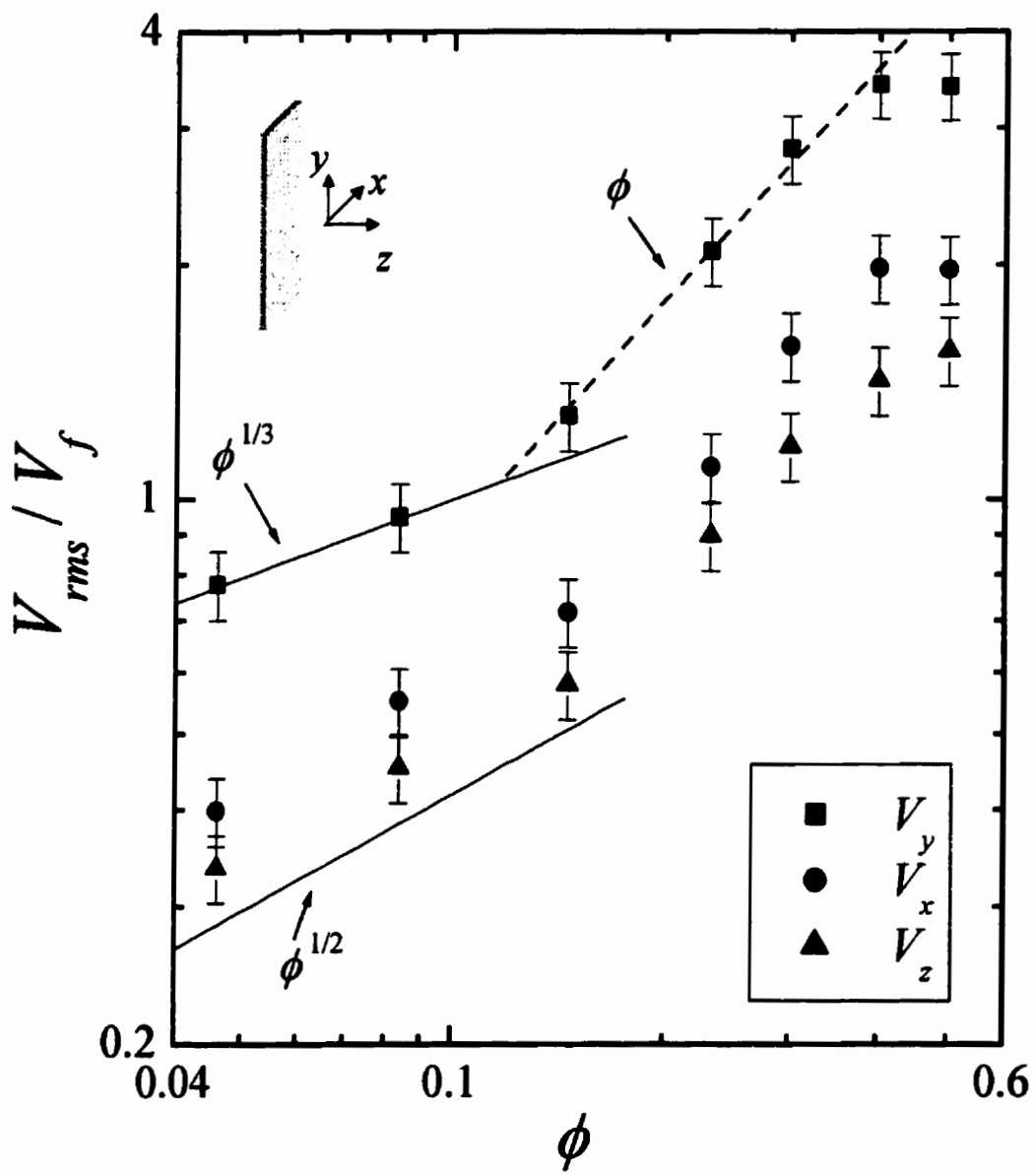


Figure 5.3.6: The measured rms velocity components normalized by the fluidization velocity, plotted as a function of ϕ , for the $L_z = 36.5$ mm sample with $Re = 0.9$.

5.3.4 Local Relative Velocity Fluctuations

DAWS measures the relative motion of scatterers separated by the transport mean free path of the ultrasonic wave, thus determining the relative mean square velocity. In Section 2.3.2, Eq. (2.79) relates $\Delta V_{rel}(l^*)$ to the spatial particle velocity correlation function at a particle separation of l^* . Thus by measuring $\Delta V_{rel}(l^*)$ for different l^* (by changing the ultrasonic frequency) as well as ΔV_{rms} , the spatial correlations between particle velocities can be probed. This is illustrated in Fig. 5.3.7, by plotting ΔV_{rel} as a function of l^* , for two different volume fractions, and fitting Eq. (2.79) to the data, assuming an exponentially decaying velocity correlation function. Of the two data sets chosen, the $\phi = 0.15$ data is representative of a good fit, and the $\phi = 0.23$ data is one of the poorer fits. Nonetheless, even the poorer fit is quite good, except perhaps for the data point at the highest value of the transport mean free path. At small particle separations, ΔV_{rel} scales as the square root of the separation distance l^* , consistent with an exponential decay of the velocity correlation function. At larger particle separations the velocity correlations weaken, and the relative velocity of the particles approaches $\sqrt{2} V_{rms}$, the value expected for particles that move randomly. As ΔV_{rel} approaches $\sqrt{2} V_{rms}$, both the data and theory rollover, at a separation corresponding to the instantaneous velocity correlation length ξ , defined by the exponential decay length of the velocity correlation function.

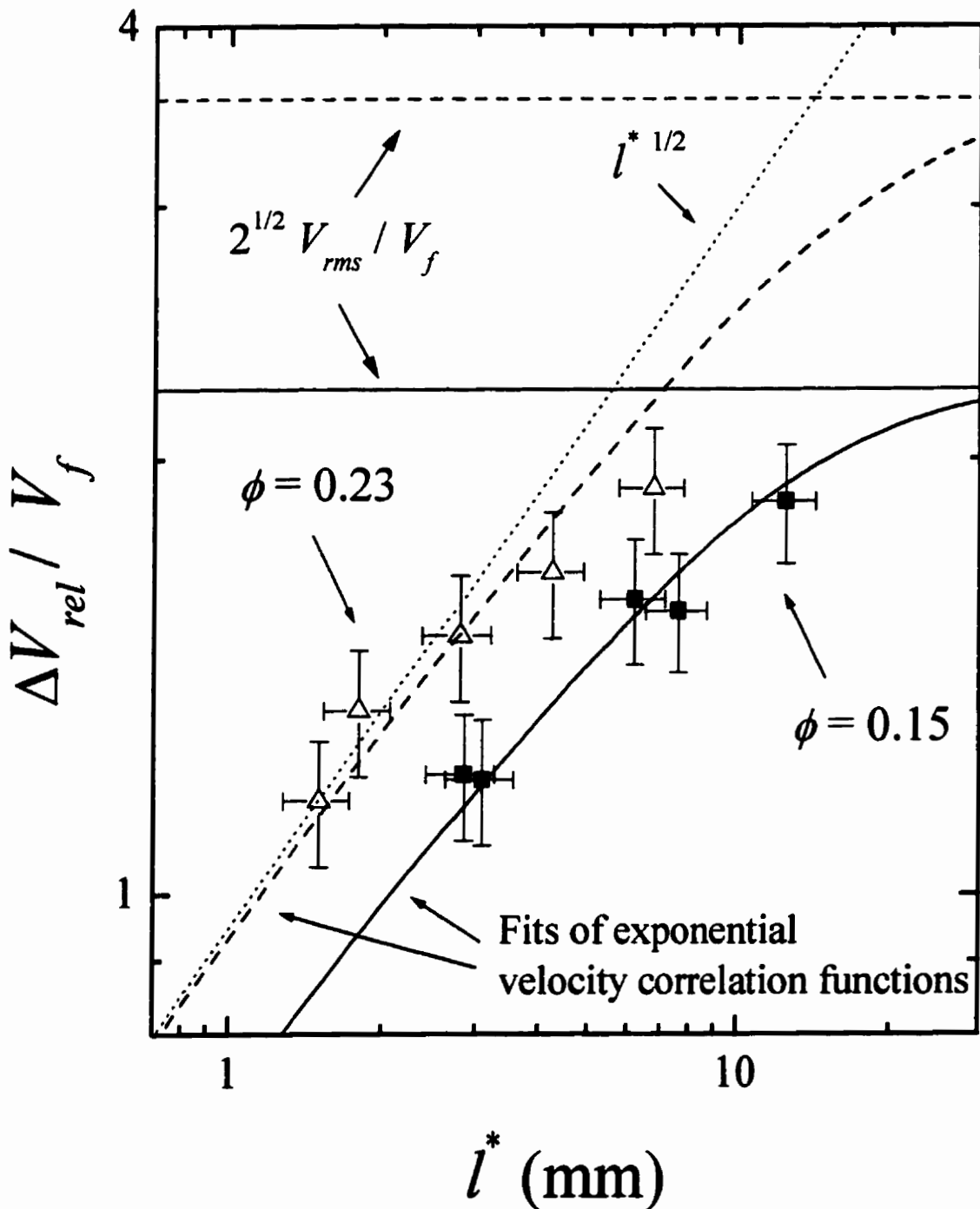


Figure 5.3.7: The measured rms relative velocity as a function of particle separation l^* , normalized by the fluidization velocity. Two volume fractions are shown, along with fits from Equation (2.79) with an exponentially decaying velocity correlation function.

In Fig. 5.3.8, ΔV_{rel} data from all of the samples are plotted on normalized scales. The relative velocity is normalized by the corresponding rms velocity, and the particle separation is normalized by the measured instantaneous velocity correlation length. Remarkably, all of the data collapse onto a single curve, corresponding to an exponential velocity correlation function. This scaling means that the spatial velocity correlation function is well described by an exponential decay in all of our samples and for effective particle separations spanning two orders of magnitude. Thus the measured instantaneous velocity correlation lengths, ξ , are found in a consistent manner for all of our samples and volume fractions, and therefore the results can be directly compared to each other.

While DAWS measurements give a probe of the extent of the instantaneous spatial velocity correlations in fluidized suspensions, they also allow the relative motion of *nearest neighbor* particles to be measured. The reason for this is illustrated in Fig. 5.3.9, where I have plotted the minimum values of ℓ' as a function of ϕ , and compared these values with an estimate of the average nearest-neighbor interparticle separation [Cowan *et al.* 2000]. Over much of the volume fraction range, the minimum particle separation measured is comparable to the nearest neighbor distance; it is only at the lowest volume fractions that DAWS begins to measure the relative motion of next nearest neighbors. Furthermore, by using the scaling of the relative velocity that was demonstrated in Fig. 5.3.8, one can extrapolate or interpolate ΔV_{rel} to the nearest neighbor particle separation. This means that DAWS is a direct probe of the local motion of the particles, right down to the shortest distances over which the relative motion can be defined in the suspensions.

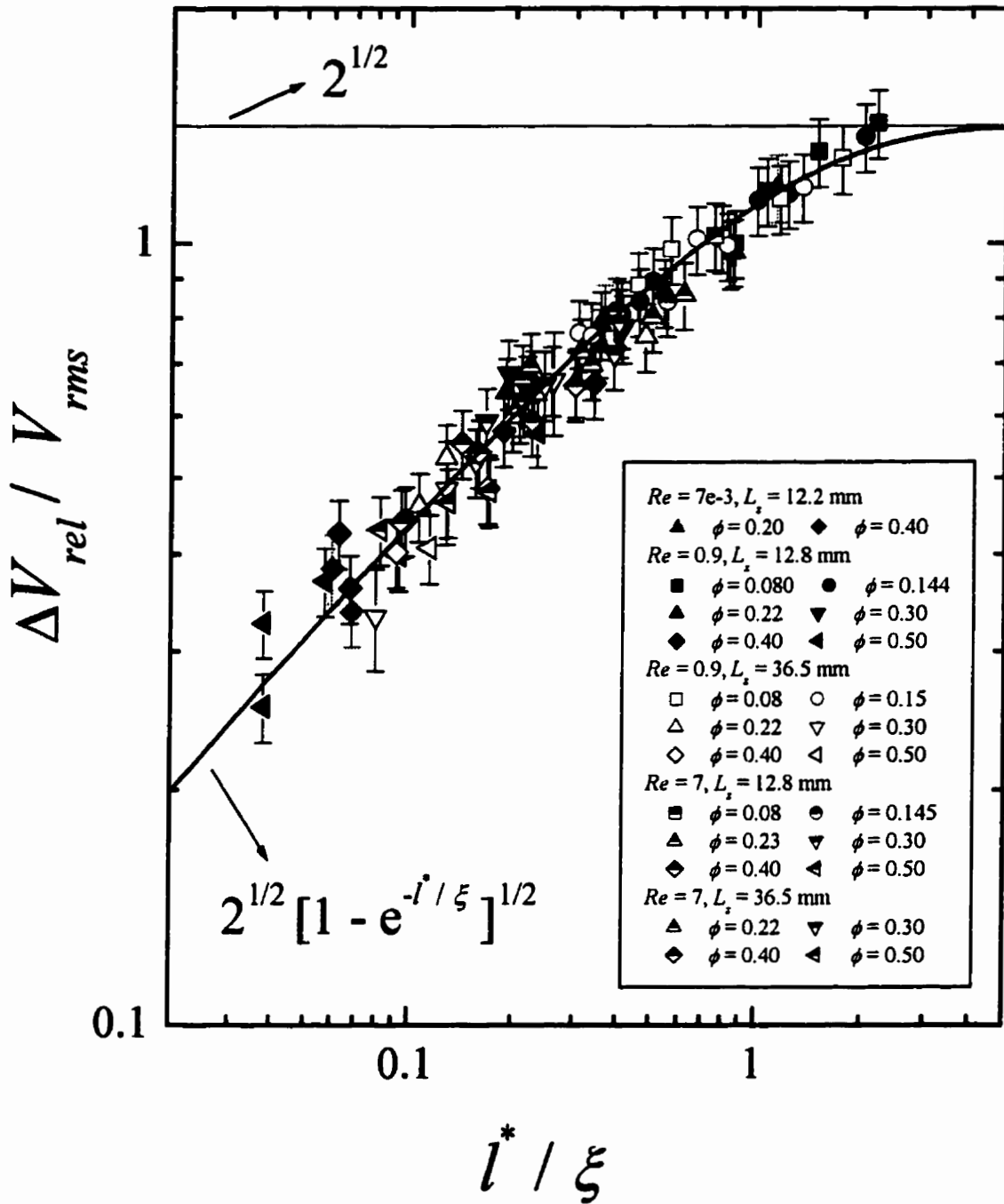


Figure 5.3.8: The relative velocity scaled by the rms velocity, and plotted as a function of the particle separation scaled by the measured correlation length. Data from all of the samples fall onto the same curve, governed by an exponentially decaying velocity correlation function.

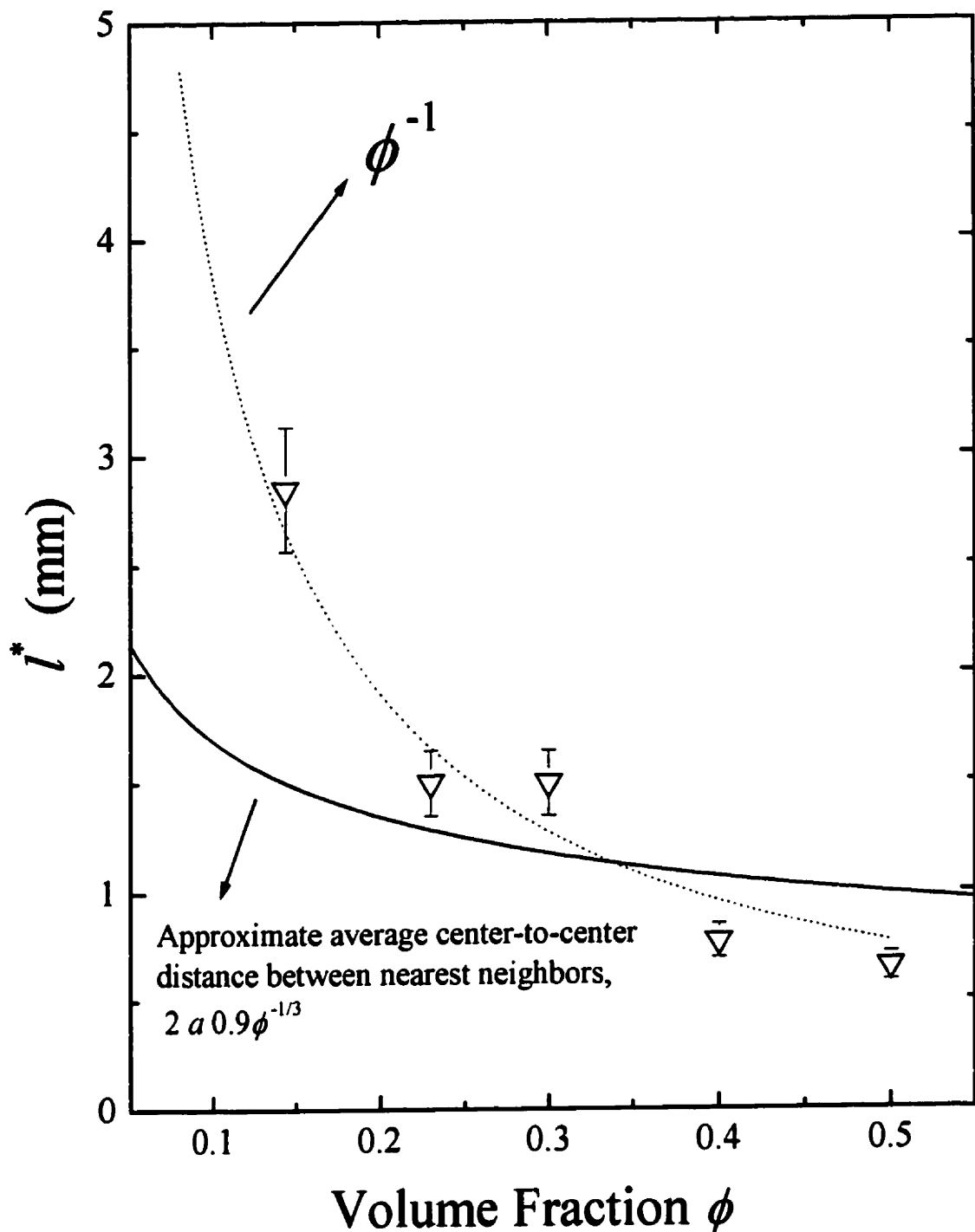


Figure 5.3.9: The shortest values of i^* used in relative velocity measurements, compared with the average nearest neighbor separation of the particles.

In Fig. 5.3.10(a), the relative velocity of nearest neighbors (normalized by the fluidization velocity) is plotted as a function of the volume fraction, for all three sample thicknesses L_z at a Reynolds number of 0.9. The data from the three sample sizes agree with each other remarkably well, with the only significant difference showing up at the lowest volume fraction. The overall magnitude of the local relative velocity is of order the fluidization velocity, and not much smaller than the rms particle velocity. The data have a $\phi^{1/3}$ dependence from low volume fractions up to 40%, above which the relative velocity drops down again. Measuring the local relative velocity means that we can measure the local strain rate in the suspension, defined by

$$\Gamma = \frac{\Delta V_{rel}(r_n)}{r_n} , \quad (5.10)$$

where r_n is the nearest neighbor separation. This strain rate is plotted in Fig. 5.3.10(b), normalized by the characteristic time that it takes the fluid to travel a bead radius, a/V_f . The strain rate is quite large, approaching a maximum of about 0.6, indicating that there are large local rearrangements of the particles taking place in a relatively short period of time. The local strain rate has a $\phi^{2/3}$ dependence at volume fractions less than 40%, and it is independent of L_z .

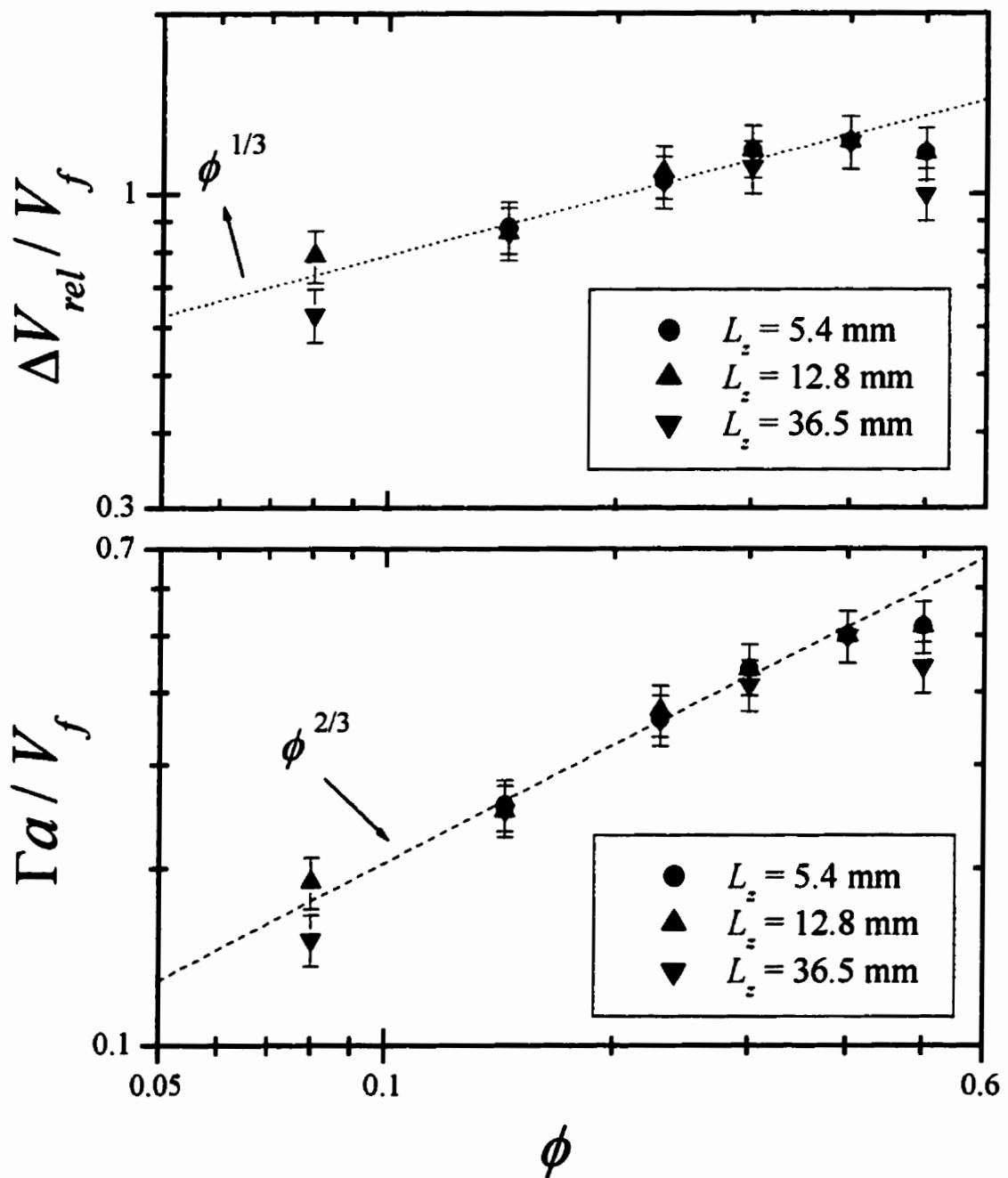


Figure 5.3.10: The relative rms velocity and average local strain rate, extrapolated or interpolated to the nearest neighbor particle separation. Data from all three sample thicknesses at a Reynolds number of 0.9 are shown.

5.3.5 Velocity Correlation Lengths

By using DSS to measure the mean square displacement of the particles in the suspension, both the rms velocity and a crossover or correlation time can be determined. This correlation time, when multiplied by the rms velocity, gives the dynamic correlation length d_c , which is the rms distance traveled by a particle before its velocity is changed through interactions with its neighbors (mediated by the fluid). As discussed in the last section, by using both DAWS and DSS the instantaneous particle velocity correlation length can also be measured. The instantaneous correlation length is the average distance over which the instantaneous velocities of particles are correlated, i.e. the size of the correlated region in a “snapshot” of the velocities of the particles at one instant in time. In this section, our results for both of these correlation lengths will be discussed and compared.

Far-field DSS gives access to the dynamic correlation lengths in all three directions, e.g. the average distance traveled in the x direction before the x -component of the rms velocity is changed. The technique also gives the three-dimensional dynamic correlation length, i.e. the average distance traveled before the full 3-d rms velocity is changed. The components of the dynamic correlation length are plotted in Fig. 5.3.11 for the thickest sample, at a Reynolds number of 0.9. The most striking feature of the data is that the vertical (y) component of the dynamic correlation length changes significantly with volume fraction, and is generally larger than the x and z -components, which do not change very much as the volume fraction is varied. In this thickest sample, the z -component is only slightly less than the x -component on average (both are of order 5-7

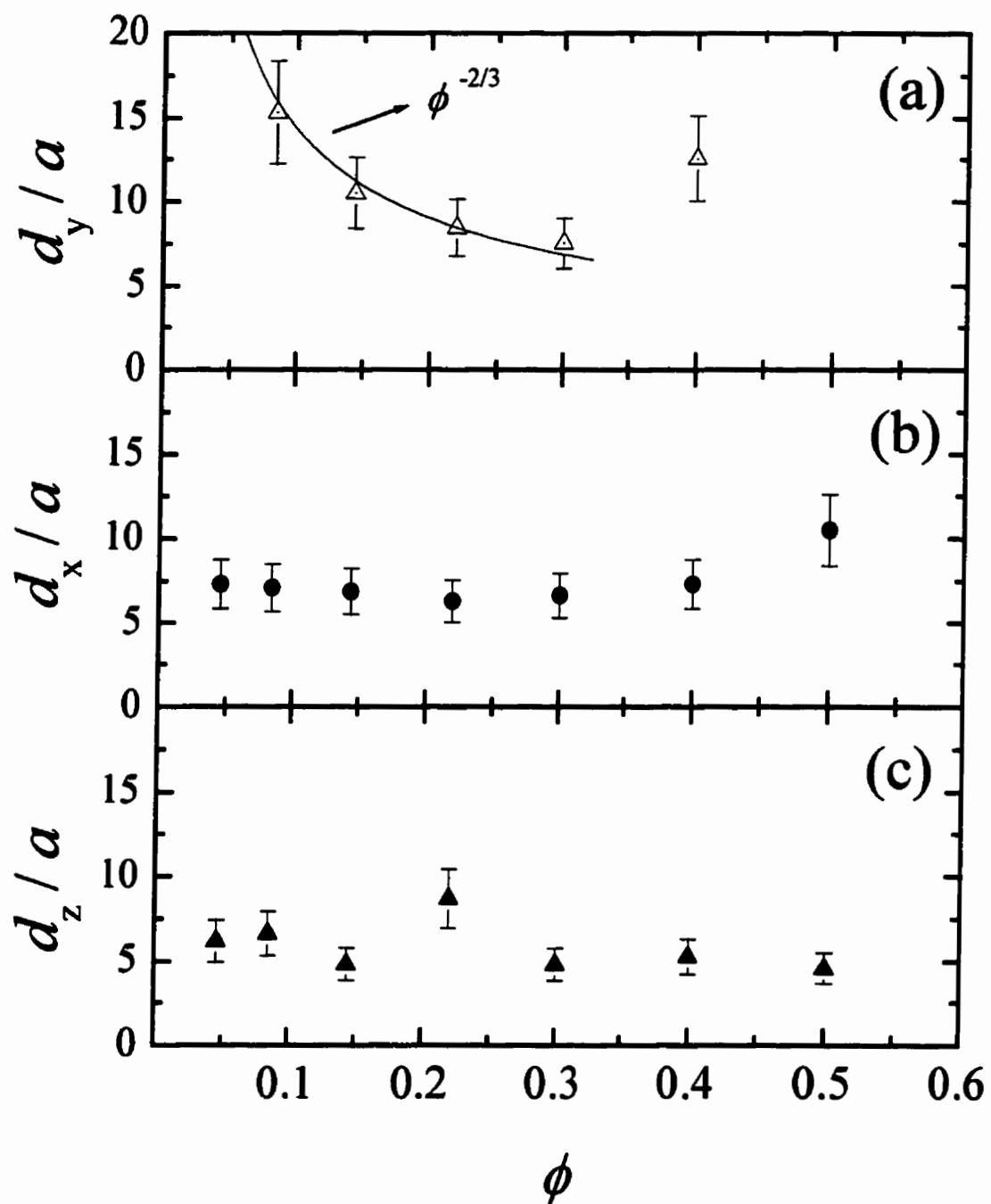


Figure 5.3.11: The components of the dynamic correlation length, normalized by the particle radius and plotted as a function of volume fraction.

bead radii), while the y -component is up to two times larger, varying from 7 to 15 bead radii over the range of volume fractions measured. The y -component has an approximately $\phi^{-2/3}$ dependence on volume fraction up to about $\phi = 0.30$, above which it increases. The horizontal components are independent of ϕ within error bars, with the z -component about 0.8 times the size of the x -component, approximately the same as the ratio of the rms velocity components found earlier [Fig. 5.3.5]. Recall [from Table 3.3] that the sample thickness L_z is 36.5 mm (83 bead radii), the width L_x is 178 mm (407 a) and the height is 450 mm (1030 a), so that all of the measured dynamic correlation lengths shown in Fig. 5.3.11 are considerably less than the dimensions of the fluidized bed.

The full three-dimensional dynamic correlation length can also be found by combining the data taken along the three directions; the result is plotted in Fig. 5.3.12, along with the instantaneous correlation length. The dynamic correlation length has a $\phi^{-1/3}$ dependence at low volume fractions, up to $\phi = 0.30$. It is smaller than the instantaneous correlation length, by a factor of about 1.5 at low volume fractions, giving the physical picture of large instantaneously correlated regions, or swirls, which break apart as the particles interact. The instantaneous correlation length also has a $\phi^{-1/3}$ dependence at low volume fractions, and again the magnitude is in excellent agreement with video imaging measurements at lower Reynolds numbers [Segrè *et al.* 1997]. However, above about $\phi = 0.15$, the instantaneous correlation length begins to increase quite quickly, with an approximately linear ϕ dependence. As a result, the dynamic length is up to a factor of 4 smaller than the instantaneous correlation length at large volume fractions, meaning that the correlated swirls are relatively short lived. Note that the low volume fraction $\phi^{-1/3}$

dependence of the instantaneous correlation length corresponds to a correlation volume, ξ^3 , with a ϕ^{-1} dependence, and thus the number of particles in the correlated swirl remains constant at low volume fractions. However at large volume fractions we find that the volume of the correlated region increases as approximately ϕ^3 , meaning that the number of particles in a correlated swirl in our fluidized suspensions increases, as approximately ϕ^4 . This observation is in contrast to the results of recent video imaging experiments on low Reynolds number sedimenting spheres [Segrè *et al.* 2001], which found that the number of particles in the correlated regions remained roughly constant at high volume fractions just as at low volume fractions.

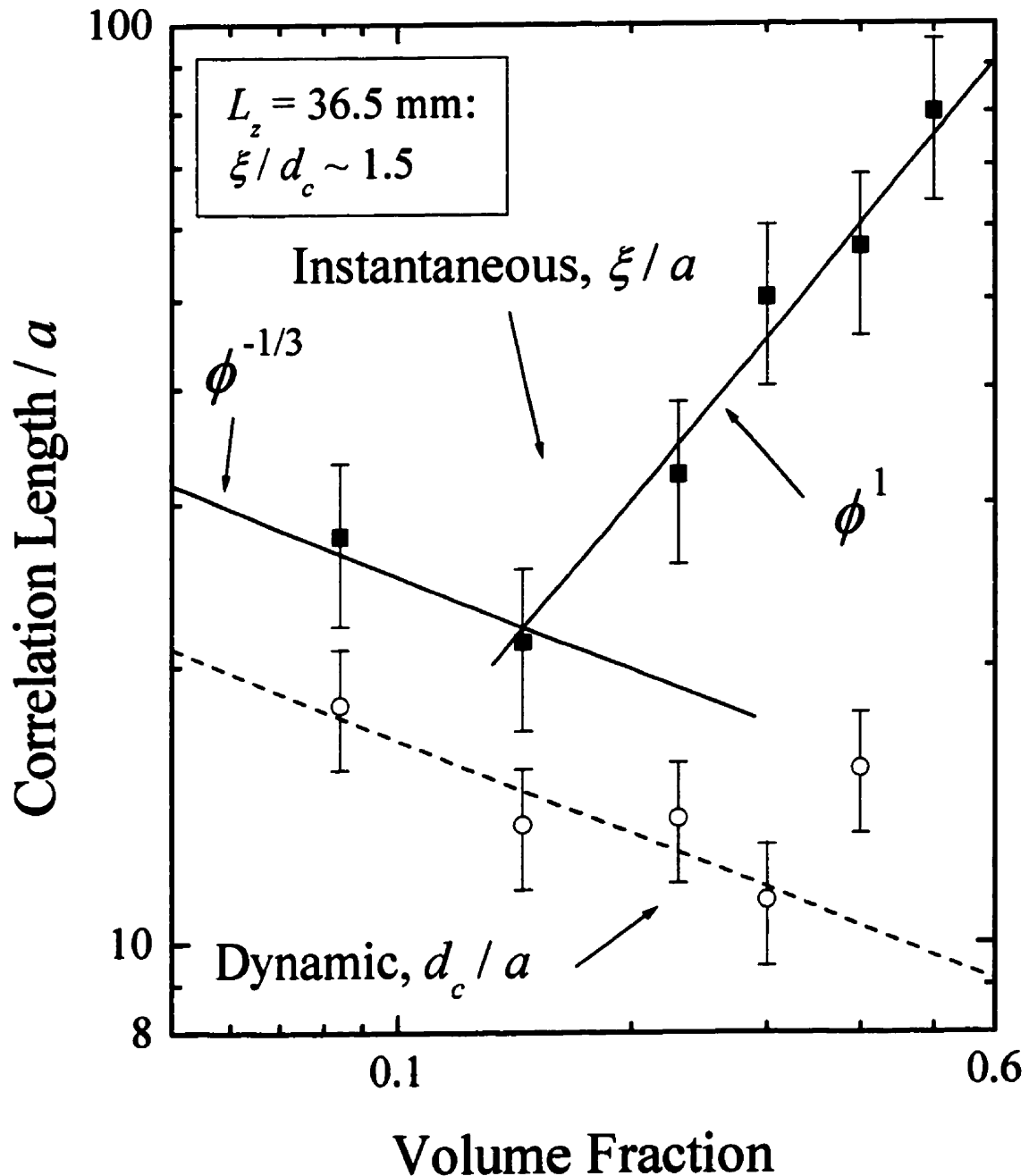


Figure 5.3.12: The three-dimensional instantaneous and dynamic correlation lengths, normalized by the particle radius and plotted as a function of volume fraction.

5.3.6 Discussion of the Volume Fraction Dependence

The results from the last sections described the scaling of the correlation lengths and average particle velocities with the volume fraction of particles in the suspension. We found the following scaling relations:

$$\begin{aligned}
 \frac{V_{rms}}{V_f} &\sim \frac{V_{rms}}{V_o} \sim \phi^{1/3} & \phi < 0.1 \\
 \frac{V_{rms}}{V_f} &\sim \phi & \phi > 0.1 \\
 \xi/a &\sim \phi^{-1/3} & \phi < 0.15 \\
 \xi/a &\sim \phi & \phi > 0.15 \\
 d_c/a &\sim \phi^{-1/3} & \phi < 0.3 \\
 \frac{\Delta V_{rel}(r_{nn})}{V_f} &\sim \phi^{1/3} & \phi < 0.4 \\
 \Delta V_{rel}(r) &\sim r^{1/2} & r < \xi
 \end{aligned} \tag{5.11}$$

Here r_{nn} is the average nearest neighbor distance, which scales as $\phi^{-1/3}$. As far as we are aware, theories have only attempted to model the rms velocity and the instantaneous correlation length. In the low volume fraction limit we do not see the scaling laws predicted by Koch & Shaqfeh [1991] or Levine *et al.* [1998], and the existence of a instantaneous correlation length smaller than the system size rules out the simple Caflisch & Luke [1985] scaling. However, Brenner [1999] does predict the volume fraction scaling that we observe [Sec. 2.4.2].

To understand these scaling laws in more detail we consider the simple heuristic “blob” model, following Hinch *et al.* [1988], Segrè *et al.* [1997 & 2001] and Brenner [1999]. In this model we consider a correlated blob of particles moving with an average

velocity V_y in the vertical direction. The volume of the average blob will be $\sim \xi_x \xi_y \xi_z$. If the particle distribution is random, the average number of particles in the blob, $\langle N \rangle_\xi$, will fluctuate as $\Delta N_\xi = \sqrt{\langle N \rangle_\xi}$, leading to a net deficit or surplus of particles compared to the average background. This will lead to a buoyant force, F_B on the blob, which will be balanced by a viscous drag, F_D :

$$F_B = \frac{4}{3}\pi a^3 \Delta \rho g [\Delta N_\xi] = \frac{4}{3}\pi a^3 \Delta \rho g \phi^{\frac{1}{2}} \sqrt{\frac{\xi_x \xi_y \xi_z}{a^3}} \quad (5.12)$$

$$F_D = 6\pi\eta \sqrt{\xi_x \xi_z} V_y .$$

Balancing these two forces leads to

$$\frac{V_y}{V_o} \sqrt{\frac{a}{\xi_y}} = \phi^{\frac{1}{2}} . \quad (5.13)$$

If we identify the size of the “blob” with the instantaneous correlation length, this equation relates the vertical components of the rms velocity and instantaneous correlation length. Since the vertical components dominate the horizontal components, Eq. (5.13) also approximately relates the full 3-d rms velocity and instantaneous correlation length¹. Also note that at constant volume fraction this result means that the correlation length will be proportional to the square of the rms velocity. The low volume fraction scaling laws found in our experiments are consistent with Eq. (5.13).

Segrè *et al.* [2001] have proposed a way to extend the “blob” model to the high volume fraction regime. To do this they use an estimate of the effective viscosity of a

¹ Although we can not separate the spatial components of ξ using DAWS, the data from Segrè *et al.* [1997 & 2001] implies that the difference between the ratios $V_y/\sqrt{\xi_y}$ and $V/\sqrt{\xi}$ is only $\sim 5\%$ in a sample that is sufficiently thick that the x and z -components are equivalent.

non-Brownian suspension $\eta(\phi)$ instead of the fluid viscosity in Eq. (5.12). As well, they argue that the fluctuation in the number of particles in the blob can no longer simply be $\sqrt{\langle N_\xi \rangle}$, because volume exclusion effects reduce the available particle configurations (i.e. the particle positions can no longer be entirely random because the spheres can not overlap). Therefore the number fluctuations are suppressed by a factor of $\langle \Delta N \rangle / \sqrt{\langle N \rangle} = \sqrt{S(0, \phi)}$ for very large volumes (or very large $\langle N \rangle$), where $S(0, \phi)$ is the static structure factor in the $q = 0$ limit [Segrè *et al.* 2001, Russel *et al.* 1989, Lei *et al.* 2001]. More generally [Hansen & McDonald 1976], the number fluctuations are given by

$$\frac{\langle \Delta N \rangle^2}{\langle N \rangle} = 1 + \frac{\langle N \rangle}{V} \int_V [g^{(2)}(r, \phi) - 1] d^3 r, \quad (5.14)$$

where V is the volume of interest and $g^{(2)}$ is the pair distribution function, which is related to $S(q, \phi)$ through its Fourier transform

$$S(q, \phi) = 1 + \frac{\langle N \rangle}{V} \int_{-\infty}^{\infty} [g^{(2)}(r, \phi) - 1] e^{-iq \cdot \vec{r}} d^3 \vec{r}. \quad (5.15)$$

If the particle positions are uncorrelated, $g^{(2)} = 1$, and Eq. (5.14) gives random Poisson statistics. If, on the other hand, the average value of the pair distribution function in the volume of interest is not 1, then the number fluctuations can be either suppressed or enhanced. Also, note that it is only for an effectively infinite volume (or equivalently average number of particles) that the relationship $\langle \Delta N \rangle / \sqrt{\langle N \rangle} = \sqrt{S(0, \phi)}$ holds true.

Allowing for the possibility that $\Delta N_\xi \neq \sqrt{\langle N \rangle_\xi}$ and accounting for the ϕ dependence of η in Eq. (5.12), the original scaling argument [Eq. (5.12)] becomes

$$\frac{V_{rms}}{V_f} \sqrt{\frac{a}{\xi}} \equiv \phi^{\frac{1}{2}} \left[\frac{\eta(0)}{\eta(\phi)} \frac{\Delta N_\xi}{\sqrt{\langle N \rangle_\xi}} \frac{V_o}{V_f(\phi)} \right]. \quad (5.16)$$

The left hand side of Eq. (5.16) is plotted in Fig. 5.3.13(a) for all of the samples with $Re = 0.9$. The different sample thicknesses agree with each other within error bars, and they scale as $0.93\phi^{1/2}$. This means that at this Reynolds number

$$\left[\frac{\eta(0)}{\eta(\phi)} \frac{\Delta N_\xi}{\sqrt{\langle N \rangle_\xi}} \frac{V_o}{V_f(\phi)} \right] \approx 0.93. \quad (5.17)$$

This relation is in contrast to the results of Segrè *et al.* [2001], where the quantity in the square brackets was not independent of ϕ , but varied from 0.9 at $\phi = 0.1$ to 0.5 at $\phi = 0.5$.

To explain their results, Segrè *et al.* [2001] have approximated the number fluctuations by $\Delta N_\xi / \sqrt{\langle N \rangle_\xi} \approx \sqrt{S(0, \phi)}$, and used an expression for $S(0, \phi)$ based on volume exclusion effects in a random Brownian particle system, arguing that this expression will also hold for non-Brownian particles. They have also proposed an approximate form for $\eta(0)/\eta(\phi)$, based on measurements in suspensions of nm-sized colloidal particles. The effective viscosity of a suspension of these suspensions of Brownian particles is approximately given by, [Russel *et al.* 1989]

$$\frac{\eta(\phi)}{\eta(0)} = \left[1 - \frac{\phi}{0.63} \right]^{-2} \quad (5.18)$$

in the low shear rate limit, and

$$\frac{\eta(\phi)}{\eta(0)} = \left[1 - \frac{\phi}{0.71} \right]^{-2} \quad (5.19)$$

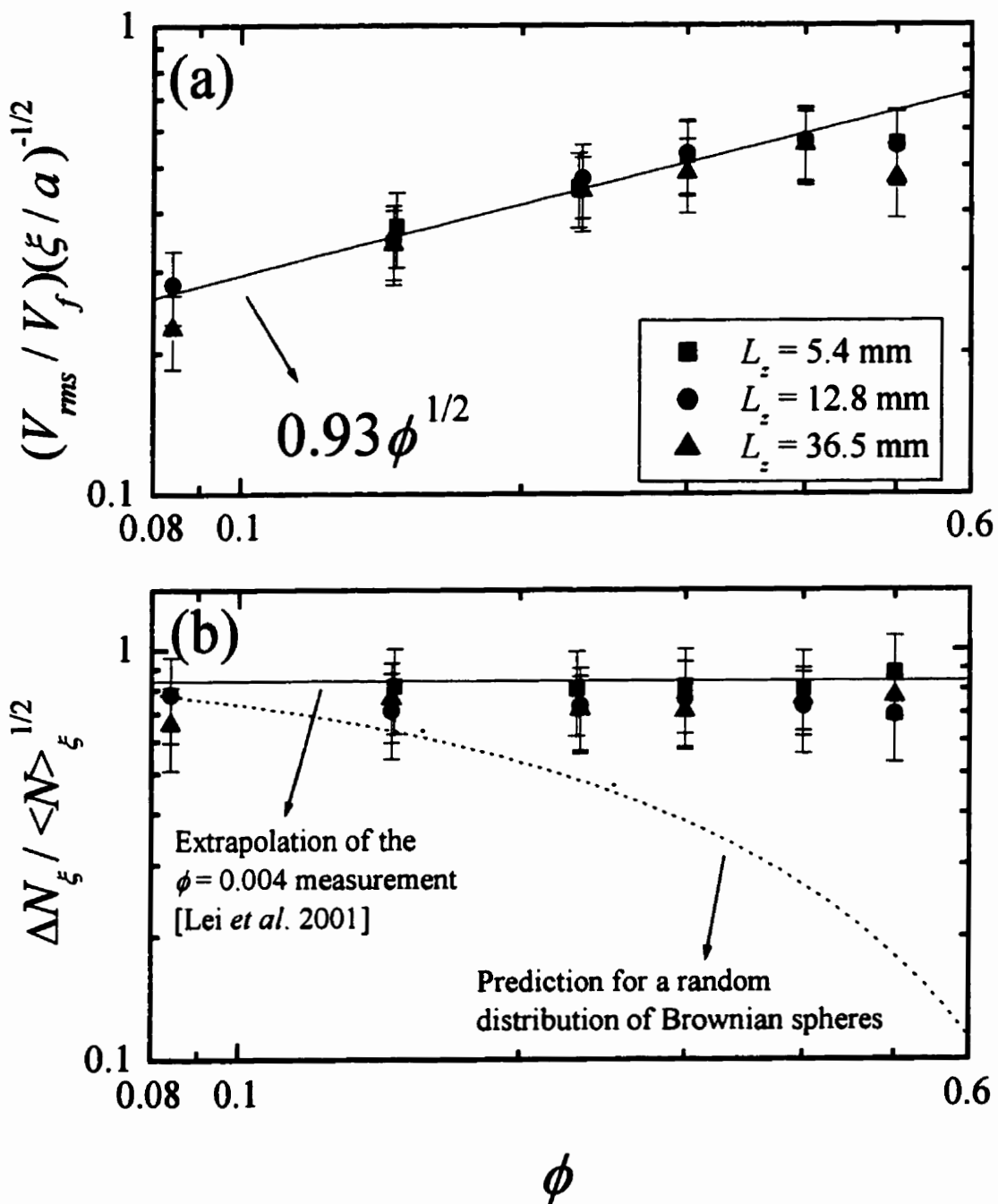


Figure 5.3.13: (a) The high volume fraction scaling of the “blob” model, for all of the $Re = 0.9$ data.
 (b) The estimate of the number fluctuations in the correlation volume, using the estimate of the effective viscosity and the data in (a).

in the high shear rate limit. Segrè *et al.* [2001] have chosen to use the high shear rate limit for $\eta(\phi)$. They argue that at high shear rates viscous effects dominate Brownian motion, which suggests that the high shear rate result may be more applicable to non-Brownian suspensions. Using these assumptions, they find quite good agreement with their data for the instantaneous correlation length and rms velocity fluctuations.

However, the basic assumption of the Segrè *et al.* [2001] model for $S(0,\phi)$, namely that without volume exclusion effects the particle number fluctuations follow the Poisson distribution, has been called into question by recent measurements by Lei *et al.* [2001]. In these video imaging experiments, the number fluctuations were measured directly in a very dilute sedimenting suspension ($\phi = 0.004$), where volume exclusion effects are negligible. Nonetheless, quite strong suppression of the number fluctuations was seen, especially for large volumes (or large $\langle N \rangle$) and long sedimentation times, suggesting that there is a small amount of long range order in the particle positions. This suppression also evolves during sedimentation, at least in relatively large cells. For a random Poisson distribution of particle positions, as the length scale is increased, the rms velocity will also increase; i.e. the rms velocity will diverge with increasing sample size as per the Caflisch & Luke [1985] result. However, suppression of number fluctuations as the length scale is increased would have the effect of suppressing the expected divergence of the velocity fluctuations with sample size [c.f. Eq. (5.16)], in effect setting a velocity correlation length. In fact, the decay of the number fluctuations as the sampling volume is increased can be viewed as the mechanism that leads to an instantaneous velocity

correlation length [Lei *et al.* 2001].

Using Eq. (5.16), our data can be used to estimate the suppression of the fluctuations in the number of particles in a correlation volume:

$$\frac{\Delta N_\xi}{\sqrt{\langle N \rangle_\xi}} \sim \frac{V_{rms}}{V_o} \left[\phi \frac{\xi}{a} \right]^{\frac{1}{2}} \frac{\eta(\phi)}{\eta(0)}. \quad (5.20)$$

To model the effective viscosity of our suspensions we use the low shear rate limit [Eq. (5.18)], whereas Segrè *et al.* [2001] used the high shear rate viscosity. We use the low shear rate viscosity because it diverges at random close packing ($\phi = 0.63$), consistent with our observation that the suspension no longer acts as a fluid when it is not fluidized and has settled at random close packing. The results of using this viscosity and our data to estimate the number fluctuations in the correlation volume are shown in Fig. 5.3.13(b). Also shown in Fig. 5.3.13(b) is the extrapolation of the measured number fluctuations in a correlation volume at $\phi = 0.004$ from Lei *et al.* [2001], although this is admittedly only an estimate, since they have not yet reached the steady state in their experiments (the number fluctuations are still evolving in time)². Our data are essentially independent of volume fraction and sample thickness over the entire volume fraction range measured, and are similar in magnitude to the estimate from Lei *et al.* [2001]. Also shown for comparison is the suppression of the number fluctuations expected in a random distribution of Brownian spheres due to volume exclusion effects (in large sample volumes) [Segrè *et al.* 2001]. If the decay of the suppression of the number fluctuations with increasing sampling volume

² In fact, recent video imaging measurements of sedimentation in cells that were much larger than those in Segrè *et al.*'s experiments [1997 & 2001] suggest that equilibrium is never reached if the cell dimensions are large ($L_s \gg \xi$) [Shang-You Tee & D. A. Weitz, personal communication]. This finding is in contrast to fluidization, where we reach equilibrium even in our largest cell.

is what sets the instantaneous velocity correlation length, one would expect that $\Delta N/\sqrt{\langle N \rangle}$ measured in a correlation volume will be a constant value, independent of the actual size of the correlation volume, and thus the volume fraction and cell size. This is what we see in Fig. 5.3.13(b), implying that the decay of the number fluctuations is the underlying mechanism behind the instantaneous velocity correlation length. The question of what causes the number fluctuation decay remains unresolved, and some possibilities will be addressed in the next two sections.

The “blob” model only considers the effect of the rms velocity and instantaneous correlation length, taking the view that these are what control the scaling of the dynamics. Another perspective on the dynamics is to consider the local fluctuations in the velocities of neighboring particles, which give rise to the local relative velocity measured by DAWS. As the length scale, r , is increased, i.e. as we look at the relative velocity of particles further apart in the suspension, the relative velocity increases as $r^{1/2}$. This divergence of ΔV_{rel} with sample size is eventually cut-off at larger lengths, once the r^{-1} dependence of the fluid flow field is cut-off by wall, inertial effects, or other intrinsic effects [Sec. 2.4.2, and Sections 5.3.7 and 8]. From this perspective, the size of the rms velocity can be seen to be the result of the magnitude of the rms local relative velocity, and the length scale ξ at which this divergence is cut-off:

$$V_{rms} \approx \frac{\Delta V_{rel}(r_{nn})}{\sqrt{2}} \sqrt{\frac{\xi}{r_{nn}}}, \quad r_{nn} \ll \xi \quad (5.21)$$

$$V_{rms} \xi^{-\frac{1}{2}} \approx \Delta V_{rel}(r_{nn}) / \sqrt{2r_{nn}} .$$

Given the measured volume fraction scaling summarized in Eq. (5.11), our data are

consistent with this interpretation at both high and low volume fractions. This is shown in detail in Fig. 5.3.14, which plots Eq. (5.21) as a function of volume fraction. In that figure we see that Eq. (5.21) holds true for all Reynolds numbers and sample sizes investigated.

As was shown previously in Fig. 5.3.10, the local relative velocity is independent of sample thickness L_z , whereas we shall see in the next section that both the rms velocities and correlation lengths increase as the sample size is increased. This reinforces the picture that the collective dynamics are controlled by both the local behavior of the particles, which is independent of sample size, and the correlation length, which we shall see is controlled by both sample size and inertial effects for the range of cell sizes studied in this thesis.

The “blob” model and the local fluctuation model of the volume fraction scaling provide different and complementary perspectives on what controls the particle dynamics. In the “blob” model, it is statistical fluctuations in the number of particles in a correlated region that controls the dynamics - a large-scale, collective point of view. In the local fluctuation picture, the local interactions and resulting local velocity fluctuations ultimately control the magnitude of the rms velocity, in combination with a correlation length that is imposed by either boundary conditions, inertial effects, or other intrinsic effects (as will be discussed in Sections 5.3.7 and 8). Equation (5.21) and Fig. 5.3.14 suggest that ΔV_{rel} is a fundamental quantity, which sets the ratio $V_{rms}/\sqrt{\xi}$. This realization, one important consequence of our DAWS measurements, should motivate the development of a fundamental theory for ΔV_{rel} .

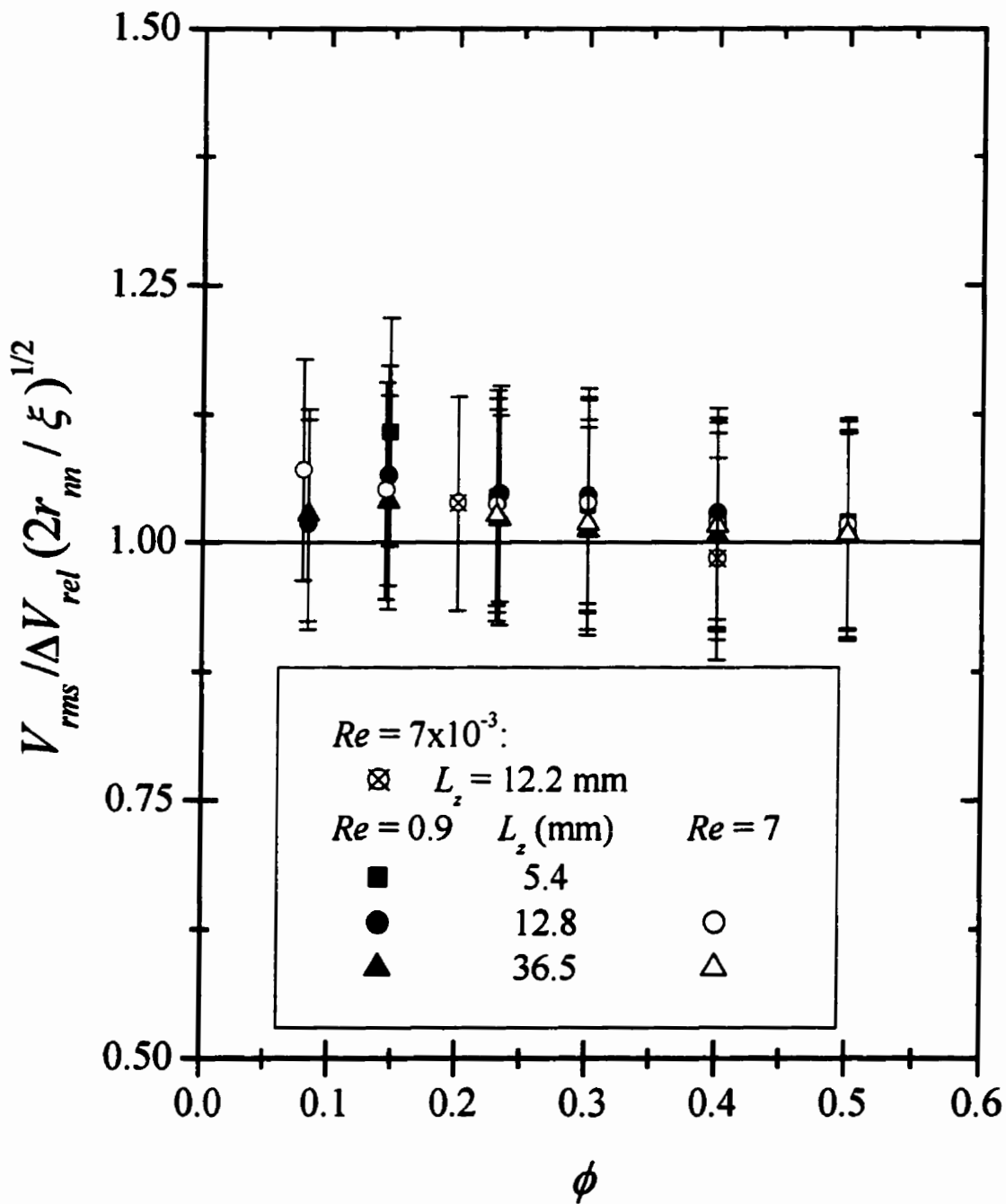


Figure 5.3.14: The demonstration of the agreement of our data with the volume fraction scaling from the local fluctuation model, for all of our samples.

5.3.7 Sample Size Dependence

To investigate the sample size dependence, three different sample thicknesses (L_z) where used: 5.4 mm (= 12.3 α), 12.8 mm (= 29.3 α) and 36.5 mm (= 83.4 α). Depending on the volume fraction, these thicknesses range from a small fraction of ξ up to several times ξ . The rms velocities and instantaneous and dynamic correlation lengths were measured for each thickness, at volume fractions ranging from 0.04 to 0.5. In this section, we will first present the results of this investigation, and then discuss their implications.

The components of the rms velocity for the three thicknesses are plotted in Fig. 5.3.15. Despite some scatter in the data, the same general volume fraction dependence is seen for all three thicknesses. All three components show a decrease as the sample thickness is reduced; however the decrease is much larger for the z -component. At low volume fractions (< 20%), we compared the results from the different thicknesses by fitting a $\phi^{1/3}$ power law to the data. The coefficients of the fits are plotted in Fig. 5.3.16 for all three components, along with the total rms velocity. The x and y components both show approximately the same $L_z^{1/6}$ scaling, and since the vertical component dominates the full three dimensional rms velocity, it also shows this scaling. However the z -component changes more quickly, varying approximately as $L_z^{1/3}$.

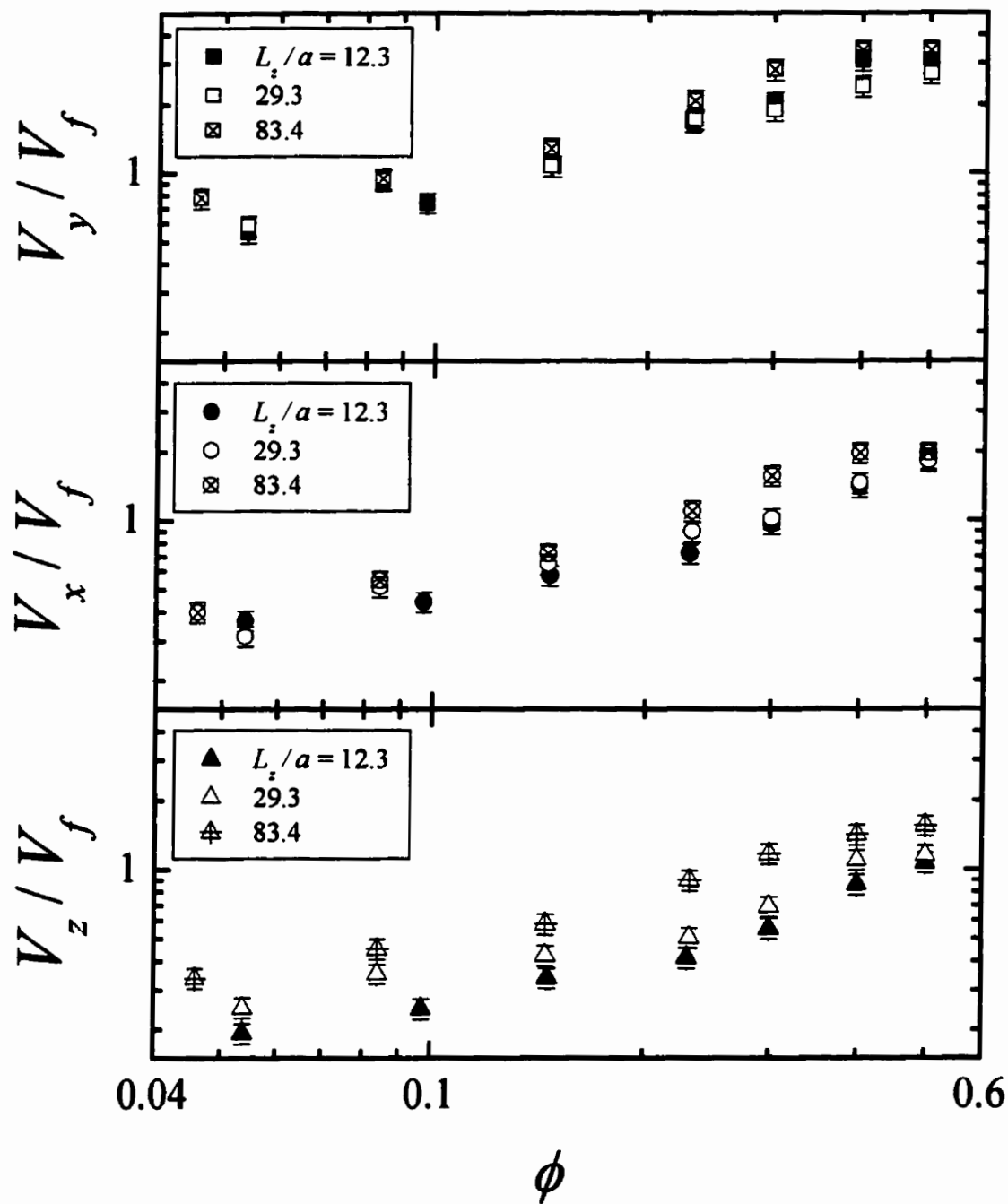


Figure 5.3.15: The components of the rms particle velocity for the three different values of L_z , normalized by the fluidization velocity and plotted as a function of volume fraction.

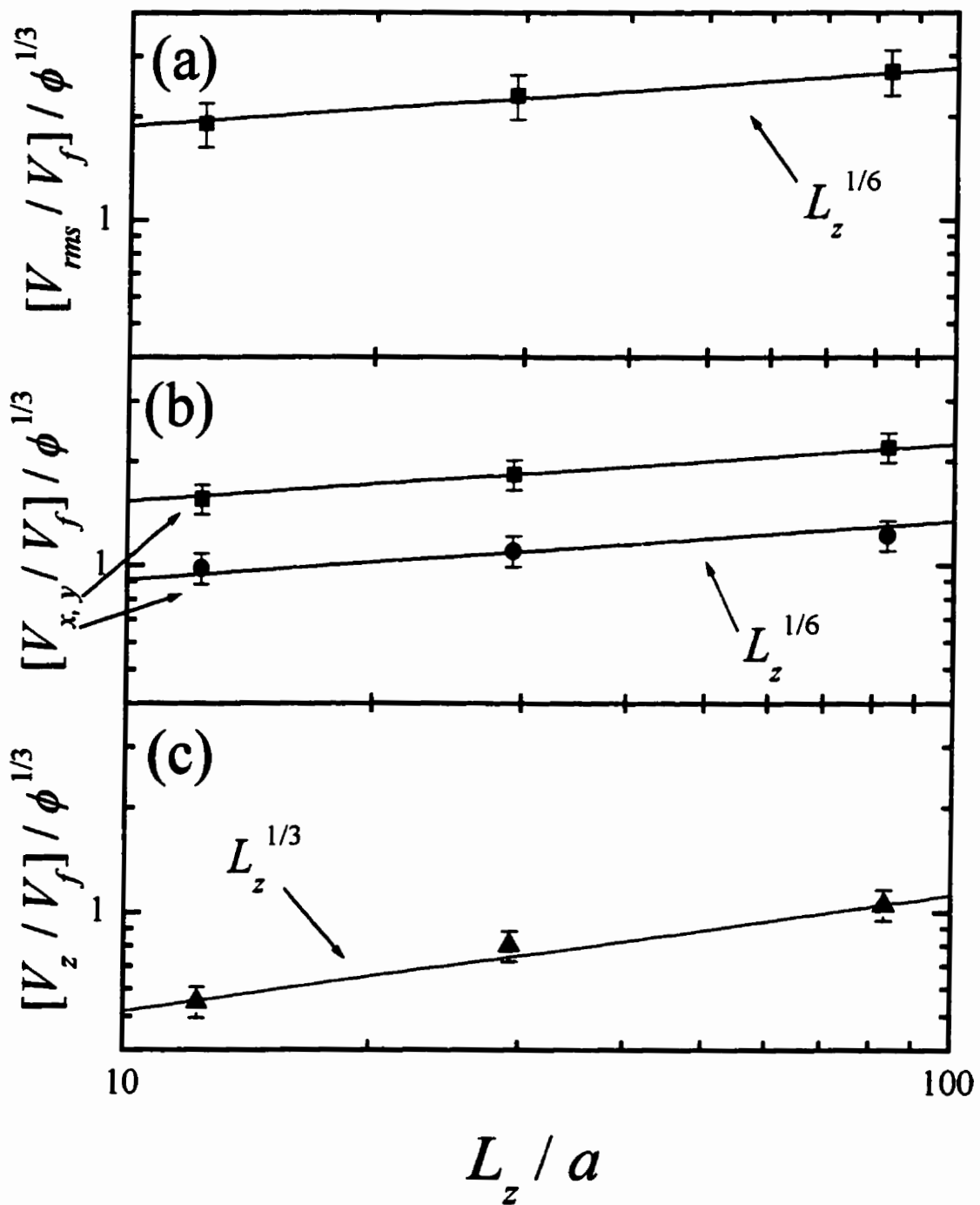


Figure 5.3.16: The scaling of the rms velocity components with L_z .

The dynamic correlation lengths for all three directions were also measured, except for the y direction in the thinnest sample, where d_y could not be determined at most of the volume fractions due to experimental difficulties [Fig. 5.3.17]. Once again, the same general volume fraction dependence is seen in all three samples, with the vertical component changing rapidly as $\phi^{-2/3}$ at low volume fractions and the horizontal components both remaining roughly independent of volume fraction. As the thickness is changed from $83.4 \text{ } \alpha$ to $29.3 \text{ } \alpha$ all of the lengths decrease. However, in going from $L_z/\alpha = 29.3$ to 12.3 there is no significant change in any of the three lengths. This trend is borne out in the full three-dimensional dynamic correlation lengths as well [Fig. 5.3.18], which continue to show the low volume fraction scaling of $\phi^{-1/3}$, and no change from the $29.3 \text{ } \alpha$ to $12.3 \text{ } \alpha$ samples. To compare the data from cells with different thicknesses, we fitted the vertical and 3-dimensional dynamic correlation lengths with $\phi^{-2/3}$ and $\phi^{-1/3}$ respectively. The two horizontal components were compared by fitting a constant to the data (i.e. averaging the lengths from all volume fractions).

The measured instantaneous correlation lengths in the three samples are plotted in Fig. 5.3.19. The data from all of the samples scales as $\phi^{-1/3}$ at low volume fractions, and as approximately ϕ at high volume fractions, allowing us to use fits of these expressions to our data when comparing our results for different thicknesses. This approach provided a good way of smoothing the fluctuations in the data, giving a more reliable measure of the thickness dependence. At low volume fractions we find that the instantaneous correlation lengths get steadily smaller as the sample thickness is reduced. At large volume fractions we again find a decrease in the length when going from the $83.4 \text{ } \alpha$ sample to the

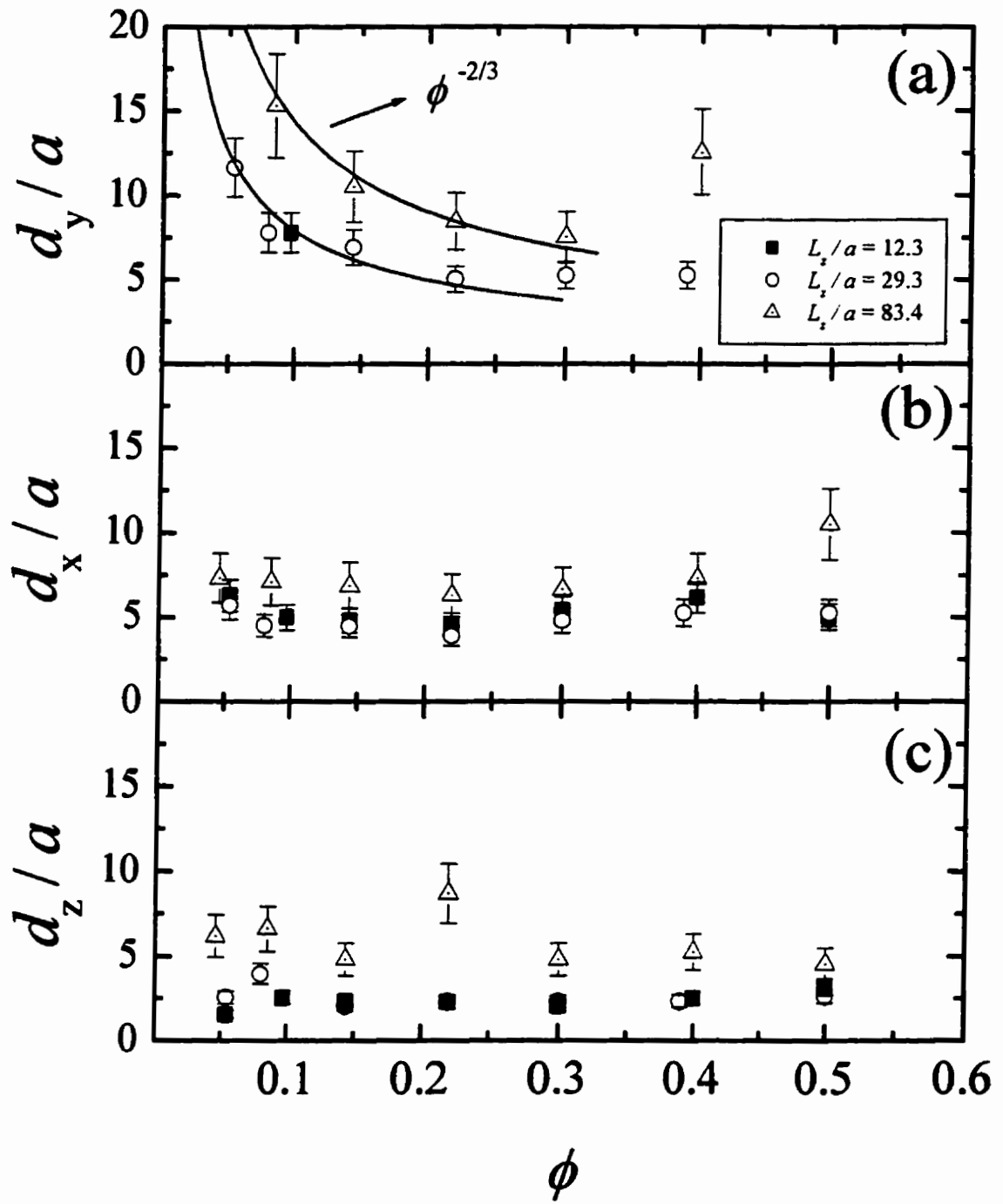


Figure 5.3.17: The components of the dynamic correlation length, for all three sample thicknesses.

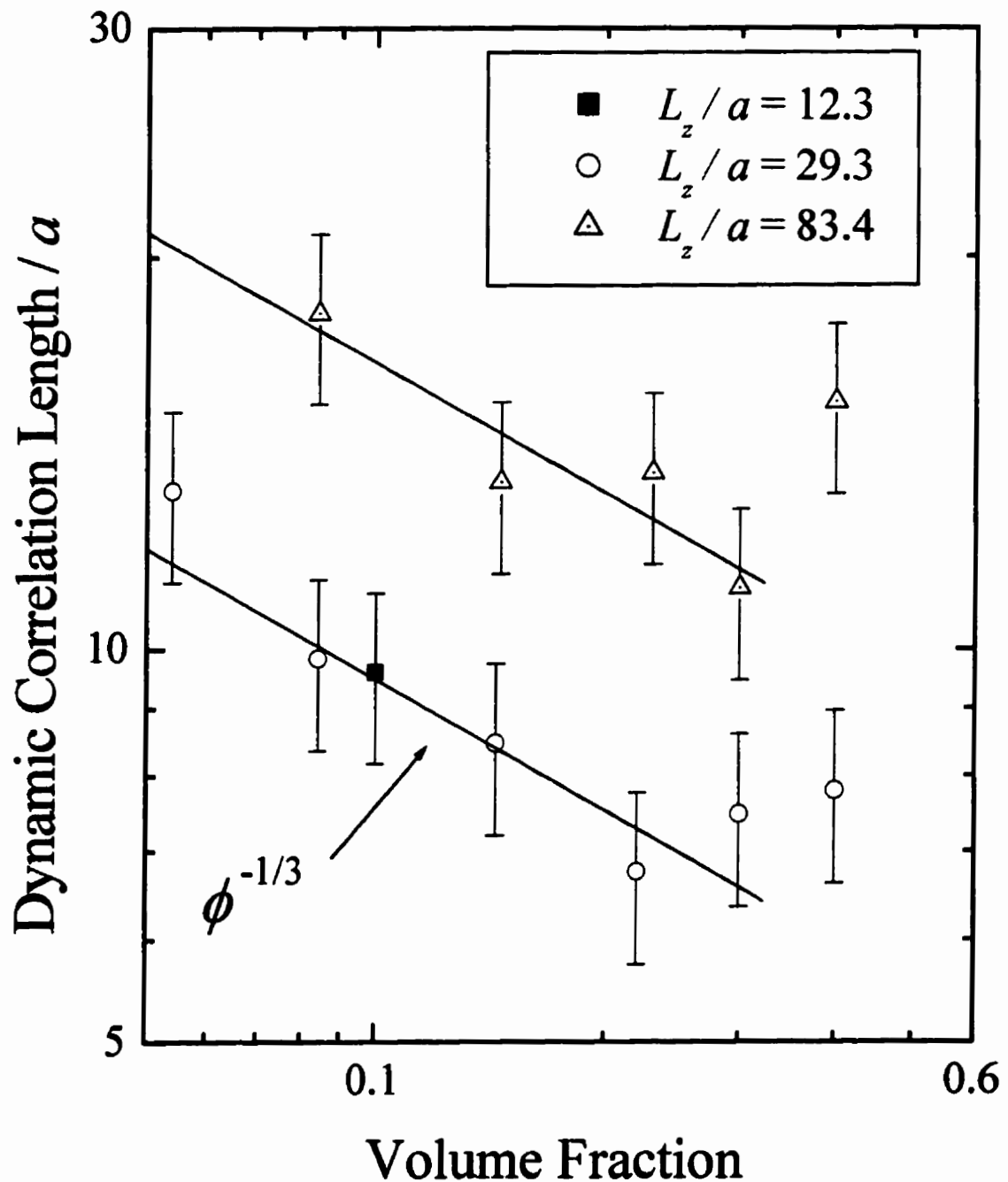


Figure 5.3.18: The full three dimensional dynamic correlation length, for all sample thicknesses.

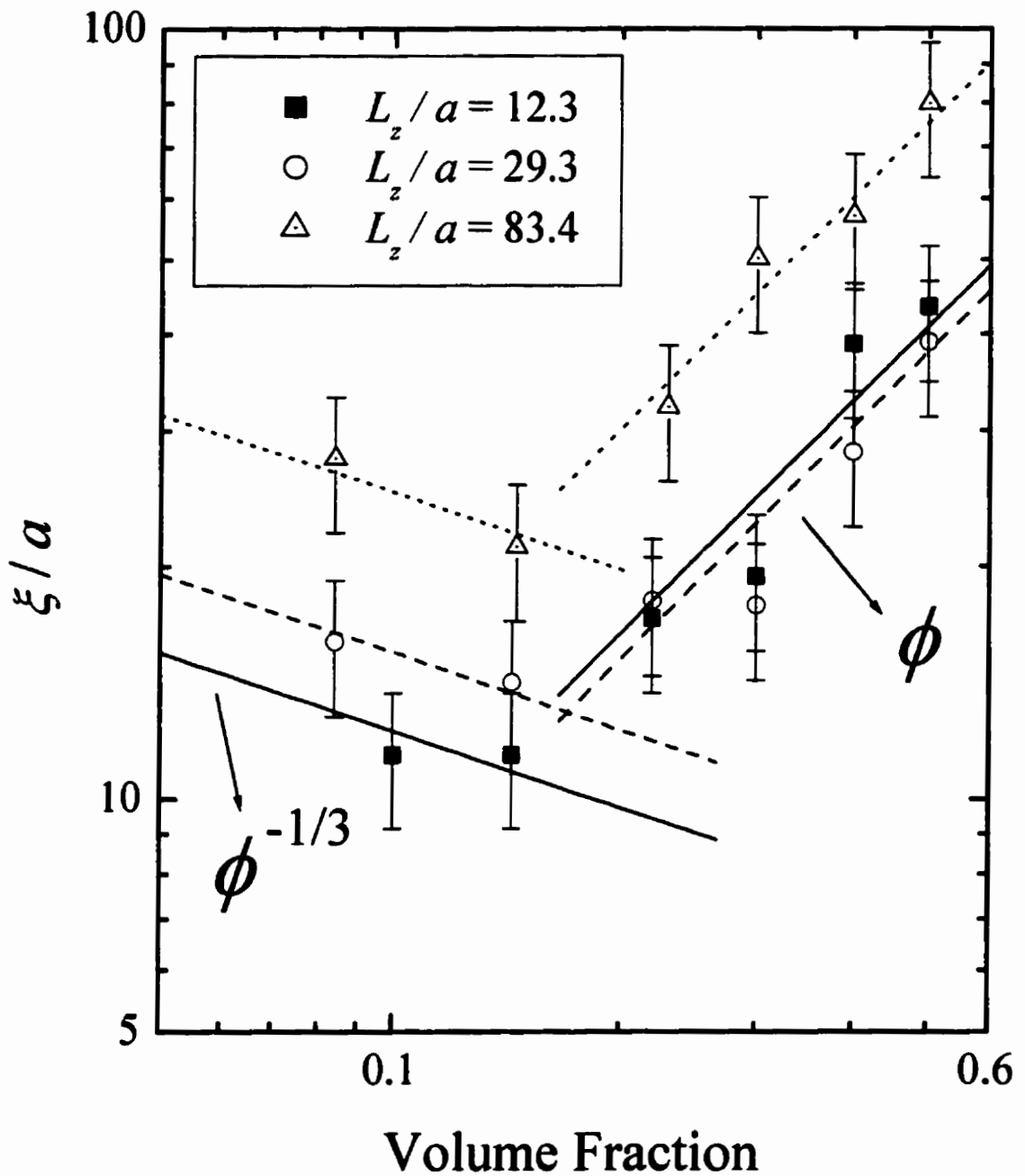


Figure 5.3.19: The instantaneous correlation length, for all sample thicknesses.

29.3α sample, but no significant difference in going from the 29.3α sample to the 12.3α sample.

The scaling of the dynamic and instantaneous correlation lengths with sample thickness is shown in Fig. 5.3.20. Panel (a) shows the three-dimensional dynamic length, with a curve with a dependence of $L_z^{1/3}$. In panel (b), the three components of the dynamic correlation length are shown, along with curves showing $L_z^{1/3}$ and $L_z^{2/3}$ behavior. The $L_z^{1/3}$ curve fits the vertical component data for all three thicknesses, and the x -component data from the two thickest samples, but not the data from the thinnest sample. The $L_z^{2/3}$ curve fits the z -component data from the two thickest samples, but once again not the data from the thinnest sample. The reason that the thinnest sample does not fall on the curves within error bars, for the two horizontal components, is that there is no measured change in the any of the components of the dynamic correlation length going from the $L_z / a = 12.3$ to 29.3 samples. In the case of the z -component this is perhaps understandable, because in the 29.3α sample the dynamic length is approximately $2a$, or the diameter of a particle, so it may have reached a minimum value. Then, assuming that the coupling between the different spatial components fixes the ratio of the lengths, one might expect that the x and y components will also saturate, as seen in our data.

The scaling of the instantaneous correlation length is shown in panel (c) for the low volume fractions and panel (d) for high volume fractions. The low volume fraction data scales as $L_z^{1/3}$, quite convincingly. The high volume fraction data is also consistent with a $L_z^{1/3}$ dependence, although not as convincingly. Thus both the dynamic and instantaneous three-dimensional correlation lengths scale approximately as $L_z^{1/3}$. Recall

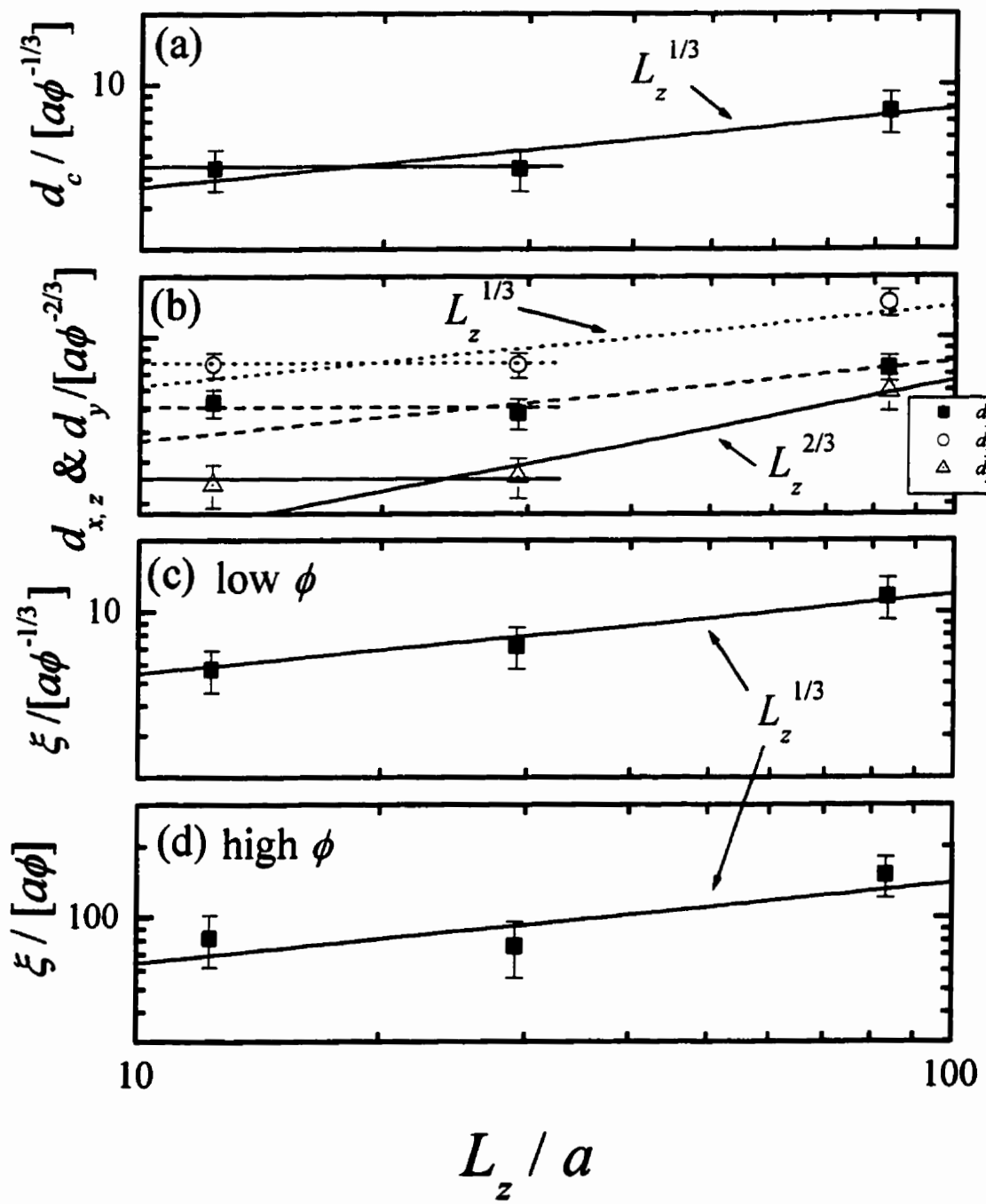


Figure 5.3.20: The scaling of the dynamic and instantaneous correlation lengths with L_z .

that from both the “blob” model and the local fluctuation model, we expect that the vertical component of the instantaneous correlation length will scale as the square of the vertical rms velocity (at constant volume fraction). Since we expect that ξ is dominated by its y and x components, this means that the measured $L_z^{1/3}$ dependence for the instantaneous correlation length is consistent with the $L_z^{1/6}$ dependence measured for the x and y components of the rms velocity.

To investigate the thickness dependence in more detail we look at the scaling of the anisotropy between the x and z components, by plotting the ratio of the components of the rms velocity and dynamic length [Fig. 5.3.21]. These component ratios are an average over the entire volume fraction range (0.05 to 0.5). Also, the symmetry of the system in the horizontal direction means that, for example, the bed with a thickness $L_z = 12.8$ mm and width $L_x = 178$ mm is completely equivalent to one with a thickness $L_z = 178$ mm and a width $L_x = 12.8$ mm, i.e. swapping the labels does not change anything. Thus we have plotted the component ratios for six values of L_z / L_x in Fig. 5.3.21. The symmetry in the horizontal direction further dictates that if $L_z = L_x$, the two horizontal directions will be equivalent, and the components of the rms velocity and correlation length should be equal. The measured ratio of V_z to V_x is equal to $(L_z / L_x)^{1/6}$, which is consistent with the low volume fraction scaling relations found for V_z and V_x separately. The fit to the velocity ratio data also passes through 1 when the thickness and width are equal, which suggests that this scaling law holds for all values of L_z / L_x , and not just for the extremely anisotropic beds that we have looked at. On the other hand the $(L_z / L_x)^{1/3}$ scaling found for the dynamic length ratio is only valid when the width and thickness of the bed are quite

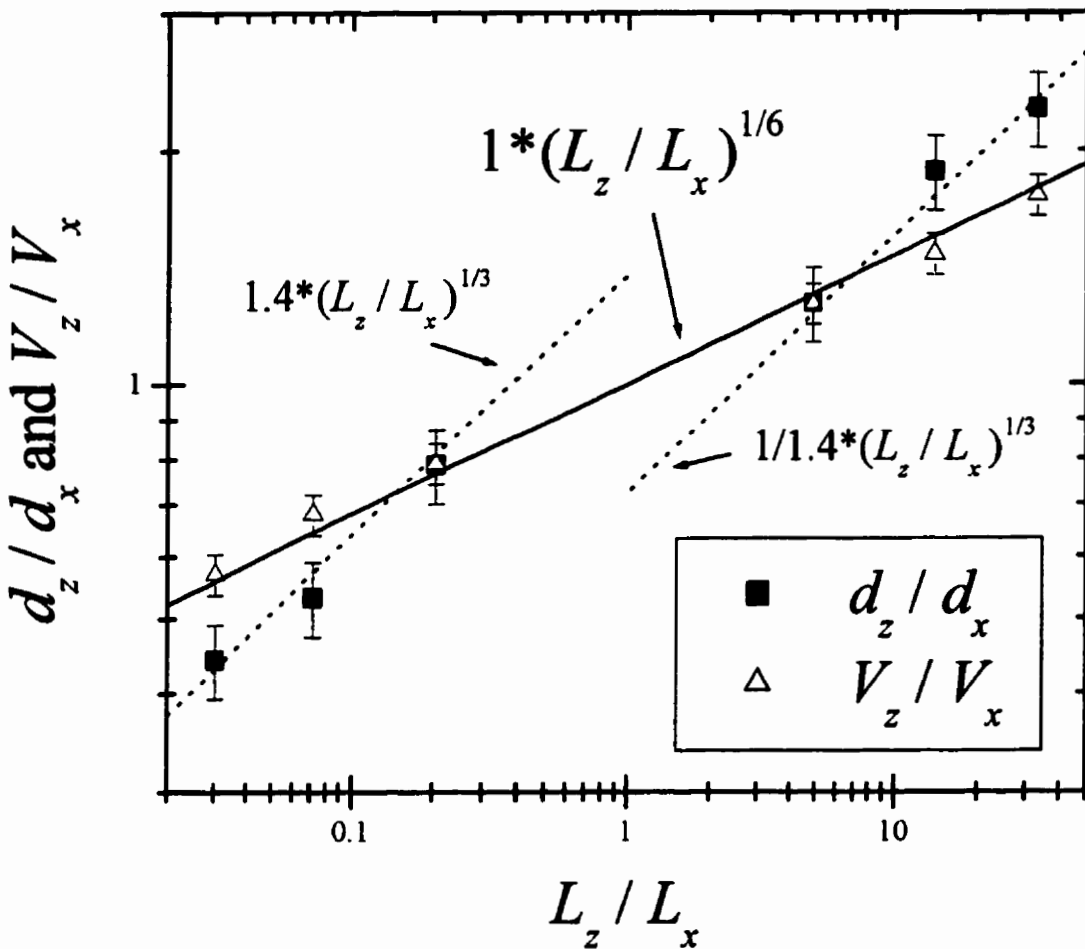


Figure 5.3.21: The scaling of the x - z anisotropy with L_z .

different, as the extrapolations do not pass through 1.

Our basic findings are that while the velocity in the x and y directions do not depend strongly on the smallest dimension of the container, the velocity in the z direction does depend more strongly on L_z . We also see that the L_z dependence of the correlation lengths is the square of that for the velocities, as expected. At low volume fractions the measured scaling is

$$\begin{aligned}
\frac{V_{rms}}{V_f} &\sim 1.28 \left[\frac{L_z}{a} \right]^{1/6} \phi^{1/3} \\
\frac{V_y}{V_f} \text{ and } \frac{V_x}{V_f} &\sim \{1.04 \text{ and } 0.62\} \left[\frac{L_z}{a} \right]^{1/6} \phi^{1/3} \\
\frac{V_z}{V_f} &\sim 0.24 \left[\frac{L_z}{a} \right]^{1/3} \phi^{1/3} \\
\frac{\xi}{a} &\sim 2.55 \left[\frac{L_z}{a} \right]^{1/3} \phi^{-1/3}.
\end{aligned} \tag{5.22}$$

The anisotropy in the horizontal velocities scales as

$$\frac{V_z}{V_x} \sim \left[\frac{0.24 L_z^{1/3}}{a^{1/3}} \right] / \left[\frac{0.62 L_x^{1/6}}{a^{1/6}} \right] \sim 1.0 \left[\frac{L_z}{L_x} \right]^{1/6}. \tag{5.23}$$

We do not measure any change in the components of the dynamic correlation length in going from the thinnest cell to the $29.3\text{-}a$ -thick cell; however the dynamic correlation lengths are larger in the thickest cell. Our measurements have been taken in cells whose thickness ranges from 0.3 to 4.2 times the instantaneous correlation length, while the width and height are always larger than ξ .

Previous experiments on sedimenting spheres [Nicolai & Guazzelli 1995, Nicolai *et al.* 1995, Peysson & Guazzelli 1998 and Segrè *et al.* 1997] have measured the rms velocity in sample cells of different sizes using imaging techniques, although only the x and y components of the velocity were measured. Nicolai & Guazzelli [1995], Nicolai *et al.* [1995] and Peysson & Guazzelli [1998] tracked the trajectory of several silvered particles in their sedimenting suspension, extracting the rms velocity fluctuations from the time average for each particle. In these experiments, the smallest dimension of the cell was changed, while holding the others constant. In particle tracking experiments like these, the

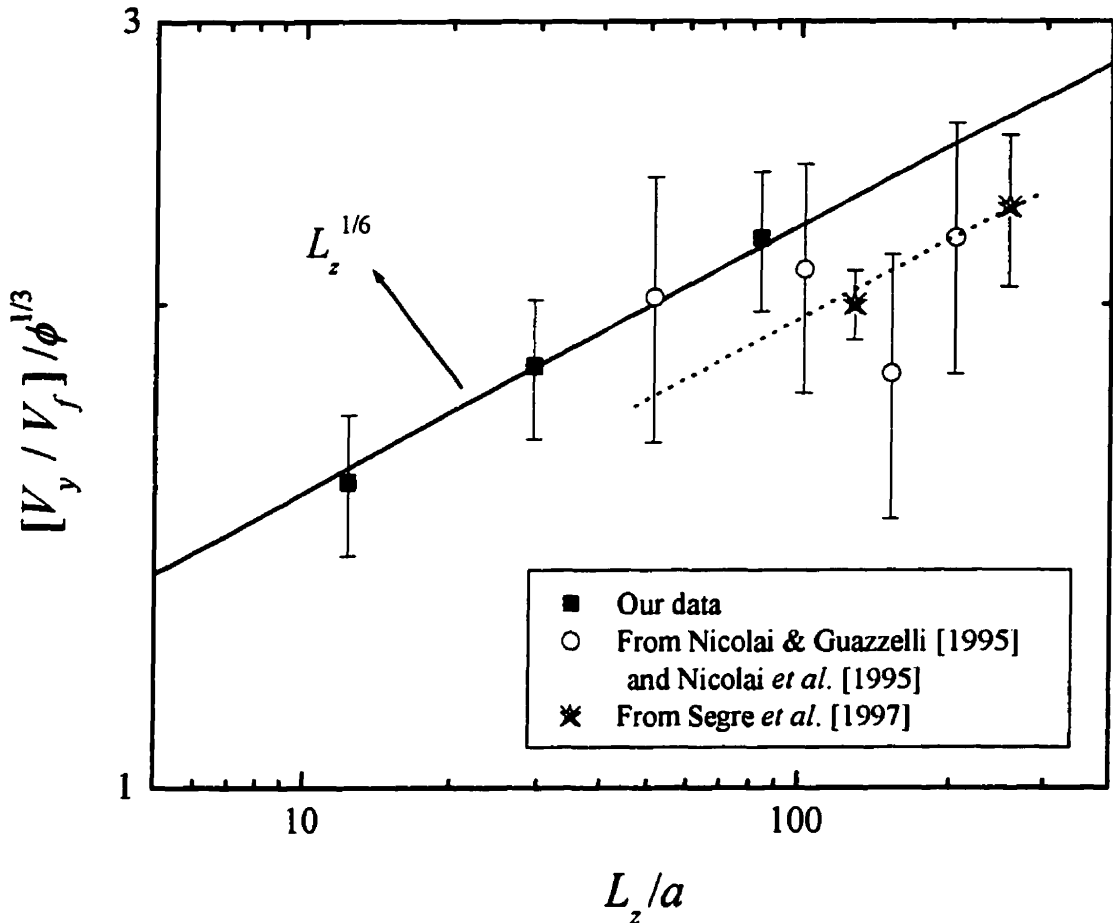


Figure 5.3.22: Comparison of our data with the sedimentation experiments of Segre *et al.* [1997], Nicolai & Guazzelli [1995] and Nicolai *et al.* [1995].

particles will spend longer near the walls where V_{ms} is smaller, thus the average is weighted more by the low values of V_{ms} . By contrast, our DSS measurements give equal weights to particles at all depths in the cell. Segre *et al.* [1997] used particle image velocimetry techniques, taking two snap-shots of a large number of particles, separated by a short time. From these images, the velocities of clusters of ~ 4 spheres were extracted, and from the spatial average the x and y components of the rms velocity fluctuations were determined. Due to the local averaging of the vector velocity over these small clusters of

particles, we would expect that Segrè *et al.*'s [1997] measurements underestimate the magnitude of the rms velocity by a small amount. In these experiments, the thickness and width of the sample cells were generally changed simultaneously, preserving the same aspect ratio of 10.

Neither of these sets of experiments reports a variation in the rms velocity with the smallest dimension of the container. However, they have not looked at the dynamics in the direction of the smallest dimension of the container (the thickness L_z), where we see the strongest effect. Furthermore, considering their rather large error bars, their measurements are not inconsistent with the weak $L_z^{1/6}$ dependence that we observe in the x and y directions. In Fig. 5.3.22 a comparison between the measured vertical components of the rms velocity in our experiments and these previous experiments is shown. The data from Nicolai & Guazzelli [1995] and Nicolai *et al.* [1995] have considerable scatter and quite large error bars, because they generally only measured one volume fraction for each cell thickness. Nonetheless, their data are consistent with ours in the region where the cell thicknesses overlap. Figure 5.3.22 only includes data from the two cells where Segrè *et al.* [1997] see a $\phi^{1/3}$ dependence on volume fraction. Their thin cells (compared to the interparticle separation at their extremely low volume fractions) can be interpreted as being in Brenner's dilute limit, which leads to a $\phi^{1/2}$ dependence [Brenner 1999 and Section 2.4.2], so that the data from these cells are in a different regime. Their two remaining rms velocity data points are generally smaller than our results, as expected, but do nonetheless show an increase with increasing thickness. In our data, we see an effect that has not previously been observed, a weak but significant scaling of the rms velocity

with the smallest dimension of the cell.

Our data are clearly not in agreement with the simple Caflisch & Luke [1985] $V_{rms} \sim L^{1/2}$ scaling. Neither do we see the scaling predicted by Koch & Shaqfeh's [1991] theory [Eq. (2.116)] by or Levine *et al.* [1998] [Eq. (2.117)]. The main discrepancy between these theoretical predictions and our data is that our measured instantaneous correlation length depends on the sample thickness, even when ξ is smaller than L_s , the smallest dimension of the cell. In Koch & Shaqfeh's and Levine *et al.*'s theories, as well as in the sample size scaling ideas in Segrè *et al.* [1997], the instantaneous correlation length is expected to scale as the sample dimension L , until $\xi \sim L$, at which point it becomes independent of L . In our samples, the correlation length is always smaller than the largest dimension of the cell, and yet we do see scaling of ξ with thickness, controlled by the smallest dimension of the cell, which is itself often larger than ξ . Thus our data strongly suggest that wall effects play an important role in setting the dynamics in fluidized suspensions.

As far as we know, only Brenner [1999] has explicitly considered the effects of the walls on the dynamics of the particles. Our results for the scaling of the velocities and correlation lengths are not in agreement with Brenner's theory [Sec. 2.4.2], in part because he assumes that the scaling is isotropic, whereas we see different scaling in different directions. In his theory, he also assumes that the z-component of the dynamic correlation length scales linearly with the sample thickness, a result that we do not observe. Therefore the simple assumptions used in his theory are not sufficient, and a better theory is needed to describe the effects of the sample cell walls.

5.3.8 Reynolds Number Dependence

All of the data discussed above was taken using a 75% glycerol/water solution as the fluid, which gave a particle Reynolds number of 0.9 at 27 °C. We have also investigated the Reynolds number dependence of the fluidization dynamics, by changing the percentage of glycerol in the fluid. Data were taken at four particle Reynolds numbers, 7×10^{-3} , 0.3, 0.9 and 7, corresponding to the low to intermediate range. The low Reynolds number (7×10^{-3}) and $Re = 0.3$ data were taken in the original cells with thicknesses of 12.2 mm (27.9α) and 7.76 mm (17.7α), whereas the $Re = 0.9$ and 7 data were taken in the new cells with thicknesses 12.8 mm (29.3α) and 36.5 mm (83.4α). The rms velocity data with $Re = 0.3$ and $L_z = 12.2$ mm (27.9α) were not completely trustworthy, due to problems with clogged pores in the diffuser, and are therefore not used here. Only the $Re = 0.9$ and 7 data were taken using the far-field DSS technique, so that it is only for these samples that we have measured the three spatial components of the rms velocity and dynamic correlation length separately.

The components of the rms velocity are shown in Fig. 5.3.23, normalized by the appropriate fluidization velocity. The top panel shows the two Reynolds numbers (0.9 and 7) in the 29.3α -thick cell, while the bottom panel shows the data taken in the 83.4α cell. In the 83.4α -thick cell we were only able to attain volume fractions greater than about 0.20 at $Re = 7$, because of the flow rate limitations of our pumping system. One of the main effects that we see is an overall average reduction in the magnitude of all of the components of the rms velocity at the higher Reynolds number in the $L_z = 83.4\alpha$ sample. In the $L_z = 29.3\alpha$ cell, the velocities are reduced at the lowest volume fraction, but are not

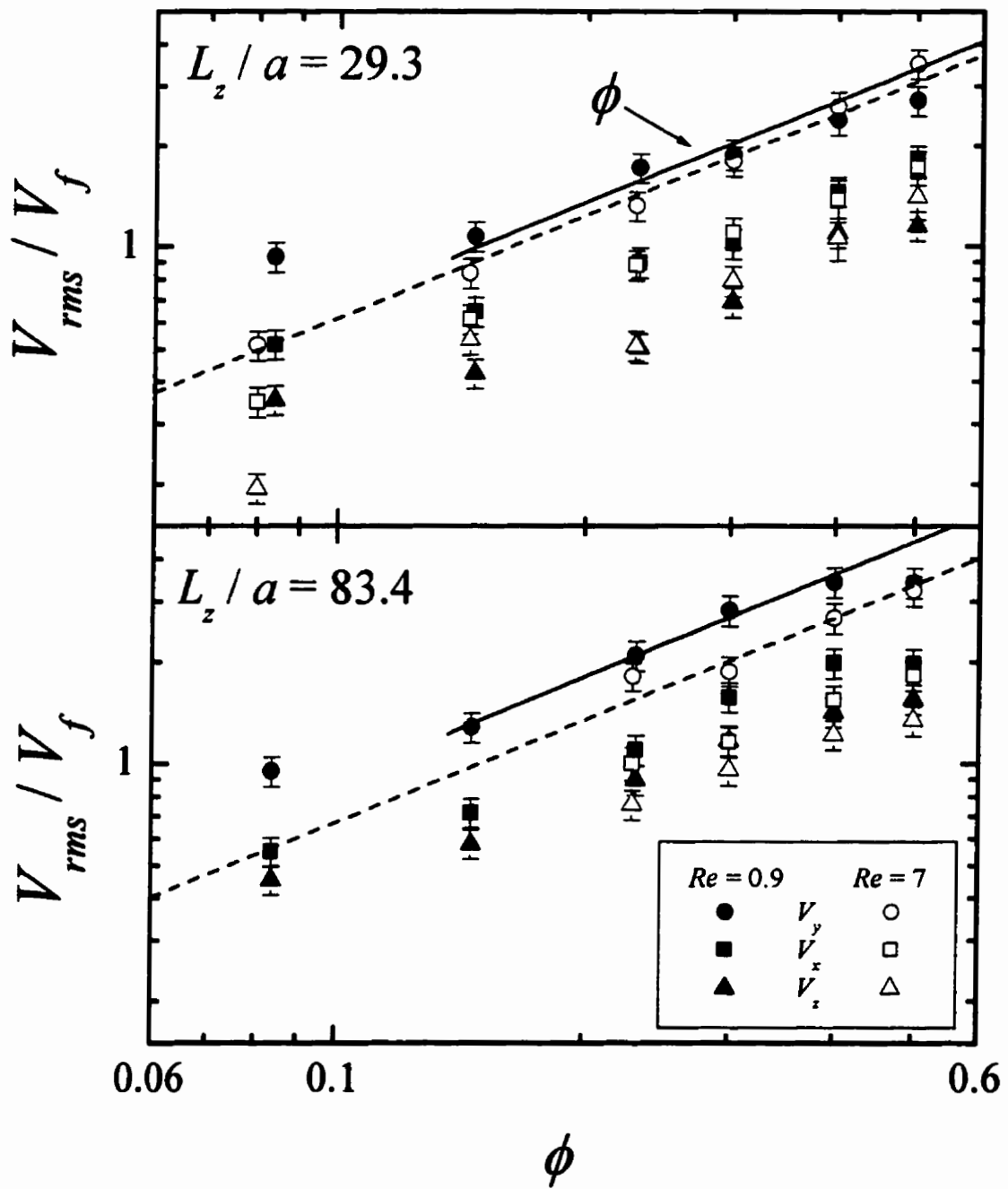


Figure 5.3.23: The volume fraction dependence of the components of the rms velocity, plotted for two Reynolds numbers. Solid lines are fits of a linear volume fraction dependence to the lower Re data at high ϕ , dashed lines are fits to the higher Re data at all ϕ .

significantly different at the higher volume fractions. Thus at the larger Reynolds number, the volume fraction dependence is now approximately ϕ^1 over the *entire* range of measured volume fractions.

The ratio of the components of the rms velocities at the high Reynolds number are plotted in Fig. 5.3.24. The ratio of V_z to V_x is (within our error bars) roughly independent of volume fraction. The value of the ratio is also the same as that found at all ϕ at the lower Reynolds number (0.9) at each of the two sample thicknesses used, although the scatter of the data is larger at the larger Re . However, the ratio of V_y to V_x has a different behavior at the high Reynolds number. It is no longer independent of volume fraction, starting at about 1.8 at high volume fractions (in agreement with the $Re = 0.9$ data) and then decreasing as the volume fraction decreases, to about 1.25 at $\phi \sim 0.10$. This is in contrast to the $Re = 0.9$ data, where the ratio is independent of ϕ .

To compare the $Re = 7 \times 10^{-3}$ data and the higher Reynolds number data, we have plotted the full 3-dimensional velocity for all of our samples in Fig. 5.3.25. In the top panel the data from the $L_z / a = 17.7, 27.9$ and 29.3 cells are plotted. The data in the top panel are all consistent with each other within error bars at all Reynolds numbers, except at the lowest volume fractions, where the rms velocity at the highest Reynolds number is smaller. This suggests that at the highest Re the low ϕ (< 0.2) rms velocity has a different ϕ dependence, with the data falling on the same linear dependence seen at all Re at high ϕ . The bottom panel shows the rms velocity in the thick sample. Although at each volume fraction the data at $Re = 0.9$ and 7 differ by approximately one error bar, all the data points at $Re = 7$ fall below the corresponding data at $Re = 0.9$. Therefore there is a

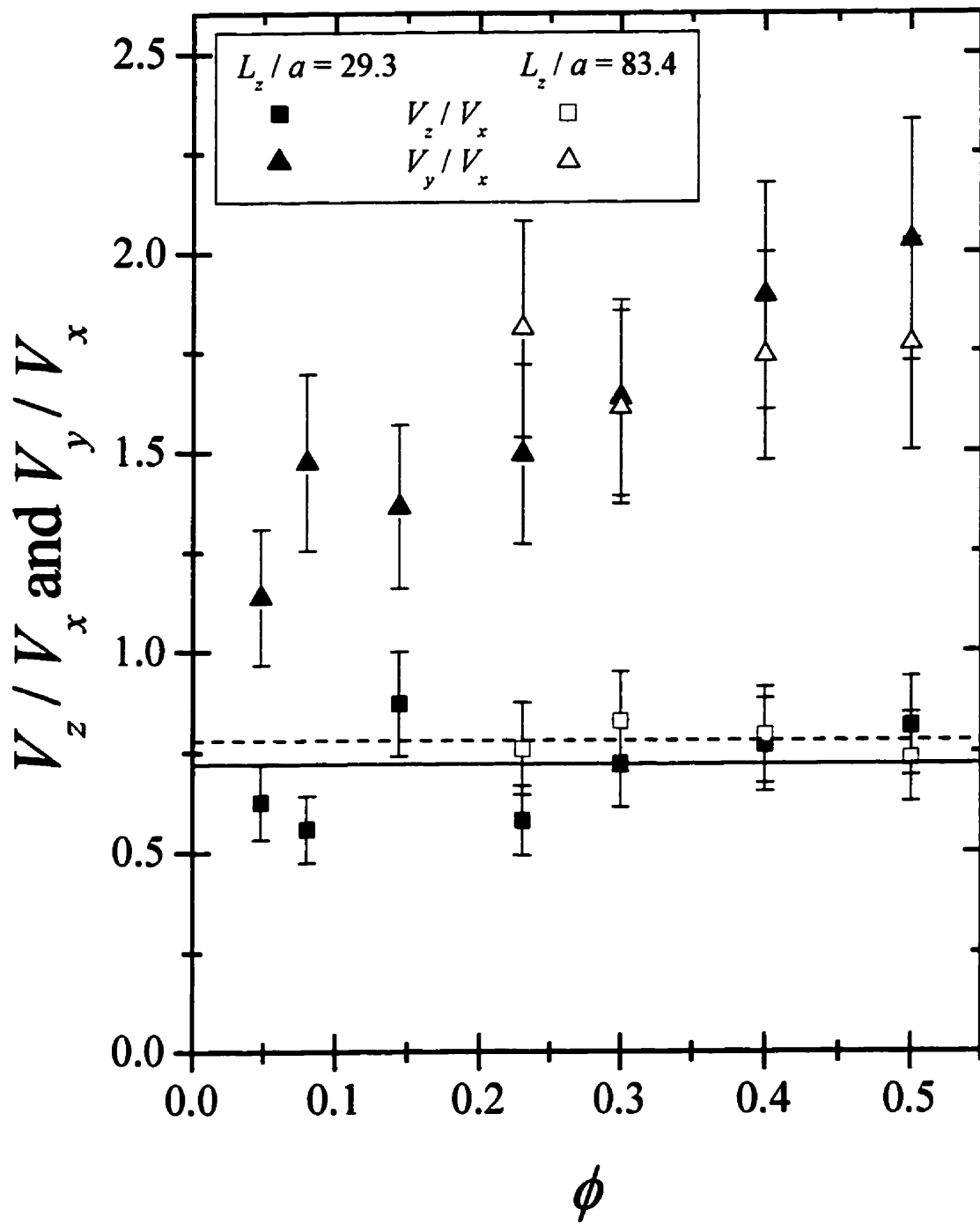


Figure 5.3.24: The ratio of the components of the rms velocity at $Re = 7$, with lines drawn to guide the eye.

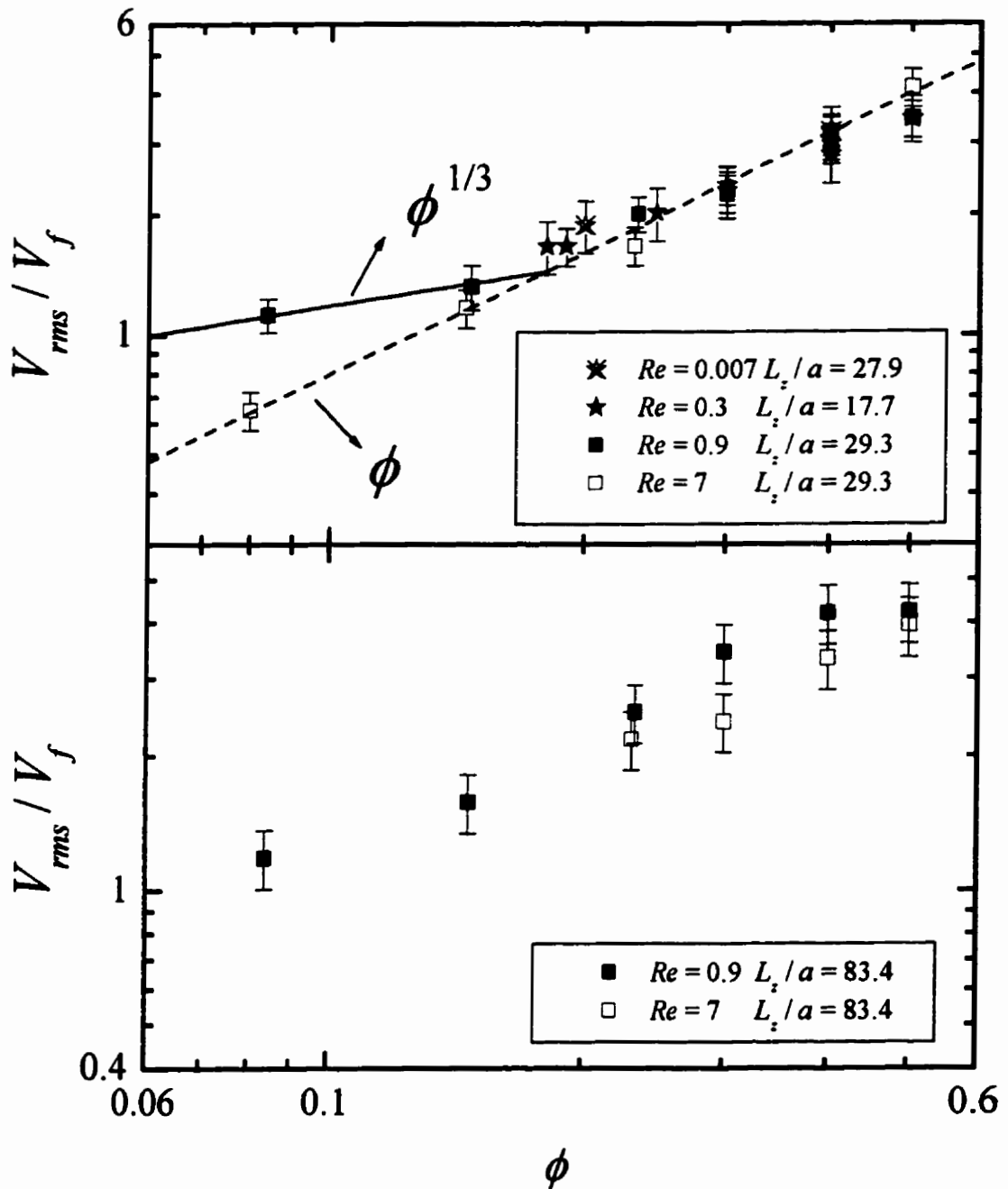


Figure 5.3.25: The volume fraction dependence of the full rms velocity, plotted for several Reynolds numbers and two sample thicknesses, with power law fits drawn to guide the eye.

small but significant decrease in the rms velocity at the higher Re in this thick sample even at high ϕ , as was seen earlier for the individual velocity components [Fig. 5.3.23].

The components of the dynamic correlation length in the 29.3 and 83.4α samples, at $Re = 0.9$ and 7 , are plotted in Fig. 5.3.26. The open symbols represent the high Reynolds number correlation lengths. Any slight differences that may exist between the data at different Re are difficult to see directly, although the high Re data may be on average slightly larger than the lower Reynolds number data. Both of the horizontal components are essentially independent of volume fraction, within error bars, for both Reynolds numbers. The vertical component was hard to measure, because of difficulties in following the particles for a long enough time, but from the limited data, it appears that the vertical component could have a similar ϕ dependence at both Reynolds numbers. Figure 5.3.27 shows the full three-dimensional dynamic correlation lengths in the $27.9\text{-}\alpha$ -thick cell at $Re = 7\times 10^3$, and the $29.3\text{-}\alpha$ -thick cell at $Re = 0.9$ and 7 . There is a slight difference between the dynamic correlation lengths at the different Reynolds numbers, although the differences are not large compared to the experimental uncertainty. The trend is that the dynamic correlation length appears to increase weakly with increasing Reynolds number.

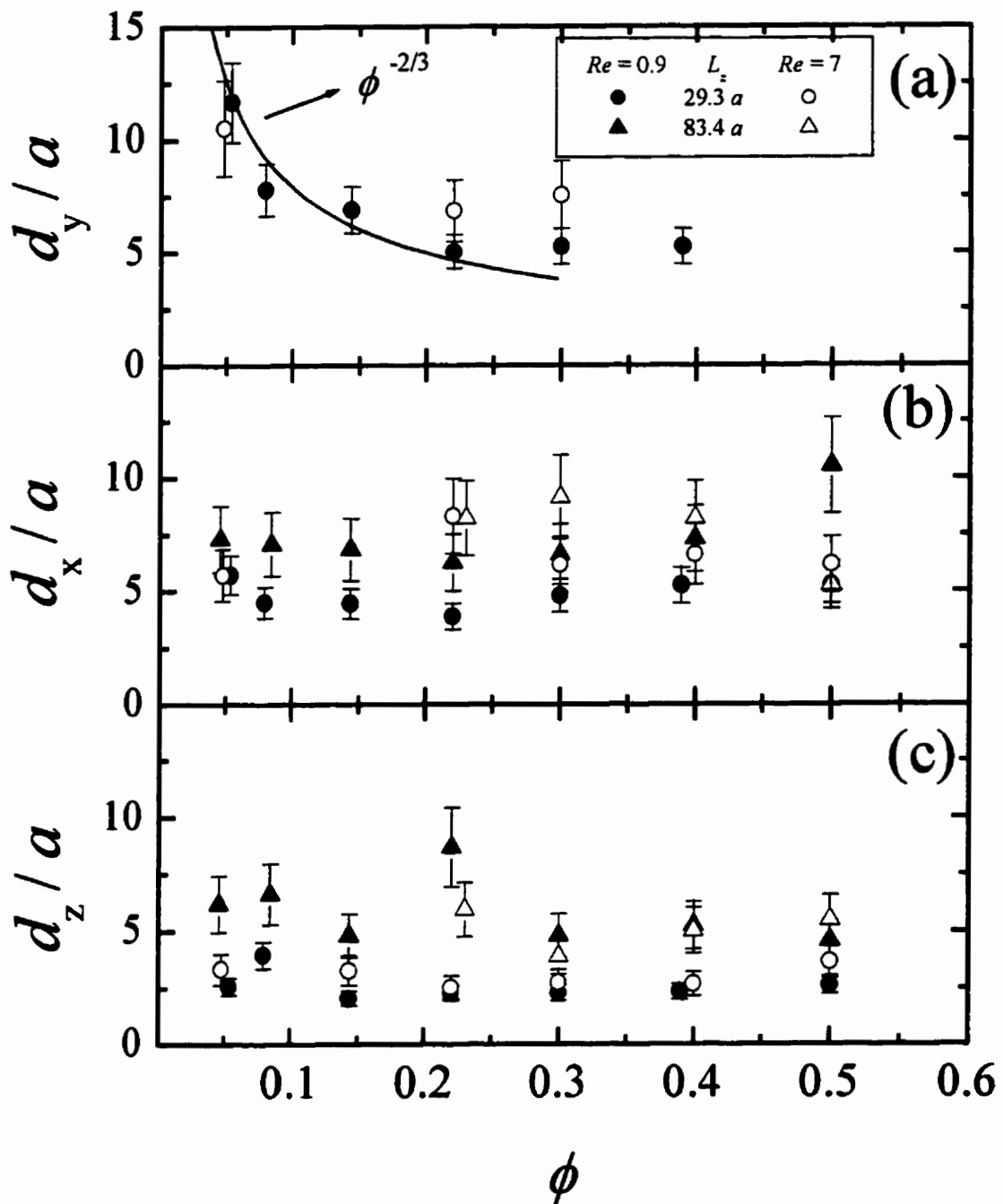


Figure 5.3.26: The volume fraction dependence of the components of the dynamic correlation length, plotted for several Reynolds numbers and sample thicknesses.

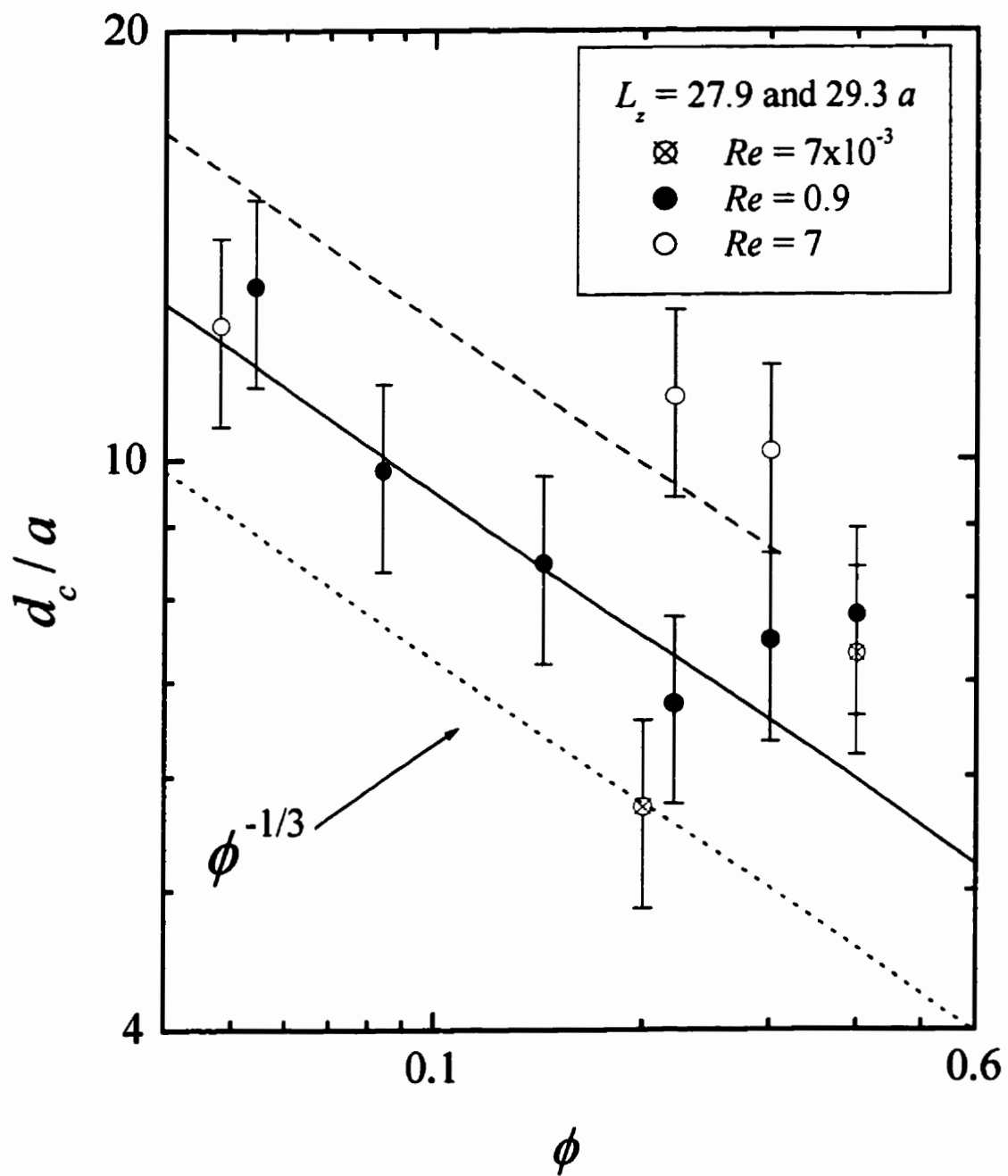


Figure 5.3.27: The volume fraction dependence of the full three dimensional dynamic correlation length, plotted for several Reynolds numbers. The lines are fits of a $\phi^{-1/3}$ power law to the data.

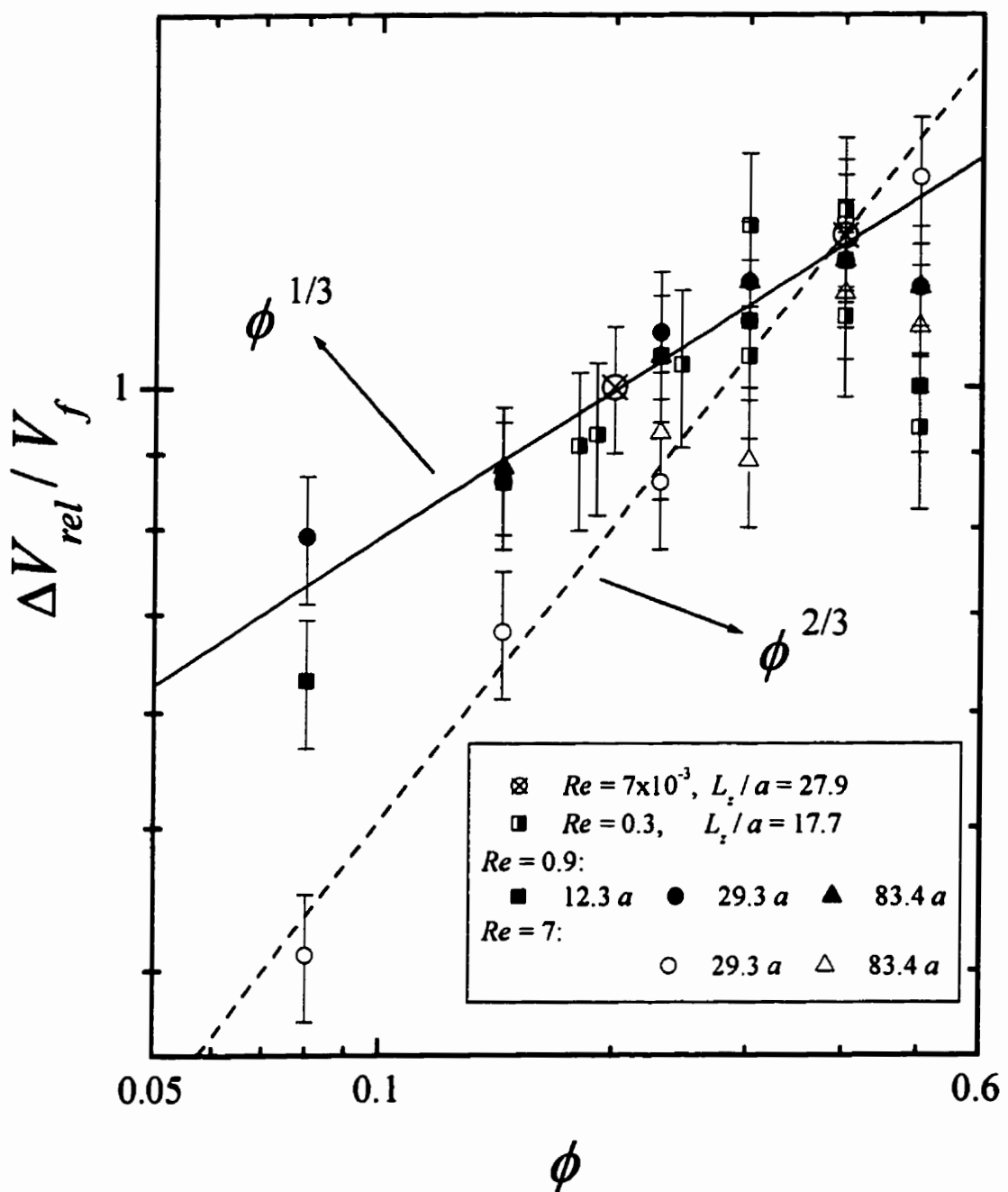


Figure 5.3.28: The volume fraction dependence of the local relative velocity measured with DAWS, plotted for several Reynolds numbers.

Another quantity whose Reynolds number dependence is of interest is the local relative velocity of the particles. In Fig. 5.3.28 the local relative velocities for the samples with $Re = 0.9$ is re-plotted [c.f. Fig. 5.3.10], along with the data from the $Re = 7 \times 10^{-3}$, 0.3 and 7 samples³. The low Reynolds number data are the same within experimental uncertainties as the intermediate Reynolds number data. However, the high Reynolds number data are different at the lowest ϕ . The ϕ dependence is very different, scaling as approximately $\phi^{2/3}$ instead of $\phi^{1/3}$ at low volume fractions up to $\phi = 0.4$. Figure 5.3.28 also shows that the relative motion of neighbors in the suspension at low volume fractions is slower at larger Reynolds numbers (when normalized by the fluidization velocity, which increases as $Re^{1/2}$). One possible physical explanation for this effect may be the presence of wakes that are generated by particles moving at a large velocity relative to the fluid (due to inertial effects in the fluid) [e.g. Koch 1993]. These wakes may tend to pull neighboring particles along, coupling the local motion of particles more effectively than the purely viscous effects that dominate at lower Re , and leading to less relative motion between neighboring particles. One may further expect that wakes will have a stronger effect when the velocity of the particles relative to the fluid ($\sim V$) is at its largest, which on an absolute scale occurs at low volume fractions, where we see the largest differences.

The instantaneous correlation length is plotted in Fig. 5.3.29 for $Re = 7 \times 10^{-3}$, 0.9, and 7. The instantaneous correlation lengths at the low and intermediate Reynolds numbers are the same within error bars (for the 27.9- and 29.3- α -thick samples respectively). At large volume fractions, the ϕ dependence remains approximately ϕ^1 for

³ The $Re = 0.3$ data has appeared previously in Cowan *et al.* [2000]; however it has been reanalyzed using the more complete theory that we have since developed, leading to an increase in ΔV_{rel} of 15-20%.

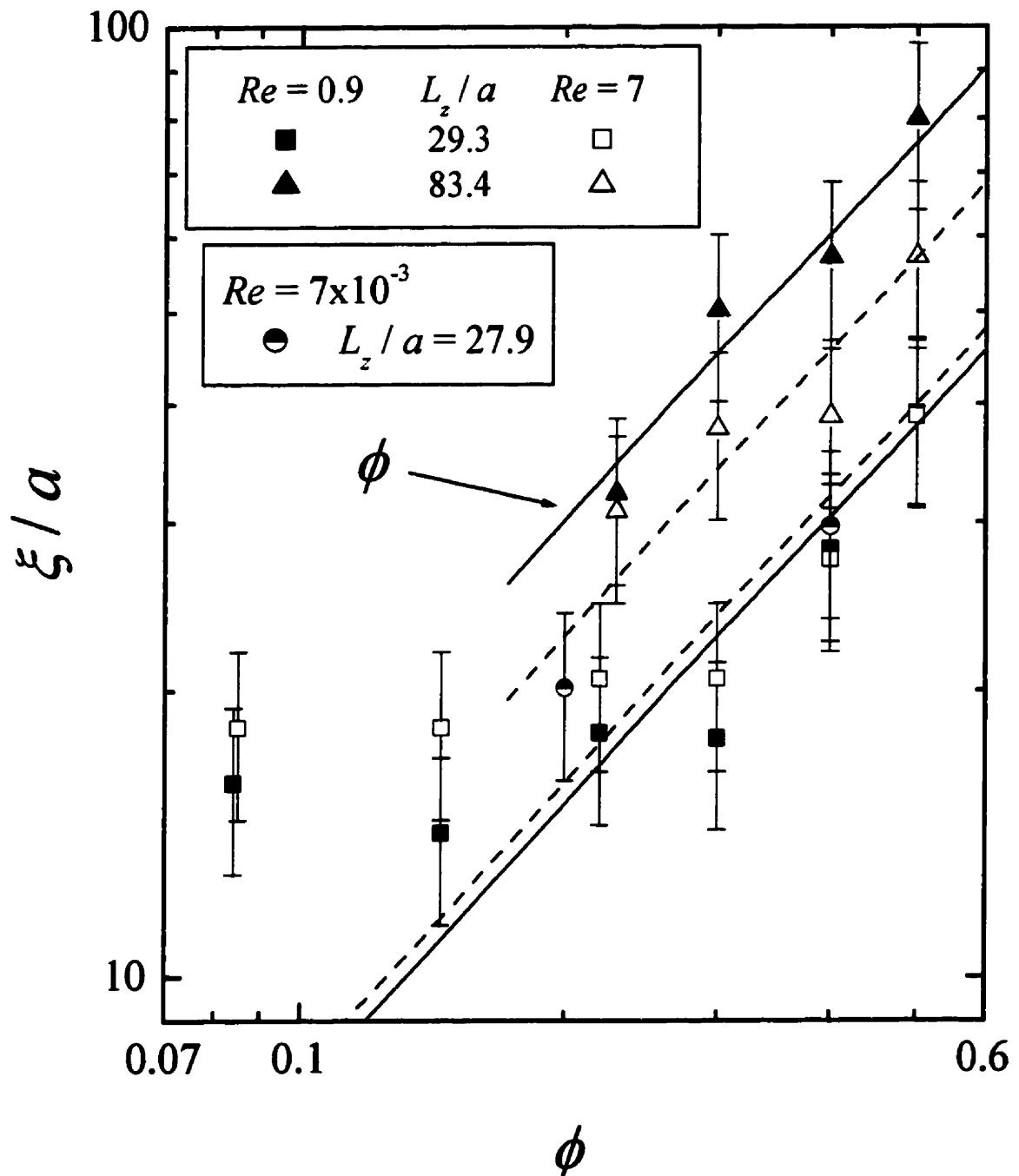


Figure 5.3.29: The volume fraction dependence of the instantaneous correlation length, plotted for several Reynolds numbers and sample thicknesses. Solid lines are fits to the data represented by the solid symbols and the dashed lines are fits to the data represented by the open symbols.

both of the higher Reynolds numbers. In the $L_z / \alpha = 29.3$ samples there is no measurable difference between the lengths, within error bars, at large volume fractions. The $Re = 7$ instantaneous correlation lengths are smaller on average than the $Re = 0.9$ instantaneous correlation lengths in the $83.4\text{-}\alpha$ -thick sample cell.

To look at the Reynolds number and L_z scaling of the dynamics in more detail, we use power-law fits to the ϕ dependence to average over the fluctuations inherent in the data, so that the data from the different samples can be more meaningfully compared. For the rms velocities we fit ϕ^1 to the high volume fraction data for $Re = 7\times 10^{-3}$ and 0.9, and to all volume fractions for $Re = 7$. The results are plotted in Fig. 5.3.30, with the full rms velocities in the top panel, and the components in the bottom panel. For the two thinner samples (closed symbols) the rms velocity does not change significantly with Reynolds number. However, in the thickest sample (open symbols), the rms velocities all decrease significantly going from the intermediate to the high Reynolds number. This same pattern is echoed by the instantaneous correlation length, plotted in the bottom panel of Fig. 5.3.31. The observed thickness and Reynolds number dependence is in qualitative agreement with the ideas of Brenner [1999] [Sec. 2.4.2]. Following the ideas of Hinch [1988], Brenner proposed that as the Reynolds number is increased in a sample with a fixed thickness, eventually the screening length due to inertial effects becomes smaller than the screening distance due to wall effects, at which point both the correlation length and rms velocity will decrease with further increases in the Reynolds number. Thus for the thinner sample, with its already smaller correlation lengths due to wall effects, the Reynolds number would have to be increased above 7 to see the effects of inertial

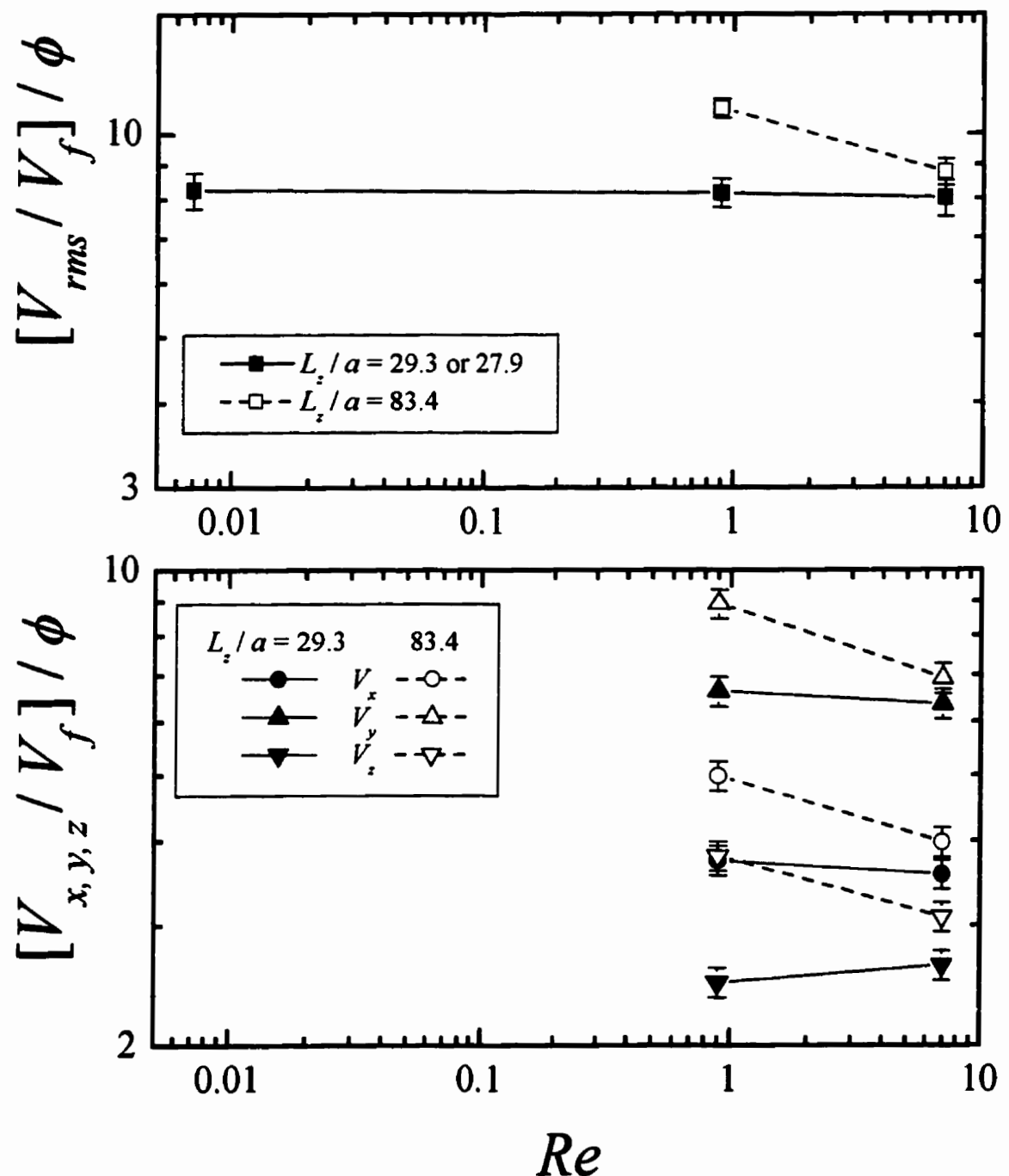


Figure 5.3.30: The large volume fraction scaling of the rms velocity with particle Reynolds number, lines are drawn as a guide to the eye.

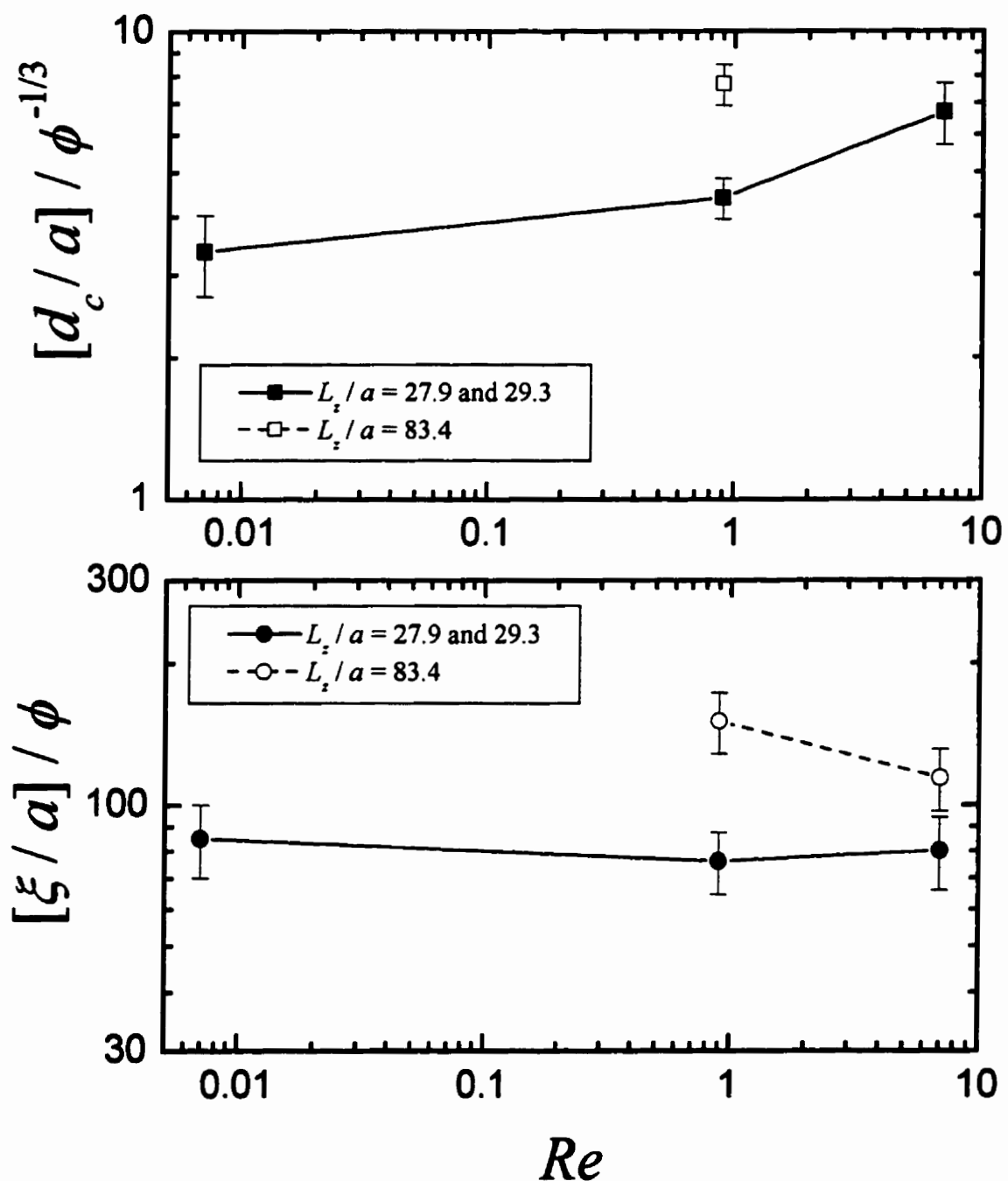


Figure 5.3.31: The scaling of the correlation lengths with particle Reynolds number, lines are drawn to guide the eye.

screening, whereas in the thicker sample, where wall effects are weaker, we can already see a decrease due to inertial effects. We can extrapolate the Re dependence that Brenner expects in the inertial regime ($\xi \sim Re^{-2/3}$, $V_{rms} \sim Re^{-1/3}$) back from the $L_z = 83.4 a$, $Re = 7$ data points to find the critical Reynolds number at which inertial effects begin to dominate over wall effects in the $L_z / a = 83.4$ cell. This is done by assuming that the $Re = 0.9$ data points in the thickest sample are still in the low Reynolds number limit, where the rms velocity and instantaneous correlation length are independent of Reynolds number. Then by extrapolating back from the $Re = 7$ data points to this level, we can roughly estimate the Reynolds number at which inertial effects become important in a cell of this particular thickness. The results are $Re_c = 4.2$ from the spatial correlation length and $Re_c = 3.9$ from the rms velocity, which are consistent with each other within experimental uncertainties. We would also expect, from the same extrapolations, that inertial effects would begin to change the spatial correlation length and rms velocity in the $L_z / a = 29.3$ sample at a Reynolds number of about 10. Thus the overall qualitative behavior of the instantaneous correlation length and rms velocity as a function of Re and L_z agrees with Brenner's theory. However, the low volume fraction scaling of the rms velocity appears to change at the highest Reynolds number, and this is not predicted by Brenner's theory.

The dynamic correlation length on the other hand appears to show different behavior. In contrast to the instantaneous correlation length, the dynamic length appears to increase from the lowest to the intermediate to the highest Reynolds number. This means that the dynamic and instantaneous correlation lengths become closer to each other at the highest Reynolds number.

The volume fraction scaling that was previously presented for $Re = 0.9$ in Fig. 5.3.13 (from the “blob” model) is somewhat different at the highest Reynolds number, although the low $Re = 7 \times 10^{-3}$ and 0.9 data are the same [Fig. 5.3.32(a)]. Instead of the $\phi^{1/2}$ dependence seen at lower Re , the data are seen to scale approximately as $\phi^{5/6}$ at the highest Reynolds number. This measured scaling, and Eq. (5.16), give

$$\left[\frac{\eta}{\eta(\phi)} \frac{\Delta N_\xi}{\sqrt{\langle N \rangle_\xi}} \frac{V_o}{V_f(\phi)} \right] \sim \phi^{\frac{5}{6}} \quad (5.24)$$

at $Re = 7$. In comparison, at lower Reynolds numbers the term in the square brackets was found to be a constant, roughly independent of volume fraction. Also, the observed scaling of the local relative velocity at the high Reynolds number ($\phi^{2/3}$) is consistent with the observed scaling of $V_{ms}/\xi^{1/2}$, through the use of Eq. (5.21).

Since V_f/V_o does not change significantly with Reynolds number [Section 5.3.1], the different behavior found in Eq. (5.24) at the highest Reynolds number suggests that one or both of the number fluctuations or effective viscosity are Reynolds number dependent. It is reasonable to assume that the suppression of the number fluctuations in a correlation volume is constant and independent of Reynolds number, since the decay of the number fluctuations with increasing length scales may be the mechanism that leads to the velocity correlation length [Lei *et al.* 2001 and Sec. 5.3.7]. If we interpret our data using this assumption, we deduce that the effective viscosity at $Re = 7$ has the different volume fraction dependence shown by the open symbols in Fig. 5.3.32(b). This suggests that inertial effects, largely through their influence on the local relative velocity, also modify the effective viscosity of suspensions of non-Brownian particles.

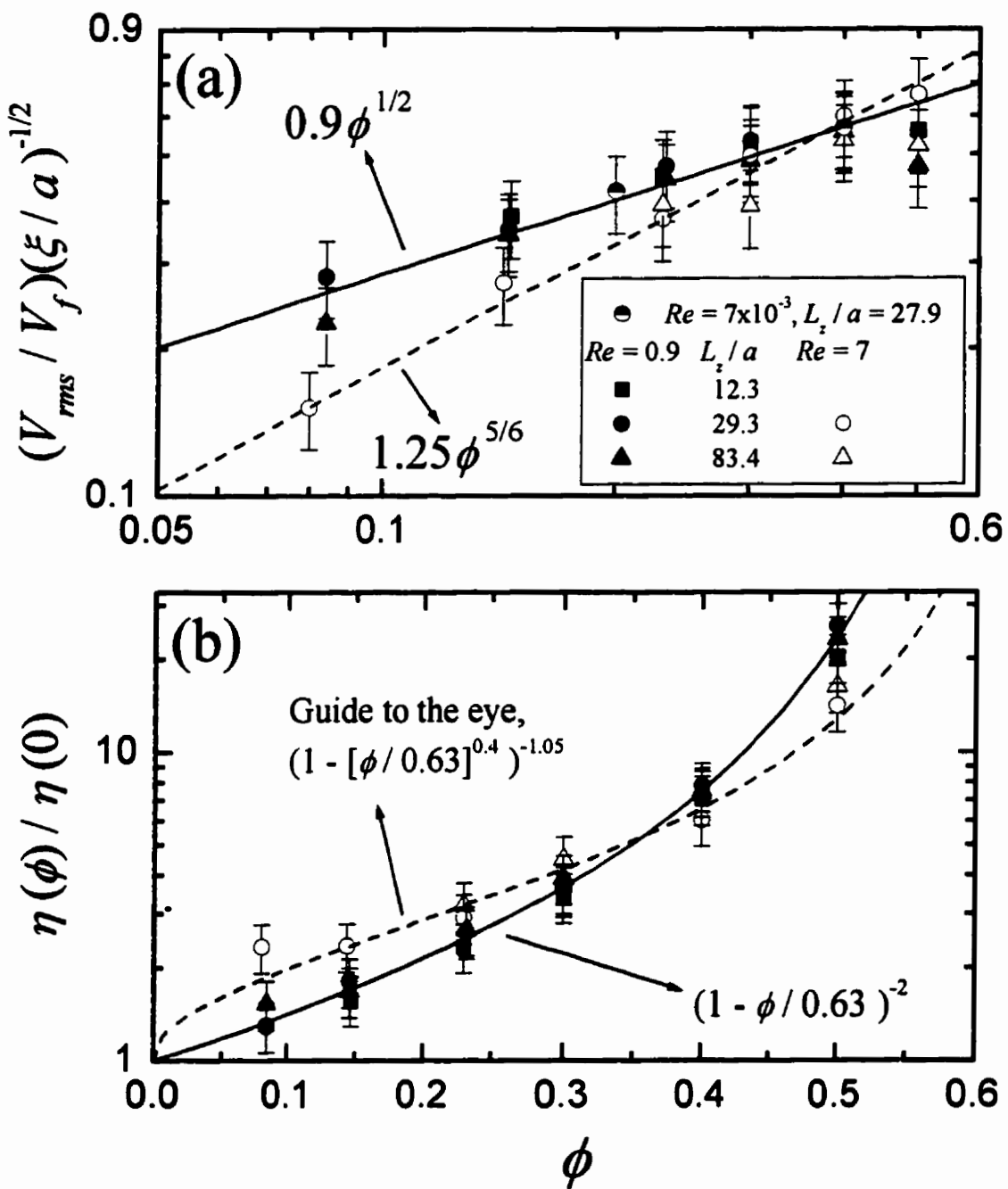


Figure 5.3.32: (a) The volume fraction scaling from the “blob” model, at high and low particle Reynolds numbers.
 (b) The estimated effective viscosity is plotted in the bottom panel.

6. Conclusions

6.1 Wave Propagation

Wave propagation can be split conceptually into a ballistic and a scattered component. By using the ability of ultrasonic detectors to measure the field, these two components can be measured separately in our experiments. The spectral function approach, using a coated sphere scatterer model, allows us to calculate the ballistic propagation parameters, as well as the diffusion parameters that approximately describe the propagation of the scattered waves.

We have measured the parameters that govern the ballistic propagation of ultrasound through fluidized suspensions of glass beads in a glycerol and water solution, and investigated their dependence on the volume fraction of the scatterers [Cowan 1997 and Cowan *et al.* 1998]. Our data are in excellent agreement with the theoretical predictions of the spectral function approach. The good agreement between our ballistic theoretical model and experimental results suggests a physical picture for ballistic wave propagation. In the intermediate frequency regime, the strong scattering causes the material properties of the medium to become renormalized, with the result that the effective medium in which the glass beads are embedded takes on some of the character of the scatterers themselves. Since it is precisely this renormalized effective medium that is sensed by the coherent ballistic wave, the phase and group velocities become significantly affected by the scattering; as a result, both velocities exhibit considerable dispersion, even though they describe the propagation of the small fraction of the incident pulse that is *not*

scattered out of the forward direction. To model this behavior, we determine the dispersion curve using a spectral function approach, in which we calculate how the scattering properties of a coated elastic sphere are modified by the coupling to the embedding medium. Thus, we are able to accurately calculate the renormalization of the effective medium and hence to correctly account for the frequency and volume fraction dependence of both the phase and group velocities. Furthermore, by examining the energy densities as a function of frequency, we identify two microscopic mechanisms for the velocity dispersion that is observed in our experiments: in addition to resonant scattering from the glass beads, where a significant fraction of the energy is trapped in the solid particles, we demonstrate the existence of “tortuosity slowdown”, where the wave energy is mostly confined to the tortuous fluid pathways. Since the bulk of the acoustic energy remains in the fluid, both of these effects cause the dispersion to become greater as the volume fraction of the scatterers is increased, in agreement with our experimental results and with the quantitative predictions of our theoretical model.

We have also measured the ensemble-averaged scattered intensity of ultrasound in these fluidized suspensions, and compared the experimental results to the predictions of the diffusion approximation. The agreement between the diffusion approximation and our data is quite good. This allows us to reaffirm that the diffusion approximation provides a good description of the average transport of wave intensity through a strongly scattering sample, provided the sample is sufficiently thick compared to the mean free path of the wave. Using the diffusion approximation, we can measure the diffusion coefficient and the absorption coefficient. The agreement between our data and the diffusion coefficients

calculated using the spectral function approach is very good, justifying the simple physical picture underlying our model. This model relates the energy and group velocities by averaging the time delay caused by resonant scattering in a single scatterer over the scattering angle. This extra time delay slows (our possibly speeds up) the speed at which the wave diffuses, and in our system this causes the energy velocity to be slower than the group velocity. The good agreement between the experimental and calculated diffusion coefficients in fluidized suspensions, as well as the direct comparison between experiment and theory for l^* that was made at random close packing [Schriemer *et al.* 1997], provide strong justification for our use of the calculated transport mean free path and energy velocity in the analysis of DAWS experiments in these systems.

6.2 Spectroscopy Techniques

We have tested the Siegert relation, which relates the field and intensity autocorrelation functions, and is of utmost importance in optical applications. To do this we take advantage of the ability to measure the ultrasonic wave field directly, allowing us to compare the field and intensity autocorrelation function directly. In our single scattering experiments, we have found that for our system, where the motion of the scatterers is correlated on length scales that are comparable to the scattering volume, the Siegert relation fails. However, in systems where the particle motions are not correlated, the Siegert relation would be expected to hold. In multiple scattering experiments, the Siegert relation can also fail if the number of scattering events is small, but we have found that the Siegert relation holds for $n > 10$. This occurs even though the motion of particles in the average volume that contains scattering paths of this length is still correlated. The

reason for the success of the Siegert relation for long multiply scattered paths is that the direction of the scattering wave vector becomes randomized, so that even though the motion of the particles is correlated, the resulting contributions to the phase change of the scattering path are not correlated. This result is quite general, as it depends only on the properties of diffusing waves, and not on the details of the system. These experiments suggest that care must be taken in applying the Siegert relation when correlations in the motion of scatterers exist over an appreciable length scale.

Two new experimental techniques have been developed and tested; Dynamic Sound Scattering (DSS) uses singly scattered ultrasound to measure the mean square displacement of scatterers, and Diffusing Acoustic Wave Spectroscopy (DAWS) uses multiply scattered ultrasound to measure the relative mean square displacement of scatterers separated by a transport mean free path. The approximations underlying pulsed DAWS were tested by measuring the scattered field at different travel times (or path lengths) through the sample. The results showed the expected behavior: for short paths, contributions from the first and last scatterer were significant, and thus the displacements deduced from the simple relationship in Eq. (2.73) depended on the path length. However, as the paths increased in length, this effect became negligible, and Eq. (2.73) accurately determined the relative mean square displacement for $n > 20$. One important consequence of these results is that, provided the measured path length is chosen to be long enough, the pulsed DAWS technique can be used on samples that are only a mean free path thick. Unlike in the continuous wave case, in our pulsed experiments no complicated corrections that go beyond the diffusion approximation (e.g. using the

telegrapher equation) are needed to analyze the data. DAWS was also tested by using both plane wave and point source input waves, the results of which agreed well with each other. The detailed tests that we have performed lend confidence to our interpretation of our DAWS measurements.

Two different implementations of DSS were developed, a near-field and a far-field technique. The near-field apparatus is more compact and convenient to use, but the analysis of the results is cumbersome, and it can not separate the spatial components of the rms particle displacements. The far-field technique can measure the three components of the rms particle displacements independently, and therefore gives more information about the motion of the particles than the near-field technique does. The results of the two techniques agree with one another to within 5%, giving an important validation of the complicated analysis needed to interpret the near-field data.

We have also investigated the fluctuations in the phase of the scattered sound caused by the motion of the scatterers. Our model for the phase difference probability distribution gives a very accurate description of the measured probability distribution. This excellent agreement has allowed us to relate the phase fluctuations to the relative mean square displacement of the scatterers, as in DAWS.

When DAWS and DSS are combined together, they can measure many aspects of the dynamics of the scattering particles. DSS gives the three components of the rms particle velocity, and the three components of the dynamic correlation length (the average distance traveled before a particle's velocity changes significantly). By combining the rms velocity measurements with DAWS measurements of the relative particle velocities at

interparticle separations spanning a wide range of values, the spatial velocity correlation function can be measured. Thus we are able to measure the instantaneous velocity correlation length, i.e. the distance over which the velocities of different particles are correlated in a “snap-shot” of the sample [Cowan *et al.* 2000].

These techniques are ideally suited to the measurement of fluidized suspensions with high volume fractions and large, mm-sized particles. By contrast, current light scattering techniques, because of light’s much shorter wavelengths, are most useful for μm -scale particles. The larger particles have different and interesting dynamics: higher Reynolds numbers are easily attainable, and there is no measurable Brownian motion, so that hydrodynamic interactions dominate. Another competing technique, direct imaging of the particles using digital video cameras, works best at low volume fractions. There must be some index contrast between the particles and the fluid in order to see particles, but the sample must be transparent enough to image particles in the middle of the sample, which means that imaging gets steadily more difficult as the volume fraction increases and the suspension becomes more opaque. Therefore, DAWS and DSS are best suited to a class of suspensions to which the previously available experimental techniques are least suited, and this class of suspensions is also of interest from both a technological and a basic physics standpoint.

6.3 Fluidized Bed Dynamics

We have used our new ultrasonic techniques, DAWS and DSS, to measure the rms velocity fluctuations and correlation lengths of particles in fluidized suspensions. In particular we have investigated the scaling of these quantities with volume fraction, the

smallest sample dimension, and Reynolds number.

At low volume fractions and Reynolds numbers less than 1, the behavior that we observe for the rms velocity and instantaneous correlation length agrees with the behavior seen in video imaging measurements of sedimenting suspensions at very low Re [Segrè *et al.* 1997]. However at larger volume fractions, the scaling of our data differs significantly from that found in video imaging measurements [Segrè *et al.* 2001], leading to the conclusion that the dynamics of fluidized and sedimenting particles can be quite different. While this conclusion is not entirely unexpected, for the reasons discussed in Section 2.4, the differences between fluidization and sedimentation are frequently overlooked.

To understand the scaling of our data, we have presented two complementary pictures of the volume fraction scaling of the rms velocity and instantaneous correlation length. In the first picture, we look at the scaling of the rms velocity of a “blob” of particles of size ξ , by balancing the viscous drag and the gravitational driving force caused by local variations in the density of the suspension [Segrè *et al.* 1997, Brenner 1999, Segrè *et al.* 2001 and Lei *et al.* 2001]. If the size of the blob corresponds to the correlation volume, then the rms velocity of the “blob” will be equivalent to the rms velocity of all particles in the system. This model therefore gives a relationship between the instantaneous correlation length and the rms velocity, but does not determine the magnitude of either. At low volume fractions we find that the scaling predicted by this model is in agreement with our data, as was also found in the sedimentation measurements of Segrè *et al.* [1997]. At larger volume fractions the scaling relationship becomes more complicated, because the viscosity of the suspension differs from that of the pure fluid and

becomes volume fraction dependent, and because the particle number fluctuations may become volume fraction dependent due to volume exclusion effects [Segrè *et al.* 2001]. If we use an estimate of the effective viscosity of the fluidized suspension, our data can be used to estimate the suppression of the number fluctuations in a correlation volume relative to random Poisson statistics. In contrast to Segrè *et al.* [2001], we find that the suppression of the number fluctuations in the correlation volume is independent of volume fraction, and significant even at small volume fractions. This result is supported by the recent direct measurements of the number fluctuations of Lei *et al.* [2001]. They find that the number fluctuations are suppressed at long length scales, suggesting that the decay of the number fluctuations is what cuts off the increase in the rms velocity with sample size and therefore sets the velocity correlation length. Thus the mechanism behind the instantaneous velocity correlation length is identified as the decay of the number fluctuations, which implies that the suppression of the number fluctuations in the correlation volume should be a constant value.

The second picture of the volume fraction scaling takes quite a different perspective. Instead of starting with rms velocity fluctuations in the correlation volume, we start by considering the relative motion of neighboring particles in the suspension. The relative velocity of particles separated by a distance r scales as $r^{1/2}$, until the growth of the fluctuations is suppressed at the instantaneous correlation length. Therefore, the magnitude of the rms particle velocity in the sample is set by both the magnitude of the relative velocity of nearest neighbors, and the correlation length ξ . We have found that the simple relationships predicted by this local view of the dynamics hold at all of the

Reynolds numbers, sample sizes and volume fractions we have investigated, implying that

ΔV_{rel} is a quantity that is of fundamental interest, setting the ratio $V_{rms}/\sqrt{\xi}$.

Theoretically, the challenges for a microscopic theory of the dynamics are the development of models for ΔV_{rel} and the instantaneous velocity correlation length.

To learn more about what sets ξ , we have investigated the system size dependence of the velocity fluctuations. The overall picture of the sample size dependence of the rms velocity that emerges from our data is qualitatively similar to that proposed by Brenner [1999]. As the smallest dimension of the cell is increased, both the instantaneous correlation length and the rms velocity fluctuations increase, but we see anisotropic behavior, which is not consistent with Brenner's simple scaling arguments. Nonetheless, Brenner's wall effect ideas do lead to predictions that are qualitatively consistent with our observations, in that we do find in our experiments that the increase in both the correlation length and rms velocity is controlled by the smallest dimension of the sample, even in cells that are already larger than the correlation length. As far as we know, our experiments are the first to report measurements of all three components of the rms velocity, with other workers only measuring the velocity in the vertical direction and along the largest horizontal direction. The weak $L_z^{1/6}$ dependence that we see in the x and y components of the rms velocity has not been observed in other experimental investigations in sedimenting suspensions [Nicolai & Guazzelli 1995 and Segrè *et al.* 1997], due largely to their rather large error bars. Our experiments also suggest that the increase in the rms velocity fluctuations with sample size is not without limit. For a given particle Reynolds number, as the cell size is increased, eventually the screening length due to wall effects will become

so large that the screening length due to inertial effects will dominate, and further increases in the sample size will not change the correlation length or the rms velocity. We see evidence of this inertial screening effect in the scaling of the instantaneous correlation length and rms velocity in the $Re = 7$ suspensions. Overall, our data give valuable new experimental evidence to elucidate the mechanisms that either slow down or cut off the divergence of V_{rms} with system size that was originally predicted by Caflisch & Luke [1985].

Appendices

A. Average Wall Reflection Coefficient

In Section 2.2.3, the boundary conditions for diffusing sound intensity were expressed in terms of the angle dependent wall reflection coefficient, $R(\theta)$. The wall reflection coefficient can be determined from the reflection coefficients for each boundary in the wall, as indicated in Fig. A.1. The calculation is complicated by the fact that there is mode conversion from the longitudinal to shear at the sample/wall and wall/water interfaces. Thus, we require 4 transmission coefficients and 9 reflection coefficients, which are given by [Brekhovskikh 1960 and Shutilov 1988 (with corrections)]:

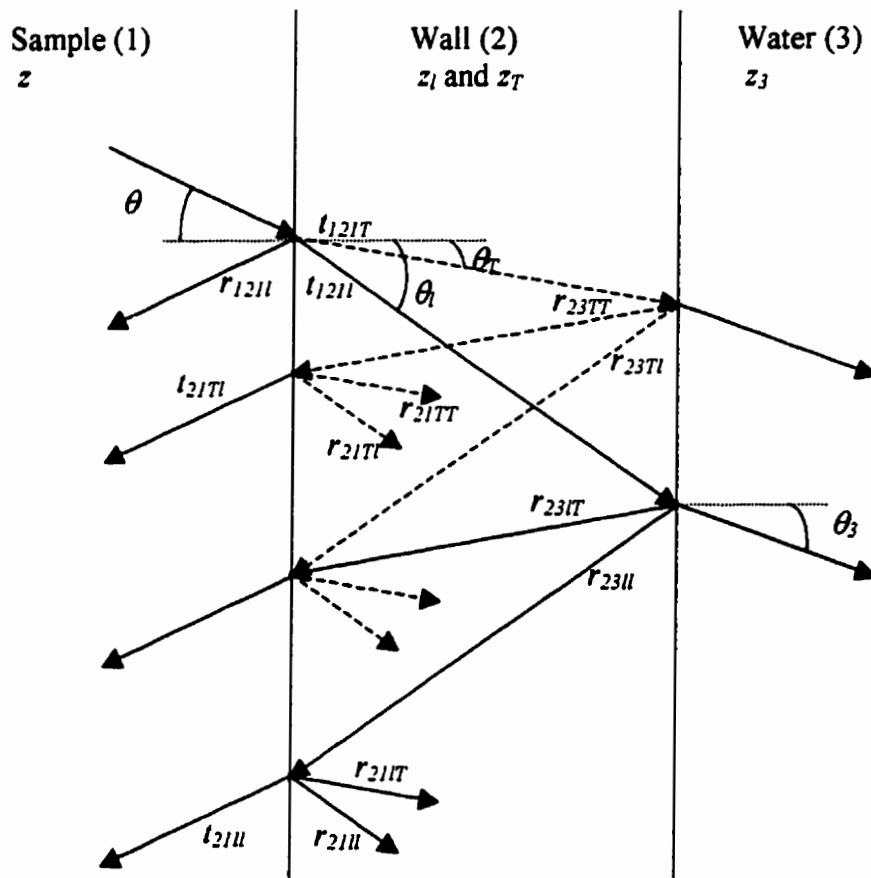


Figure A.1: Wall geometry for reflection coefficients.

$$t_{12ll} = \frac{2z \cos[2\theta_T]}{z_l \cos^2[2\theta_T] + z_T \sin^2[2\theta_T] + z} \left[\frac{\cos \theta}{\cos \theta_l} \right] \quad (\text{A.1})$$

$$t_{12lT} = \frac{-2z \sin[2\theta_T]}{z_l \cos^2[2\theta_T] + z_T \sin^2[2\theta_T] + z} \left[\frac{\cos \theta}{\cos \theta_T} \right] \quad (\text{A.2})$$

$$t_{21ll} = [1 - r_{21ll}] \frac{\cos \theta_l}{\cos \theta \cos[2\theta_T]} \quad (\text{A.3})$$

$$t_{21Tl} = -[1 - r_{21Tl}] \frac{1}{2 \sin \theta_T \cos \theta} \quad (\text{A.4})$$

$$r_{12ll} = \frac{z_l \cos^2[2\theta_T] + z_T \sin^2[2\theta_T] - z}{z_l \cos^2[2\theta_T] + z_T \sin^2[2\theta_T] + z} \quad (\text{A.5})$$

$$r_{23ll} = \frac{z_T \sin^2[2\theta_T] + z_3 - z_l \cos^2[2\theta_T]}{z_T \sin^2[2\theta_T] + z_3 + z_l \cos^2[2\theta_T]} \quad (\text{A.6})$$

$$r_{23lT} = \frac{c_T}{c_l} [1 - r_{23ll}] \frac{\sin[2\theta_l]}{\cos[2\theta_T]} \quad (\text{A.7})$$

$$r_{23TT} = \frac{z_l \cos^2[2\theta_T] + z_3 - z_T \sin^2[2\theta_T]}{z_l \cos^2[2\theta_T] + z_3 + z_T \sin^2[2\theta_T]} \quad (\text{A.8})$$

$$r_{23Tl} = \frac{z_T \sin \theta_T \cos^2 \theta_T}{z_l \cos^2[2\theta_T] + z_3 + z_T \sin^2[2\theta_T]} \left[\frac{\cos[2\theta_T]}{2 \cos[\theta_l]} \right] \quad (\text{A.9})$$

$$r_{21ll} = \frac{z_T \sin^2[2\theta_T] + z - z_l \cos^2[2\theta_T]}{z_T \sin^2[2\theta_T] + z + z_l \cos^2[2\theta_T]} \quad (\text{A.10})$$

$$r_{21Tl} = \frac{c_T}{c_l} [1 - r_{21ll}] \frac{\sin[2\theta_l]}{\cos[2\theta_T]} \quad (\text{A.11})$$

$$r_{21Tl} = \frac{z_l \cos^2[2\theta_T] + z - z_T \sin^2[2\theta_T]}{z_l \cos^2[2\theta_T] + z + z_T \sin^2[2\theta_T]} \quad (\text{A.12})$$

$$r_{21Tl} = \frac{z_T \sin \theta_T \cos^2 \theta_T}{z_l \cos^2[2\theta_T] + z + z_T \sin^2[2\theta_T]} \left[\frac{\cos[2\theta_T]}{2 \cos[\theta_l]} \right] \quad (\text{A.13})$$

$$\begin{aligned} z &= v_p [\{1 - \phi\} \rho_{fluid} + \phi \rho_{glass}] / \cos \theta \\ z_l &= c_l \rho_{wall} / \cos \theta_l \\ z_T &= c_T \rho_{wall} / \cos \theta_T \\ z_3 &= c_{water} \rho_{water} / \cos \theta_3 \end{aligned} \quad (\text{A.14})$$

Using Eqs. (A.1) to (A.14), and including the effect of the attenuation of the shear and longitudinal modes in the plastic walls, the net reflection coefficient $R(\theta)$ can be calculated to arbitrary order in the number of reflections. In practice, it was only necessary to run the calculation to 3rd order before the reflections were negligible. The angular dependent wall reflection coefficient can be substituted into Eq. (2.50), completing the description of the boundary conditions for the diffusion approximation.

B. DAWS Wall Corrections

In Section 4.2.1, the correction to the DAWS sampling time due to the extra travel time through the output wall is given by an angular average [Eq. (4.5)]

$$t_w = \left\langle \frac{L_{wall}}{c_{wall}} \left\{ \frac{1}{\cos[\theta_{wall}]} - 1 \right\} + \frac{d}{c_{water}} \left\{ \frac{1}{\cos[\theta_{water}]} - 1 \right\} \right\rangle_\theta,$$

where θ_{wall} and c_{wall} are the angle and velocity of either the shear (θ_T, c_T) or longitudinal (θ_l, c_l) mode in the wall. To perform the average we begin by assuming that the scattered waves are diffusive, which results in an approximately uniform angular distribution of the scattered intensity at the boundary of the sample. However, for an output angle θ , there are two rings at the sample-wall interface with radii given by $r_i(\theta)$ and $r_T(\theta)$, from which the sound will reach the hydrophone [Fig. B.1]. These two different radii result from the longitudinal and shear modes in the wall, and are given by

$$\begin{aligned} r_i(\theta) &= d \tan \theta_{water} + L_{wall} \tan \theta_l \\ r_T(\theta) &= d \tan \theta_{water} + L_{wall} \tan \theta_T . \end{aligned} \quad (\text{B.1})$$

This results in a weighting factor of $r(\theta)d\theta$ in the angular/mode average. Also weighting the average is the angle and mode dependent transmission coefficient of the wall, given by (not including multiple reflections in the walls, which are small):

$$\begin{aligned} T_i(\theta) &= t_{12u} t_{23u} \exp \left[-\frac{L_{wall}}{l_d \cos \theta_l} \right] \\ &= \frac{\cos \theta}{\cos \{\theta_{water}\} [z_T \sin^2[2\theta_T] + z_l \cos^2[2\theta_T] + z] [z_T \sin^2[2\theta_T] + z_l \cos^2[2\theta_T] + z_{water}]} \frac{4 z z_l \cos^2\{2\theta_T\} \exp \left[-\frac{L_{wall}}{l_d \cos \theta_l} \right]}{[z_T \sin^2[2\theta_T] + z_l \cos^2[2\theta_T] + z_{water}]} \end{aligned} \quad (\text{B.2})$$

for the longitudinal mode, and

$$T_T(\theta) = t_{12\pi} t_{23T} \exp\left[-\frac{L_{wall}}{l_{ar} \cos \theta_T}\right]$$

$$= \frac{\cos \theta}{\cos \{\theta_{water}\} [z_T \sin^2[2\theta_T] + z_l \cos^2[2\theta_T] + z]} \frac{4zz_T \sin^2\{2\theta_T\} \exp\left[-\frac{L_{wall}}{l_{ar} \cos \theta_T}\right]}{[z_T \sin^2[2\theta_T] + z_l \cos^2[2\theta_T] + z_{water}]} \quad (B.3)$$

for the shear mode. In addition, the hydrophone detector has an angle dependent response given approximately by $\cos[\theta_{water}]$. By using Snell's law, all of the angles can be expressed in terms of θ , and the average in Eq. (4.5) can be done numerically:

$$t_w = \frac{\int [2\pi r_l(\theta)] T_l(\theta) t_{wl}(\theta) \cos \theta_w d\theta + \int [2\pi r_T(\theta)] T_T(\theta) t_{wT}(\theta) \cos \theta_w d\theta}{\int [2\pi r_l(\theta)] T_l(\theta) \cos \theta_w d\theta + \int [2\pi r_T(\theta)] T_T(\theta) \cos \theta_w d\theta}, \quad (B.4)$$

where t_{wl} and t_{wT} are the angle dependent delay times for the longitudinal and shear modes respectively. The small contributions to the integral from r 's that are larger than the input beam radius are also eliminated from the integrals. The results of this average are presented in Table B.1.

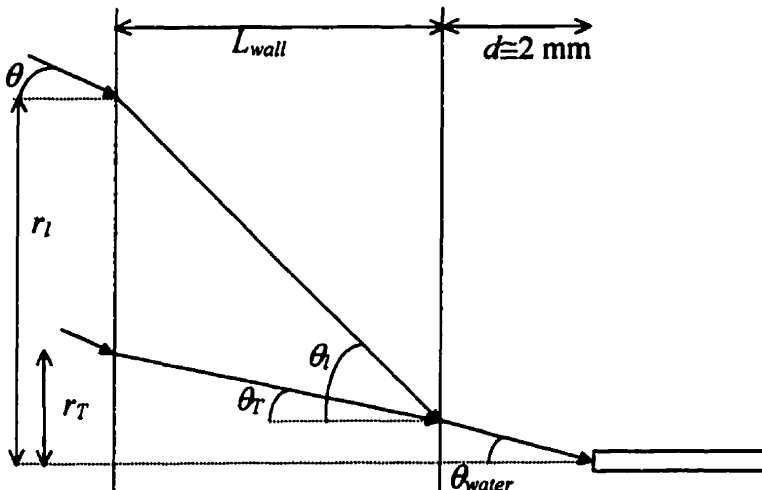


Figure B.1: Wall corrections for DAWS.

Walls	Sample v_p (mm/ μ s)	t_w (μ s)
$L_{wall} = 6.35 \text{ mm},$ $c_t = 2.75, c_T = 1.2 \text{ mm}/\mu\text{s}$	2.0	2.8
	1.5	2.6
$L_{wall} = 9.50 \text{ mm},$ $c_t = 2.75, c_T = 1.2 \text{ mm}/\mu\text{s}$	2.0	3.5
	1.5	3.4
$L_{wall} = 9.50 \text{ mm},$ $c_t = 2.23, c_T = 1.1 \text{ mm}/\mu\text{s}$	2.0	4.7
	1.5	4.4
$L_{wall} = 12.71 \text{ mm},$ $c_t = 2.23, c_T = 1.1 \text{ mm}/\mu\text{s}$	2.0	5.3
	1.5	4.9

Table B.1: DAWS timing corrections

C. Near-Field DSS Calculations

To relate the near-field DSS sampling times to the scattering angle, and \vec{q} , we need to consider the ray diagram in Fig. C.1. There is a range of input angles, with different amplitudes; for the 0.5 MHz plane wave transducer used for these measurements, the amplitude versus angle was approximately Gaussian with a -3 dB point at about $\pm 4^\circ$. The rays then enter the wall, where they are refracted into a different direction, θ_{op} . There is also coupling into a small amplitude shear wave, but the input angles from the transducer are small enough that this is negligible. As the rays enter the sample, they are refracted into an angle θ_o . At a depth, s , the sound is scattered towards the hydrophone, and on its way it passes through the exit wall as either a shear or longitudinal wave. The time it takes to travel this path, relative to the time it takes the ballistic pulse to travel straight to the hydrophone, is given by

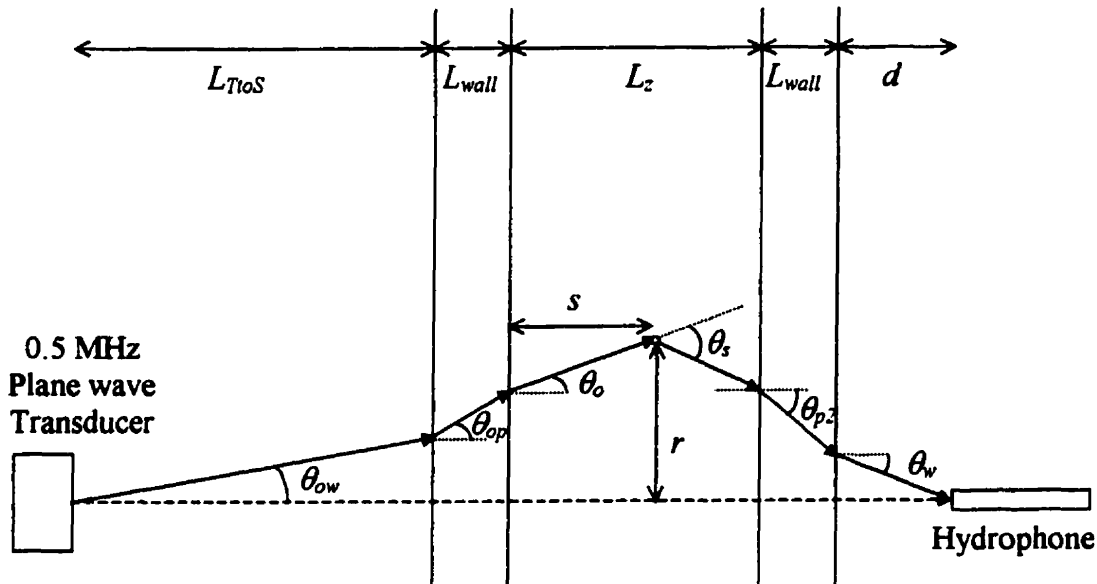


Figure C.1: Near field DSS timing calculation.

$$t_s = \frac{L_{Tos}}{c_w} \left[\frac{1}{\cos \theta_{ow}} - 1 \right] + \frac{L_{wall}}{c_{wall}} \left[\frac{1}{\cos \theta_{op}} - 2 \right] + \frac{L_{wall}}{c_{wall2} \cos \theta_{p2}} + \frac{s}{v_g \cos \theta_o} + \frac{L_z - s}{v_g \cos \{\theta_s - \theta_o\}} - \frac{L_z}{v_g} + \frac{d}{c_w} \left[\frac{1}{\cos \theta_w} - 1 \right], \quad (\text{C.1})$$

where the phase velocity in the exit wall can be that of either the longitudinal or shear modes. We can also write two equations for the scattering radius (the perpendicular distance to the scattering point from the ballistic path through the sample [Fig. C.1]):

$$r(s) = L_{Tos} \tan \theta_{ow} + L_{wall} \tan \theta_{op} + s \tan \theta_o \quad (\text{C.2})$$

and

$$r(s) = \{L - s\} \tan \{\theta_s - \theta_o\} + L_{wall} \tan \theta_{p2} + d \tan \theta_w. \quad (\text{C.3})$$

For a particular scattering depth (s), sampling time, and wall mode, Eqs. (C.1) to (C.3) can be inverted numerically to find the scattering angle (θ_s), the input angle (θ_{ow}), and the scattering radius. This gives a range of possible scattering and input angles (corresponding to the range of scattering depths from $s = 0$ to $s = L_z$) for each wall mode. For the longitudinal case, the range of possible angles is quite tight [Fig. C.2], so we use the mean value of the angles in the correlation function. However for the shear case, the range of angles is larger, so we must average the correlation function over the scattering depth (s). Since the field detected by the hydrophone is composed of a superposition of uncorrelated waves that have gone through the exit wall as either a shear or longitudinal mode, the field correlation function, for a particular sampling time t_s , can be decomposed into a shear and a longitudinal part:

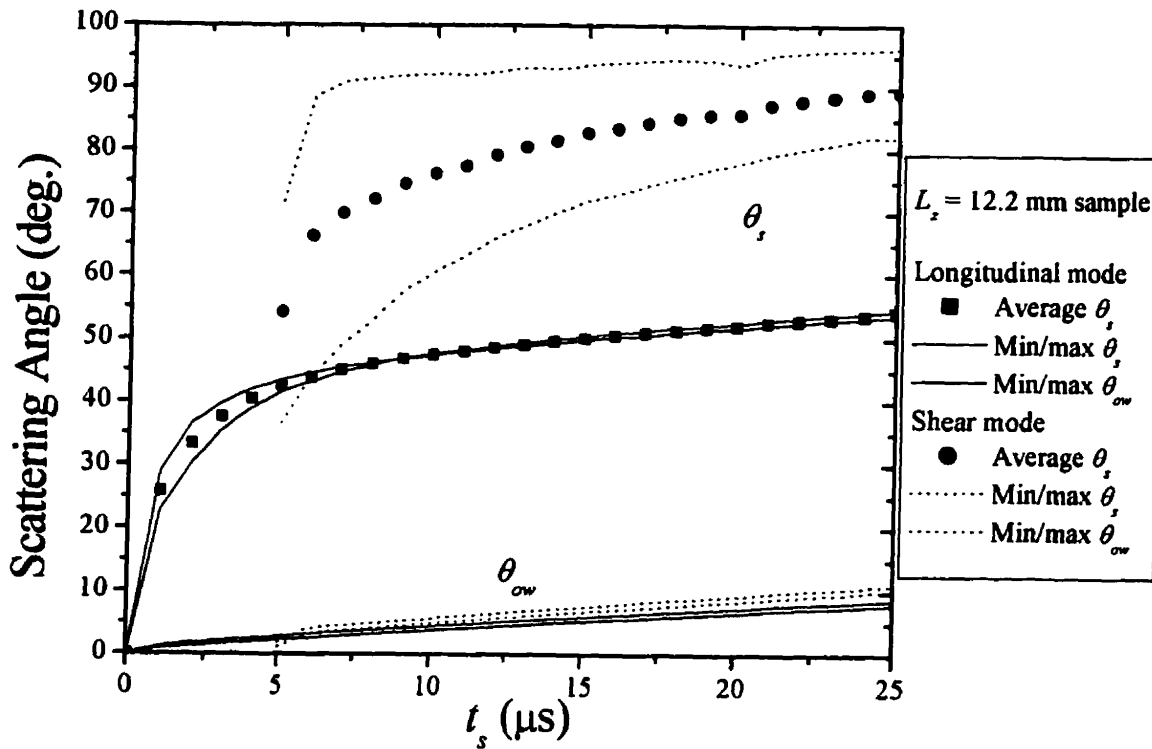


Figure C.2: Allowed scattering and input angles for the longitudinal and shear wall modes.

$$\begin{aligned}
 g_1(\tau) &= \frac{\langle \{\psi_L(t) + \psi_T(t)\} \{\psi_L^*(t+\tau) + \psi_T^*(t+\tau)\} \rangle}{\langle \{\psi_L(t) + \psi_T(t)\} \{\psi_L^*(t) + \psi_T^*(t)\} \rangle} \\
 &= \frac{\langle \psi_L(t) \psi_L^*(t+\tau) \rangle + \langle \psi_T(t) \psi_T^*(t+\tau) \rangle}{\langle \psi_L(t) \psi_L^*(t) \rangle + \langle \psi_T(t) \psi_T^*(t) \rangle} \\
 &\equiv \frac{g'_L(\tau) + g'_T(\tau)}{g'_L(0) + g'_T(0)}
 \end{aligned} \tag{C.4}$$

where

$$g'_L(\tau) = \frac{\int A_L(t') \langle e^{i\Delta\theta_L(\tau,t')} \rangle u^2(t'-t_s) dt'}{\int u^2(t'-t_s) dt'} \tag{C.5}$$

and

$$g'_T(\tau) = \frac{\iint u^2(t'-t_s) A_T(s, t') \langle e^{i\Delta\theta_T(\tau,s,t')} \rangle dt' ds}{\iint u^2(t'-t_s) dt' ds}. \tag{C.6}$$

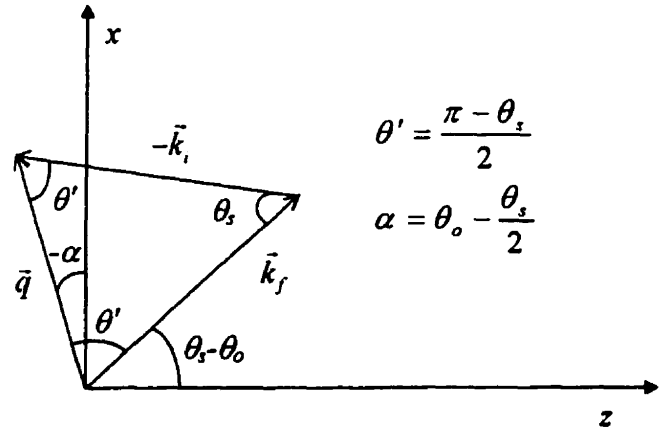


Figure C.3: Scattering vector geometry.
Coordinate system as in Figure 4.4.1.

Here, $A_L(t')$ and $A_T(s, t')$ give the relative intensities of the longitudinal and shear components respectively (the details of which will be discussed below), $\Delta\phi_L(\tau, t') = \bar{q}_L(t') \cdot \Delta\vec{r}(\tau)$ and $\Delta\phi_T(\tau, s, t') = \bar{q}_T(s, t') \cdot \Delta\vec{r}(\tau)$ are the phase changes due to the motion of the particles, and $u(t')$ is the input pulse envelope.

Figure C.3 shows the scattering vector, \bar{q} , which is inclined above the x - y plane by an angle $\alpha = \theta_o - \theta_s/2$. There is cylindrical symmetry about the z -axis, so the set of possible \bar{q} forms a cone. This gives

$$\begin{aligned} q_x &= q \cos \alpha \cos \beta \\ q_y &= q \cos \alpha \sin \beta \\ q_z &= q \sin \alpha , \end{aligned} \tag{C.7}$$

where β is the angle of rotation about the z -axis. The phase average can be expanded to give

$$\langle e^{-i\Delta\phi} \rangle = 1 - \frac{1}{2} \langle \Delta\phi^2 \rangle = 1 - \frac{1}{2} \left\langle \left(q_x \Delta r_x + q_y \Delta r_y + q_z \Delta r_z \right)^2 \right\rangle . \tag{C.8}$$

Substituting Eq. (C.7) into (C.8), averaging over β , and using

$$\begin{aligned}\langle \cos^2 \beta \rangle &= \langle \sin^2 \beta \rangle = \frac{1}{2} \\ \langle \cos \beta \rangle &= \langle \sin \beta \rangle = \langle \cos \beta \sin \beta \rangle = 0 \\ q^2 &= 4k^2 \sin^2 \left[\frac{\theta_s}{2} \right]\end{aligned}\quad (\text{C.9})$$

gives

$$\langle e^{-i\Delta\phi} \rangle = 1 - 2k^2 \sin^2 \left[\frac{\theta_s}{2} \right] \left\{ \left[\frac{1}{2} \langle \Delta r_x^2 \rangle + \frac{1}{2} \langle \Delta r_y^2 \rangle \right] \cos^2 \alpha + \langle \Delta r_z^2 \rangle \sin^2 \alpha \right\}. \quad (\text{C.10})$$

For the longitudinal case, α is about -17° , giving $\cos^2 \alpha = 0.92$ and $\sin^2 \alpha = 0.08$, which means that the contribution of the z -component to Eq. (C.10) is very small. For the shear case, α is about -30° , giving $\cos^2 \alpha = 0.75$ and $\sin^2 \alpha = 0.25$, which, given that $\langle \Delta r_z^2 \rangle$ is already small, and that the shear component is smaller than the longitudinal one, means that the z -component contributes very little to the phase change in this case too.

\therefore

$$\langle e^{-i\Delta\phi} \rangle = 1 - k^2 \sin^2 \left[\frac{\theta_s}{2} \right] \cos^2 \alpha \langle \Delta r^2 \rangle', \quad (\text{C.11})$$

where the measured mean square displacement $\langle \Delta r^2 \rangle'$ is approximately equal to the full 3-dimensional mean square displacement $\langle \Delta r^2 \rangle$ (because the z -component of the mean square displacement tends to be small),

$$\begin{aligned}\langle \Delta r^2 \rangle' &= \langle \Delta r_x^2 \rangle + \langle \Delta r_y^2 \rangle + 2 \tan^2 \alpha \langle \Delta r_z^2 \rangle \\ &\approx \langle \Delta r_x^2 \rangle + \langle \Delta r_y^2 \rangle \approx \langle \Delta r^2 \rangle.\end{aligned}\quad (\text{C.12})$$

The longitudinal component of the field autocorrelation function can be simplified

to

$$g_L(\tau) = \frac{\int u^2(t' - t_s) A_L dt'}{\int u^2(t' - t_s) dt'} \left[1 - k^2 \langle \Delta r^2(\tau) \rangle \frac{\int u^2(t' - t_s) A_L \sin^2 \left\{ \frac{\theta_s(t')}{2} \right\} \cos^2 \alpha dt'}{\int u^2(t' - t_s) A_L dt'} \right]$$

$$g_L(\tau) \equiv \bar{A}_L [1 - \bar{C}_L \langle \Delta r^2(\tau) \rangle]. \quad (\text{C.13})$$

The shear component can similarly be simplified to

$$g_T(\tau) = \frac{\int u^2(t' - t_s) \left[\int A_T ds \right] dt'}{\int u^2(t' - t_s) dt'} \left[1 - k^2 \langle \Delta r^2(\tau) \rangle \frac{\int u^2 \left[\int ds A_T \sin^2 \left\{ \frac{\theta_s}{2} \right\} \cos^2 \alpha \right] dt'}{\int u^2(t' - t_s) \left[\int A_T ds \right] dt'} \right]$$

$$g_T(\tau) \equiv \bar{A}_T \{1 - \bar{C}_T \langle \Delta r^2(\tau) \rangle\}. \quad (\text{C.14})$$

From Eq. (C.4), this gives an overall field correlation function of

$$g_1(\tau) = 1 - \frac{\bar{C}_L + \frac{\bar{A}_T}{\bar{A}_L} \bar{C}_T}{1 + \frac{\bar{A}_T}{\bar{A}_L}} \langle \Delta r^2(\tau) \rangle$$

$$\equiv 1 - \bar{C} \langle \Delta r^2(\tau) \rangle = \exp[-\bar{C} \langle \Delta r^2(\tau) \rangle]. \quad (\text{C.15})$$

The factor \bar{C} can be found by numerically evaluating the integrals in Eq. (C.13) and (C.14), given the weighting amplitudes and angles.

The angular dependence of the longitudinal weighting factor is given by

$$A_L = \int_{s=0}^{L_z} \left[A_{in} A_{sc} T_L \right]^2 r \cos \theta_w \frac{dr}{dt_s} ds$$

$$= L_z \left[A_{in} A_{sc} T_L \right]^2 r \cos \theta_w \left\{ \frac{dr}{dt_s} \right\} \quad (\text{C.16})$$

where A_{in} is the normalized amplitude of the input wave at the angle θ_{ow} , A_{sc} is the scattering amplitude from a coated glass bead at the scattering angle θ_s , T_l is the output wall transmission for a longitudinal wave at the angle θ_{pl} , the factor of $r \frac{dr}{dt_s}$ represents the scattering volume sampled in a time dt_s , and $\cos\theta_w$ is the angular response of the detector. The shear weighting factor can be written,

$$A_T = [A_{in} A_{sc} T_l]^2 r \cos\theta_w \frac{dr}{dt_s}. \quad (\text{C.17})$$

The angular dependence of the scattering amplitude from a single coated sphere in the effective medium can be calculated using the spectral function method [Section 2.1.3]. The wall transmission coefficients can be calculated by using Eq. (B.2) for the longitudinal case, but since the shear wall incident angles are larger than the longitudinal critical angle, Eq. (B.3) for the shear case must be modified to

$$T_l = \frac{\cos\{\theta_s - \theta_o\}}{\cos\{\theta_{water}\}} \cdot \frac{4z_T \sin^2\{2\theta_T\} \exp\left[-\frac{L_{wall}}{l_{at} \cos\theta_T}\right]}{\sqrt{\{z_T \sin^2\{2\theta_T\} + z_{water}\}^2 + |z_p|^2 \cos^4\{2\theta_T\}} \sqrt{\{z_T \sin^2\{2\theta_T\} + z\}^2 + |z_p|^2 \cos^4\{2\theta_T\}}} \quad (\text{C.18})$$

where

$$|z_p|^2 = \frac{z_l^2}{\left\{ \frac{c_l}{v_p} \sin\{\theta_s - \theta_o\} \right\}^2 - 1}$$

for $[\theta_s - \theta_o] > \theta_{critical,l}$.

By expressing all of the angle and amplitude factors as a function of the sampling

time and s , \bar{C}_L , \bar{C}_T , \bar{A}_L , and \bar{A}_T can all be calculated, as shown in Fig. C.4. Then, given the longitudinal and shear results, \bar{C} can be evaluated for both sample thicknesses. The results of this process are shown in Fig. 4.3.1.

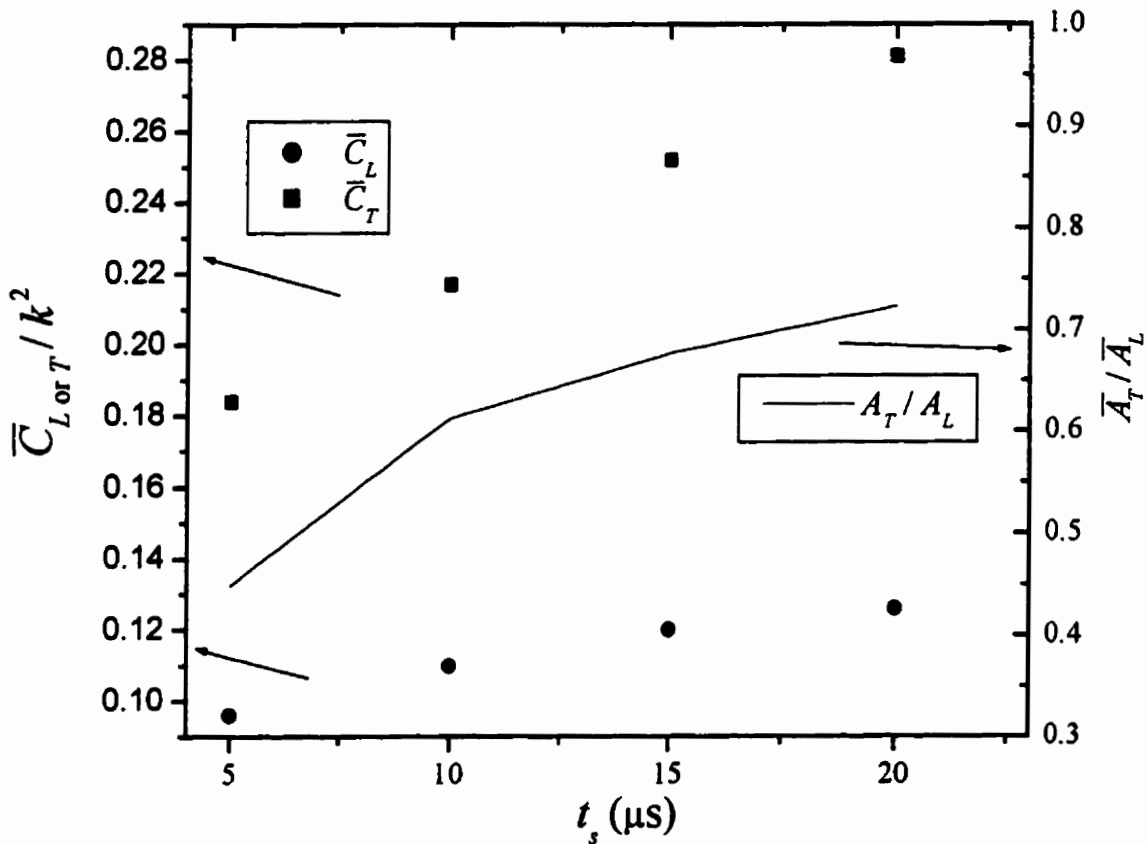


Figure C.4: Comparison of shear and longitudinal modes for the $L_z = 12.2$ mm sample.

D. Ballistic Results used in DAWS and DSS

60% Glycerol/water glass bead suspension					
<i>f</i> (MHz)	<i>v_p</i> (mm/μs)	<i>v_E</i> (mm/μs)	<i>l_r</i> (mm)	<i>v_E</i> (mm/μs)	<i>l'</i> (mm)
$\phi = 0.045$					
0.250	1.67	-	-	-	-
$\phi = 0.080$					
0.250	1.68	-	-	-	-
2.25	1.63	1.66	4.7	1.56	6.0
$\phi = 0.144$					
0.250	1.70	-	-	-	-
1.00	1.63	1.56	7.4	1.56	7.4
1.20	1.62	1.57	4.4	1.51	4.4
1.60	1.62	1.59	2.75	1.42	3.15
2.25	1.61	1.63	2.55	1.43	3.25
$\phi = 0.23$					
0.250	1.71	-	-	-	-
0.80	1.68	1.58	8.3	1.58	8.3
1.00	1.65	1.54	4.5	1.54	4.5
1.20	1.64	1.50	2.8	1.40	2.8
1.60	1.61	1.53	1.7	1.32	1.9
2.25	1.59	1.66	1.7	1.36	2.0

Table D.1: Ballistic parameters used for DAWS & DSS.

60% Glycerol/water glass bead suspension (cont.)

<i>f</i> (MHz)	<i>v_p</i> (mm/μs)	<i>v_E</i> (mm/μs)	<i>l_s</i> (mm)	<i>v_E</i> (mm/μs)	<i>l'</i> (mm)
$\phi = 0.30$					
0.250	1.75	-	-	-	-
0.80	1.67	1.53	6.6	1.53	6.6
1.00	1.63	1.45	3.5	1.39	3.5
1.20	1.59	1.42	2.1	1.21	2.2
1.60	1.55	1.48	1.3	1.20	1.5
2.25	1.55	1.65	1.3	1.34	1.4
$\phi = 0.40$					
0.250	1.80	-	-	-	-
0.80	1.69	1.50	5.1	1.50	5.1
1.00	1.62	1.36	2.7	1.24	2.7
1.20	1.57	1.32	1.6	1.04	1.7
1.60	1.51	1.38	0.98	1.05	1.14
$\phi = 0.50$					
0.250	1.87	-	-	-	-
0.80	1.76	1.45	4.25	1.45	4.25
1.00	1.65	1.28	2.1	1.11	2.2
1.20	1.56	1.22	1.3	0.891	1.4

Table D.1 (cont.): Ballistic parameters used for DAWS & DSS.

75% Glycerol/water glass bead suspension

<i>f</i> (MHz)	<i>v_p</i> (mm/μs)	<i>v_E</i> (mm/μs)	<i>l_s</i> (mm)	<i>v_E</i> (mm/μs)	<i>l'</i> (mm)
$\phi = 0.045$					
0.250	1.85	-	-	-	-
$\phi = 0.080$					
0.250	1.85	-	-	-	-
0.80	1.84	1.80	21	1.80	21
1.00	1.83	1.79	14	1.79	14
1.20	1.81	1.77	8.8	1.73	9.5
1.60	1.81	1.79	5.2	1.68	6.8
2.25	1.80	1.78	4.2	1.67	5.5
$\phi = 0.144$					
0.250	1.87	-	-	-	-
0.80	1.83	1.78	12.5	1.78	12.5
1.00	1.82	1.72	7.6	1.72	7.6
1.20	1.80	1.72	6.2	1.65	6.2
1.60	1.78	1.74	2.5	1.55	2.85
2.25	1.77	1.76	2.3	1.57	3.1
$\phi = 0.23$					
0.250	1.90	-	-	-	-
0.80	1.84	1.79	6.75	1.79	6.75
1.00	1.81	1.65	4.25	1.65	4.25
1.20	1.78	1.63	2.8	1.52	2.8
1.60	1.79	1.67	1.4	1.44	1.5
2.25	1.71	1.51	1.45	1.28	1.8

75% Glycerol/water glass bead suspension (cont.)

<i>f</i> (MHz)	<i>v_p</i> (mm/μs)	<i>v_E</i> (mm/μs)	<i>l_r</i> (mm)	<i>v_E</i> (mm/μs)	<i>l'</i> (mm)
$\phi = 0.30$					
0.250	1.97	-	-	-	-
0.80	1.84	1.72	6.5	1.72	6.5
1.00	1.81	1.59	3.2	1.59	3.2
1.20	1.77	1.60	2.0	1.47	2.0
1.60	1.70	1.59	1.4	1.21	1.5
2.25	1.67	1.65	1.4	1.34	1.7
$\phi = 0.40$					
0.250	2.03	-	-	-	-
0.80	1.84	1.70	4.2	1.70	4.2
1.00	1.77	1.49	2.3	1.49	2.3
1.20	1.73	1.53	1.1	1.39	1.2
1.60	1.67	1.51	0.69	1.04	0.77
2.25	1.62	1.74	0.70	1.32	0.83
$\phi = 0.50$					
0.250	2.07	-	-	-	-
0.80	1.88	1.59	4.0	1.59	4.0
1.00	1.79	1.41	1.6	1.41	1.6
1.20	1.74	1.43	0.90	1.29	0.98
1.60	1.60	1.38	0.55	0.869	0.65
2.25	1.58	1.70	0.55	1.22	0.65

94% Glycerol/water glass bead suspension

<i>f</i> (MHz)	<i>v_p</i> (mm/μs)	<i>v_E</i> (mm/μs)	<i>l_s</i> (mm)	<i>v_E</i> (mm/μs)	<i>l'</i> (mm)
$\phi = 0.20$					
0.415	1.87	1.90	60	-	-
1.0	1.82	1.64	10	1.64	10
1.6	1.76	1.70	3.0	1.46	3.2
2.25	1.76	1.57	2.5	1.33	3.1
$\phi = 0.30$					
0.415	1.90	1.86	35	-	-
0.80	1.85	1.72	5.3	1.72	5.3
1.0	1.81	1.65	3.1	1.65	3.1
1.6	1.73	1.60	0.95	1.22	1.0
2.25	1.71	1.70	0.84	1.38	1.0
$\phi = 0.40$					
0.415	1.95	1.97	31	-	-
0.80	1.86	1.67	3.8	1.67	3.8
1.0	1.81	1.57	2.1	1.57	2.1
1.6	1.70	1.47	0.70	1.01	0.78
2.25	1.64	1.59	0.75	1.21	0.89
$\phi = 0.50$					
0.415	2.01	1.86	20	-	-
0.80	1.89	1.62	3.3	1.62	3.3
1.0	1.81	1.50	1.6	1.50	1.6
1.6	1.66	1.55	0.50	0.977	0.59
2.25	1.57	1.58	0.56	1.14	0.66

References

- M. P. van Albada, B. A. van Tiggelen, A. Lagendijk and A. Tip, "Speed of Propagation of Classical Waves in Strongly Scattering Media", *Phys. Rev. Lett.* **66**, 3132, 1991.
- N. W. Ashcroft and N. D. Mermin, *Solid State Physics*, Saunders College, 1976.
- B. J. Berne and R. Pecora, *Dynamic Light Scattering*, John Wiley and Sons, 1976.
- D. Bicout and G. Maret, "Multiple light scattering in Taylor-Couette flow", *Physica A* **210**, 87, 1994.
- D. Bicout and R. Maynard, "Diffusing wave spectroscopy in inhomogeneous flows", *Physica A* **199**, 387, 1993.
- L. Brekhovskikh, *Waves in Layered Media*, Academic Press, 1960.
- M. P. Brenner, "Screening mechanisms in sedimentation", *Phys. of Fluids* **11**, 754, 1999.
- K. Busch, C. M. Soukoulis and E. N. Economou, "Transport and scattering mean free paths of classical waves", *Phys. Rev. B* **50**, 93, 1994.
- K. Busch and C. M. Soukoulis, "Transport Properties of Random Media: A New Effective Medium Theory", *Phys. Rev. Lett.* **75**, 3442, 1995.
- K. Busch and C. M. Soukoulis, "Transport Properties of Random Media: An Energy-Density CPA Approach", *Phys. Rev. B* **54**, 893, 1996.
- R. E. Caflisch and J. H. C. Luke, "Variance in the sedimentation speed of a suspension", *Phys. Fluids* **28**, 759, 1985.
- H. S. Carslaw and J. C. Jaeger, *Conduction of Heat in Solids*, 2nd edition, Oxford University Press, London, 1959.
- B. Chu, *Laser Light Scattering*, 2nd edition, Academic Press, 1991.
- M. L. Cowan, J. H. Page and D. A. Weitz, "Velocity Fluctuations in Fluidized Suspensions Probed by Ultrasonic Correlation Spectroscopy", *Phys. Rev. Lett.* **85**, 453, 2000.
- M. L. Cowan, K. Beaty, J. H. Page, Z. Liu and Ping Sheng, "Group velocity of acoustic waves in strongly scattering media: Dependence on the volume fraction of scatterers", *Phys. Rev. E* **58**, 6626, 1998.

- M. L. Cowan, "Group velocity in strongly scattering media", *Phys. in Canada* **53(4)**, 145-6, 1997.
- J. F. Davidson, R. Clift and D. Harrison, editors, *Fluidization*, 2nd edition, Academic Press, 1985.
- A. K. Didwania and G. M. Homsy, "Flow regimes and flow transitions in liquid fluidized beds", *Int. J. Multiphase Flow*, **7**, 563, 1981.
- DOW Chemical, *OPTIM Glycerine*, 1989.
- D. J. Durian, "The Influence of Boundary Reflection and Refraction on Diffusive Photon Transport", *Phys. Rev. E* **50**, 857, 1994.
- W. C. Elmore and M. A. Heald, *Physics of Waves*, McGraw-Hill, 1969.
- F. J. Flanigan, *Complex Variables: Harmonic and Analytic Functions*, Dover, 1972.
- J. P. Fouque, editor, *Diffuse Waves in Complex Media*, NATO Science Series C, Vol. 531, 1999.
- C. G. B. Garrett and D. E. McCumber, "Propagation of a Gaussian Light Pulse through an Anomalous Dispersion Medium", *Phys. Rev. A* **1**, 305, 1970.
- A. Z. Genack, P. Sebbah, M. Stoytchev and B. A. van Tiggelen, "Statistics of Wave Dynamics in Random Media", *Phys. Rev. Lett.* **82**, 715, 1999.
- J. W. Goodman, *Statistical Optics*, Wiley, 1985.
- J.M. Ham, S. Thomas, E. Guazzelli, G. M. Homsy and M. C. Anselmet, "An experimental study of the stability of liquid-fluidized beds", *Int. J. Multiphase Flow* **16**, 171, 1990.
- J. M. Ham and G. M. Homsy, "Hindered Settling and Hydrodynamic Dispersion in Quiescent Sedimenting Suspensions", *Int. J. Multiphase Flow* **14**, 533, 1988.
- J. P. Hansen and I. R. McDonald, *Theory of Simple Liquids*, Academic, 1976.
- E. J. Hinch, in *Disorder in Mixing*, edited by E. Guyon *et al.*, Kluwer Academic, p. 153, 1988.
- M. K. Hinders, "Extinction of sound by spherical scatterers in a viscous fluid", *Phys. Rev. A* **43**, 5628, 1991.
- A. Ishimaru, *Wave Propagation and Scattering in Random Media*, Academic Press, 1978.

Xiaodun Jing, Ping Sheng and M. Zhou, "Acoustic and electromagnetic quasimodes in dispersed random media", *Phys. Rev. A* **46**, 6513, 1992.

I. P. Jones, *Acoustic Correlation Spectroscopy of Strongly Scattering Media*, M.Sc. thesis, University of Manitoba, 1996.

D. L. Koch and E. S. G. Shaqfeh, "Screening in sedimenting suspensions", *J. Fluid Mech.* **224**, 275, 1991.

D. L. Koch, "Hydrodynamic diffusion in dilute sedimenting suspensions at moderate Reynolds numbers", *Phys. Fluids A* **5**, 1141, 1993.

R. H. J. Kop, Pedro de Vries, R. Sprik and Ad Lagendijk, "Observation of Anomalous Transport of Strongly Multiple Scattered Light in Thin Disordered Slabs", *Phys. Rev. Lett.* **79**, 4369, 1997.

A. J. C. Ladd, "Dynamical simulations of sedimenting spheres", *Phys. Fluids A* **5**, 299, 1993.

A. J. C. Ladd, "Hydrodynamic Screening in Sedimenting Suspensions of non-Brownian Spheres", *Phys. Rev. Lett.* **76**, 1392, 1996.

A. J. C. Ladd, "Sedimentation of homogeneous suspensions of non-Brownian spheres", *Phys. Fluids* **9**, 491, 1997.

A. Lagendijk and B. A. van Tiggelen, "Resonant multiple scattering of light", *Physics Reports* **270**, 143-215, 1996.

P. -A. Lemieux, M. U. Vera and D. J. Durian, "Diffusing-light spectroscopies beyond the diffusion limit: The role of ballistic transport and anisotropic scattering", *Phys. Rev. E* **57**, 4498, 1998.

X. Lei, B. J. Ackerson and P. Tong, "Settling Statistics of Hard Sphere Particles", *Phys. Rev. Lett.* **86**, 3300, 2001.

A. Levine, S. Ramaswamy, E. Frey and R. Bruinsma, "Screened and Unscreened Phases in Sedimenting Suspensions", *Phys. Rev. Lett.* **81**, 5944, 1998.

F. C. MacKintosh and S. John, "Diffusing-wave spectroscopy and multiple scattering of light in correlated random media", *Phys. Rev. B* **40**, 2383, 1989.

G. Maret and P. E. Wolf, "Multiple Light Scattering from Disordered Media. The Effect of Brownian Motion of Scatterers", *Z. Phys. B* **65**, 409, 1987.

- N. Menon and D. J. Durian, "Diffusing-Wave Spectroscopy of Dynamics in a Three-Dimensional Granular Flow", *Science* **275**, 1920, 1997.
- H. Nicolai, B. Herzhaft, E. J. Hinch, L. Oger and E. Guazzelli, "Particle velocity fluctuations and hydrodynamic self-diffusion of sedimenting non-Brownian spheres", *Phys. Fluids* **7**, 12, 1995.
- H. Nicolai and E. Guazzelli, "Effect of the vessel size on the hydrodynamic diffusion of sedimenting spheres", *Phys. Fluids* **7**, 3, 1995.
- J. H. Page, M. L. Cowan and D. A. Weitz, "Diffusing acoustic wave spectroscopy of fluidized suspensions", *Physica B* **279**, 130, 2000.
- J. H. Page, I. P. Jones, H. P. Schriemer, M. L. Cowan, Ping Sheng and D. A. Weitz, "Diffusive transport of acoustic waves in strongly scattering media", *Physica B* **263-264**, 37, 1999.
- J. H. Page, Ping Sheng, H. P. Schriemer, I. Jones, X. Jing and D. A. Weitz, "Group Velocity in Strongly Scattering Media", *Science* **271**, 634, 1996.
- J. H. Page, H. P. Schriemer, A. E. Bailey and D. A. Weitz, "Experimental test of the diffusion approximation for multiply scattered sound", *Phys. Rev. E* **52**, 3106, 1995.
- Panametrics, *Ultrasonic Transducers*, Panametrics Inc., 1991.
- Y. Peysson and E. Guazzelli, "An experimental investigation of the intrinsic convection in a sedimenting suspension", *Phys. Fluids* **10**, 44, 1998.
- D. J. Pine, D. A. Weitz, P. M. Chaikin and E. Herbolzheimer, "Diffusing-Wave Spectroscopy", *Phys. Rev. Lett.* **60**, 1134, 1988.
- W. H. Press, S. A. Teukolsky, W. T. Vetterling and B. P. Flannery, *Numerical Recipes in C*, Second Edition, Cambridge University Press, 1992.
- V. M. Ristic, *Principles of Acoustic Devices*, John Wiley and Sons, New York, 1983.
- W. B. Russel, D. A. Saville and W. R. Schowalter, *Colloidal Dispersions*, Cambridge University Press, 1989.
- L. Ryzhik, G. Papanicolaou and J. Keller, "Transport equations for elastic and other waves in random media", *Wave Motion* **24**, p. 327-370, 1996.
- H. P. Schriemer, M. L. Cowan, J. H. Page, Ping Sheng, Z. Liu and D. A. Weitz, "Energy Velocity of Diffusing Waves in Strongly Scattering Media", *Phys. Rev. Lett.* **79**, 3166, 1997.

H. P. Schriemer, *Ballistic and Diffusive Transport of Acoustic Waves in Random Media*, Ph.D. thesis, University of Manitoba, 1997.

P. N. Segrè, E. Herbolzheimer and P. M. Chaikin, "Long-Range Correlations in Sedimentation", *Phys. Rev. Lett.* **79**, 2574, 1997.

P. N. Segrè, F. Loi, P. Umbanhowar and D. A. Weitz, "An effective gravitational temperature for sedimentation", *Nature* **409**, 594, 2001.

A. R. Selfridge, "Approximate Material Properties in Isotropic Materials", *IEEE Transactions on Sonics and Ultrasonics* **SU-32**, 381, 1985.

Ping Sheng, *Introduction to Wave Scattering, Localization, and Mesoscopic Phenomena*, Academic Press, 1995.

V. A. Shutilov, *Fundamental Physics of Ultrasound*, Gordon and Breach Science Publishers, 1988.

S. Temkin, "Viscous attenuation of sound in dilute suspensions of rigid particles", *J. Acoust. Soc. Am.* **100**, 825, 1996.

B. A. van Tiggelen, A. Lagendijk, M. P. van Albada and A. Tip, "Speed of light in random media", *Phys. Rev. B* **45**, 12233, 1992.

B. A. van Tiggelen, P. Sebbah, M. Stoytchev and A. Z. Genack, "Delay-time statistics for diffuse waves", *Phys. Rev. E* **59**, 7166, 1999.

P. Tong, W. I. Goldburg and C. K. Chan, "Turbulent transition by photon-correlation spectroscopy", *Phys. Rev. A* **37**, 2125, 1988.

H. Voigt and S. Hess, "Comparison of the intensity correlation function and the intermediate scattering function of fluids: a molecular dynamics study of the Siegert relation", *Physica A* **202**, 145, 1994.

R. L. Weaver and W. Sachse, "Diffusion of ultrasound in a glass bead slurry", *J. Acoust. Soc. Am.* **97**, 2094, 1995.

D. A. Weitz, D. J. Pine, P. N. Pusey and R. J. A. Tough, "Nondiffusive Brownian Motion Studied by Diffusing-Wave Spectroscopy", *Phys. Rev. Lett.* **63**, 1747, 1989.

J. Z. Xue, E. Herbolzheimer, M. A. Rutgers, W. B. Russel and P. M. Chaikin, "Diffusion, Dispersion, and Settling of Hard Spheres", *Phys. Rev. Lett.* **69**, 1715, 1992.

A. G. Yodh, P. D. Kaplan and D. J. Pine, "Pulsed diffusing-wave spectroscopy: High resolution through non-linear optical gating", *Phys. Rev. B* **42**, 4744, 1990.

Z. Q. Zhang, I. P. Jones, H. P. Schriemer, J. H. Page, D. A. Weitz, and Ping Sheng,
“Wave transport in random media: The ballistic to diffusive transition”, *Phys. Rev. E* **60**,
4843.

J. X. Zhu, D. J. Pine and D. A. Weitz, “Internal reflection of diffusive light in random
media”, *Phys. Rev. A* **44**, 3948, 1991.